Rapport SGC 099

GAS CO-FIRING FOR NO_x REDUCTION IN COAL-FIRED BOILERS

Fredrik Brogaard

Lund University

April 1999

Rapport SGC 099
ISSN 1102-7371
ISRN SGC-R--99--SE

Rapport SGC 099

GAS CO-FIRING FOR NO_x REDUCTION IN COAL-FIRED BOILERS

Fredrik Brogaard

Lund University

April 1999

FOREWORD

RD&D-projects performed by the Swedish Gas Centre, will usually be presented in reports, available to each and everyone who wants to share the results of a project.

SGC prints and publishes the reports but the writers of each report are responsible for the accuracy of the content. Everyone making use of any description, results etc, will do this on his own responsibility. Excerpts from a report may be used if the source is indicated

A register, showing SGC-reports published to date, will be found at the end of this report.

Swedish Gas Centre (SGC) is a joint venture of energy gas business organisations. SGC:s primary mission is to co-ordinate the joint Research, Development and Demonstration (RD&D) efforts that are performed within the Swedish gas industry. The shareholders of SGC are: The Swedish Gas Association, Sydgas, Sydkraft, Gothenburg Energy, Lund Energy and Helsingborg Energy.

This project has been founded by:

Sydgas
NUTEK

SWEDISH GAS CENTRE

Johan Rietz
President

Sammanfattning

Denna rapport dokumenterar ett projekt vars syfte var att reducera NO_x-emissioner från koleldade kraftverk genom att samelda kol och naturgas. Projektet löper från försöksarbete i International Combustion Inc:s testanläggning med enstaka brännare och dess utvärdering till fullskaleinstallation med brännare på flera nivåer i det tangentialeldade Västhamnsverket i Helsingborg.

Under försöksarbetet testades och jämfördes fyra olika brännare och brännarkonfigurationer i NO_x-reducerande hänseende. Basfallet för jämförelsen var den så kallade datumbrännaren, ursprungligen installerad i Västhamnsverket, vilken ger en helt oförankrad flamma. Brännare nummer två var FAN-brännaren (*Flame Attached Nozzle*), en låg-NO_x-brännare med en som antyds av namnet flamma förankrad på brännarmunstycket. Brännarfall tre och fyra var en modifiering av FAN-brännaren med sidomunstycken för gaseldning arrangerade på sådant sätt att gas och sekundärluft blandas. Fall tre var sålunda sameldning med kol och naturgas och fall fyra eldning med enbart kol i den modifierade FAN brännaren.

Försöksarbetet uppenbarade en 20-25 procentig reduktion av NO_x-emissionerna när den modifierade FAN-brännaren sameldades med 10 % naturgas, baserat på värmevärde, jämfört med endast koleldning i samma brännare. Detta betyder att en NO_x-reduktion utöver den 10 procentiga vinsten genom ersättning av kol med naturgas kunde konstateras. Termiskt NO_x uteslöts som förklaring till detta fenomen eftersom inga signifikanta temperaturskillnader vid brännarvägg eller brännarmunstycke kunde uppmätas mellan de båda fallen.

För att finna förklaring till denna reduktion utvecklades en CFD-modell med hjälp av fluidmekanikprogrammet FLUENT v.4.3. Den geometriska modellen baserades i detalj på den tredimensionella utformningen av den modifierade FAN-brännaren utifrån originalritningar. Den inkluderade alla väsentliga delar av brännaren och täckte åtta meter av eldstaden för att rymma hela flamlängden så som den mätts upp under försöksarbetet. Förutom balansekvationer för rörelsemängd, kemiska specier och energi inkluderade den matematiska modellen kompletterande modeller för turbulens, turbulent reaktionshastighet, dispergerad kolpartikelfas och värmestrålning. Modellen omfattade nära 36000 beräkningsceller och löstes med finita volymsmetoden.

Kvävekemin representerades med en högtemperaturapproximation av empiriska kinetiska uttryck utvecklade av Mitchell och Tarbell [22] innefattande N_2, HCN, NH_3 och NO. Termiskt NO_x togs inte med på grund av dess relativa obetydlighet vid jämförelse av de två brännarfallen. En möjligen mera tveksam exkludering var uteslutandet av heterogena NO_x-reaktioner men det fanns ingen praktisk eller tillförlitlig metod att ta med dessa.

Den 20-25 procentiga reduktionen reproducerades av modellen och kunde förklaras genom förbrukning av sekundärluft nära brännaren till följd av naturgasförbränning. Denna förbrukning var av stor vikt för NO_x-reduktionen på grund av skapandet av en lågstökiometrisk zon i ett område kritiskt för bildandet av NO_x. Vidare syntes det osannolikt att reburningreaktioner skulle vara av någon större betydelse för NO_x-reduktionen sedan naturgasen förbrukades i ett område där endast lite NO_x bildades.

Tyvärr kunde de intressanta resultaten från försöksarbetet inte reproduceras i fullskala i Västhamnsverket. En orsak till detta kan vara en övervärdering av den modifierade FAN brännarens NO_x-reducerande kapacitet jämfört med datumbrännaren. Även om sameldning

med 10 % naturgas i den modifierade FAN-brännaren gav 20-25 % reduktion jämfört med eldning med endast kol i samma brännare gav inte det sistnämnda fallet någon reduktion jämfört med datumbrännaren utan tvärtom en ökad emission av NO_x. Detta antogs bero på högre temperaturnivåer i brännarens närhet i det modifierade FAN-brännarfallet (högre nivåer av termiskt NO_x) jämfört med datum- och original FAN-brännare. Man antog att temperaturskillnaderna var en effekt av försöksanläggningens konstruktion och att dessa inte skulle uppstå i fullskaleoperation.

För att jämföra original och modifierad FAN-brännare togs sidomunstyckena i den geometriska beräkningsmodellen bort och en simulering av original FAN-brännarens flamstruktur utfördes. Simuleringen gav en förklaring till de markanta temperaturskillnaderna i de båda fallen. När sidomunstyckena tillfogas brännaren förstoras sekundärluftsintagets area vilket skapar en kraftigare luftcirkulation nära brännaren. Detta leder till högre temperaturer vid brännarvägg och brännarmunstycke vilket konstaterats under det praktiska försöksarbetet. Dessutom förändrar sidomunstyckena fluiddynamiken i brännarens närhet vilket har konsekvenser för brännarens NO_x-prestanda. Slutsatsen är att original FAN-brännaren vilken gav mindre NO_x-emissioner än datumbrännaren inte kan göras ekvivalent med den modifierade FAN-brännaren i NO_x-hänseende enbart genom en temperaturkorrelation. Skillnaden mellan original och modifierad FAN-brännare bör istället ses i ljuset av fluiddynamiska förändringar uppkomna genom tillfogandet av sidomunstycken för gasbrännare.

Summary

This report describes a project attempting to reduce NO_x emissions from coal fired boilers by co-firing natural gas in close connection to the coal burners. The project runs from the test rig work at International Combustion Inc.'s single burner, front wall fired, test rig and its evaluation to the full scale installation at Västhamnsverket in Helsingborg.

During the test rig work four types of burners and burner configurations were compared regarding NO_x reducing capability. The base line case was the datum burner, the burner originally installed at Västhamnsverket, which gives a totally detached flame. The second was the flame attached nozzle burner (FAN burner) which is a low NO_x burner developed by Int. Comb. Inc. with, as indicated by its name, a flame attached to the burner nozzle. The third and fourth were a modification of the FAN burner with compartments for gas burners attached to the side of the burner so as to mix gas and secondary air. This modification is referred to as the modified FAN burner in the report. Case three was then the modified FAN burner with gas co-firing and case four coal only firing.

The test work revealed a 20-25 % reduction of NO_x when co-firing 10 % gas based on heat input with the modified FAN burner compared to the modified FAN burner firing coal only. This means that there was an accelerated NO_x reduction exceeding the 10 % nitrogen in coal lost when replacing coal for gas. Thermal NO_x was excluded as the source of this reduction since the structure of the flames were approximately the same and burner wall and nozzle temperatures were in the same range for both cases.

To find the explanation for the measured reduction, a CFD-model was developed using the software package FLUENT v.4.3. The model was based on the full three dimensional geometry of the modified FAN burner from original drawings. It included essential parts of the burner and covered eight metres of the furnace to contain the entire flame length as measured in the test rig. Besides the standard balance equations for momentum, chemical species and enthalpy submodels for turbulence, turbulent reaction rate, dispersed phase and radiation were included in the model. The model comprising nearly 36000 computational cells was solved with the finite volume technique.

The nitrogen chemistry was predicted with an empirical reaction scheme developed by Mitchell and Tarbell[22], approximated to high temperatures, including N_2, HCN, NH_3 and NO. Thermal NO_x was not included in the scheme because of its relative unimportance when comparing the two flame cases. A perhaps more severe restriction was the exclusion of heterogeneous NO_x reactions, but there was no practical and reliable way to include these.

The 20-25 % reduction was reproduced by the model and was explained by consumption of secondary air by the natural gas portion close to the burner. This consumption was essential for the reduction since it created a low stoichiometric zone in the area critical for NO_x formation. Furthermore it did not seem likely from the calculated flame structure that reburning reactions had a major part in the reduction, since natural gas was burned out in an area where little NO_x was formed. On the contrary, the reduction effect was caused by preburning gas with air critical for NO_x formation. Finally, if reburning can be regarded as *in furnace* fuel staging, the co-firing technique should be called *in burner* fuel staging resembling *in burner* air staging in low NO_x burners.

Unfortunately the interesting test rig results could not be reproduced in the multi-level, tangentially-fired burner system at Västhamnsverket. One cause of this could be an overestimation of the modified FAN burner reduction capacity, firing coal only, compared to the datum burner. Although co-firing 10 % gas gave a 20-25 % reduction compared to coal only firing in the modified FAN burner case, the coal only firing modified FAN burner did not give any reduction compared to the datum burner. This fact was thought to be due to the higher temperatures in the burner vicinity created in the modified FAN burner case compared to the datum and unmodified FAN burner case, i.e. an increase in thermal NO_x in the modified FAN burner case. This was not thought to occur in full scale operation.

To compare the original FAN burner with the modified FAN burner, gas burner compartments were removed from the model and the original FAN burner flame structure was calculated with data from the test rig work. This calculation gave an explanation for the increased near burner temperatures in the case of the modified FAN burner. When the gas burner compartments were added to the burner the secondary air inlet area was increased, which created a more vigorous recirculation close to the burner. This leads to higher temperatures at the burner wall and burner nozzle as was also found during the test work. In addition, the inclusion of the gas burner compartements changed the fluid dynamics in the burner neighbourhood which had consequences for the NO_x performance. The conclusion is that the original FAN burner, which performed better than the datum burner regarding NO_x, is not made equivalent to the modified FAN burner on just a temperature levelized basis. The difference in performance of these two burners should be referred to the flow field changes caused by the addition of the side gas burner compartments.

Contents

Chapter 1

Introduction

1.1 Control of NO_x emissions in coal fired boilers

During the eighties and nineties there has been an increasing demand for lowering emissions of pollutants such as SO_x, NO_x and unburnt hydrocarbons from fossile fuel based powerplants as well as automobiles. The growing concern is due to the now well documented environmental effects of acid rain and the suspected impact of hydrocarbons on public health and the degradation of the atmospheric ozone layer. Tightening of governmental regulations have forced the development of new technologies to deal with the problem.

Focusing on NO_x emissions from coal fired powerplants which is the subject of this study, emission controlling measures are generally divided into primary and secondary [14]. Primary measures aim at reducing the production of pollutants during combustion and secondary measures remove already formed pollutants from flue gases. Secondary measures include both catalytic methods, such as the SCR process, and noncatalytic such as the injection of reducing chemicals like ammonia or urea into fluegases (SNCR). SCR and SNCR are generally more effective than the primary measures in reducing NO_x but they are also more expensive regarding both installation and maintenance. Developing more efficient primary measures is therefore a more attractive proposition before resorting to secondary measures.

Primary measures are divided into air and fuel staging with air staging further divided into *in furnace* and *in burner* air staging. The purpose of both air and fuel staging is to keep the stoichiometric ratio in the main combustion zone as low as possible in order to suppress oxidation of fuel nitrogen without getting problems with slagging, corrosion or excess unburnt carbon in ash. This is achieved by gradually mixing air and fuel in the furnace. In fuel staging or reburning part of the fuel is injected above the main combustion zone and in *in furnace* air staging part of the combustion air is injected through, for example, over fire (OFA), over burner (OBA) or intermediate air (IA) ports the names referring to position in the furnace [14].

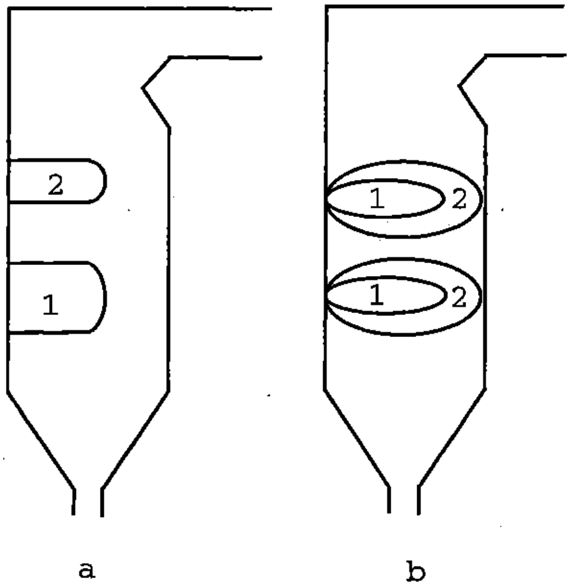

Figure 1.1: Primary measures. a. furnace staging b. burner staging 1. primary combustion 2. secondary combustion.

With *in burner* air staging the idea is to gradually mix combustion air with the fuel in the direction of the burner as distinguished from *in furnace* air staging where air is staged in the vertical direction of the furnace. The intention is, as with *in furnace* air staging, to delay combustion by reducing the amount of available oxygen in the near burner main combustion zone and in this way disfavour fuel nitrogen oxidation. This is achieved by low NO_x burners. The burner air in low NO_x burners is parted into primary for conveying coal particles and secondary for staging, where secondary air is often swirled to improve mixing and flame stabilization. The exact design and arrangement of low NO_x burners differs between manufacturers.

In practice combinations of all the above mentioned NO_x controlling techniques are used. For retrofit on existing boilers the availability for different types of modifications is very site dependent and so is the resulting NO_x reduction. Plant size, burner configuration (wall or tangentially firing) and coal type are important factors limiting NO_x reduction potential at a specific site. Adding further complication to the picture it is generally not possible to add the theoretical NO_x reduction of two NO_x reducing measures when combined.

1.2 The Helsingborg project

As mentioned, secondary measures are for economic reasons a last resort when primary measures fail to realize desired NO_x reduction. The project being studied in this report is an attempt to reach NO_x levels achieved by SCR and SNCR by combining *in furnace* air staging and an advanced low NO_x burner co-firing natural gas in a tangentially-fired system.

The project was initiated through a dialogue between the natural gas company Sydgas AB and the power company Helsingborg Energi AB regarding the possibility of reducing NO_x emissions by co-firing with natural gas from Helsingborg AB's coal fired powerplant Västhamnsverket in Helsingborg. The idea was not to use the traditional *in furnace* fuel staging or reburning technique, but a concept more similar to *in burner* fuel staging resembling *in burner* air staging.

The comparison between the co-firing technique employed in this project and reburning requires closer consideration since they both involve the use of natural gas. Reburning was developed as an abatement technique from the observation that hydrocarbon free radicals can recycle the NO formed back to HCN [14, 17]. It was found that light hydrocarbon fuels are the most effective for this purpose which is the reason for using natural gas as the reburning fuel. Although reburning can be viewed as a staging technique aimed at lowering the stoichiometric ratio in the main combustion zone, the natural gas also has a direct participation in the nitrogen chemistry. The natural gas is burned in the post flame gases from the primary coal combustion where hydrocarbon free radicals attack and recycle NO formed during the primary combustion.

It is not obvious that natural gas has any direct involvement in the nitrogen chemistry in the co-firing technique being studied in this project. The co-firing technique at hand should probably be viewed as a mere *in burner* fuel staging technique and has, in this sense, a distinct difference from the reburning technique. No experience from either laboratory, pilot or fullscale testing of a similar co-firing technique is known to the author and the project is therefore regarded as pioneering.

The prospects for the co-firing technique were good and after an inquiry among burner manufacturers worldwide, Rolls Royce International Combustion Inc. was chosen as the contractor for the project.

International Combustion performed a series of tests with different burner and gas arrangements in their test facility in Derby and the results were so encouraging that the decision was made to install a full scale test burner configuration at Västhamnsverket. The full scale installation was realized during the autumn of 1995.

Unfortunately the positive results from the test rig work could not be reproduced in the full scale operation at Västhamnsverket and at the time of writing no attempts to overcome this have succeeded.

This report is partly a summary of the results and experience from the project as a whole, ranging from the test rig work in Derby to the full scale operation at Västhamnsverket. However, the main focus of the report is an attempt to explain the interesting results from the test rig work in a theoretical framework by use of computational fluid dynamics. Finally, by the way in which the full scale project has developed there will also be an attempt to find which factors could explain the less than successful full scale operation.

Chapter 2

The test rig work

The test work was carried out in International Combustion's combustion test facilities in Derby, England. The results from the test work were compiled into a report [1] from which the following material is taken.

2.1 Test work strategy

The idea of the test work was to use an existing low NO_x burner developed by International Combustion which was proven to have performed well in commercial operation, combined with some sort of *in burner* natural gas co-firing. The low NO_x burner chosen was the flame attached nozzle (FAN) burner.

The FAN burner was designed to provide attachment of the flame at the upper and lower edges of the burner mouth. The attached flame envelopes the central core of fuel which is then devolatilized and ignited under low stoichiometric conditions which in turn disfavours fuel nitrogen oxidation. In other words, flame attachment delays and dilutes mixing of bulk fuel and oxidizer in the direction of the burner axis thus suppressing fuel nitrogen oxidation. The FAN burner has been installed with success in U.S. boilers giving up to 50 % NO_x reduction from baseline data [4].

The possibility of using natural gas co-firing was identified in two principal ways. Firstly by bulk mixing coal and gas by placing the gas nozzles inside the coal pipe at the entrance to the coal nozzle and secondly via separate gas burners, which being attached to the sides of the FAN burner, allow gas to be mixed with secondary burner air. The FAN burner with side gas burners will henceforth be called modified FAN burner. Bulk mixing via a single lance inserted inside the coal pipe was also found to be possible and tests were performed with this configuration. However the concept was abandoned due to the potential risk of backfire along the coal pipe.

For a comparison with FAN burner performance, baseline data was needed. These were collected by running tests with the original burner installed at Västhamnsverket called the datum burner which, like the FAN burner, was developed by International Combustion.

2.2 Experimental

The test facilities are centred around a main water cooled combustion chamber of internal dimensions 21.34 m in length and 5.5 × 5.5 m in crossection. This is at the burner end internally covered with high alumina refractory tiles and ceramic fibre insulation blankets to accomplish a hot environment. The chamber is capable of housing and testing full scale burners and is rated at 88 MW thermal heat input. Auxiliary equipment for supply and control of fuel and combustion air is contained in buildings connected to the chamber.

A burner cell consisting of a lower oil burner, a central coal burner and an upper air compartment for auxiliary air was used for all test runs the only difference being the switching of the coal burners. The oil burner was only used for oil firing in connection with the datum burner when establishing baseline data and in all other cases it was solely used as auxiliary air inlet.

The primary fuel was a polish coal which is the main fuel used at Västhamnsverket. For comparison additional tests were performed with a Venezuelan and a South African coal.

The amount of natural gas in relation to coal was set on a thermal basis i.e. when co-

Test parameters		range
Furnace load	(MW)	
coal		14.5–25
gas		0.3–8
Flowrate	(kg/s)	
coal		0.5–0.85
PA		1.3–2
SA		3.2–11.5
Temperature	(°C)	
PA		66–74
SA		171–340

Table 2.1: Range of test parameters. PA = primary air, SA = secondary and auxiliary air.

firing 10 % natural gas, 10 % of the total thermal input is confined to the natural gas portion.

For studying the effect on NO_x, burner tests were performed as parametric studies with one parameter varied and the rest fixed. The main parameters varied were:

- SA flow rate (excess air)
- SA temperature
- PA/PF ratio
- thermal input
- percent gas

The range of test parameters are outlined in table 2.1.

Flue gas sampling was made at the rear of the chamber by use of a stainless steel sampling tube. Sampled gas depleted of particulate matter and water vapour was led to analyzing equipment where its content of NO_x, O_2, CO and CO_2 was determined. O_2 analysis was carried out with a paramagnetic, NO_x with a chemiluminiscent and CO and CO_2 with an infrared gas analyzer. All analyses were made on a time averaged basis.

2.3 Results

2.3.1 Datum burner

A linear relationship between NO_x readings and excess air was found in the range of 2–5 % O_2 in fluegases. The constant of proportionality was about 40 ppm NO_x/% O_2 and at 3 % O_2 and a thermal input of 23 MW, a NO_x reading of about 160 ppm was estimated.

Besides excess air, the effect of varying the PA/PF ratio was investigated whereby a decreasing ratio was found to give increasing NO_x readings. Flame lengths for the datum burner were in the range 8.5–11.5 m and carbon in ash 15–20 % when firing coal only.

2.3.2 FAN burner

The oxygen dependence of the FAN burner, firing coal only, was similar to the datum burner with about the same constant of proportionality. At 3 % O_2 and a thermal input of 23 MW the NO_x reading (135 ppm) for the FAN burner was substantially lower than for the datum burner highlighting the NO_x reducing capacity of the FAN burner.

In contrast to the datum burner a decreased PA/PF ratio gave, in the case of the FAN burner, decreasing NO_x readings. Flame lengths were in the same range as for the datum burner but at the same thermal input and amount of excess air the FAN burner flame was about 1–1.5 m shorter. Carbon in ash figures showed an improvement compared to the datum burner but CO concentrations were slightly higher in the case of the FAN burner.

The gas bulk mixing arrangement gave an improvement of about 15 % compared to the FAN burner firing coal only. Varying the amount of gas between 5–18 % did not change the NO_x reduction significantly over the 15 % level, but carbon in ash increased with increasing gas input.

Furnace temperature, as measured on a metal plate on the burner end wall increased from about 970 to 1050 °C when switching from coal only firing to bulk mixed gas co-firing. This indicated higher flame temperatures in the burner vicinity and stronger flame attachment in the co-firing case, additional confirmation being provided by visual observations.

2.3.3 Modified FAN burner

Firing coal only, the modified FAN burner showed an increase in NO_x concentration as compared to the unmodified FAN burner. The NO_x levels were in the same range as for the datum burner at comparable heat input, combustion air preheat and excess air. The oxygen dependence of NO_x was found to follow a linear relationship in this case also but with a higher constant of proportionality of about 64 ppm/O_2. At 3 % O_2 the estimated NO_x level was about 180 ppm, i.e. 12 % higher than the datum burner level.

With the separate gas firing arrangement a NO_x reduction of about 24 % compared to firing coal only was achieved at 3 % O_2. Optimal reduction was obtained at 10% gas, and here the NO_x characteristics were studied further as a function of varying PA/PF ratio and combustion air preheat. Increasing the PA flow rate from 1.4–1.8 kg/s (29 %) at 0.72 kg coal/s increased NO_x by 10 %, and lowering the SA preheat from 329–171 °C, at approximately 3 % O_2, decreased NO_x from 137 to 119 ppm, i.e. 13 %.

Higher furnace wall temperatures were recorded for the modified FAN burner (1080–1100 °C) as compared to the unmodified FAN burner, but no significant difference between coal only and gas co-firing was found in this case.

Optical pyrometer measurements recorded slightly lower flame temperatures in the case of gas co-firing than in the case of coal only firing. Heat flux measurements also indicated coal burnout at a later stage in the co-firing case. Two subsequent peaks were observed, the first relating to natural gas burnout and the second to coal burnout while in the coal only case only one smooth peak close to the burner was observed.

2.4 Evaluation

The most interesting result from the test work was the 24 % reduction from the modified FAN burner co-firing gas compared to coal only firing. About 10 % of this is related to substituting coal for natural gas i.e. 10 % of the fuel nitrogen had been removed. The remaining 14 % of the reduction was then accounted for by the firing arrangement and can be explained in terms of mixing of the fuel and oxidizer and flame structure.

The effect closely resembles NO_x reductions achieved by reburning but there is also significant differences between these two firing techniques. In reburning, natural gas is injected into combustion products from primary coal firing. In the case of the modified FAN burner there is indications from heat flux measurements that natural gas is burnt out before the coal burns out, perhaps in regions of intense coal pyrolysis and devolatilization. It is also noted there is the possibility that natural gas co-firing directly delays coal burnout.

As was seen the modified FAN burner firing coal only did not achieve any NO_x reduction compared to the datum burner (fig. 2.1).

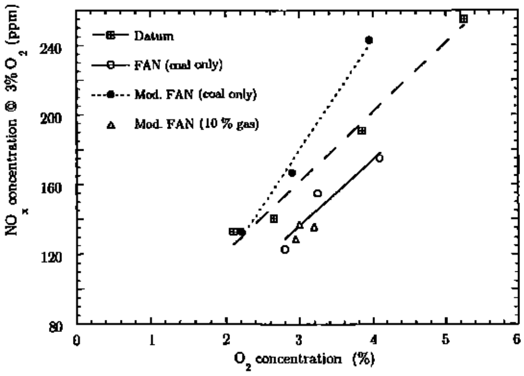

Figure 2.1: NO_x concentration as a function of excess air. Results as measured at 23 MW thermal input.

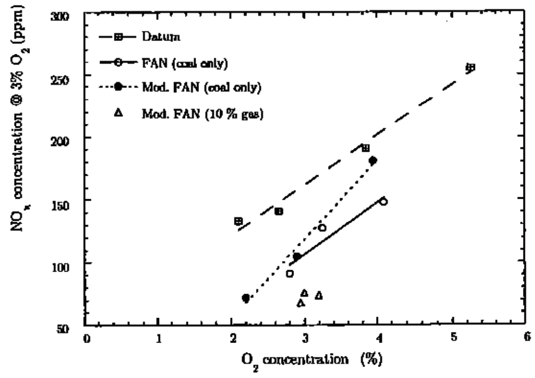

Figure 2.2: NO_x concentration as a function of excess air correlated to datum burner temperature.

This was considered to be entirely related to the high flame temperatures close to the burner due to strong flame attachment in the case of the modified FAN burner. The attached flame is stabilized by radiation from the refractory tile covered walls near the burner thus creating flame temperatures that are too high in this region. The high flame temperatures are in turn thought to be responsible for the high NO_x readings caused primarily by an increase in thermal NO_x.

Based on this imbalance in heat extraction some kind of temperature correction had to be made and for this purpose a temperature factor was derived from tests with the modified FAN burner co-firing gas at different levels of combustion air preheat. A linear relation between furnace wall temperature and NO_x concentration with a constant of proportionality of 0.26 ppm/°C was found suitable. Correlating FAN burner and modified FAN burner results to the datum burner wall temperature by use of this factor it was concluded that on a temperature levelized basis the FAN burner and the modified FAN burner firing coal only were fully comparable regarding NO_x reducing capacity (fig. 2.2).

With this major assumption the test work results were summarized as:

At 3 % O_2, comparable heat input and combustion air preheat, the modified FAN burner firing coal only was capable of reducing datum burner NO_x levels by approximately 17 %. Co-firing 10 % natural gas will give a further decrease of about 20 %.

2.5 Scale up

In Helsingborg baseline tests were performed firing the same polish coal as in the test rig and a baseline NO_x level of 133 ppm (3 % O_2) was established. The goal for NO_x after burner modifications was set to 83 ppm, i.e. a 40 % reduction from baseline.

Due to the decisive differences between the single burner horizontal firing in the test rig and the tangentially-fired system at Västhamnsverket some sort of comparison or translation of test rig data had to be done.

Based on previous experience a factor of 1.6 between NO_x levels at Västhamnsverket and the test rig was applied i.e. the 133 ppm boiler baseline level is equivalent to 83 ppm in the test rig. This low level was not achieved in the test rig due to the extremely low main burner zone stoichiometry in the boiler when operating with over fire air. To translate test rig data to these low stoichiometric conditions, use was made of the linear relationships between NO_x and excess air established during the test work (fig. 2.1). Extrapolating the datum burner linear relation down to 83 ppm is found to be equivalent to 1 % O_2 in flue gases. By extrapolation, at 1 % O_2, the FAN burner excess air relation gives a NO_x reading of 63 ppm. Co-firing 10 % gas at this level then gives a further 20 % reduction to 50 ppm. By using the factor of 1.6 and translating back to the performance of the boiler gives a figure of 80 ppm which is the NO_x level estimated when installing the modified FAN burners.

Chapter 3

Coal combustion modelling

3.1 Introduction

When trying to reveal the processes responsible for the formation and destruction of chemical species in a flame, one generally has to proceed in close association with the experimental data. Theoretical models are developed from experimental measurements and tested through mathematical modelling. If the model results are not in agreement with the measurements then there is an error in the model. This fact stresses the importance of reliable data when evaluating any theoretical model.

In the present case the determining factors are being searched for that can explain the 24 % NO_x reduction when co-firing natural gas compared to coal only firing with the modified FAN burner. Experimental data are scarce and are limited to the inlet conditions and flue gas levels for the major species measured at the end of the furnace some 21 m downstream of the burner. This data is supplemented by indications of flame, burner and furnace wall temperatures, approximate flame lengths and flame photographs. With no in flame data it is obvious that whatever the model chosen to describe the flame processes, there is no possibility to positively determine the decisive mechanisms. Modelling results should therefore only be regarded as working hypotheses.

Coal combustion modelling is a very time consuming business due to the many submodels that have to be included and for economic reasons, because time is money, model simplifications have to be made whenever possible. In this case the modest amount of data precludes most of the traditional simplifications in geometrical and dimensional representation. As the burner and its flowfield are essentially three dimensional a reasonable flame description has to resemble as closely as possible the burner geometry in all three principal directions. For this reason it was decided to use a well tested commercial fluid dynamic software for the modelling work. The FLUENT software package was available and contains, besides fluid dynamic models, submodels for chemically reacting flow, dispersed phase and radiation all of which are necessary for coal combustion modelling.

The strategy of the modelling work was to create a three dimensional physically realistic geometric representation of the burner and furnace and by the use of well tested submodels and initial conditions from the test rig report, to calculate the flame structure. The model results were then compared to available test rig data to see if measured trends could be reproduced and if explanations for the NO_x characteristics could be found.

3.2 Mathematical models

The basic models are divided into continuous phase, dispersed phase and radiation models and will be briefly described below.

3.2.1 Continuous phase

The continuous phase is modelled with the standard incompressible steady flow equations for conservation of mass, momentum, static enthalpy and chemical species:

$$\frac{\partial(\rho u_i)}{\partial x_i} = S_m \qquad (3.1)$$

$$\frac{\partial(\rho u_i u_j)}{\partial x_j} = -\frac{\partial p}{\partial x_i} + \frac{\partial \tau_{ij}}{\partial x_j} + \rho g_i + F_i \qquad (3.2)$$

$$\frac{\partial(\rho u_i h)}{\partial x_i} = \frac{\partial}{\partial x_i}\left(\frac{\mu}{Pr}\frac{\partial h}{\partial x_i}\right) + R_h + S_h \quad (3.3)$$

$$\frac{\partial(\rho u_i m_{i'})}{\partial x_i} = \frac{\partial}{\partial x_i}\left(\frac{\rho\mu}{Sc}\frac{\partial m_{i'}}{\partial x_i}\right) + R_{i'} + S_{i'} \quad (3.4)$$

where

ρ = fluid density
u_i = fluid velocity
p = static pressure
g_i = gravitational acceleration
h = static enthalpy
μ = fluid dynamic viscosity
$m_{i'}$ = massfraction of species i'
Pr = fluid Prandtl number
Sc = fluid Schmidt number

S_m, F_i, S_h and $S_{i'}$ are source terms including interaction with the dispersed phase and R_h and $R_{i'}$ are source terms due to chemical reaction. τ_{ij} is the stress tensor given by:

$$\tau_{ij} = \left[\mu\left(\frac{\partial u_i}{\partial x_j} + \frac{\partial u_j}{\partial x_i}\right)\right] - \frac{2}{3}\mu\frac{\partial u_l}{\partial x_l}\delta_{ij} \quad (3.5)$$

The conservation equations must be supplemented by an equation of state and under the assumption of ideal gas behaviour and ignoring compressibility effects this is given by:

$$\rho = \frac{p_{op}}{RT\sum_{i'}\frac{m_{i'}}{M_{i'}}} \quad (3.6)$$

where

T = temperature
R = gas constant
$M_{i'}$ = molecular weight of species i'
p_{op} = operating pressure

Turbulence model

As coal combustion in large furnaces is inevitably turbulent, a turbulence model has to be provided. The model of choice is the k-ϵ model [15, 16] which closes the time averaged conservation equations with transport equations for the turbulent kinetic energy and its dissipation rate. The major assumptions for closure are isotropic turbulent viscosity and gradient transport of fluctuating quantities.

Time averaging is done by resolving the instantaneous quantities in the conservation equations into their mean and fluctuating parts by setting $\phi = \overline{\phi} + \phi'$ and then averaging over a time interval that is long compared to the turbulent fluctuations, noting that $\overline{\phi'} = 0$. After averaging the conservation equations take the form:

$$\frac{\partial(\overline{\rho u_i u_j})}{\partial x_j} = -\frac{\partial\overline{p}}{\partial x_i} + \frac{\partial}{\partial x_j}\left(\overline{\tau}_{ij} - \overline{\rho}\overline{u_i'u_j'}\right) + \overline{\rho}g_i + \overline{F}_i \quad (3.7)$$

$$\frac{\partial(\overline{\rho u_i}\overline{\phi})}{\partial x_i} = \frac{\partial}{\partial x_i}\left(\frac{\mu}{\sigma_\phi}\frac{\partial\overline{\phi}}{\partial x_i} - \overline{\rho}\overline{u_i'\phi'}\right) + \overline{R}_\phi + \overline{S}_\phi \quad (3.8)$$

where ϕ is h or $m_{i'}$ and σ the corresponding Prandtl and Schmidt numbers. The new terms on the righthandside of the equations are interpreted as augmentations of momentum, enthalpy and species fluxes caused by turbulent velocity fluctuations. By analogy with kinetic theory these fluxes are assumed linearly dependent on gradients of mean quantities according to (overbars on mean quantities have been dropped)[13]:

$$\rho u_i'u_j' = \rho\frac{2}{3}k\delta_{ij} - \mu_t\left(\frac{\partial u_i}{\partial x_j} + \frac{\partial u_j}{\partial x_i}\right) + \frac{2}{3}\mu_t\frac{\partial u_l}{\partial x_l}\delta_{ij} \quad (3.9)$$

$$\rho u_i'h' = -\frac{\mu_t}{\sigma_h}\frac{\partial h}{\partial x_i} \quad (3.10)$$

$$\rho u_i'm_{i,}' = -\frac{\mu_t}{\sigma_m}\frac{\partial m_{i,}}{\partial x_i} \quad (3.11)$$

where

k = turbulent kinetic energy
μ_t = turbulent viscosity
σ_h = turbulent Prandtl number
σ_m = turbulent Schmidt number

From relations (3.9-3.11) it is seen that on replacing the laminar transport coefficients in (3.2-3.4) by the sum of the laminar and turbulent coefficients, the time mean conservation equations will retain the same form as their laminar counterparts.

To close the set of turbulent conservation equations the turbulent viscosity has to be modelled. In k-ϵ theory the turbulent viscosity is modelled as a product of a turbulent velocity and length scale and by dimensional reasoning it is, in this context, defined as:

$$\mu_t = \rho C_\mu \frac{k^2}{\epsilon} \tag{3.12}$$

where C_μ is an empirical constant and ϵ the dissipation of turbulent kinetic energy which by definition is given by:

$$\epsilon = \mu \left(\frac{\partial u_i'}{\partial x_j} \right)^2 \tag{3.13}$$

The turbulent kinetic energy defined as:

$$k = \frac{1}{2} \sum_i \overline{u_i'^2} \tag{3.14}$$

is found from its transport equation,

$$\frac{\partial(\rho k)}{\partial t} + \frac{\partial(\rho u_i k)}{\partial x_i} = \frac{\partial}{\partial x_i} \left(\frac{\mu_t}{\sigma_k} \frac{\partial k}{\partial x_i} \right) + G_k - \rho\epsilon \tag{3.15}$$

where G_k is the rate of production of turbulent energy,

$$G_k = \mu_t \left(\frac{\partial u_j}{\partial x_i} + \frac{\partial u_i}{\partial x_j} \right) \frac{\partial u_i}{\partial x_i} \tag{3.16}$$

and $C_{1\epsilon}, C_{2\epsilon}, \sigma_k$ and σ_ϵ empirical constants which strictly are dependent on boundary conditions.

To close the set of conservation equations a transport equation for the dissipation rate is constructed:

$$\frac{\partial(\rho\epsilon)}{\partial t} + \frac{\partial(\rho u_i \epsilon)}{\partial x_i} = \frac{\partial}{\partial x_i} \left(\frac{\mu_t}{\sigma_\epsilon} \frac{\partial \epsilon}{\partial x_i} \right) + C_{1\epsilon} \frac{\epsilon}{k} G_k - C_{2\epsilon} \rho \frac{\epsilon^2}{k} \tag{3.17}$$

Chemical reaction

The laminar chemical reaction rate is given by FLUENT as a n:th order Arrhenius expression of the general form:

$$R_{i'k} = -\nu_{i'k} M_{i'} T^{\beta_k} A_k \prod_{j'} C_{j'}^{\nu_{j'k}} \exp(-E_k/RT) \tag{3.18}$$

where

$R_{i'k}$ = reaction rate for species i' in reaction k
$\nu_{i'k}$ = molar stoichiometric coefficient for species i' in reaction k
$M_{i'}$ = molecular weight of species i'
β_k = temperature exponent
A_k = pre-exponential factor
$C_{j'}$ = molar concentration of reactant j'
$\nu_{j'k}$ = exponent on concentration of reactant j' in reaction k
E_k = activation energy for reaction k

The rate of formation and destruction of chemical species appearing in the source term $R_{i'}$ of equation (3.4) is then expressed as the sum of contributions from all reactions in which the species participates according to

$$R_{i'} = \sum_k R_{i'k} \tag{3.19}$$

Chemical reaction is also a source of enthalpy and is included in the source term R_h of equation (3.3) by the expression:

$$R_h = \sum_{i'} \left(h_{i'}^\circ + \int_{T_{ref_{i'}}}^{T} c_{p_{i'}} dT \right) R_{i'} \tag{3.20}$$

where $h_{i'}^\circ$ is the heat of formation and $c_{p_{i'}}$ the specific heat of species i'.

As the flow is turbulent an expression for the time mean reaction rate is needed. FLUENT offers three different formulations for this, the PDF approach, flame front tracking for premixed flames [19] and a generalization of the Magnussen-Hjertager eddy breakup model [20]. In the present case there is little to choose from but the eddy breakup model.

The eddy breakup model relates the turbulent reaction rate to the lifetime of large turbulent eddies which is given by the quotient k/ϵ. This assumes that chemical reactions are fast compared to turbulent mixing. The turbulent reaction rate is calculated with the following two expressions:

$$R_{i'k} = \nu_{i'k} M_{i'} A \rho \frac{\epsilon}{k} \frac{m_R}{\nu_{Rk} M_R} \tag{3.21}$$

$$R_{i'k} = \nu_{i'k} M_{i'} A B \rho \frac{\epsilon}{k} \frac{\sum_P m_P}{\sum_P \nu_{Pk} M_P} \tag{3.22}$$

where

m_R = mass fraction of reactant giving the smallest value of $R_{i'k}$
m_P = mass fraction of any product in reaction k
A = empirical constant
B = empirical constant

When calculating the turbulent time mean reaction rate these two expressions are compared to the Arrhenius rate and the smallest (limiting) of the three is taken as the actual reaction rate.

3.2.2 Dispersed phase

The dispersed, or as in this case the coal particle phase, is represented as discrete particles traveling through the continuous phase flow field. This means that each discrete particle represents a fraction of the total coal mass flow. A prerequisite for this approach is that the particle phase is dilute enough for particle-particle interactions to be ignored since such effects are not included.

The particle history is calculated in a lagrangian reference frame which means that the particle position and velocity as a function of time is found from integration of the forces acting on the particle as it travels through the stationary continuous phase. The particle position, $\mathbf{x}_p$ is found from [18]

$$\mathbf{x}_p = \mathbf{x}_{p0} + \int_0^t \mathbf{u}_p dt \tag{3.23}$$

and the particle velocity from the force balance

$$\frac{d\mathbf{u}_p}{dt} = F_D(\mathbf{u} - \mathbf{u}_p) + \mathbf{g}(\rho_p - \rho)/\rho_p \tag{3.24}$$

where

$$F_D = \frac{18\mu}{\rho_p D_p^2} \frac{C_D Re}{24} \tag{3.25}$$

$$Re = \frac{\rho D_p |\mathbf{u}_p - \mathbf{u}|}{\mu} \tag{3.26}$$

$$C_D = a_1 + a_2/Re + a_3/Re^2 \tag{3.27}$$

and

$\mathbf{u}_p$ = particle velocity
$\mathbf{u}$ = fluid velocity
ρ_p = particle density
ρ = fluid density
D_p = particle diameter
$\mathbf{g}$ = gravitational acceleration
Re = relative Reynolds number
C_D = drag coefficient
a_1, a_2, a_3 = empirical constants

When the flow is turbulent the particles are affected by the random eddy motion. Turbulence dramatically increases the particle dispersion and this has to be accounted for when calculating trajectories if a realistic description is to be achieved.

The instantaneous continuous flow field velocity is given by $u_i = \overline{u_i} + u_i'(t)$ but the continuous phase solution only gives the time mean velocity which means that some way of estimating $u_i'(t)$ has to be found if the effects of turbulence are to be incorporated in (3.24).

This is done by the use of a random walk method where the fluctuating velocity component is found from the r.m.s. value of velocity fluctuations, $\sqrt{\overline{u_i'^2}}$, which from k-ϵ theory is simply $\sqrt{2k/3}$. $u_i'(t)$ can now be calculated as

$$u_i' = \zeta \sqrt{2k/3} \tag{3.28}$$

where ζ is a normally distributed random number applied during a characteristic time interval. This time interval is taken as the lifetime of the turbulent eddy the particle traverses and is given by

$$\tau_e = 0.3 \frac{k}{\epsilon} \tag{3.29}$$

When τ_e is reached a new value of ζ is applied.

The combustible coal particle is parted into three separate fractions: volatiles, char and ash. Combustion of coal particles is as a consequence treated as a sequence of four steps: particle heatup, devolatilization, char burnout and inert heating or cooling of remaining ash.

Particle heatup is the first phase in the particle life. Heat transfer during this phase is described by:

$$m_p c_p \frac{dT_p}{dt} = hA_p(T_\infty - T_p) \tag{3.30}$$

where h is the heat transfer coefficient calculated from

$$\frac{hD_p}{k_\infty} = 2.0 + 0.6 Re^{\frac{1}{2}} Pr^{\frac{1}{3}} \tag{3.31}$$

and

m_p = particle mass
c_p = particle heat capacity
A_p = particle surface area
T_p = particle temperature
T_∞ = fluid temperature
k_∞ = fluid thermal conductivity
D_p = particle diameter
Pr = fluid Prandtl number
Re = relative Reynolds number, Eq. (3.26)

When the particle reaches the devolatilization temperature, T_{vap}, volatiles begin to evolve. The mass loss is modelled as a first order process regarding remaining volatiles according to the expression [3]:

$$-\frac{dm_p}{dt} = k(m_p - (1 - f_{v0})m_{p0}) \tag{3.32}$$

where,

$$k = A\exp(-E/RT) \tag{3.33}$$

m_{p0} the initial particle mass and f_{v0} the initial mass fraction volatiles.

Accounting for heat loss as a consequence of mass loss, an extra term is added to the particle heat balance during the devolatilization phase:

$$m_p c_p \frac{dT_p}{dt} = hA_p(T_\infty - T_p) + \frac{dm_p}{dt} h_{fg} \tag{3.34}$$

where h_{fg} is the latent heat of vaporization of volatiles.

As volatiles evolve the particle diameter changes which is described by:

$$\frac{D_p}{D_{p0}} = 1 + (C_{sw} - 1)\frac{m_{p0} - m_p}{f_{v0} m_{p0}} \tag{3.35}$$

where D_{p0} is the initial particle diameter and C_{sw} the swelling coefficient which has a value larger than one if the particle expands and less than one if it contracts.

When all volatiles are evolved the char combustion phase commences. Gas phase oxygen diffuses to the particle surface and reacts with the remaining char which is assumed to be pure carbon, forming carbon monoxide or dioxide which in turn diffuses out to the bulk gas.

The rate of consumption of char is influenced by the char surface reaction rate as well as the oxidizer diffusion rate. Which process is limiting depends on temperature, particle diameter and oxygen partial pressure. Accounting for this char consumption is modelled as [7, 2]:

$$\frac{dm_p}{dt} = -\pi D_p^2 P_O \frac{R_1 R_2}{R_1 + R_2} \tag{3.36}$$

where,

$$R_1 = C_1 \frac{[(T_p + T_\infty)/2]^{0.75}}{D_p} \tag{3.37}$$

$$R_2 = C_2 \exp(-E/RT) \tag{3.38}$$

C_1, C_2 are empirical constants and P_O the oxidizer partial pressure.

Particle heat transfer during char combustion is modelled as:

$$m_p c_p \frac{dT_p}{dt} = hA_p(T_\infty - T_p) - f_h \frac{dm_p}{dt} H_{reac} \tag{3.39}$$

where H_{reac} is the heat of surface reaction and f_h the fraction of this heat absorbed by the particle.

The combusting particles are sources of momentum, heat and mass in the continuous phase which is included in the source terms of the flow equations (3.1-3.4). The source terms for a particle passing through a continuous phase control volume are modelled as:

$$\mathbf{F} = \frac{18\mu C_D Re}{\rho_p D_p^2 24}(\mathbf{u}_p - \mathbf{u})\dot{m}_p \Delta t \tag{3.40}$$

$$S_h = \left[\frac{\overline{m}_p}{m_{p0}} c_p \Delta T_p + \frac{\Delta m_p}{m_{p0}} \left(-h_{fg} + h_{pyrol} \int_{T_{ref}}^{T_p} c_{pi} dT \right) \right] \dot{m}_{p0} \tag{3.41}$$

$$S_m = \frac{\Delta m_p}{m_{p0}} \dot{m}_{p0} \tag{3.42}$$

where

Δt = integration time step
$\overline{m}_p$ = average mass of particle in control volume
m_{p0} = initial mass of particle
c_p = particle heat capacity
ΔT_p = particle temperature change in control volume
Δm_p = particle mass change in control volume
h_{fg} = volatile latent heat of vaporization
h_{pyrol} = volatile heat of pyrolysis
$c_{p,i}$ = volatile heat capacity
T_p = particle control volume exit temperature
T_{ref} = enthalpy reference temperature
$\dot{m}_{p0}$ = initial mass flow rate of particle injection

Particle injections can be specified in terms of groups where one group includes a number of injections having the same physical properties. The injections covered by the group may however have differing sizes and represent differing massflows. The distribution of massflow and particle sizes over the injections can be determined using the Rosin-Rammler distribution [18] from which the massfraction of particles having a diameter greater than D is given by

$$M_D = \exp\left(- \left(\frac{D}{\overline{D}} \right)^n \right) \tag{3.43}$$

where $\overline{D}$ is the mean diameter and n the spread parameter. If the Rosin-Rammler distribution is used for a group, FLUENT automatically assigns sizes and massflows over the injections using (3.43).

3.2.3 Radiation

Radiation is modelled with the discrete transfer radiation model (DTRM) [25] which integrates the radiation transfer equation

$$\frac{dI}{ds} = \frac{a\sigma T^4}{\pi} + aI \tag{3.44}$$

where,

I = radiation intensity
a = absorption coefficent
σ = Stefan-Boltzmanns constant

along rays emanating from domain boundaries. It ignores scattering and assumes that boundary walls are diffuse i.e. incident radiation is isotropically reflected.

Composition and temperature dependence of the absorption coefficient is handled through the weighted sum of gray gases model(WSGGM) [5]. The absorption coefficient is calculated as:

$$a = -\ln(1-\epsilon)/s \tag{3.45}$$

where,

$$\epsilon = \sum_{i=0}^{I} a_{\epsilon,i}[1 - \exp(-\kappa_i ps)] \tag{3.46}$$

and

ϵ = emissivity
$a_{\epsilon,i}$ = emissivity weighting factor for i^{th} gray gas
κ_i = absorption coefficient for i^{th} gray gas
p = sum of partial pressures for absorbing gases
s = ray pathlength

$a_{\epsilon,i}$ and κ_i are found from tabulated experimental data as a function of temperature and partial pressures of CO_2 and H_2O.

3.2.4 Boundary conditions

For the purpose of the present model four types of domain boundaries are used: inlet, outlet, wall and symmetry.

Inlet boundaries

Inlet boundaries are where the flow enters the computational domain and are specified in terms of fluid velocity, fluid temperature, mass fractions of species, turbulence parameters and radiation emissivity. Diffusion fluxes of scalar quantities normal to the boundary are set to zero at the inlets.

The boundary conditions for the turbulent kinetic energy and its dissipation rate are set in terms of intensity and lengthscale. The turbulent intensity is defined as the quotient of the r.m.s. velocity fluctuation and the mean velocity according to

$$I = \frac{\sqrt{2k/3}}{u} \tag{3.47}$$

The inlet value for k is thus found from the input of intensity.

The dissipation rate is determined from the lengthscale through

$$\epsilon = C_\mu^{\frac{3}{4}} \frac{k^{\frac{3}{2}}}{l} \tag{3.48}$$

where l is the lengthscale.

Outlet boundaries

Outlet boundaries can be applied at cross-sections of the flow where the flowfield is fully developed. That is, where diffusion fluxes in the direction normal to the boundary are zero or can safely be neglected as having negligible influence on the solution. This is because of the zero diffusion flux boundary condition specifying outlets.

The only quantity that has to be set at outlet boundaries is radiation emissivity.

Wall boundaries

At wall boundaries the fluid velocity is set to zero and the temperature is given a constant value. In order to solve the momentum equations in the near wall computational cells the shear stress τ_w has to be estimated.

Turbulent boundary layers at solid walls are divided into a thin, near wall, viscous sublayer and an outer, fully turbulent layer. In these layers the shear stress is assumed to be constant and adopting the value at the wall.

In the turbulent layer, shear stress is calculated through the following three expressions [18]:

$$\frac{u_p}{u^*} = \frac{1}{\kappa}\ln(Ey^+) \tag{3.49}$$

$$u^* = \sqrt{\frac{\tau_w}{\rho}} \tag{3.50}$$

$$y^+ = \frac{\rho k_p^{\frac{1}{2}} C_\mu^{\frac{1}{4}} \Delta y}{\mu} \tag{3.51}$$

where

u_p = fluid velocity at near wall point p
E = empirical constant
k_p = turbulent kinetic energy at point p
κ = von Karmans constant
C_μ = empirical constant
Δy = distance from point p to the wall

and based on dimensional analysis, u^* the turbulent velocity scale relevant for the inner boundary layer, y^+ a scaled normal distance from the wall and (3.49), a solution to the equation:

$$\frac{\partial u}{\partial y} = \frac{u^*}{\kappa y} \tag{3.52}$$

(3.51) is an empirical fit to turbulent flow data and is valid for y^+ larger than 15–20. y^+ is generally calculated from the assumption that production and dissipation of turbulent energy is equal in the inner boundary layer which yields the following expression for y^+:

$$y^+ = \frac{\rho u^* \Delta y}{\mu} \tag{3.53}$$

FLUENT uses this expression to control that (3.51) is valid. If y^+ from (3.51) is lower than 11.225 it is assumed that the calculation point is in the viscous sublayer where (3.49-3.51) are not applicable. In this case the laminar approximation is used for calculation of τ_w:

$$\tau_w = \mu \frac{\partial u}{\partial y}\Big|_{wall} \simeq \frac{\Delta u}{\Delta y} \tag{3.54}$$

where Δu is the fluid velocity at the calculation point ($u_{wall} = 0$).

With the near wall value of shear stress calculated and assuming zero normal gradient at the wall, the transport equation for turbulent kinetic energy can be solved and again under the assumption of equality between production and dissipation of turbulent energy the dissipation rate at the wall is given by:

$$\epsilon = \frac{C_\mu^{\frac{3}{4}} k_p^{\frac{3}{2}}}{\kappa y} \tag{3.55}$$

Heat transfer at walls is calculated through:

$$q = h_f(T_w - T_f) + q_{rad} \tag{3.56}$$

In turbulent boundary layers heat transfer is, by analogy to the shear stress calculation, given by the following expression:

$$\frac{k_f(\Delta T/\Delta y)}{q} = \frac{1}{\kappa y^+}\frac{Pr_t}{Pr}\ln(Ey^+) + \frac{1}{y^+}\left(\frac{Pr_t}{Pr}\right)^{\frac{5}{4}} \frac{\frac{\pi}{4}}{\sin\frac{\pi}{4}}\left(\frac{A}{\kappa}\right)^{\frac{1}{2}}\left(\frac{Pr}{Pr_t} - 1\right) \tag{3.57}$$

where

k_f = fluid thermal conductivity
ΔT = temperature difference between calculation point and wall
q = wall heat flux
Pr = fluid Prandtl number
Pr_t = turbulent fluid Prandtl number
A = van Driest constant

The radiation heat flux to the surface is found from,

$$q_{rad}^- = \int I^- d\Omega \tag{3.58}$$

where Ω is the hemispherical solid angle and I^- is the intensity of the incoming ray. The outgoing heat flux is then the sum of the reflected radiation and the emissive power of the surface according to:

$$q_{rad}^+ = (1 - \epsilon_w) q_{rad}^- + \epsilon_w \sigma T_w^4 \tag{3.59}$$

Consequently q_{rad} in (3.56) is:

$$q_{rad} = \epsilon_w q_{rad}^- \tag{3.60}$$

Finally the intensity of an outgoing ray is given by

$$I_0 = \frac{q_{rad}^+}{\pi} \tag{3.61}$$

Symmetry boundaries

At symmetry boundaries all fluxes are assumed zero which means practically no net flow across the boundary. This is expressed as zero normal velocity and zero normal gradients of all quantities at the bounding surface.

3.2.5 Solution procedures

The continuous phase conservation equations (3.1-3.4, 3.15, 3.17) are transformed to finite difference equations and solved using the control volume technique whereby the computational domain is divided into discrete volume elements and the balance of mass, momentum and scalars is satisfied for each element using the divergence theorem. The coupled mass and momentum equations are discretized and solved by the SIMPLE algorithm.

Cell centre values obtained in the above way are used to interpolate the cell face values by a power law scheme which solves a one-dimensional convection-diffusion equation for the variation between cell centres and faces.

The solution proceeds iteratively until the balance for all quantities is satisfied for all cells at which point the solution is converged.

Particle trajectory calculations are performed at a preset number of iterations. The number of iterations between trajectory calculations is dependent on how severly the continuous phase solution is affected through the source terms (3.40-3.42). The radiation transfer equation (3.44) is likewise solved at a preset number of iterations.

The developing solution is kept track of by the residuals which are the summed and weighted imbalance of conserved quantities throughout the domain. The residuals are reported every iteration and should, for a stable solution, be monotonically decreasing. Convergence is determined in terms of the sum of the residuals for all conserved quantities. When this sum decreases a predetermined value, the solution is terminated and judged converged.

3.3 Test rig burner and furnace models

3.3.1 Model cases

The purpose of the modelling work was to find possible explanations for the NO_x reductions achieved when co-firing natural gas compared to firing coal only with the modified FAN burner. These two flame cases then had to be calculated and compared. Based on similar levels of excess air, combustion air preheat and thermal input test runs 44 and 49 from the test rig report[1] were chosen for comparison. Test run 44, the co-firing case firing 10 % natural gas, gives a 23 % NO_x reduction compared to test run 49. For comparison between FAN and modified FAN burner both firing coal only the gas nozzle was removed from the model and using the same inlet conditions as in test run 24 the FAN burner flame was calculated. These three flame cases were the basis for the modelling work (table 3.1).

Parameters		Test no. 44	49	24
Furnace load	(MW)			
coal		20.8	23.6	23.7
gas		2.3	0	0
Flow rates	(kg/s)			
coal		0.72	0.82	0.81
PA		1.40	1.37	1.47
SA		5.67	6.32	5.84
Temperatures	(°C)			
PA		72.1	70.5	67.2
SA		333	330	336
Flame length	(m)	8.5	8.5	8.5
Flue gas (dry basis)				
O_2	(vol%)	2.95	2.90	2.45
CO_2	(vol%)	16.6	17.1	17.5
CO	(ppm)	90	73	65
NO_x	(ppm)	129	168	110
Carbon in ash	(%)	15	-	13.5

Table 3.1: Parameters of test rig runs 44, 49 and 24. PA = primary air, SA = secondary and auxiliary air.

3.3.2 Geometric representation and computational boundaries

The geometric representation of the FAN and modified FAN burner was based on original drawings. It was found from these that two symmetry planes could be introduced i.e. a quarter of the burner was sufficient for the geometric model. The symmetry planes are outlined in figure 3.1 which shows a front view of the modified FAN burner. It should be noted that symmetry in terms of geometry is not a sufficient condition for all over symmetry since the flowfield across these boundaries may not be symmetric. For example, the gravitational field is not symmetric across horizontal planes which affects particle trajectories particularly. For the purpose of the model these effects were not considered in order to keep the number of computational cells down.

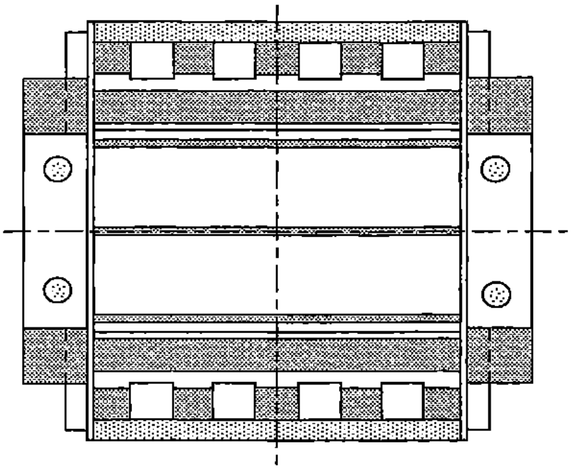

Figure 3.1: Modified burner front view showing the horizontal and vertical symmetry planes.

The next step was to decide where the vertical coal burner inlet plane should be placed. Due to the complex interior burner geometry it was soon discovered that a 3D-model could not include the entire burner down to the end of the coal pipe. This would require a very dense grid and thus computational times far beyond the project life time. It was noted that the burner

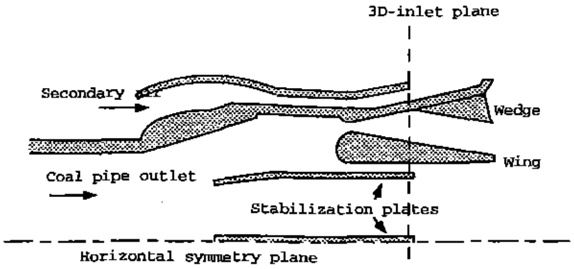

Figure 3.2: Principal sketch of 2D-model geometry

interior, in a broad sense, could be regarded as two dimensional from the end of the coal pipe up to a vertical plane at the back edge of the triangular wedges on the upper and lower edge of the burner mouth. This plane was found to be a suitable inlet for the 3D-model if inlet conditions could be found from a 2D-model covering the burner flowfield from the end of the coal pipe up to the 3D inlet plane (fig.3.2).

Taking into consideration one half of the burner above the horizontal dividing symmetry plane, the 3D inlet plane is divided into three inlets by a central and an upper stabilization plate and a wing. The wing, in connection with the wedges, forms a diffuser unit that enhances turbulent particle dispersion at the upper edge of the burner mouth and thus creates the necessary conditions for flame attachment. The purpose of the 2D-model was then to find the inlet conditions for the 3D-model for these three divisions in terms of massflow, velocity profiles, turbulent conditions and particle massflow and size distribution.

With the exception of the coal burner inlets, secondary air and gasburner compartments had to be represented in the 3D-model. No special considerations were made for their interiors and from the drawings their furnace outlets were taken as inlets to the computational domain. The auxiliary air inlet was taken as quadratic with an edge the size of the burner upper edge. It was placed half a burner diameter above the burner in the vertical direction and in line with the burner mouth in the axial direction.

With the burner geometry set, the furnace size had to be decided. The height and width had to be large enough to prevent flame impingement on the bounding walls and it had to be long enough to cover the essential details of the flame. With this in mind the quarter of the furnace being modelled was given the dimensions 0.8 m wide, 0.8 m high and 8 m long. The length was based on flame lengths from the test rig report.

The computational grid was constructed in body fitted coordinates to achieve smooth gridlines that were as closely coupled to the geometry and flowfield as possible and which extended to almost 36000 computational cells. The outline of the 3D model is seen by figures A1 and A2.

3.3.3 Physical models and properties

The physical models are based on the mathematical models described previously.

Continuous phase

Viscosity, thermal conductivity and the diffusion constant may optionally be set in FLUENT as a function of chemical composition and temperature. Under the assumption of dominating turbulent transport they were set to constant values for air at 273 K and 1 atm. for all species.

The specific heat can likewise optionally be composition and temperature dependent. For the purpose of the model, a polynomial fit to specific heat for air as a function of temperature was used.

The empirical constants appearing in the transport equations for turbulent kinetic energy and its dissipation rate may be changed. However, they were kept at their standard values [16] (table 3.2).

Combustion chemistry The gas phase combustion reactions were described by the following global steps

$$C_mH_nO_l + \frac{m-l}{2}O_2 \rightarrow mCO + \frac{n}{2}H_2 \qquad (3.I)$$

$$CH_4 + \frac{1}{2}O_2 \rightarrow CO + 2H_2 \qquad (3.II)$$

$$CO + \frac{1}{2}O_2 \rightarrow CO_2 \qquad (3.III)$$

$$H_2 + \frac{1}{2}O_2 \rightarrow H_2O \qquad (3.IV)$$

Property	Value
Viscosity (kg/m s)	$1.72 \cdot 10^{-5}$
Thermal conductivity	0.024 W/m K
Diffusion constant (m^2/s)	$2.88 \cdot 10^{-5}$
Heat capacity (J/kg K)	$963 + 0.1178T - 1.162 \cdot 10^{-5} T^2$
Turbulence constants	
C_μ	0.09
$C_{1\epsilon}$	1.44
$C_{2\epsilon}$	1.92
σ_k	1.0
σ_ϵ	1.3
σ_h	0.7
σ_m	0.7

Table 3.2: Gas phase physical properties and $k - \epsilon$ constants

where $C_mH_nO_l$ is a pseudomolecule representing the volatiles evolving from coal particles and CH_4, methane, represents the natural gas portion.

Gas phase combustion reactions were assumed to be infinitely fast compared to turbulent mixing i.e. no special considerations were made for the kinetics of these reactions. The Arrhenius pre-exponential factors were set to the highest possible values and energies of activation were taken from Hautmann et al. [12]. This ensured that the reaction rates were always limited by the Magnussen-Hjertager mixing rate (3.21-3.22). The mixing rate constants, A and B were set to 4 and 0.5 as suggested by the original authors [20].

It should be noted that the eddy breakup model was developed for the case of a single step, irreverible combustion reaction and not for intermediate steps such as CO oxidation. CO and H_2 were included in the model to obtain a reasonable resolution of the temperature field.

Species	Molecular weight (kg/kmol)	Heat of formation (J/kmol)
$CH_{1.22}O_{0.14}$	15	$-2.46 \cdot 10^7$
CH_4	16	$-7.49 \cdot 10^7$
CO	28	$-1.11 \cdot 10^8$
CO_2	44	$-3.94 \cdot 10^8$
H_2	2	0
H_2O	18	$-2.42 \cdot 10^8$
HCN	27	$1.30 \cdot 10^8$
NH_3	17	$-4.59 \cdot 10^7$
NO	30	$9.05 \cdot 10^7$
N_2	28	0
O_2	32	0

Table 3.3: Properties of chemical species

Nitrogen chemistry It is generally accepted that NO_x from pulverized coal flames is formed through three distinct pathways termed thermal, prompt and fuel-NO_x [14, 22]. Thermal NO_x is formed by oxidation of molecular nitrogen in the combustion air [29] and is highly temperature and oxygen dependent. [10]. Prompt NO_x is the result of hydrocarbon fragments attacking molecular nitrogen [6, 10]. This route has a weak temperature dependence and is only of significance in very fuel rich flames. Fuel-NO_x is the all overshadowing source of NO_x and occurs by oxidation of the nitrogen content in coal. Fuel NO_x has a weak temperature dependence in turbulent flames and is primarily sensitive to oxygen partial pressure [23].

Coal nitrogen can be oxidized either homogeneously through devolatilized gas phase nitrogen species or heterogeneously [24] through nitrogen remaining in the char. Gas phase nitrogen species are the product of pyrolysis of heterocyclic nitrogen compounds in the coal structure such as pyridine, quinoline and pyrrole. Experimental evidence [24] shows that the primary pyrolysis products are HCN and to a smaller extent NH_3. Gas phase HCN rapidly decays to NH_i species which in turn are either oxidized to NO or reduced to N_2 by attack of NO [11]. The interaction of these species involves a large number of elementary steps and radical intermediates [8] but is globally described as interactions between four nitrogen subsystems: CN(mostly HCN), NH_i(NH, NH_2, NH_3), NO and N_2 [11, 22]. A global reaction scheme describing the nitrogen chemistry assumes that these subsystems are internally equilibrated and can be each represented by a single species.

In the present model it is assumed that the entire coal nitrogen content is devolatilized (no heterogeneous reactions) and instantaneously forms HCN. The gas phase chemistry is described by the reaction scheme developed by Mitchell and Tarbell [22] where NH_3 represents the NH_i subsystem:

$$\mathrm{HCN} + \mathrm{H_2} + \frac{1}{2}\mathrm{O_2} \rightarrow \mathrm{NH_3} + \mathrm{CO} \qquad (3.V)$$

$$\mathrm{NH_3} + \frac{1}{2}\mathrm{O_2} \rightarrow \mathrm{NO} + \frac{3}{2}\mathrm{H_2} \qquad (3.VI)$$

$$\mathrm{NH_3} + \mathrm{NO} \rightarrow \mathrm{N_2} + \frac{3}{2}\mathrm{H_2} \qquad (3.VII)$$

The reaction rates are

$$R_{HCN} = -k_1 C_{HCN} C_{O_2} \qquad (3.62)$$

$$R_{NH_3} = -\frac{k_2 C_{NH_3} C_{O_2}}{1 + k_3 C_{O_2}} \qquad (3.63)$$

$$R_{NH_3} = -k_4 C_{NH_3} C_{NO} \qquad (3.64)$$

where the concentrations are in kmole/m^3 and

$$k_1 = 1.613 \cdot 10^{14}\, T \exp(-3.28 \cdot 10^8/RT) \qquad (3.65)$$

$$k_2 = 2.893 \cdot 10^{19}\, T \exp(-4.18 \cdot 10^8/RT) \qquad (3.66)$$

$$k_3 = 5.66 \cdot 10^{-7}\, T \exp(1.75 \cdot 10^8/RT) \qquad (3.67)$$

$$k_4 = 5.172 \cdot 10^{13}\, T \exp(-2.30 \cdot 10^8/RT) \qquad (3.68)$$

where the energies of activation are in J/kmole. Reaction rates (3.62) and (3.64) were easily implemented into FLUENTS rate expression (3.18) but (3.63) needed some sort of simplification. At high temperatures expression (3.63) simplifies to

$$R_{NH_3} = -k_2 C_{NH_3} C_{O_2} \qquad (3.69)$$

This expression is valid for temperatures > 1800 K. At low temperatures and high oxygen concentrations it is obviously not valid, but since the flame temperatures are in the range 1500-2000 K and the study is, in essence, comparative and not quantitative the approximation was thought justified.

Thermal and prompt NO_x were not included in the kinetic model mostly because no suitable global kinetic scheme was found but also because of their relative unimportance in pulverized coal flames [27]. A more severe restriction is the exclusion of heterogeneous reactions but there was no practical way to account for these with the available models.

The remaining question was the turbulence-chemistry interaction. The eddy break up model is developed for fast combustion reactions in premixed flames where the kinetics can be neglected. The nitrogen chemistry is several orders of magnitude slower than the combustion reactions but generally not slow enough to be unaffected by turbulent mixing [27]. To deal with this, the nitrogen chemistry was calculated with A and B in (3.21-3.22) kept at their original values and with very high values ($A = 10^{10}$ and $B = 1$) allowing for larger kinetic influence. This way two limiting cases could be compared and the influence of mixing and kinetics could be separated. The underlaying assumption of premixed reactants of course prevails.

Coal particle phase

Coal combustion in large furnaces at high temperatures and large heat release rates, gives volatile yields exceeding the fraction volatiles, as determined by proximate analysis. From the work of Goldberg and Essenhigh [9] it is concluded that the terminal yield may very well be a factor of 1.8 times higher than the proximate at the high heating rates in coal furnaces. A part of the volatiles forms tars and soot that is not burned off and if the factor of 1.8 is adopted to the test rig data it can be calculated from

Analysis	Massfraction (dry)
Ultimate	
C	73.99
H	4.50
N	1.14
S	0.98
O	9.19
Proximate	
volatiles	33.2
char	56.6
ash	10.2
Terminate (model composition)	
volatiles	59.76
char	30.04
ash	10.2
Gross calorific value	29.3 MJ/kg

Table 3.4: Polish coal analyses and model coal composition

carbon in ash figures, excess air and ultimate analysis, that approximately 30-40 % of the volatiles were unreacted. This calculation then excludes lower terminate yields as this would mean that the entire volatile fraction remained unreacted.

Adopting the factor of 1.8 and assuming that the char fraction consists of 100 % carbon, a volatile pseudomolecule was calculated. This molecule then represents all the hydrocarbon species the volatile fraction consists of in reality since FLUENT only allows for one volatile species per particle.

Although only one species per particle is allowed for, FLUENT gives the opportunity to define more than one set of physical properties. This means that the particle phase can be described in terms of one set of particles consisting of hydrocarbon volatiles, char and ash and another consisting solely of nitrogen volatiles. Both sets are given the same density, size distribution, devolatilization rate parameters and inlet conditions to assure that hydrocarbon and nitrogen volatiles are released in close connection to each other. As described previously the nitrogen volatiles were represented by HCN.

The devolatilization rate constants as given by (3.33) were taken from Goldberg-Essenhigh [9]. The same constants were set for both hydrocarbon and nitrogen devolatilization i.e. nitrogen volatiles were assumed to be released at a rate proportional to hydrocarbon release. It would be of some interest to change the relation between these two rates but that must be left to speculation.

The heat of formation of the hydrocarbon pseudomolecule was calculated from calorific values given in the test rig report[1] and the particle char fraction. The heat of combustion of the volatile fraction is the difference between the calorific value and the heat of combustion of the char fraction. From the calculated volatile heat of combustion, the heat of formation of the pseudomolecule could then be determined.

The latent heat of vaporization appearing in (3.34) was set to the value for ethane for both the hydrocarbon and the HCN particles and the density was set to 1300 kg/m^3.

Coal particle specific heat is a function of composition and temperature as shown by Mericks formula [21]:

$$c_p = (R/a)(g(380/T) + 2g(1800/T)) \quad (3.70)$$

where

$$1/a = C/12 + H + O/16 + N/14 + S/32 \quad (3.71)$$

$$g(x) = \exp(x)/((\exp(x) - 1)/x)^2 \quad (3.72)$$

and C, H, O, N and S are massfractions of the elements on a dry ash free basis, R is the gas constant and T the particle temperature.

Using this formulation no account needs to be taken for the heat of pyrolysis as this is included in the specific heat. This is seen if changes in composition during devolatilization is considered. Specific heat will then rise to a maximum at the highest rate of mass loss and eventually fall to the value for char. The peak in specific heat can be explained in terms of maximum rate of pyrolysis and heat absorption.

Density (kg/m^3)	1300
Heat of vaporization (J/kg)	$4.5\cdot10^5$
Heat of pyrolysis (J/kg)	$1\cdot10^5$
Heat capacity (J/kg K)	$721 - 2.62\cdot10^{-3}\,T + 1.28\cdot10^{-6}\,T^2$ $-3.14\cdot10^{-10}\,T^3 + 3.00\cdot10^{-14}\,T^4$
Devolatilization parameters	
T_{vap} (K)	400 K
Pre-exponential factor (s^{-1})	$5.5\cdot10^5$
Activation energy (J/kmol)	$7.4\cdot10^7$
Char combustion parameters	
Pre-exponential factor (kg/m^2 s Pa)	0.87
Activation energy (J/kmol)	$8.4\cdot10^7$
Diffusion coefficient (kg/m^2 s Pa)	$5.0\cdot10^{-12}$

Table 3.5: Coal particle properties

FLUENT gives the opportunity of defining the specific heat as a function of temperature using a polynomial expression and a heat of pyrolysis appearing in (3.41). The specific heat of char and unreacted coal as a function of temperature was calculated from (3.70) and fitted to polynomial expressions. The char curve was then translated to lower temperatures so as to coincide with the coal curve. A calculation of c_p as a function of temperature and massloss assuming that mass is lost at a constant rate and starts at 350°C and is complete at 1000°C then gives an estimation of the heat of pyrolysis as

$$h_{pyrol} = \int_{350}^{1000} c_{p,devol.}dT - \int_{350}^{1000} c_{p,char}dT \qquad (3.73)$$

If the heat of pyrolysis computed this way is used in connection with c_p for char as a function of temperature translated to coincide with the c_p of the unreacted coal at low temperatures a reasonable account has been taken for the heat required to heat up and devolatilize the coal particles. The c_p value is approximately valid until all the char is burned off but is not valid for the remaining ash. This error will although hardly affect the flame structure.

Particle swelling during devolatilization was considered moderate and C_{sw} in (3.35) was set to 1.1 representing a 10 % size increase.

Char burnout constants were taken from Field [7] assuming that CO is the only product of surface reaction. The heat of surface reaction was presumed to be totally-absorbed by the particle, i.e. f_h in (3.39) was set to one.

The coal particle size distribution as given in the test rig report was fitted to the Rosin-Rammler distribution and it was decided to consider the size range 5-150 μm in the calculations.

3.3.4 Boundary conditions and calculation procedures

Prior to the full 3D flame calculation the 3D coal burner inlet conditions had to be set. For this purpose an isothermal 2D calculation was performed based on the primary air flowrate from tests 44 and 49. The difference in flowrate between 44 and 49 (1.40 and 1.37 kg/s) was not considered as having a major impact on the division of massflow between the three 3D inlets, therefore one 2D calculation based on the mean of the two flowrates was used for all 3D calculations. The coalpipe inlet velocity was calculated from the cross-sectional area of the coalpipe measured from drawings and the primary air temperature using the gas law. Turbulence intensity was set to 10 % (fully developed turbulence) and the turbulence lengthscale as the height of the coalpipe.

The coal particle flow was represented by 50 particle injections evenly spread over the inlet vertical line. The particles were assumed to be in force balance with the gas phase i.e.

they had the same inlet velocity as the gas. A 1000 turbulent trajectory calculations were performed with one particle size at a time to find a statistical distribution of coal massflow over the three 3D inlets for different particle sizes. This procedure was repeated for every fifth μm size in the range 5–150 μm.

The 2D calculation gave the distribution of massflow of coal particles and primary air over the 3D coal burner inlets and, based on inlet areas and total massflow, their average velocities could be calculated. No attempt to define the inlet velocities as a function of height or width was made. Average turbulent lengthscales and intensities were also calculated from the 2D model.

The particle size distribution could be determined for each inlet and be fitted to the Rosin-Rammler parameters. The upper inlet was given 10 groups of particles evenly distributed over the inlet area with each group consisting of 4 discrete particles in the range 5-100 μm. The central inlet was given 3 groups with 3 particles each in the range 5-150 μm and the lower inlet 8 groups of 3 particles also in the range 5-150 μm. An exactly similar set was set up for the HCN phase and the total amounting to 146 discrete particle injections.

The massflow of combustion air through the secondary and gas burner inlet was, according to J.W. Allen of International Combustion, about 20 % of the total combustion air. The division of flow between secondary and gas burner was calculated on the basis of their windbox inlet areas. Normal velocities were then calculated from model inlet areas and air temperatures using the gas law. y and z components of the inlet velocity vectors were used to describe the massflow alignment with burner geometry. Turbulent lengthscales were set as the height of the inlets and the intensities set to 10 %.

The auxiliary air inlet then comprised 80 % of the combustion air and its normal velocity was, as in the other cases, computed from inlet area and air temperature using the gas law. Turbulent quantities were set according to the method described above.

All walls including the burner were set to the constant temperature 750 K. This temperature was maintained for all runs. For the wall emissivity a discrimination was made for the front wall and burner which emissivities were set to 0.6. The other bounding walls were given the value 0.9. Inlets and outlets were assumed non-reflecting and were set to 1.0.

The combustion calculations started with a cold flow solution of the flowfield i.e. product species of the chemical reactions were turned off. When the flowfield was converged an ignition source was patched by setting a high temperature to a slice of cells across the domain close to the burner. The solution was then continued with all species turned on and radiation and trajectory calculations performed every tenth iteration. When the solution stopped changing and species residuals were below 10^{-3} the time consuming trajectory calculations were turned off and the continuous phase solution was allowed to proceed down to a residual sum of 10^{-4} at which point the solution was judged converged. The last step was included to ensure that the NH_3 and NO fields were entirely converged.

The computations were performed on a Pentium 90 MHz with 32 Mb RAM. A converged solution required about 2500 iterations and a computation time of nearly 2 weeks. The most time consuming part was the trajectory calculations requiring 30 minutes every tenth iteration. To get a reasonable statistical description of the turbulent dispersion, every particle injection was divided into four stochastic trajectories. It is possible that this was not enough and that more trajectories could be required however, four was the practical limit.

Chapter 4

Model results

4.1 2D-model

The outline and grid of the 2D-model is seen from figures A3 and A4.

4.1.1 Velocity field

The solution of the velocity field is seen in figure A5.

The major flow divider at the burner inlet is the upper stabilization plate. The part of the flow directed over the plate experiences a slight pressure build up at the backside of the wing, with an accompanying loss in mean velocity magnitude. At the wing the flow is divided and accelerated in the converging geometry. Above the wing, at the inlet to the diffuser, the pressure drops and the flow rate is raised from 12 to 35 m/s. After the passage into the diverging diffuser the flow rate rapidly decreases and turns into turbulent kinetic energy.

At the diffuser outlet the wedge creates a wake with intense recirculation. The wake intensity and size is a function of both the burner and secondary air velocity. The wake is of critical importance for flame attachment and can be imagined as a mixing bowl for secondary air and coal particles carried by burner air. Furthermore, the residence time in the near burner region is increased for coal particles taking the route over the wing into the wake, which is necessary for ignition in the near burner region. The size of the wake is seen from figure A6 showing ($-1 < u$-velocity < 1).

The bulk burner flow travels between the central and upper stabilization plates where a slight and transient acceleration occurs before it enters the furnace.

Secondary air is accelerated in the converging nozzle and enters the furnace at a velocity in the range 60-80 m/s.

The division of massflow between the 3D-inlets was determined from FLUENT's integral reports and is found in table 4.1. To simplify the discussion the 3D-inlets will from now on be called, with the uppermost, I1, I2 and I3 (fig. 3.2).

4.1.2 Turbulence

As described, turbulent kinetic energy is as created at the entrance to the diffuser unit which is of importance for particle dispersion.

In the wedge wake high levels of turbulent energy and effective viscosity is observed, confirming its disperging and mixing function (figures A7-A8).

Turbulent intensities and lengthscales for the 3D inlets were calculated by averaging values for k and ϵ at the inlet planes (table 4.2).

4.1.3 Coal particles

The stochastic trajectory calculations gave a statistic distribution of massflow over the 3D-inlets for each particle size (table 4.1). By use of the Rosin-Rammler distribution fitted to the test rig coal sieve analysis, new Rosin-

Inlet	massfraction (%)	
	gas	particles
I1	19.7	9.6
I2	8.1	15.9
I3	72.2	74.5

Table 4.1: Massflow division of primary air and coal particles over 3D burner model inlets.

Inlets	velocity (m/s)			turbulence		
	49	44	24	int. (%)	length. (m)	temp. (K)
I1	10.6	10.8	11.5	30	0.061	344
I2	15.6	15.9	16.9	9.53	0.018	344
I3	18.2	18.5	19.8	9.77	0.088	344
secondary	66.5	59.7	78.7	10	0.02	603
gasburner	23.2	24.4	-	10	0.188	603
auxiliary	25.3	22.7	23.5	10	0.413	603

Table 4.2: Inlet conditions for model cases 49, 44 and 24.

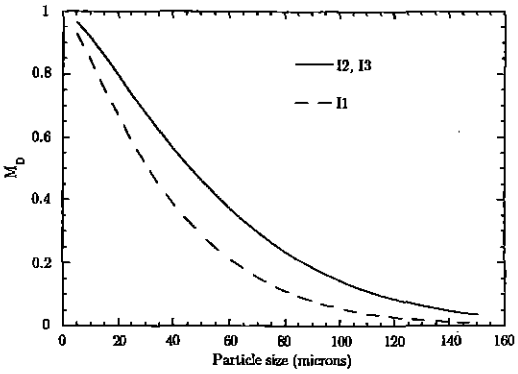

Figure 4.1: Rosin-Rammler distribution of particles at coal burner inlets.

Rammler parameters could be calculated for each of the inlets. The distribution is seen in figure 4.1. The calculation showed that no more than 9.6 % of the massflow was directed above the wing to the diffuser and I1. Furthermore, the size distribution differed significantly between I1 and the two other inlets. I2 and I3 did not substantially deviate from the original distribution, but I1 had a lower mean diameter and practically no particles larger than 100 μm. The reason for this is the lesser tendency of heavy particles to respond to changes in the surrounding gas velocity field. Lighter particles entering the burner at the top of the coal pipe follow the flowfield over the wing, while heavier particles traverse the flowlines to a larger extent and travel under the wing. Of the I1 massflow it is again the portion of light particles that are dragged into the wedge wake. Light particles are rapidly devolatilized and are therefore probably important in this critical area for ignition.

One conclusion that can be drawn from these observations is the importance of homogeneous dispersion of coal particles in the coal pipe, which is also recognized by the manufacturer. The FAN burner is supplied with a coal flow dispersal device at the entrance to the coal pipe to avoid roping.

4.2 Modified FAN burner

4.2.1 Coal only firing

Coal only firing refers to test number 49 in the test report as described earlier with the model inlet conditions shown in table 4.2.

To facilitate the discussion the z-direction is defined as the axial direction, the y-direction as the vertical direction and the x-direction as the corresponding horizontal direction. z-planes are then planes with constant z-coordinates and so forth. By analogy u, v and w are the velocity components in the x, y and z directions.

Velocity field

The basic observations from the 2D-model were confirmed by the 3D-model as seen by figure A9 which shows a x-plane at the wedge closest to the vertical symmetry plane. The wedges create a recirculation zone between the low velocity I1 air stream and the high velocity secondary air jet. The secondary air jet penetrates the auxiliary air stream with both holding higher velocity than primary air so that a free shear layer is formed at the flow boundary between the primary and secondary air streams. In the space between the burner and the auxiliary air inlet the secondary air jet gives rise to an intense recirculation zone.

Figure A10 shows the flowfield at the y-plane corresponding to the horizontal symmetry plane. From this it is seen that a recirculation zone is formed at the edge of the gasburner air jet extending almost 2.5 m downstream of the burner. The recirculation zone is bounded by the furnace walls and its extension in vertical direction is shown by the iso surface of zero w-velocity in figure A11.

Finally figure A12 is a plot of $1 > w$-velocity > -1 at a y-plane cutting through the wedges showing the recirculation zone boundaries of the wedge wakes and the furnace wall zone. It can be noticed that the more central wedge wake is larger than its neighbour.

Combustion

The finding from the 2D-model that it is only the smallest particles entering through I1 which are dragged into the wedge wakes close to the burner was confirmed by the 3D-model. Figure A13 shows particle tracks of sizes 5, 37, 68 and 100 μm entering through I1. The small particles are transited through the wedge wakes into the flow boundary between the secondary and primary stream. During the transit they are rapidly heated and devolatilized and the volatiles are subsequently ignited at the flow boundary causing flame attachment. The attached flame is seen in figure A14 showing the temperature field at the same plane as figure A9.

The core of coal particles entering through I2 and I3 travel along the burner centreline and are devolatilized and ignited further downstream. At about 1.7 m downstream of the burner axial centreline a sharp rise in temperature indicates ignition (figure A14).

The volatile reaction zone in the plane of figure A14 is seen in figure A15 which shows the predicted volatile reaction rate field. Figure A15 clearly shows how the attached flame is parted into two flame boundaries. An inner, enveloping the primary air stream, and an outer at the edge of the secondary air jet. Particles and volatiles not burned at the inner flame sheet diffuse through a region depleted of oxygen, as shown by figure A16, and eventually reaches the outer flame sheet at the boundary between secondary and primary air.

Figure A17 shows the oxygen mole fraction at a z-plane 0.5 m downstream of the burner. This illustrates how the inner and outer flame boundaries are connected at the edge of the secondary air stream entering the side of the burner above the gas burner. The high velocity side burner secondary air stream provides a shearing flame boundary but also has a cooling effect confining the attached flame to the centre of the burner upper edge. Furthermore, side burner secondary air is the explanation for the size difference of the wedge wakes seen in figure A12. Figures A18, A19 and A20 show the temperature, oxygen mole fraction and volatile reaction rate fields at the same plane as A12, confirming the cooling effect and the edge of the flame boundary.

From A17 and A19 low oxygen and high temperatures are observed in the wall recirculation zone. The explanation for this is that the strong recirculation caused by the low velocity gas burner air stream enhances dispersion of particles in the x-direction. Figures A21, A22, A23 and A24 illustrate this phenomenon by showing particle concentration, char burnout rate, temperature and oxygen mole fraction in the same plane as A10. Combustion in this zone further intensifies the recirculation and the rapid mixing which is shown by the high effective viscosity in figure A25, corresponding to figure A10.

In conclusion, two reaction zones dominate the first metre from the burner: the attached flame zone bounded by secondary and primary air and the wall recirculation zone at the edge of the gas burner air stream. The separation of these zones is most clearly seen in figure A17. The separation eventually disappears and the two zones merge at about 1 m downstream as side burner secondary air and gas burner air burns out. This is seen from figure A26 showing oxygen mole fraction at a z-plane at 1 m. After this point the flame consists of the outer flame boundary where secondary and auxiliary air is consumed and the inner boundary where primary air is consumed separated by a large zone depleted of oxygen.

Peak temperatures of about 2280 K occur in the outer reaction zone, close to the burner and in the vicinity of the maximum volatile reaction rate as shown in figure A14. In this region the oxygen supply is large and the mixing is vigorous due to the high velocity secondary air jet. Below the outer flame boundary in the area down to the burner centreline, the flame is rather cold (1200-1400 K) due to the endothermic devolatilization of the bulk particle flow and the very fuel-rich environment. Figure A27 shows the volatile mole fraction in the same plane as figure A14.

Diagram A28 shows the fate of the major species down the burner centreline. At about 1.7 m downstream of the burner, the oxygen mole fraction drops to practically zero indicating the total consumption of primary air, an observation also confirmed by figure A16. After this point the inner flame boundary vanishes and flame processes are confined to the outer flame boundary. The decay of volatiles, CO and H_2 are slow and caused by diffusion to the flame sheet. Figures A29, A30 and A31 show oxygen mole fraction, char burnout rate and temperature respectively at a z-plane 1.8 m downstream of the burner. A29 shows the small remaining part of the inner flame boundary at the centreline and the surrounding outer boundary. A30 shows the char consumption rate which coincides with the outer flame boundary and the peak in temperature shown in A31. The flame history from this point to the furnace outlet changes only in the sense that the flame boundary approaches the bounding furnace walls as oxygen is consumed. The dominating process is char burnout which reaches a maximum close to the outlet, indicated by figure A32 which shows the entire flame temperature field at a x-plane close to the vertical symmetry plane.

To get an overview of the fate of coal particles figure 4.2 shows the integrated massflow-weighted rate of devolatilization and char burnout in the flow direction. Devolatilization rises sharply for the first 1.5 m and reaches a peak at about 1.7 m, corresponding to the disappearance of the inner flame boundary, before falling and completion at 3 m. During devolatilization there is some burnout of small particles but the maximum burnout rate is not achieved until about 6 m downstream. The burnout curve shows 6 discrete peaks probably corresponding to the 6 particle sizes represented in the model.

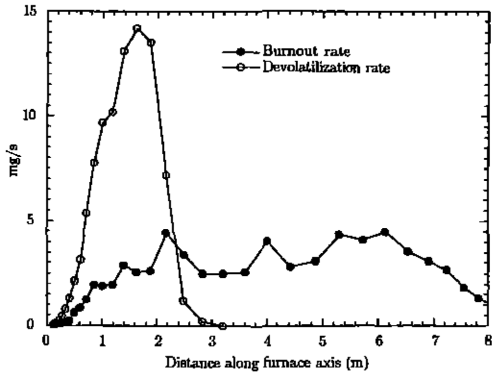

Figure 4.2: Integrated char burnout and devolatilization rate along furnace for model case 49.

Specie		Mole fraction (%)		
		49	44	24
Volatiles		1.9	2.1	2.2
O_2		4.2	3.6	3.9
CO		2.1	2.6	2.3
H_2		0.37	0.52	0.42
CO_2		12.0	12.0	12.0
H_2O		4.6	6.1	4.7
Carbon in ash	(%)	30.6	31.9	26.8
Unburnt volatiles	(%)	17.6	28.0	19.5

Table 4.3: Outlet mole fractions of major species for model cases 49, 44 and 24.

The visual flame length for case 49 was 8.5 m. This length is approximately the position that burnout ceases according to the model prediction indicating the validity of the model.

At the outlet mole fractions of major species are given by table 4.3.

Oxygen mole fraction equates approximately to what is expected at this point in the flame, compared to test rig data in table 3.1, but the relation between carbon in ash and unburnt volatiles is not in balance. This is because of the high volatile fraction set to the model coal. The terminate volatile fraction is, in reality, a function of the heating rate and the ultimate temperature and not just a function of residence time. This is the weakness of the single step devolatilization law and why it fails in flames with inhomogeneous temperature distribution. Furthermore, no account is taken for tar and soot formation which, taken together, gives the unrealistically high centreline mole fraction of volatiles seen in diagram A28. The large amount of volatiles is an uneven competitor to char burnout giving too high carbon in ash levels.

CO and H_2 levels are far too high and should only be left in trace amounts at the furnace outlet. This inability to predict intermediates is a known drawback of the Magnussen-Hjertager formulation of the turbulent reaction rate [26]. Figure A32b shows the CO mole fraction in the same plane as A9. Peak levels of about 20 % occur in the oxygen depleted zone between the inner and outer flame boundaries that persist far downstream. CO and H_2 should perhaps be left out from the volatile reaction rate but this would then give very high peak temperatures.

It was noted that an attached flame could not be achieved with the devolatilization rate parameters in table 3.5. To get flame attachment the energy of activation had to be lowered to 4.5×10^7 J/kmol. Many explanations can be offered. First of all, radiation is not included in the particle heat balance, which is a serious drawback since coal particles are good absorbers of radiation and can reach temperatures of hundreds of degrees higher than the surrounding gas, especially in this type of flame with peak temperatures close to the burner. It is not implausible that radiation has an equally important part in flame attachment as the fluid dynamics has.

The vertical temperature distribution, as seen by figure A32, seems fairly reasonable but the heat extraction in the furnace centreline direction is too low giving an accumulation of heat downstream due to the very small furnace. In the test rig, peak temperatures of about 1600 K were detected at 2 m downstream the burner and these corresponded well with the predicted point of burnout of primary air by the model.

Despite the shortcomings of the model pointed out above, the flame structure is probably reasonably predicted. The oxygen field and temperature distribution seems fair enough to render a realistic discussion of the nitrogen chemistry possible.

Case	Mole fraction (ppm)		
	HCN	NH_3	NO
49			
mixing	44.1	27.8	126.5
kinetics	0	0	434
44			
mixing	87.7	33.8	116.7
kinetics	0	0	340
24			
kinetics	0	0	498

Table 4.4: Outlet mole fractions of nitrogen species for model case 49, 44 and 24.

Nitrogen chemistry

The decay of HCN was calculated with both the Magnussen-Hjertager mixing rate and pure Arrhenius kinetics. The mixing rate calculation gave, for reasons stated above, unrealistic levels of NH_3 and HCN, i.e. a much too slow decay of intermediates. In the kinetic calculation NH_3 was, on the other hand, practically in steady state everywhere with a peak value of 68 ppm. This is not unrealistic and indicates that more faith should be put to the kinetic calculation than the mixing rate calculation. For NO levels the opposite was true. The mixing rate calculation gave more reasonable peak values of about 500 ppm while the kinetic calculation gave 3700 ppm. Outlet levels are given by table 4.4.

The mixing rate predictions are of some interest especially in connection with the cofiring case as will be described. The rest of the discussion however, will be based on the results of the kinetic calculation.

Before studying model results it is important to realise what the proposed kinetic mechanism describes. The first step is the decay of HCN evolving from coal particles during devolatilization, and this is dependent on the oxygen partial pressure as seen by rate expression (3.62). Lack of oxygen thus slows this process down and in extreme cases chokes the nitrogen chemistry at this stage. A conclusion from this is the danger of having a too low stoichiometric ratio in the primary combustion zone during staged combustion. This could give a backlash by large NO production when oxygen eventu-

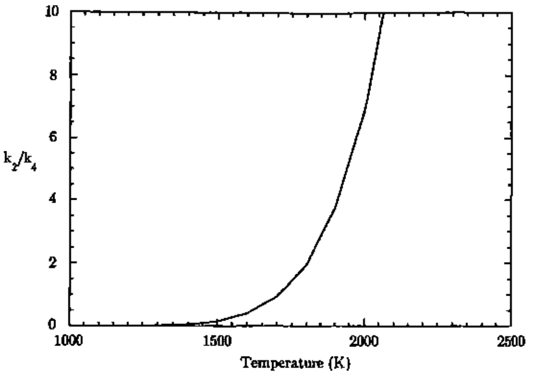

Figure 4.3: Temperature dependence of oxidation-reduction quotient

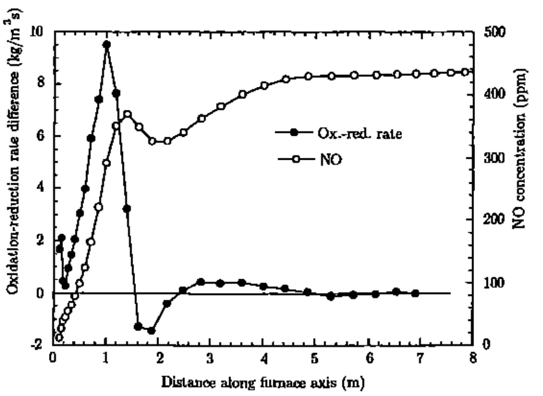

Figure 4.4: Integrated oxidation-reduction rate difference and NO mole fraction along furnace axis for model case 49.

ally becomes available in second stage combustion.

NH_3 formed from HCN is then either oxidized to NO or reduces NO formed to N_2 by reaction with NO. The aim of all combustion measures is then to minimize the quotient of the oxidation rate to the reduction rate. Taking the high temperature limit of (3.63) this quotient is described by

$$\frac{k_2}{k_4}\frac{C_{O_2}}{C_{NO}} \tag{4.1}$$

Figure 4.3 shows the temperature dependence of (4.1), $\frac{k_2}{k_4}$, and confirms the relatively weak temperature sensitivity of fuel NO production at normal combustion temperatures. It should be stressed that the oxidation-reduction quotient is even lower below 1800 K as the oxidation rate is represented by the high temperature limit. Experimental evidence of the weak temperature dependence is given by Pershing and Wendt [23] who studied the dependence of thermal and fuel NO on combustion air preheat. Only at very high temperatures was fuel NO affected by temperature and more important, lowering the preheat removed the thermal NO but kept the fuel NO at a constant level. This finding is consistent with figure 4.3.

Of critical importance on the other hand is the oxygen dependence appearing as C_{O_2} in the numerator of (4.1). It is well documented that NO production is strongly favoured by high levels of oxygen and this provides the obvious reason for the success of the air staging techniques.

Finally, reduction seems to be favoured by high levels of NO. This is a statement of the fact that NO has to be present if it is to disappear, but the situation is a little more complex. In a serie-parallell oxidation-reduction system like this, where the reduction product is to be favoured, the oxidation product NO, which is the material to be reduced, has to be produced at a fast enough rate to favour reduction over oxidation. If the oxidizer, O_2 is in excess then more NO will be produced than is reduced that is oxidation will dominate. However, if O_2 is portioned to the NH_i-pool at a very slow rate then the precise amount of NO will be produced to favour reduction. Given an infinitely long flowreactor, where O_2 could be infinitely diluted, the entire NH_i-pool could be reduced to N_2. This is the reason for the appearance of NO concentration in (4.1). In practice it points to the important influence of residence time in staged combustion which has also been studied by Wendt et al. [28]. They found that residence time between first and second stage combustion is just as important as the level of NO produced at the first stage. A large first stage NO level can be largely reduced given long enough time to the second stage combustion and the final result can be just as good or better than a low first stage NO level with a short first stage residence time. Another conclusion is the limiting effect of boiler size on achievable NO reduction.

To get an overview of the predicted nitrogen chemistry in model case 49 the integrated massweighted difference between oxidation rate of NH_3 and reduction rate of NO along the furnace axial direction is given in figure 4.4 This difference corresponds to (4.1) by being lower than zero when (4.1) is lower than one.

The first 1.5 meters the chemistry is dominated by oxidation seen by the fast raise of both NO levels and rate difference. NO mole fraction reaches a peak at 1.5 m and is then slightly reduced having a minimum at 1.8 m before increasing again. The NO reduction well corresponds to the rate difference being smaller than zero and is in the region where primary air burns out. After the well there is another oxidation zone reaching from 2.2 to 5 m where again the rate difference is slightly larger than zero. From 5 m to the outlet NO mole fraction levels out and at 7 m practically all HCN and NH_3 is consumed.

Fig. 4.4 then summarises the predicted nitrogen chemistry as four successive zones:

1. 0–1.5 m. Strong oxidation dominance and where 85 % of the outlet NO level is produced.
2. 1.5–2.2 m. Reduction zone, lowering zone one NO levels by 10 %.
3. 2.2–5.0 m. Slight oxidation dominance. Zone two minimum NO level increased by 30 %.
4. 5.0–6.9 m. Levelling out and final consumption of HCN and NH_3. No change in NO level.

An explanation for the results observed in each of these zones will be dealt with in turn.

Figures A33, A34 and A35 show HCN, NH_3 and NO mole fractions in the same plane as the oxygen field of figure A16 with which they are to be compared. HCN fills the gap between the inner and outer flame boundary and is at a maximum at the centreline just behind the point of primary air burnout. This maximum coincides with the fuel rich core of the flame and indicates that very little HCN is transformed to NH_3 in this region. NH_3 is found in an intermidiate position between the fuel rich central core and the outer flame boundary. In this area devolatilized HCN can compete with hydrocarbons for oxygen and transform to NH_3. Finally the NO field shows how the NH_3 oxidation pathway dominates at the outer flame boundary. NO peaks very close to the burner even as far down as the wedge wakes. This coincides with the maximum rate of volatiles combustion and the maximum flame temperatures. The maximum NO formation is however not, as it seems from A35, confined to the outer flame boundary all the way down through zone one. Just after the near burner peak in A35 at about 1 m downstream the maximum NO formation rate moves inwards and downwards from A35 and follows the edge between the gasburner air stream and the wall recirculation zone. This movement can be imagined as a rate diffusion against gradients of increasing oxygen mole fraction, NH_3 formation rate and rapid mixing. Figures A36, A37 and A38 show the rate of NO formation at z-planes corresponding to 0.72, 0.86 and 1.0 m in the axial direction, revealing the rate diffusion phenomenon, and figures A39, A40 and A41 show the corresponding oxygen fields. The rate diffusion process coincides with the merging of the oxygen-depleted wall recirculation zone and the attached flame boundary. It is not impossible that by a mixing action the wall recirculation zone has a subversive effect on NO reduction. Figure A42 shows the NO mole fraction at the horizontal symmetry plane and this should be compared to figures A10, A24 and A23. NO mole fraction maximum coincides with the centre of the recirculation zone and the high temperatures experienced there.

As primary and gas burner air burns out the limit of oxidation zone one is reached and reduction becomes increasingly important and competitive. Figures A43, A44 and A45 show the HCN, NH_3 and NO mole fractions respectively at the same z-plane as A29, A30 and A31 i.e. at 1.8 m downstream in the middle of reduction zone two. Reduction is favoured here because of the very small amount of remaining primary air and the relatively large amount of NO. HCN at the centreline is oxidized to NH_3 by primary air, which in turn reduces NO to N_2 much faster than being oxidized by primary air. This situation only prevails until the primary air is completely consumed which explains the very short reduction zone.

After primary air burnout, the nitrogen chemistry diffuses to the outer flame boundary, explaining oxidation zone three. At the flame boundary oxygen is in large excess compared to the small remaining level of HCN, causing oxidation to dominate and NO levels to increase again. This prevails into the levelling out zone four where HCN is finally depleted.

It should be recognized that the oxidation rate is a little overestimated due to the high temperature approximation but not to the extent that the overall trends are obscured. Controls showed that significant NH_3 oxidation occured at temperatures in the range 1500-2000 K which is a suitable range for the approximation to be valid. The mixing rate calculation showed the same trends as the kinetic calculation, i.e. the oxidation-reduction zone succession and the rate diffusion phenomena, which confirm the fact that it is mainly the oxygen mole fraction that determines the nitrogen chemistry.

If some doubt were to be cast on the predictions it should be directed to oxidation zone three. From a previous discussion it was concluded that the devolatilization is probably slower and not so severe at the low oxygen and low temperature furnace axis region. Figure A33 shows unrealistically high peak levels of HCN, as was the case for hydrocarbon volatiles. If devolatilization was slower and to a lesser extent, HCN and primary air would prevail further downstream and lengthen reduction zone two, perhaps extinguishing oxidation zone three. In such a case, the NO curve in figure 4.4 would continue downwards from its zone two minimum and eventually level out for the same reasons as the predicted levelling out of zone four.

The final conclusion is that NO emissions are determined in the very near burner region, perhaps within 2.5 m from the burner, and it is within this area that the model gives a realistic and clear picture of the events which set the stage for comparison with gas co-firing.

4.2.2 Gas co-firing

Gas co-firing refers to the test rig flame case 44 and the inlet conditions can be seen from table 4.2.

Combustion

The overall flame structure of case 44 was the same as in case 49. Flame attachment was just as strong in the co-firing case as in the case of coal only firing, giving rise to the formation of the inner and outer flame boundaries. The centreline ignition point was at the same position and the hot, wall recirculation zone could also be identified. Figures A46, A47 and A48 which are to be compared to figures A14, A23 and A24 respectively shows the similarities.

The methane gas is ignited at about 0.8 m downstream of the gasburner at the horizontal symmetry plane as shown by the methane reaction rate field of figure A49. The ignition point coincides with the centre of the wall recirculation zone shown in figure A50. Methane burns out in a very narrow zone shown by the reaction rate iso-surface of figure A51. The flame boundary forms an arc from the top edge of the gas burner into the shearlayer between the gas burner flow and side burner secondary air, down to the centre of the wall recirculation zone. On the burner side it is bounded by primary air, and to the furnace side, by the wall recirculation zone. Figure A52 showing the methane mole fraction at the horizontal symmetry plane confirming that the methane is practically burnt out within 1.5 m from the burner.

The main difference between coal only firing and gas co-firing is the higher peak temperatures in the wall recirculation zone and the larger oxygen depletion in this area as seen from figsures A47 and A48. This is a direct effect of the gas firing which also causes merging of the attached flame and the burning recirculation zone slightly earlier. Figure A53 shows the merging flames at a z-plane 0.7 m downstream of the burner. The core of the flame has a significantly slower temperature increase down the centreline than in the coal only firing case, as seen from figure A53b. This is an effect of the smaller amount of fuel in this area and the oxygen depletion caused by the burnout of the methane. Peak temperatures occured, as in case 49, at the outer attached flame boundary close to the wedge wakes and were in the same range i.e. about 2300 K. Outlet mole fractions of the major species seen by table 4.3 did not diverge either from case 49, except for H_2 and H_2O which were slightly higher due to the presence of methane. One major difference though is the far higher level of unburnt volatiles and

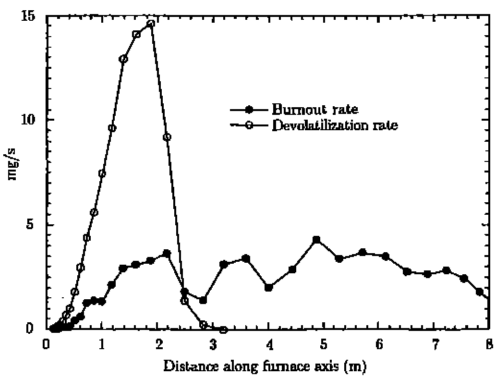

Figure 4.5: Integrated burnout and devolatilization rate along furnace for model case 44.

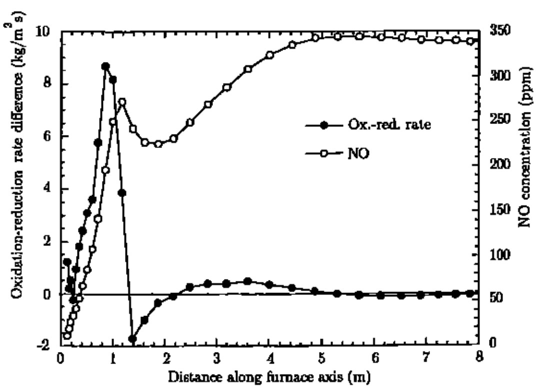

Figure 4.6: Integrated oxidation-reduction rate difference and NO mole fraction along furnace for model case 44

the slight increase in carbon in ash. This can be explained by the burnout of methane close to the burner consuming oxygen, which is then not available for volatiles and char entering the scene at a later stage.

One observation made during the test rig work was the possible delay of char burnout due to gas co-firing. Figure 4.5 shows the integrated rate of devolatilization and char burnout for case 44, which should be compared to figure 4.2 for case 49.

It is hard to see any significant differences between figures 4.2 and 4.5. Devolatilization occurs in the same area for case 44 as it does for case 49. Char burnout shows the same overall behaviour as case 49 with burnout of small particles in the devolatilization zone and a burnout rate maximum 5 to 6 m downstream.

Nitrogen chemistry

The outlet mole fractions of nitrogen species are given by table 4.4 and show a 22 % improvement in NO, based on the kinetic calculation, when co-firing gas compared to the case of coal only firing. The mixing rate calcualtion gave no more than a 10 % improvement but the interesting obsevation about the mixing results are the total amount of nitrogen species i.e. HCN + NH_3 + NO compared to case 49. In the co-firing case this sum is about 20 % larger than in case 49 showing a slower mixing rate in the case of the co-firing.

The integrated oxidation-reduction difference showed the same zonal structure as case 49 when comparing figures 4.6 and 4.4. Reduction zone two though is slightly closer to the burner and reduction of the NO peak of oxidation zone one is 18 % larger. This larger reduction is set back by a severe zone three oxidation raising the reduction zone two minimum by 50 %. It is noted that oxidation and reduction persists all the way down to the furnace outlet, which was not the case for coal only firing.

Figures A54, A55 and A56 showing HCN, NH_3 and NO mole fractions in the same plane corresponding to figures A33-A35, illustrates the similarities between case 44 and 49 and needs no further discussion. Oxidation zone one exhibits the same structure as for case 49, with strong oxidation in the vicinity of the wedge wakes and the rate diffusion phenomenon as the attached flame and the oxygen depleted wall recirculation zone merge. This happens, although a little earlier in the co-firing case, and is illustrated by figures A57, A58 and A59. These show the NO production rate at z-planes at 0.61, 0.72 and 0.86 m and figures A60, A61 and A62 show the corresponding oxygen mole fraction. Due to the faster merging of the flame zones the reduction zone two comes slightly closer to the burner. The reduction proceeds, as in the coal only case, until primary air is depleted. Oxidation zone three then succeeds by rate diffusion to the outer flame boundary and is eventually followed by the levelling out zone four about 5 m downstream, at the same point as in case 49.

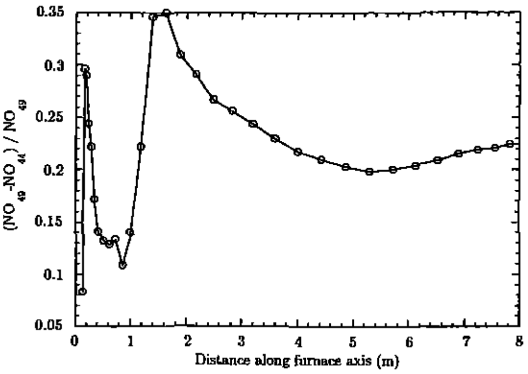

Figure 4.7: Integrated NO reduction by gas co-firing comparing cases 44 and 49 along furnace.

Where then in the flame is the large reduction in NO decided and what is the probable course? To track this down NO levels for case 44 and 49 must be compared along the furnace. Figure 4.7 shows the relation

$$\frac{[\mathrm{NO}]_{49} - [\mathrm{NO}]_{44}}{[\mathrm{NO}]_{49}} \qquad (4.2)$$

where [NO] is the integrated mole fraction NO corrected for dilution with the integrated mole fraction N_2 according to

$$[\mathrm{NO}]_{corr} = [\mathrm{NO}]_{model} \frac{0.792}{[\mathrm{N}_2]_{model}} \qquad (4.3)$$

The first meter from the burner the difference between coal only firing and gas co-firing is low (about 10-15 %) and is no more than the difference due to the exchange of coal for gas. NO formation in this area corresponds to the near burner wedge wake oxidation and the rate diffusion zone. After 1 m the performance of the gas firing case dramatically improves and reaches a peak at about 1.5 m where the difference becomes 35 %. The peak corresponds to the end of oxidation zone one i.e. in the area of maximum NO production rate for both flame cases. The area between 1 and 1.5 m in relation to velocity field, oxygen and NO mole fraction, temperature, NO production rate and methane mole fraction is shown in the horizontal symmetry plane by figures A63-68.

After the peak the improvement slowly drops to about 20 % through oxidation zone three. This is understood when comparing figures 4.6 and 4.4. Oxidation zone three is much severer in the gas co-firing case than in the coal only case. The difference is explained by the consumption of gas burner and primary air by the methane burnout in the co-firing case discussed previously. Oxidation of HCN is held back at the furnace centreline for the same reason that explained the large amount of unburned volatiles. When primary air is burned out the relatively large remaining HCN fraction diffuses to the outer flame boundary where oxidation will dominate until all HCN is consumed. In fact the choking of HCN also explains the larger reduction in reduction zone two in the co-firing case. In zone two reduction dominates because of the low level of oxygen. The more HCN present in this area the faster the production of NH_3 rolls and the more NO is reduced. It is thus quite a delicate balance deciding the final outcome of the nitrogen chemistry.

It can now be concluded that the accelerated reduction of NO levels when co-firing gas compared to coal only firing has its origin in the area where oxidation peaks in both flame cases as seen by figures 4.6, 4.4 and 4.7. The effect is then not a reduction of NO by its destruction but a lowering of its production rate. It is interesting to note that the 'production loss' zone is situated at the edge between the gas burner air stream and the wall recirculation zone, i.e. *after* the burnout of methane (figure A68). The explanation of the production loss now becomes clear. The burnout of methane consumes oxygen that is transported to an area where it is critical for NO formation causing the loss of production phenomena and thus lowering NO levels.

Methane burns out in an area where very little NO is formed. This is seen from figure 4.7 where NO levels the first meter from the burner do not show any improved reduction compared to the coal only firing case. The NO formed the first meter from the burner is produced in the near burner attached flame in vicinity of the wedge wakes. Slightly downstream the NO production rate diffuses to the edge between the merging attached flame and the oxygen depleted recirculation zone, but at this point most of the methane is burnt out.

Figures A69-71 correspond to figures A57-59 showing the methane reaction rate in the NO production rate diffusion zone. That NO levels, before and even in the rate diffusion zone, are unaffected by the presence of methane is probably due to the fact that NO the first meter from the burner is primarily produced in primary air while methane primarily consumes gas burner air.

It is thus shown that the NO reduction achieved in the test rig co-firing natural gas can be explained in terms of the oxidation-reduction system of HCN, NH_3, NO and N_2 without considering reburning reactions. The presence of reburning reactions i.e. the reduction of already formed NO by attack of hydrocarbon fragments is by no means excluded as a participator in lowering NO levels. The firing system however, is far from optimized for these kind of reactions to be important. Efficient reburning takes place when NO formed in first stage combustion is well mixed with natural gas at a second combustion stage. In this case methane burns out before the maximum NO level is reached and at a location separated from the main NO production zones. If a name should be put to this way of lowering NO levels it should not be reburning but pre-burning.

One interesting finding from the test rig work was the existence of an optimal level of natural gas. Less than 10 % gas did not produce the reducing effect and more than 10 % gave similar disappointment. This 10 % optimum could probably be created by the model in terms of the balance between reduction zone two and oxidation zone three. Too little gas would not produce the production loss effect and too much could possibly choke the HCN oxidation to an extent where a large backlash in oxidation zone three is inevitable.

4.3 Original FAN burner

The original FAN burner simulation refers to test number 24 in the test report and the model inlet conditions are seen in table 4.2.

4.3.1 Combustion

The main and important difference between the modified and the original FAN burner was the disappearance of the strong wall recirculation flame zone from the original FAN burner. Figures A72-74 shows the velocity, oxygen mole fraction and temperature fields at the horizontal symmetry plane. Oxygen is at higher levels and temperature at lower levels in the wall recirculation zone indicating ignition further downstream in the case of the original FAN burner. The explanation is the smaller radial dispersion of particles due to the high velocity secondary air stream surrounding the burner. Figure A75 shows particle concentration in the horizontal symmetry plane and should be compared to A21 for the modified FAN burner. This phenomena is the likely explanation for the higher furnace wall temperatures for the modified FAN burner registered during the test rig work.

The attached flame was just as strong in case 24 as for case 49 and 44, indicated by the temperature field of figure A76 showing the same plane as figures A14 and A46. The centreline primary air burnout point was about the same as in the other cases and the inner and outer attached flame boundaries were there, as seen by figure A76 and the oxygen field of figure A77 showing the same plane as figure A76.

Because of the missing burning wall recirculation zone the flame growth and oxygen consumption showed a significantly different progression in case 24. The conical flame boundary surrounding the primary air stream in cases 44 and 49 was confined to a very short distance in case 24, i.e. the separation of the inner and outer flame boundaries after the merging of the attached flame and the recirculation zone in the modified FAN burner case, as seen by figure A26, was not there in case 24. The flame growth should instead be imagined as the attached flame below the horizontal symmetry plane merging with the one above as the primary air burns out. The merging process is seen by figures A78-80 showing the oxygen field at z-planes 1.39, 1.62 and 1.88 m downstream of the burner.

After the burnout of the primary air the case 24 flame is, as for cases 44 and 49, confined to the outer flame boundary. Due to the high velocity secondary air stream particles are, as mentioned dispersed to a much lesser extent in the x-direction and to a greater extent in the

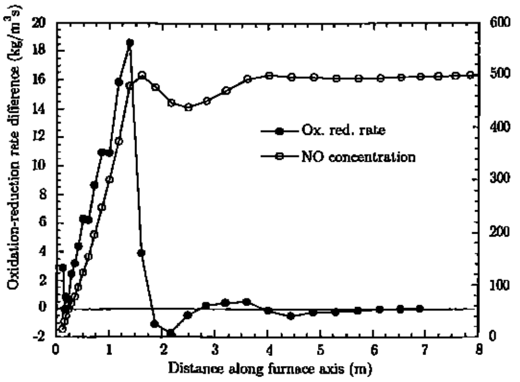

Figure 4.8: Integrated oxidation-reduction rate difference and NO mole fraction along furnace for model case 24.

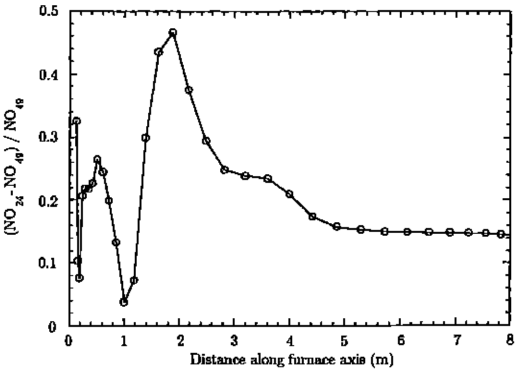

Figure 4.9: Integrated increase in NO mole fraction comparing modelcases 24 and 49 along furnace.

y-direction. This makes the flame grow faster in the direction of the furnace roof due to char burnout in the later stage of the flame and causing a stronger diffusion of oxygen to the furnace centreline in the x-direction. This phenomena is illustrated by the shape of the oxygen field in a z-plane 2.5 m downstream of the burner as shown by figure A81.

The furnace outlet levels of the major species are seen in table 4.3. The improvement in carbon in ash is noted.

4.3.2 Nitrogen chemistry

The nitrogen chemistry was only calculated with the kinetic expressions in case 24 and the outlet level of NO was 500 ppm, i.e. 15 % more than for model case 49. This is in sharp contrast to the 34 % lesser NO in test rig case 24 compared to test rig case 49 as seen by table 3.1, a result which requires an explanation.

Figure 4.8 is equivalent to figures 4.4 and 4.6 showing the oxidation-reduction rate difference for model case 24. The zonal succession with oxidation, reduction, oxidation and levelling out corresponds to cases 44 and 49, however oxidation zone three is very weak and does not raise NO levels above the peak value of oxidation zone one.

Oxidation zone one is, as in the other flame cases, divided into the near burner wedge wake oxidation zone and a rate diffusion zone starting at about 0.9 m downstream. The rate diffusion does not, however, directly coincide with the burnout of primary air and is seen in figures A82-84 showing the oxidation rate field at z-planes corresponding to 0.86, 1.01 and 1.19 m downstream. Figures A82-84 should be compared to figures A78-80 showing the merging of the attached flames just downstream of the rate diffusion zone. At 1.39 m downstream the oxidation reaches a maximum corresponding to figure A78. Comparing figure A85, showing the oxidation reaction field, with A78 reveals that this maximum coincides with the merging of the attached flames and the strong x-direction diffusion of oxygen to the centreline.

As primary air burns out reduction will dominate for a short while until the flame is entirely confined to the outer flame boundary. At this point the decay of HCN diffuses outwards and a small oxidation dominated zone occurs. Oxidation zone three is much smaller and not as severe as in case 49. In fact there are main fluid dynamical differences between the two cases that keep the the balance between oxidation and reduction for case 24 in control. Figures A86-A88 shows the HCN mole fraction at a z-plane 4.01, 4.43 and 4.87 m downstreams. Figures A89-A91, A92-A94 and A95-97 shows the oxygen mole fraction, the oxidation reaction rate and the char burnout respectively at corresponding planes. This series of figures shows how the dispersion in y-direction depletes the roof area of oxygen and how HCN diffuses in this direction away from the x-direction diffusion of oxygen. Reduction will dominate in the oxygen depleted area close to the roof thus balancing the oxidation dominated area in direction of the x-direction gradient of oxygen diffusion.

In an attempt to find where in the flame the main differences in NO formation, between the modified and original FAN burner, are situated the method of equations (4.3) and (4.4) forming the quotient

$$\frac{[\mathrm{NO}]_{24} - [\mathrm{NO}]_{49}}{[\mathrm{NO}]_{49}} \tag{4.4}$$

was used. The result is seen in figure 4.9 and is not as easily interpreted as when case 44 and 49 are compared. The different zones are not located at the same distances from the burner but there is some information to extract. One interesting feature is the more severe oxidation for case 24 the first 0.5 m from the burner. This first part of oxidation zone one corresponds to the near burner attached wedge wake zone for both cases. This is an effect of the strong flame attachment in both cases and the larger velocities of both primary and secondary air in case 24 causing a more rapid mixing and a larger supply of oxygen.

The dipping of the curve at 1 m refers to case 49 reaching its maximum oxidation rate before case 24. This is also the explanation for the fast rise to a maximum at 1.9 m which relates to the maximum oxidation rate of case 24 and corresponds to case 49 entering the reduction zone at this point. The difference between the minimum and maximum compared to the level at 0.5 m suggests that the oxidation maximum is just as severe in both cases.

After the maximum reached by case 24 the difference between the two cases then diminishes due to the effective balance of oxidation and reduction in case 24 and the larger oxidation in zone three for case 49.

The conclusion from this is that model case 24 is disfavoured in comparison to case 49 by the large near burner oxidation. If the near burner oxidation was on the level of case 49 i.e. the curve of figure 4.9 was vertically translated to zero at 0.5 m, case 24 would perform better than case 49. The reason the original FAN burner performed better than the modified FAN burner is then not just a temperature correlation due to imbalance in heat extraction but an effect of the significant fluid dynamical differences between the two burners.

The shortcomings of the devolatilization model used have been described and become important when comparing cases 24 and 49. It was an experimental fact that the modified FAN burner flame was more strongly attached than the original FAN burner flame. A fact confirmed by the higher burner and near burner wall temperatures registred in the modified burner case. The model could not distinguish between this two cases regarding flame attachment because of the problematic devolatilization. If the flame is not firmly attached, the devolatilization may not be so severe and accordingly the fuel NO production not so large in the near burner region.

Furthermore there is the problem of the critically small model furnace. The length of the furnace was acceptable for the nitrogen chemistry predictions but the width seems to be the limiting factor. A wider furnace would probably be a disadvantage for NO production in case 49 due to more pronounced x-direction dispersion of the coal particles and a wider flame merging zone where NO production is critical. The reverse could very well be true for case 24 as this would diminish the forced x-direction diffusion of oxygen critical for NO in case 24.

4.4 Conclusion

In the limitations of the models used and the boundary conditions employed the computer calculation for the test rig cases 49, 44 and 24 has revealed the following hypotheses:

- Case 49 showed how the low velocity gas burner enhances x-direction dispersion and creates a burning wall recirculation zone.

- NO formation in case 49 was critical at the merging point of the burning recirculation zone and the attached flame.

- The presence of the burning recirculation zone could be detrimental for NO control due to the rapid mixing of gas burner air and possible devolatilization in this area.

- Case 44 showed how the near burner burnout of gas burner air by natural gas lowered NO by 22 %. This indicates that gas burner air in the wall recirculation zone is critical for NO formation in the modified burner case.

- The NO reductions found during the test work when co-firing gas with the modified burner can be explained without resorting to reburning reactions. Gas was found to burn out in regions where little NO was formed. The decisive point was the air that was burned and the phenomena could be described as pre-burning of air critical for NO formation.
- In case 24, the original burner case the burning recirculation zone disappeared due to the high velocity secondary air stream surrounding the burner preventing x-direction dispersion of particles. This explains the higher wall temperatures detected for the modified burner during the test work.
- Case 24 showed 15 % higher outlet levels of NO than case 49 which was the reverse of the finding from the test rig work. This could be explained by the shortcoming of the devolatilization model employed and the smallness of the model furnace. Devolatilization is probably not as strong in the near burner region of the original FAN burner flame compared to the modified FAN burner flame as indicated by flame observations during the test work. The NO production was thus not so severe in this region for case 24 as for case 49. A wider furnace would probably favour case 24 in NO reduction as x-direction diffusion of oxygen, which was found critical for NO in case 24, would diminish and disfavour case 49 because x-direction particle dispersion would increase and widen the burning wall recirculation zone.
- It is suggested, on the basis of model observations showing the fluid dynamical differences between the original and modified FAN burner, that there is more than a temperature correlation distinguishing the NO_x performance of these two burners.

Chapter 5

Full scale tests

5.1 Results

Västhamnsverket has a tangentially fired boiler with three burner levels and two levels of over fire air. It has a capacity of 120 MW_t. During the years several primary combustion measures for NO_x reduction have been succesfully installed and have brought the NO_x level down to its current low level of 80 mg/MJ (133 ppm, 3 % O_2). Primary measures and their achieved NO_x levels are seen in figure 5.1.

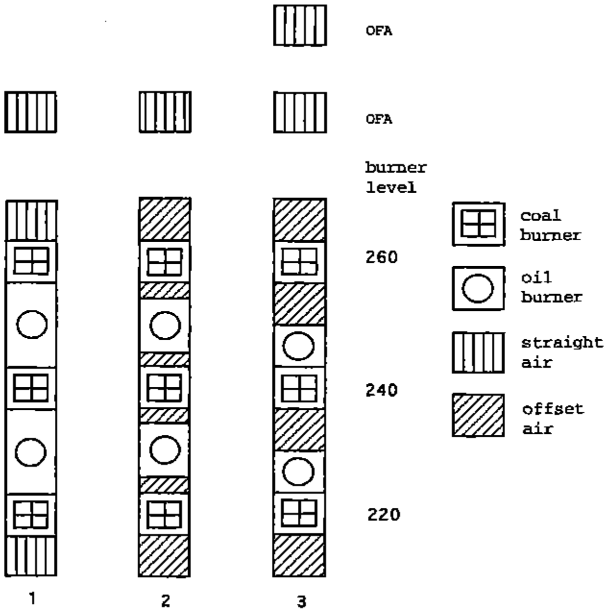

Figure 5.1: Combustion modifications made at Västhamnsverket. 1. Original installation with one level OFA. NO_x level: 280 mg/MJ 2. Partial tangential firing with offset air. NO_x level: 165 mg/MJ 3. Full tangential firing and two levels OFA. NO_x level: 80 mg/MJ

After the installation of the modified FAN burners, test runs were performed in the boiler during the autumn of 1995. NO_x levels were recorded as a function of burner level combinations and load, with and without natural gas addition. The results are shown in figs. 5.2-5.4.

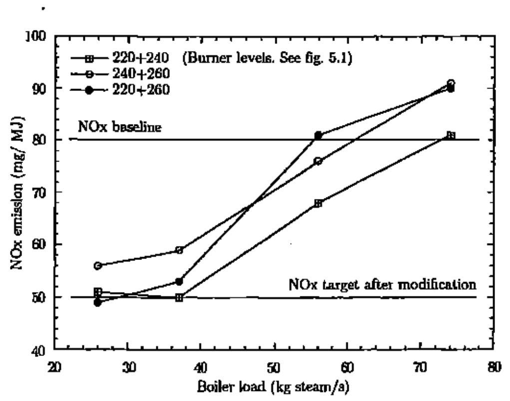

Figure 5.2: NO_x as a function of operating burner levels and furnace load at coal only firing.

Figure 5.2 shows that the modified FAN burners firing coal only performed worse than the datum burner at full load and were only compatible when the two lowest burner levels were in operation. The difference in NO_x performance between the two highest and two lowest burner levels is probably due to the longer residence times in the latter case.

Firing 10 % natural gas, the results of which are given in figure 5.3, showed a smearing out of the differences between the two highest and two lowest burner levels but operating with the two lowest levels still gave a little less NO_x. This could perhaps be an effect of the delayed burnout when co-firing with natural gas as was seen in the test rig work. A delayed burnout demands a longer residence time in the furnace to avoid fuel and thermal NO_x formation in the over fire air zone. The delay in burnout could

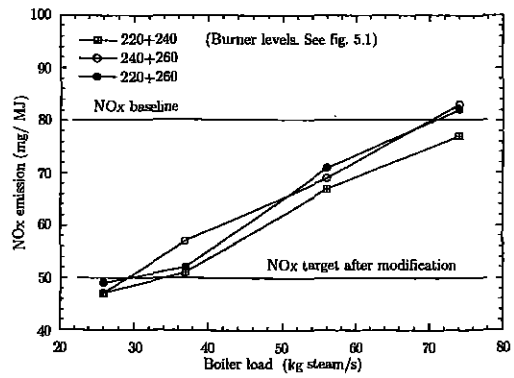

Figure 5.3: NO_x as a function of operating burner levels and furnace load at 10 % gas.

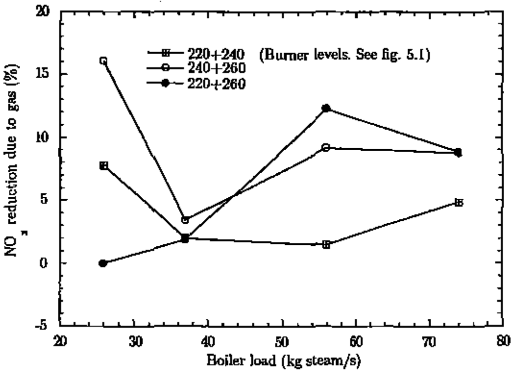

Figure 5.4: NO_x reduction by gas portion.

thus be responsible for the lesser difference between higher and lower burner levels.

Finally figure 5.4 shows the reduction achieved by the 10 % natural gas addition. In none of the cases did the reduction due to natural gas exceed the 10 % level at full load and only at the lowest load could any accelerated reduction above the 10 % level be observed. This means that in fact a larger amount of NO_x is formed relative to the load of coal in the natural gas case than in the case of coal only firing. Although the amount of data is limited there is a tendency towards a smaller effect of natural gas when operating with the lowest burner levels than with the highest. Perhaps the longer residence time when operating with the lowest burner levels together with the delayed burnout gives a more complete second stage burnout, i.e. at the OFA levels, and a deterioration of the low NO_x levels in the near burner region. When operating with the highest burner levels the second stage burnout should then not be so complete due to shorter residence time which in turn would give an apparent larger effect of the natural gas portion. If this line of reasoning has any bearing it would be confirmed by a larger amount of carbon in ash when operating with the highest burner levels compared to the lowest.

The proposals given here are an attempt to give a consistent explanation for the observations found from the test rig work, the combustion modelling work and the full scale operation. To conclude, the modified FAN burner firing coal only did not achieve any reduction compared to the datum burner neither in the test rig nor in full scale operation. This has been discussed in chapter four and further in the next section. The natural gas portion did not give the expected reduction compared to coal only firing in full scale operation, an effect that was found in the test rig and explained by the modelling work. This failure is a consequence of the decisive differences between a front wall fired single burner furnace and a multi-level tangentially-fired system with over fire air. An explanation based on the full scale results has been given in this section in terms of delayed burnout.

5.2 Discussion

As described in chapter two the modified FAN burner firing coal only did not achieve any NO_x reduction compared to the datum burner and could even be regarded as slightly worse than the latter in this respect, as seen by figure 2.1. This was meant to be caused by an imbalance in heat extraction in the near burner region due to the strong flame attachment in the modified FAN burner case and an increase in NO_x due to higher peak temperatures. Based on a study of the modified FAN burner co-firing 10 % gas at different levels of secondary air preheat, a linear relation connecting wall temperatures and NO_x levels was developed. Original and modified FAN burner NO_x levels were then correlated to the wall temperature of the datum burner and the result is shown in figure 2.2. On this basis the modified and the original FAN burner were found equivalent, and poten-

		orig.FAN				mod.FAN		
Test no.		22	23	28	29	48	49	50
Furnace load								
coal	MW	23.4	24.0	23.2	23.2	23.6	23.6	23.6
gas	MW	0.3	0.3	0.0	0.0	0.0	0.0	0.0
	%gas	1.3	1.2					
Fuel and primary air								
Coal flow rate	kg/s	0.81	0.83	0.81	0.81	0.82	0.82	0.82
PA flow rate	kg/s	1.49	1.47	1.46	1.49	1.40	1.37	1.38
PA/PF ratio		1.85	1.78	1.81	1.85	1.71	1.67	1.68
PF temp.	°C	64.5	66.1	69.4	67.4	69.5	70.5	69.6
Combustion air								
Windbox air flow rate	kg/s	7.30	6.82	6.56	5.36	5.63	6.32	7.50
Windbox air temp.	°C	315	305	316	333	338	330	311
Comb. air flow rate	kg/s	8.79	8.29	8.02	6.85	7.03	7.69	8.88
Metal temp.								
Nozzle	°C	366	405	438	401	514	512	500
Furnace wall	°C	959	963	972	976	1090	1095	1095
Flame and flue gas data								
Flame length	m	8.3	8.5	8.5	8.5	10.0	8.5	8.0
O_2	%	4.10	3.25	4.10	2.80	2.20	2.90	3.95
NO_x(as meas.)	ppm	164	153	164	124	139	168	230
NO_x(3% O_2)	ppm	175	155	175	123	133	167	243
CO_2	%	13.9	16.6	15.7	17.3	17.7	17.1	15.8
CO	ppm	49	49	58	94	116	73	49
Furnace exit temp.	°C	602	605	599	605	646	662	675

Table 5.1: Data for modified and original FAN burner in figure 2.1

tial NO_x reductions up to 50 % from the datum burner were indicated with the modified FAN burner co-firing gas.

The temperature dependence of NO_x formation consists of two parts as discussed in chapter four: the creation of thermal NO_x due to fixation of nitrogen in the combustion air and the weaker temperature dependence of fuel NO_x. Thermal NO_x becomes important when flame temperatures rise over 1600-1800 K however, it can extend to lower temperatures in turbulent flames when the temperature fluctuation level is high [10]. If the temperature increases over the level of 1800 K then fuel NO_x will also eventually be effected by the temperature. However, it is the oxygen fraction that is of overshadowing importance for both thermal and fuel NO_x. As shown by Pershing and Wendt[23] thermal NO_x can be removed by lowering combustion air preheat but the NO_x reducing effect levels out on the fuel NO_x level and at some point lowering the temperature does not affect the NO_x level. This is an experimental finding that clearly indicates that there is no linear relation between NO_x level and temperature in all but very narrow ranges. In conclusion, extrapolating linear relationships can be misleading.

The linear relation used in the test rig work indicates that there is a relationship, connecting all flame cases, between burner front wall temperatures and peak flame temperatures. This must then mean that, in the case of the datum burner flame, it is the low peak temperature that is the cause of the low wall temperature and, in the case of the modified burner, it is the high peak temperature that is the cause of the high wall temperature. However, the higher wall temperatures in the FAN burner case are a result of the peak temperatures being closer to the burner than in the datum burner case, which is a detached flame and reaches peak flame temperatures further downstream than the modified burner. The datum and FAN burner could have the same peak temperatures but cause different wall temperatures as the peak temperatures occur at different locations in the furnace. The furnace wall temperature is thus not a reliable way of comparing these flames regarding peak flame temperatures and estimating thermal NO_x levels this way can be misleading.

In table 5.1 the data of the test runs providing the basis for figure 2.1 are shown. As can be seen there is no major difference in heat input or SA preheat separating the test runs but there is a clear difference in burner and wall temperatures. It is the conclusion of the modelling work that the added side gas burner compartments in the modified FAN burner case, as compared to the original FAN burner, is the cause of the rise in temperature close to the burner. Since the aerodynamics of the original FAN and the modified FAN burner are different, the NO_x-characteristics are also different. There can very well be more than thermal NO_x separating the two burner configurations. This is also suggested by an indicated stronger excess air dependence of the modified burner (figure 2.1).

The analysis presented here is based on the modelling work and empirical work on temperature dependence of NO_x in pulverized coal flames. It is limited to the interpretation of the test rig results and the estimated potential of the modified FAN burner, in comparison to the datum burner. In dealing with the failure of the modified FAN burner in the full scale operation there can be many other factors involved than the ones detailed above, mainly due to the fundamental differences between a multi-level tangentially-fired system and a single burner front wall fired furnace.

Acknowledgment

This work has been carried out with the assistance of many people, especially:

Prof. Hans T. Karlsson, Michael Grimsberg and Dr. Tommy Hertzberg at the Department of Chemical Engineering II, Jörgen Thunell, Owe Jönsson at SGC AB, Lars Nilsson at Sydgas AB, Christer Olsson and Kenneth Ekensteen at Helsingborgs Energi AB and Dr. J. W. Allen at International Combustion Inc.

Bibliography

[1] Allen, J. W.,
Investigation into the potential for NO_x emission reduction using natural gas–pulverized coal co-firing at Helsingborg,
Report, Int. Comb. Inc., Derby, England, 1994

[2] Baum, M. M., Street, P. J.,
Predicting the combustion behavior of coal particles,
Comb. Sci. Tech., vol. 3, p. 231, 1971

[3] Badzioch, S., Hawksley, P. G. W.,
Kinetics of thermal decomposition of pulverized coal particles,
Ind. Eng. Chem. Process Design and Development, vol. 9, p. 521, 1971

[4] Beal, P. R., Wilhoit, D. W.,
Advanced tangential low NO_x burner: Developments and results,
ICAC Forum, Arlington, Virginia, 1994

[5] Coppalle, A., Vervisch, P.,
The total emissivities of high-temperature flames,
Comb. Flame, vol. 49, p. 101, 1983

[6] Fenimore, C. P.,
Formation of nitric oxide in premixed hydrocarbon flames,
13:th Symp. (Int.) Comb., p. 373, 1971

[7] Field, M. A.,
Rate of combustion of size-graded fractions of char from a low rank coal between 1200–2000 K,
Comb. Flame, vol.13, p. 237, 1969

[8] Glarborg, P., Miller, J. A., Kee, R. J.,
Kinetic modeling and sensitivity analysis of nitrogen oxide formation in well-stirred reactors,
Comb. Flame, vol. 65, p. 177, 1986

[9] Goldberg, P. M., Essenhigh, R. H.,
Coal combustion in a jet-mixed stirred reactor,
17:th Symp. (Int.) Comb., p. 145, 1979

[10] Hayhurst, A. N., Vince, I. M.,
Nitric oxide formation from N_2 in flames: The importance of prompt NO,
Prog. Energy Combust. Sci., vol. 6, p. 35, 1980

[11] Haynes, G. S.,
The oxidation of hydrogen-cyanide in fuel-rich flames,
Comb. Flame, vol. 28, p. 113, 1977

[12] Hautmann, D. J., Dryer, F. L., Schug, K.
A multiple-step overall kinetic mechanism for the oxidation of hydrocarbons,
Comb. Sci. Tech., vol. 25, p. 219, 1981

[13] Hinze, J. O.,
Turbulence,
McGraw-Hill, New York, 1975

[14] Hjalmarsson, A.-K.,
NO_x control technologies for coal combustion,
IEACR report, no. 40, 1990

[15] Jones, W. P., Launder, B. E.,
The prediction of laminarisation with a two equation turbulence model,
Int. J. Heat and Mass Transfer, vol. 15, p. 301, 1972

[16] Jones, W. P., Whitelaw, J. H.,
Calculation methods for reacting turbulent flows: A review,
Comb. Flame, vol. 48, p. 1, 1982

[17] Kilpinen, P., Glarborg, P., Hupa, M.,
Reburning chemistry: A kinetic modeling study,
Ind. Eng. Chem. Res., vol. 31, p. 1477, 1992

[18] Kuo, K. K. Y.,
Principles of combustion,
John Wiley and sons, New York, 1986

[19] Libby, P. A., Williams, F. A.,
Turbulent reacting flows,
Academic Press, London, 1994

[20] Magnussen, B. F., Hjertager, J.,
On mathematical modeling of turbulent combustion with special emphasis on soot formation and combustion,
16:th Symp. (Int.) Comb., p. 719, 1976

[21] Merrick, D.,
The thermal decomposition of coal: Mathematical models of the chemical and physical changes,
in Coal Science and Chemistry, (ed. Volborth, A.), Elsevier, Amsterdam, 1987

[22] Mitchell, J. W., Tarbell, J. M.,
Kinetic model of nitric-oxide formation during pulverized coal combustion,
AIChE J., vol. 28, p. 2, 1982

[23] Pershing, D. W., Wendt, J. O. L.,
Pulverized coal combustion: The influence of flame temperature and coal composition on thermal and fuel NO_x,
16:th Symp. (Int.) Comb., p. 389, 1977

[24] Pohl, J. H., Sarofim, A. F.,
Devolatilization and oxidation of coal nitrogen,
16:th Symp. (Int.) Comb., p. 491, 1977

[25] Shah, N. G.,
A new method of comparison of radiant heat transfer in combustion chambers,
Ph. D. thesis, Imperial College of Science and Technology, London, England, 1979

[26] Smith, P. J., Fletcher, T. H.,
A study of two reaction models in turbulent coal combustion,
Comb. Sci. Tech., vol. 58, p. 59, 1988

[27] Smoot, L. D., Smith, P. J.,
Coal combustion and gasification,
Plenum, New York, 1985

[28] Wendt, J. O. L., Pershing, D. W., Lee, J. W., Glass, J. W.,
Pulverized coal combustion: NO_x *formation mechanisms under fuel-rich and staged combustion conditions,*
17:th Symp. (Int.) Comb., p. 77, 1979

[29] Zeldovich, J.,
The oxidation of nitrogen in combustion and explosions,
Acta Physicochemica USSR, vol. 21, p. 577, 1946

Appendix A

Model results

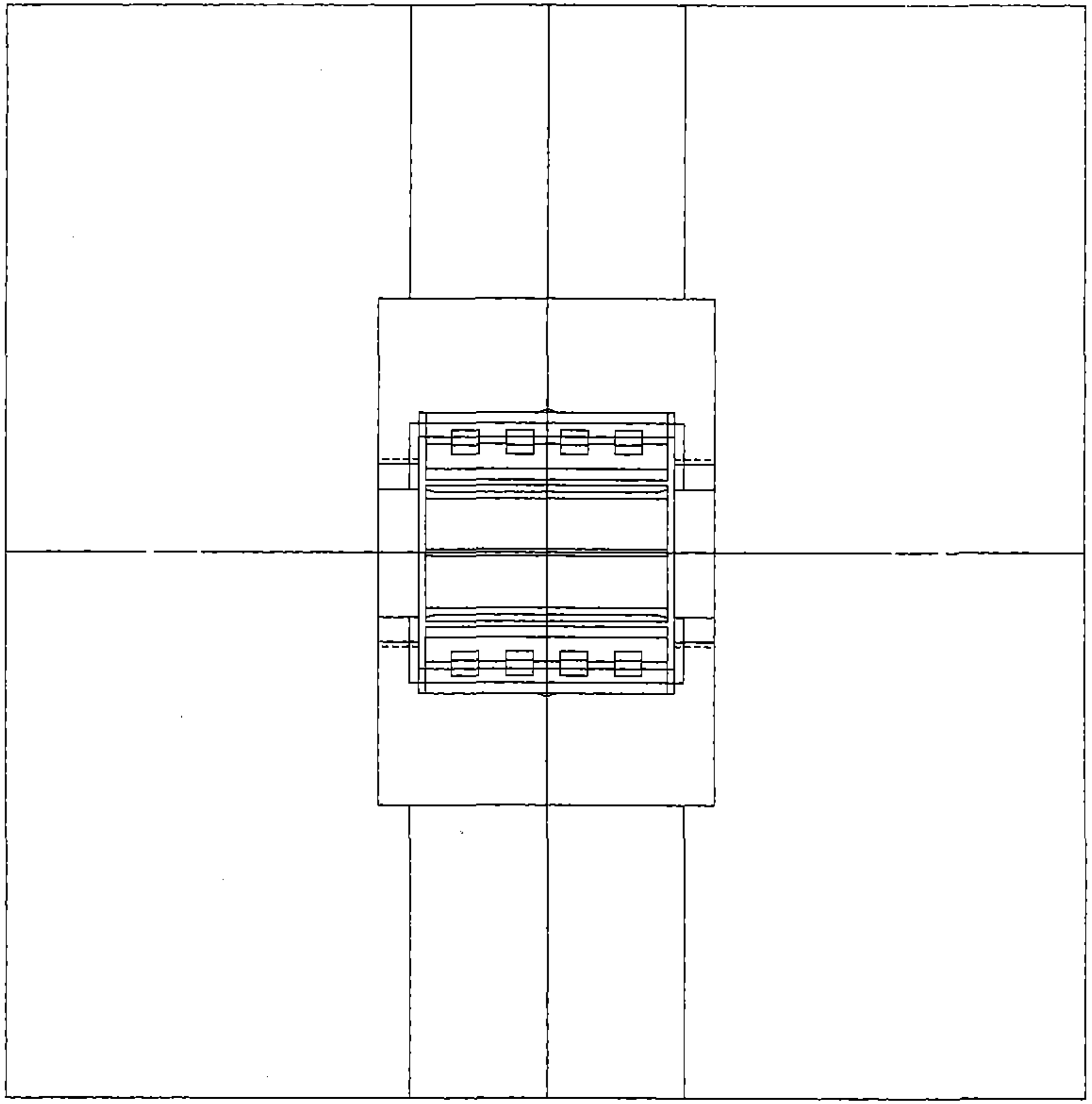

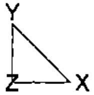

fig A1, modified FAN-burner model
Front view including symmetry planes

Sep 02 1996
Fluent 4.32
Fluent Inc.

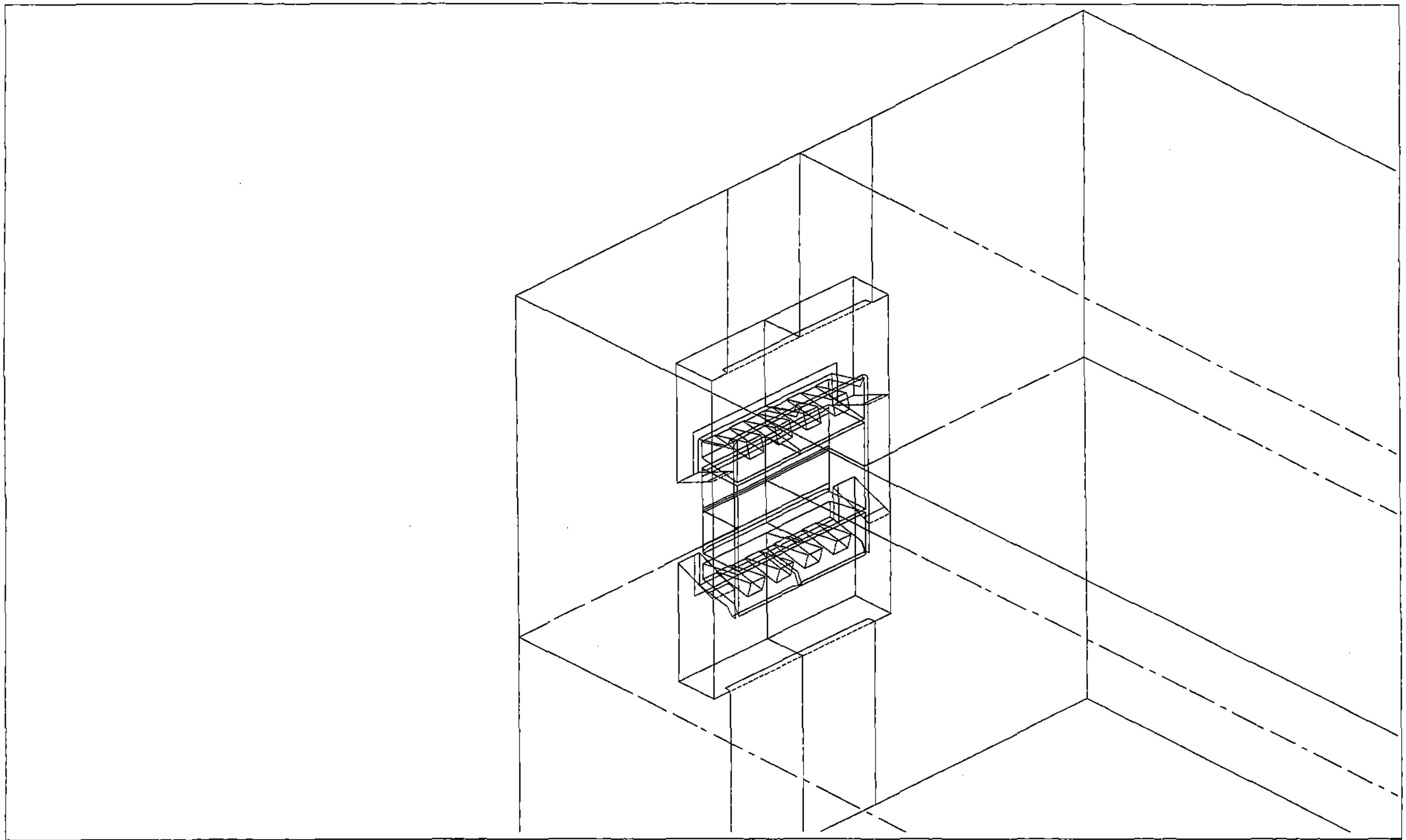

fig A2, modified FAN-burner model
Perspective view including symmetry planes

Sep 02 1996
Fluent 4.32
Fluent Inc.

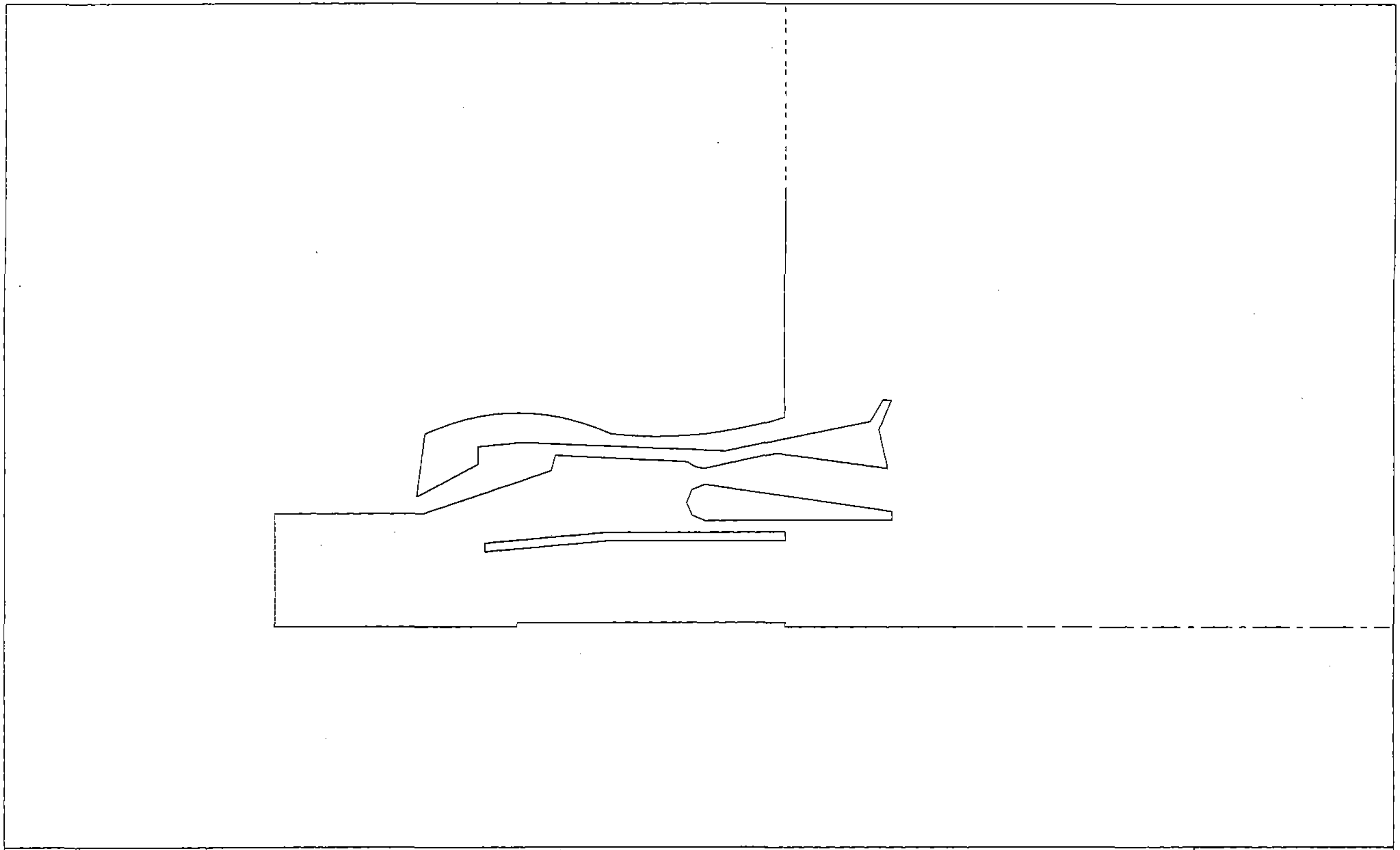

fig. A3, 2D-model
Outline

Sep 02 1996
Fluent 4.32
Fluent Inc.

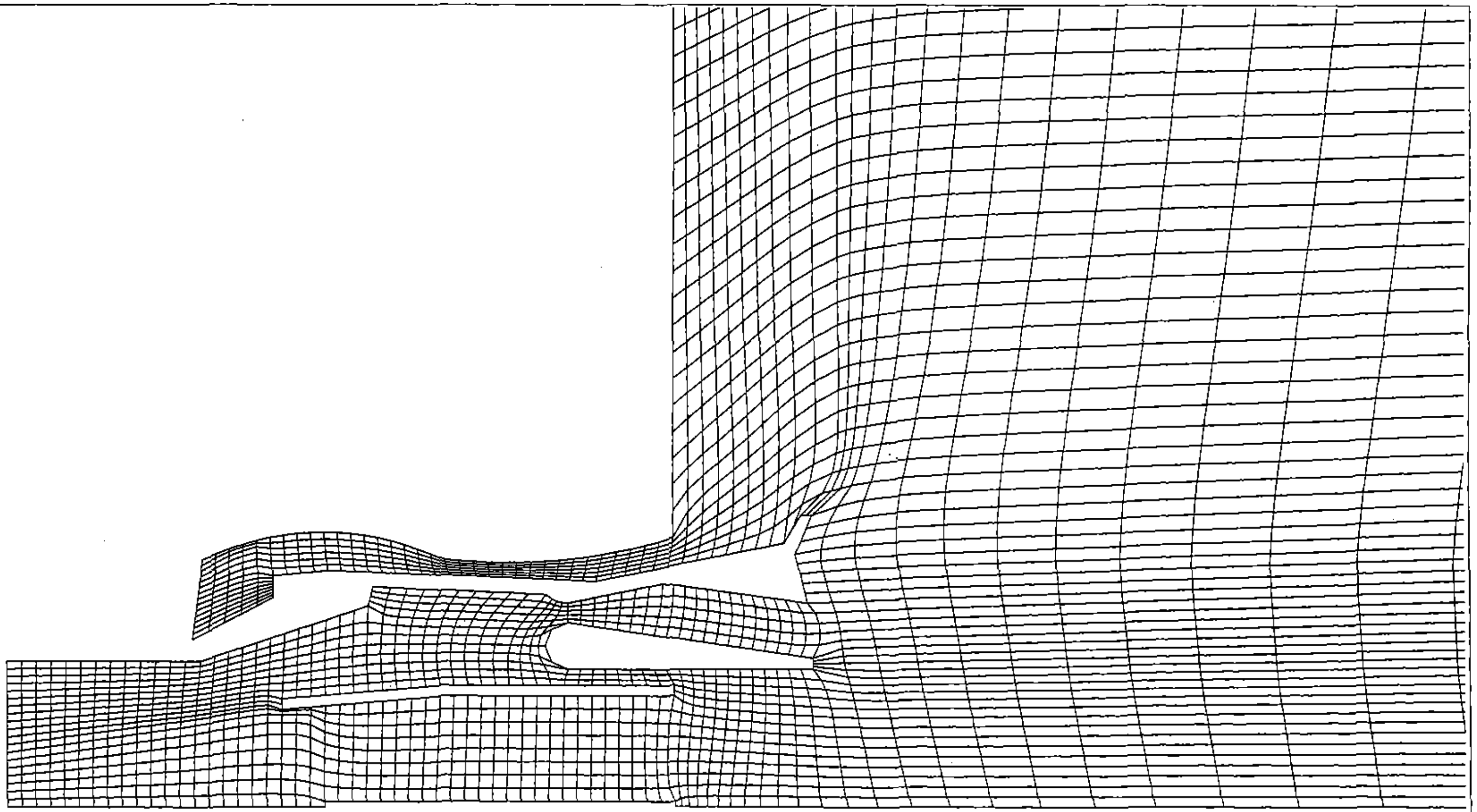

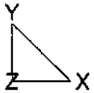

fig. A4, 2D-model
Grid (100 X 80)

Sep 02 1996
Fluent 4.32
Fluent Inc.

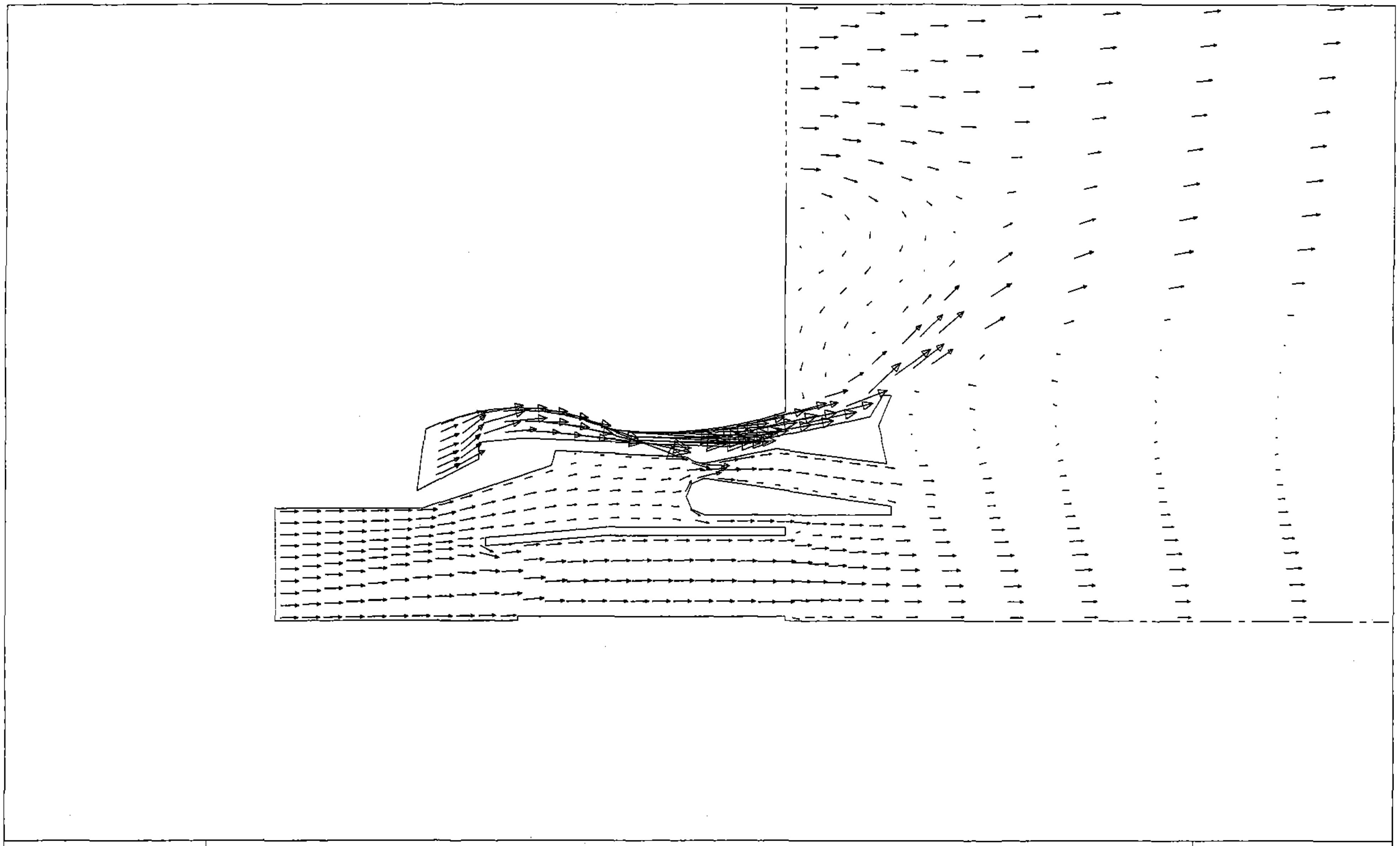

fig. A5, 2D-model
Velocity Vectors (M/S)
Max = 1.212E+02   Min = 2.771E-01

Sep 02 1996
Fluent 4.32
Fluent Inc.

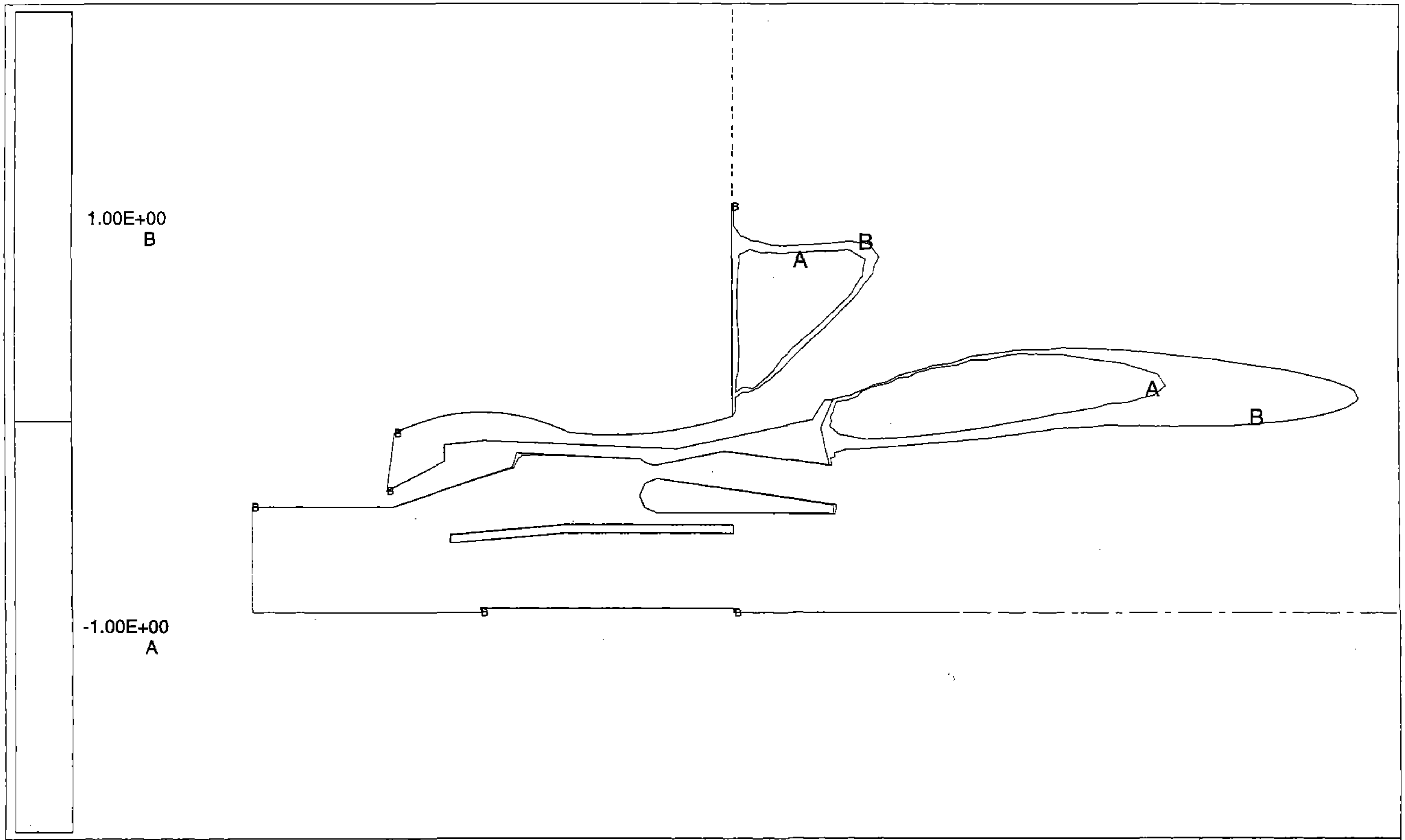

fig. A6, 2D-model
U-Velocity (M/S)
Max = 1.000E+00 Min = -1.000E+00

Sep 02 1996
Fluent 4.32
Fluent Inc.

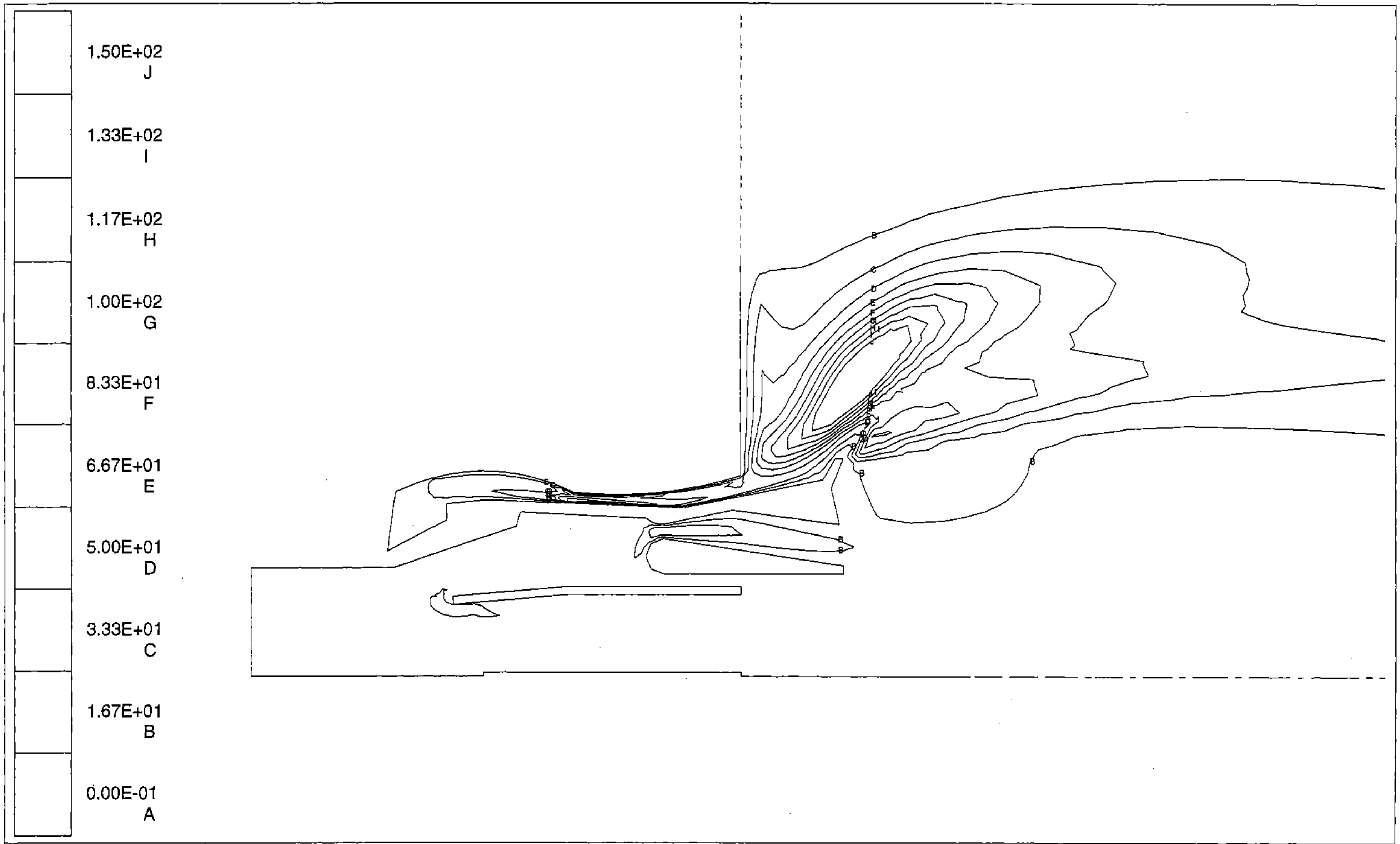

fig. A7, 2D-model
K.E. Of Turbulence (M2/S2)
Max = 1.500E+02   Min = 0.000E-01

Nov 19 1998
Fluent 4.47
Fluent Inc.

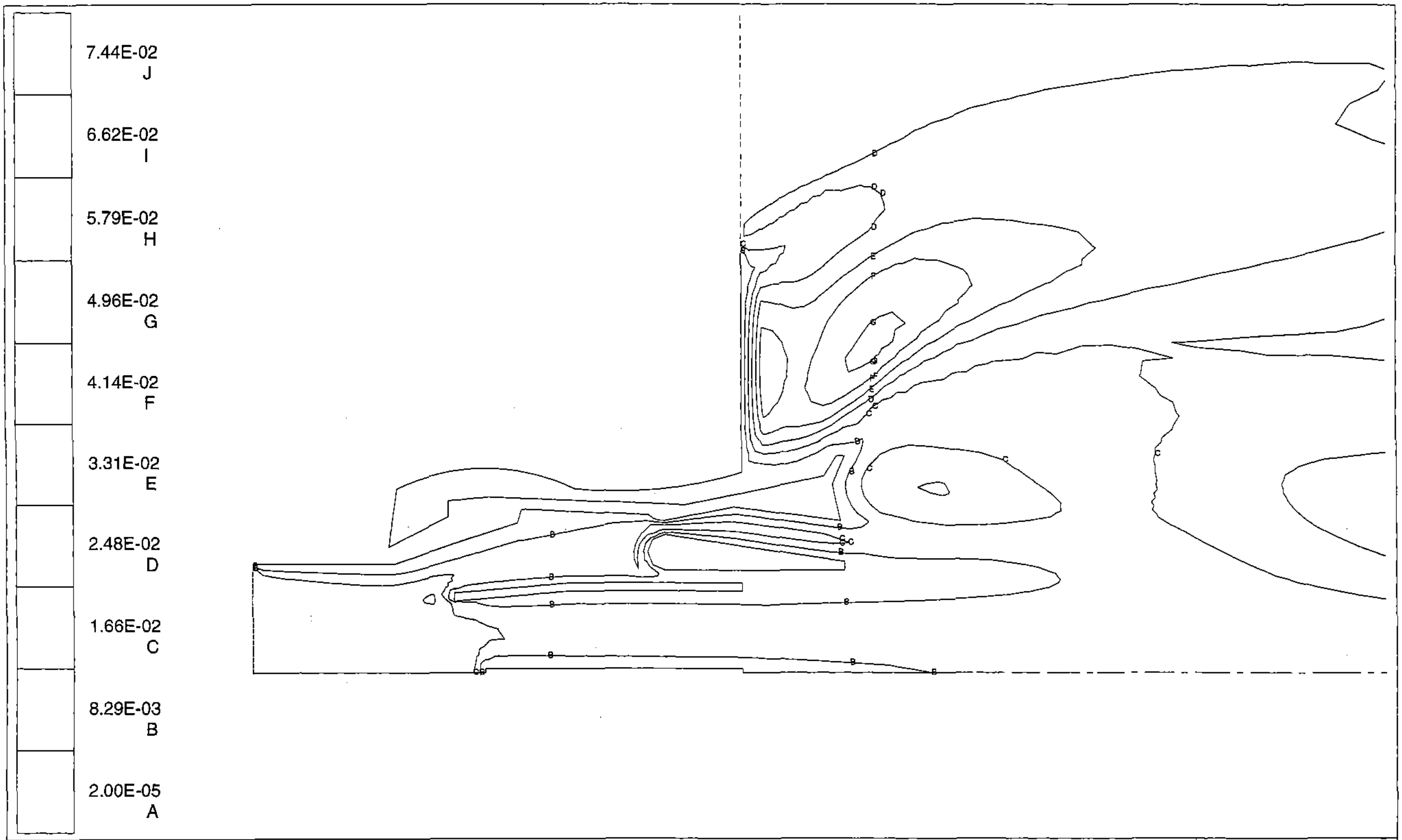

fig. A8, 2D-model
Effective Viscosity (Kg/M-S)
Max = 7.444E-02   Min = 2.000E-05

Nov 19 1998
Fluent 4.47
Fluent Inc.

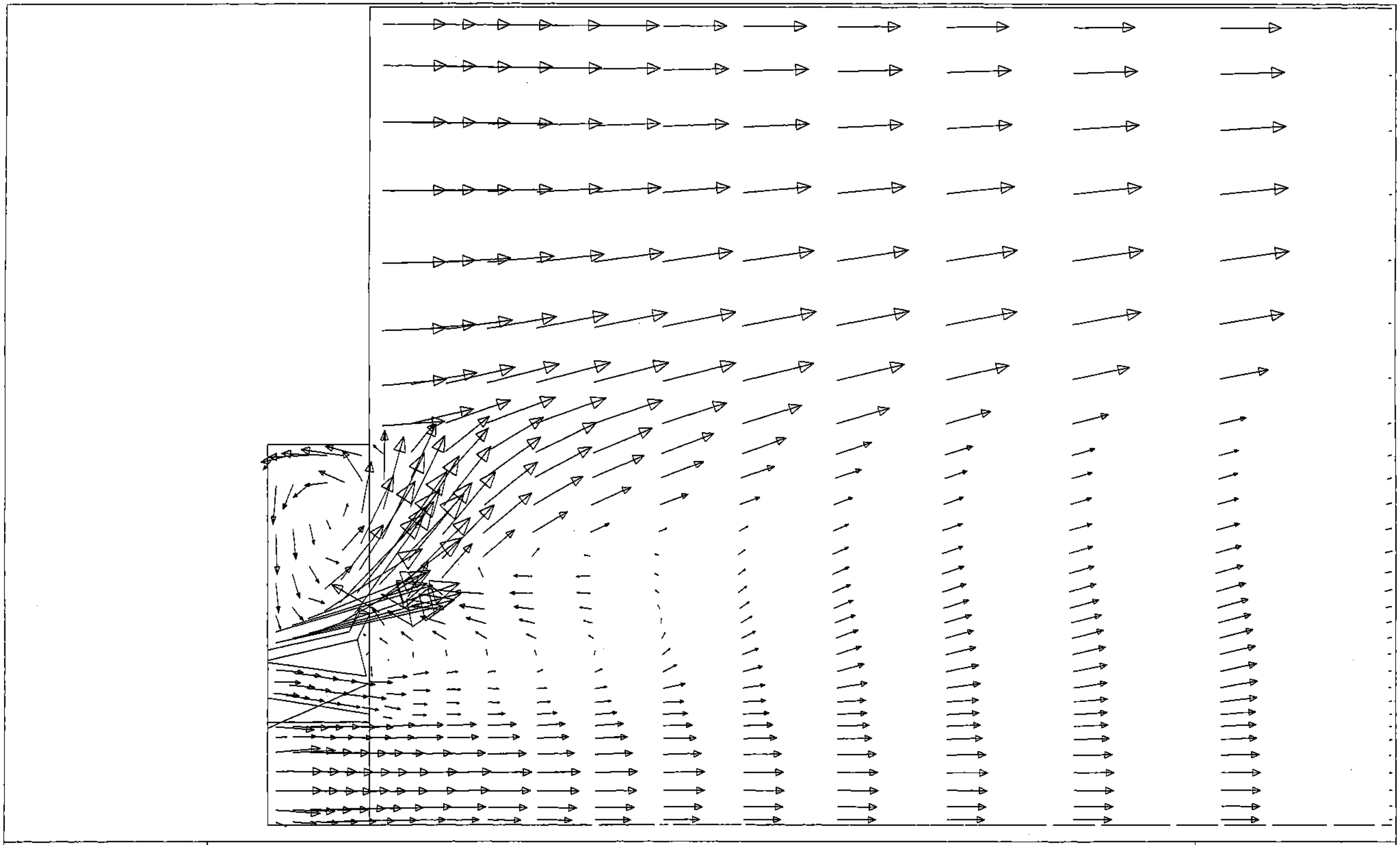

fig. A9, case 49
Velocity Vectors (M/S)
Lmax = 6.781E+01   Lmin = 1.658E+00

Sep 01 1996
Fluent 4.32
Fluent Inc.

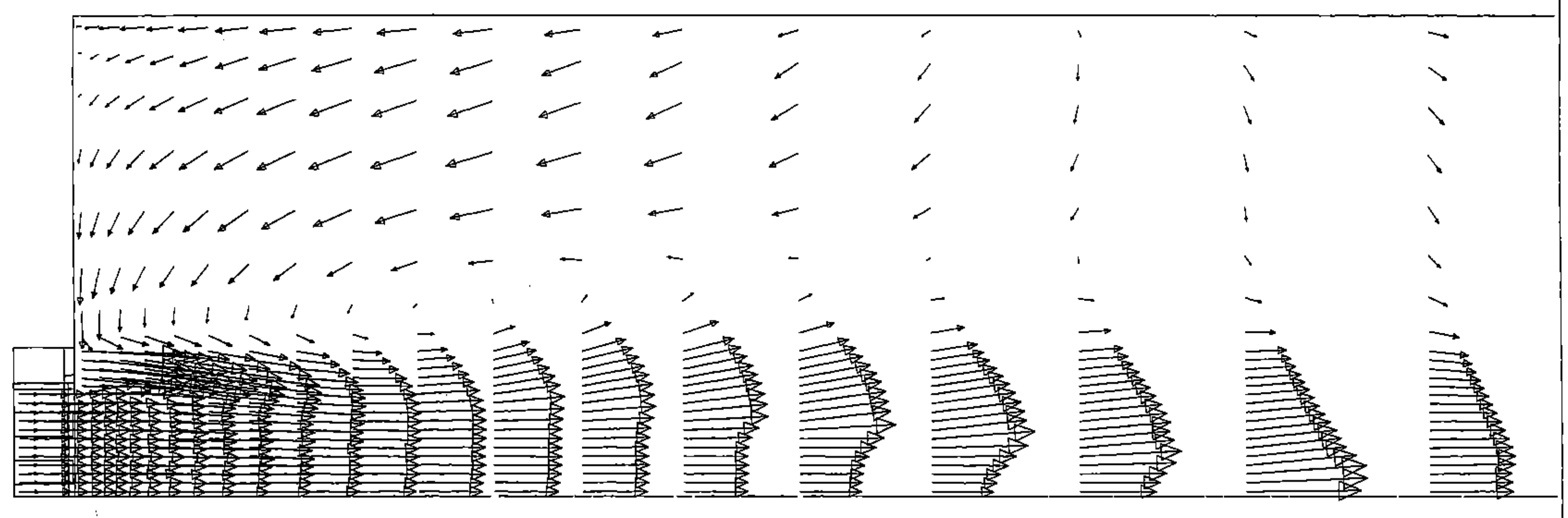

fig. A10, case 49
Velocity Vectors (M/S)
Lmax = 2.737E+01   Lmin = 8.001E-01

Sep 01 1996
Fluent 4.32
Fluent Inc.

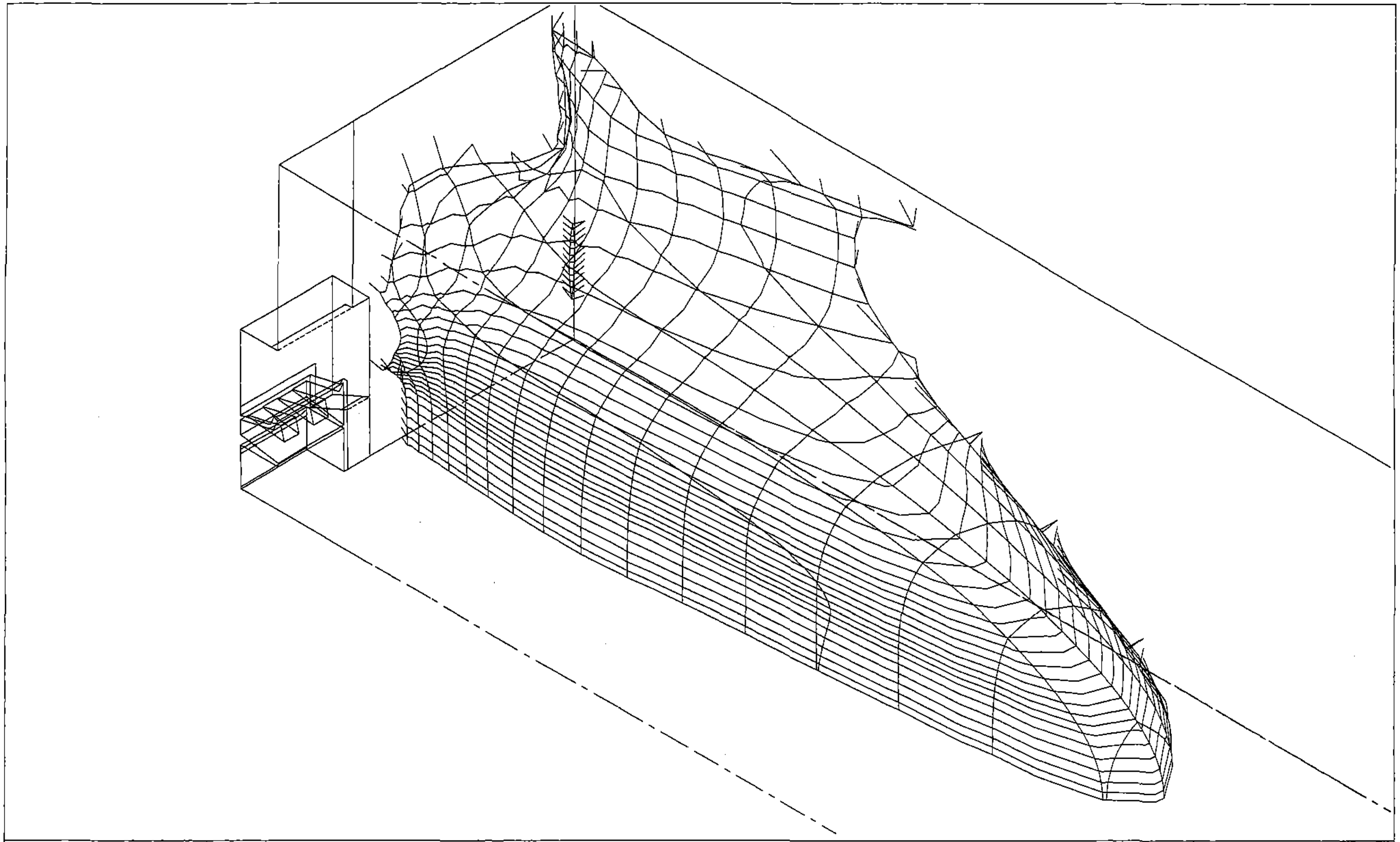

fig. A11, case 49
Surface Of Constant W-Velocity (M/S)
Value = 0.000E-01

Sep 01 1996
Fluent 4.32
Fluent Inc.

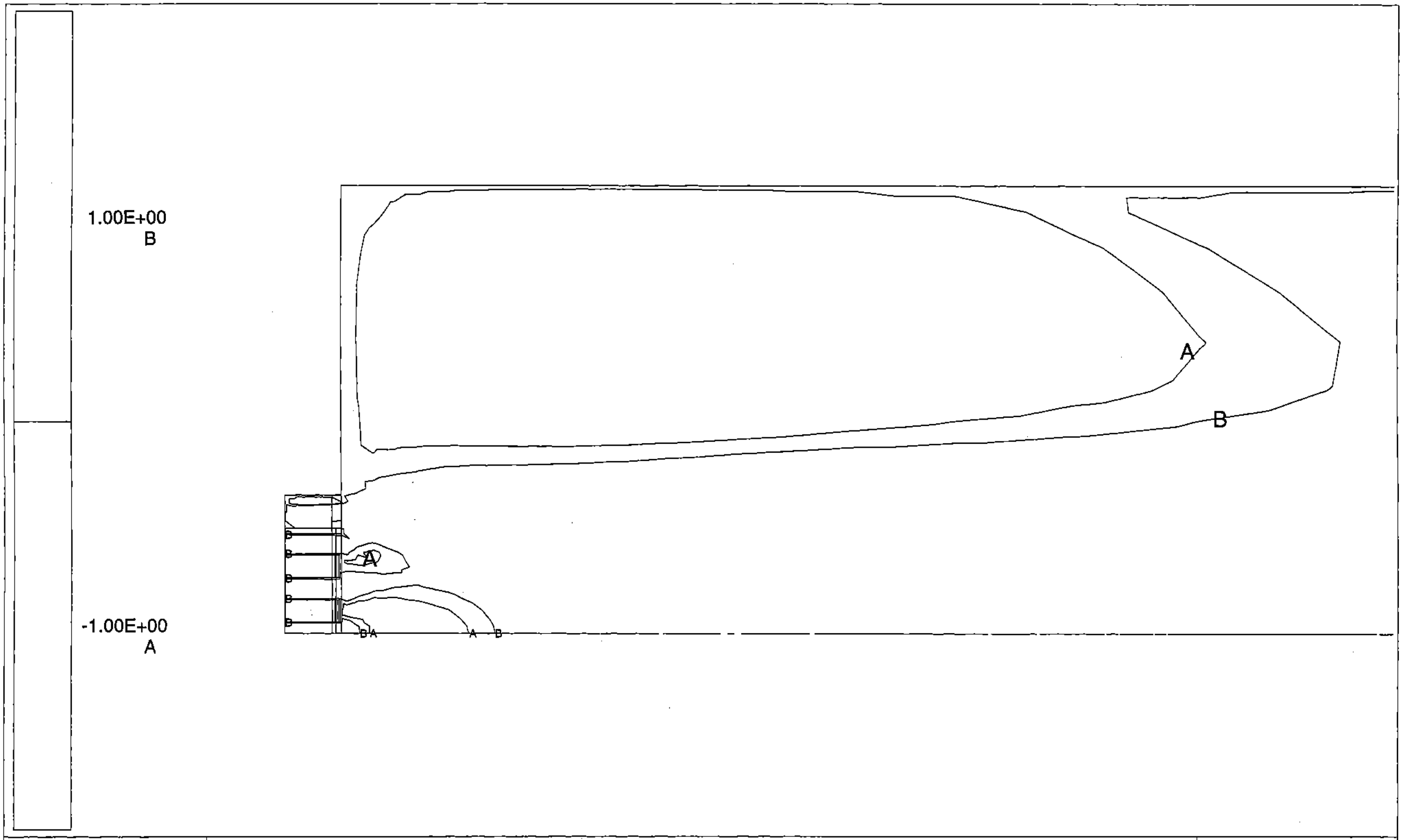

fig. A12, case 49

W-Velocity (M/S)

Lmax = 1.000E+00   Lmin = -1.000E+00

Sep 01 1996

Fluent 4.32

Fluent Inc.

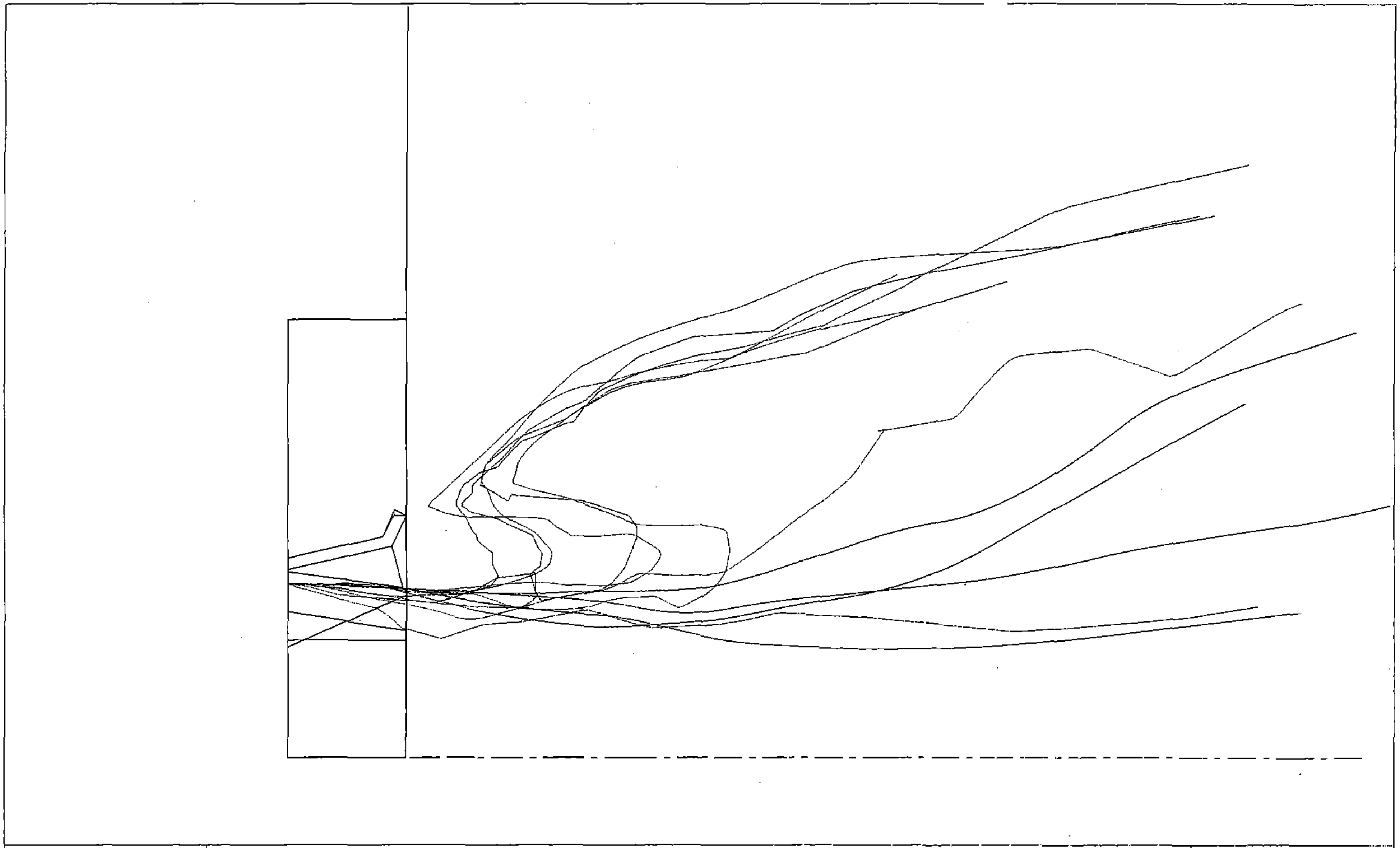

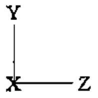

fig. A13, case 49

Particle tracks

Blue=5, green=37, yellow=68, red=100 micron

Jul 29 1996

Fluent 4.32

Fluent Inc.

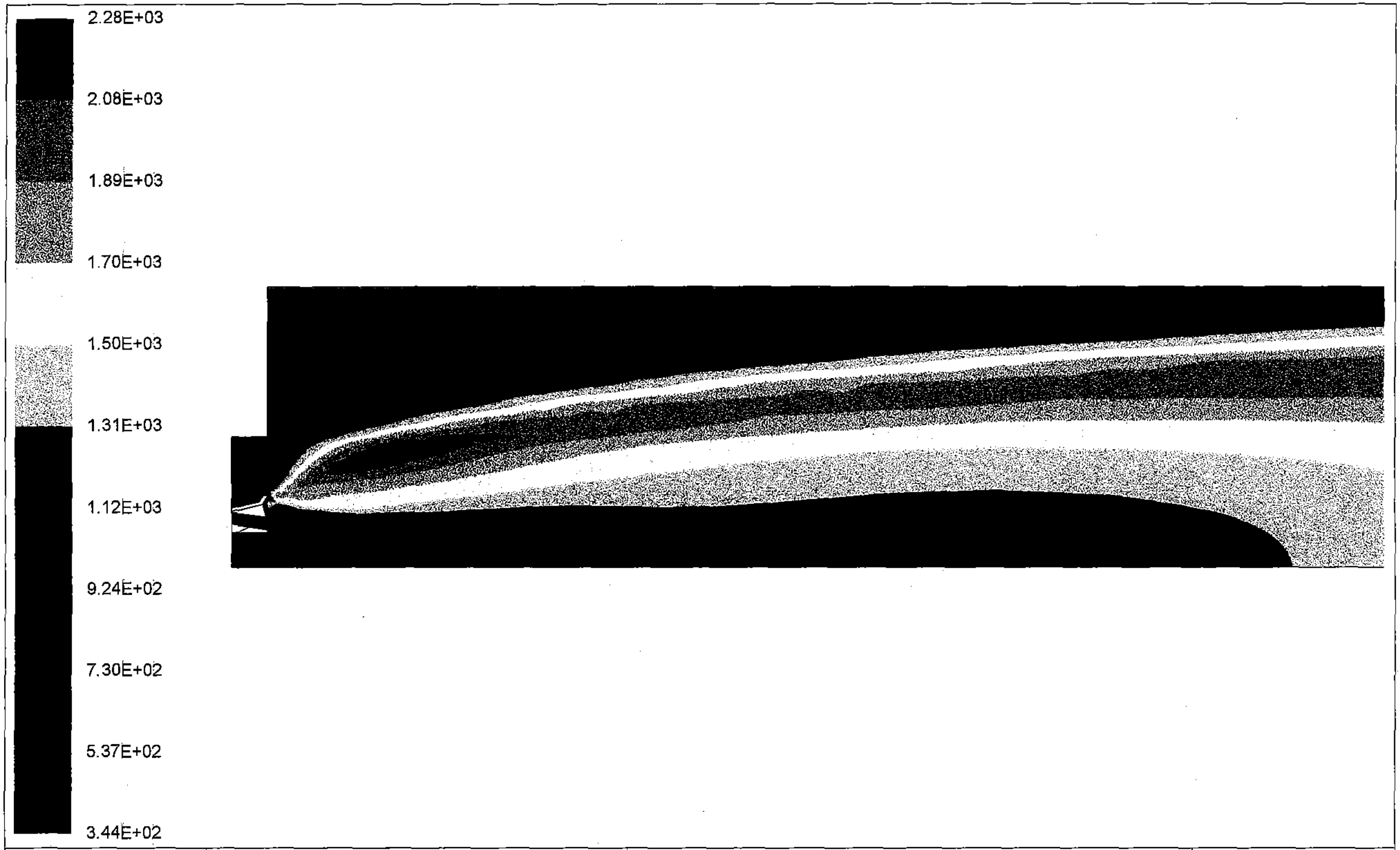

fig A14, case 49
Temperature (K)
Lmax = 2.276E+03   Lmin = 3.440E+02

Nov 26 1998
Fluent 4.47
Fluent Inc.

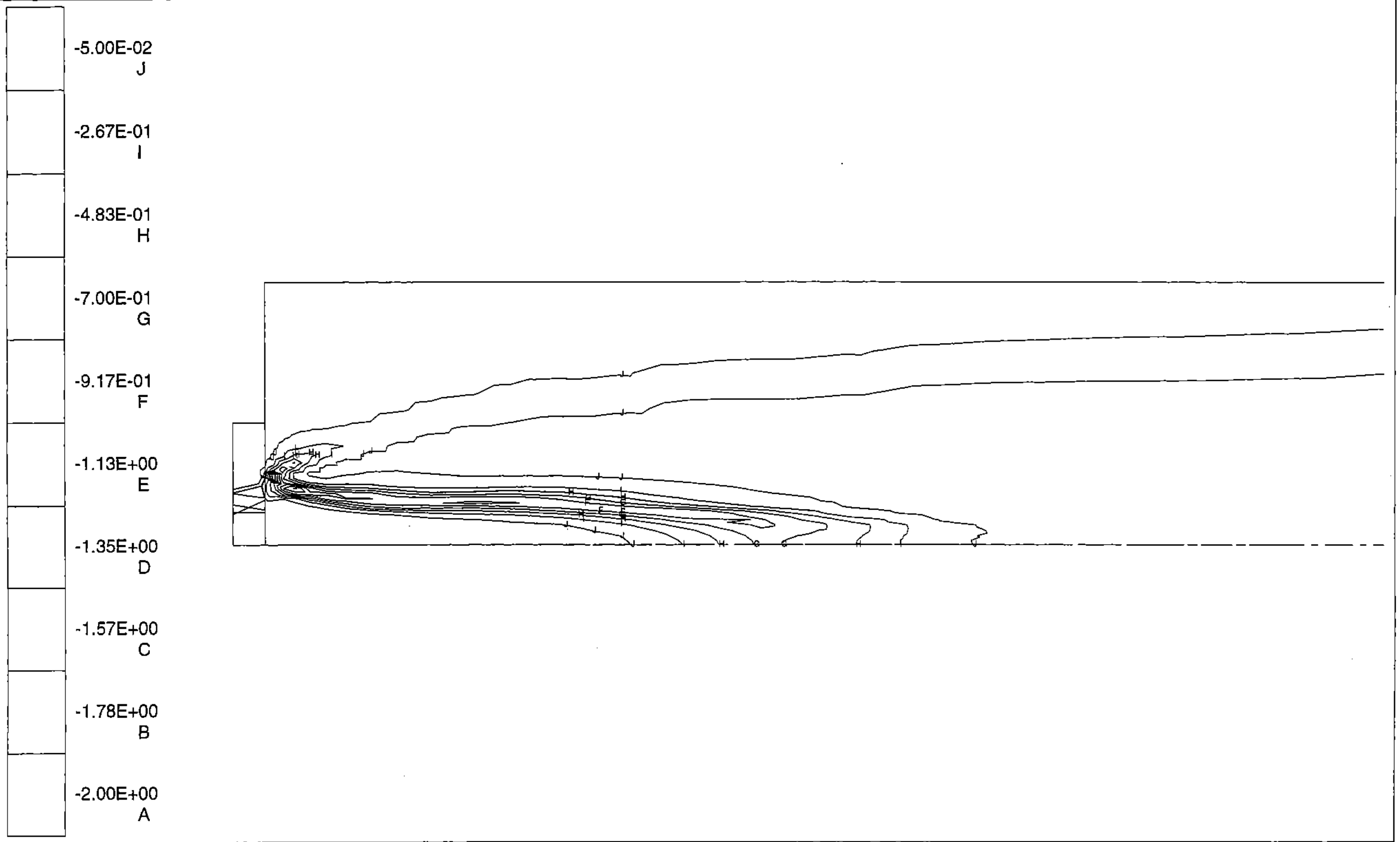

fig. A15, case 49

Volatile reaction rate (kg/M3/s)

Lmax = -5.000E-02   Lmin = -2.000E+00

Nov 19 1998

Fluent 4.47

Fluent Inc.

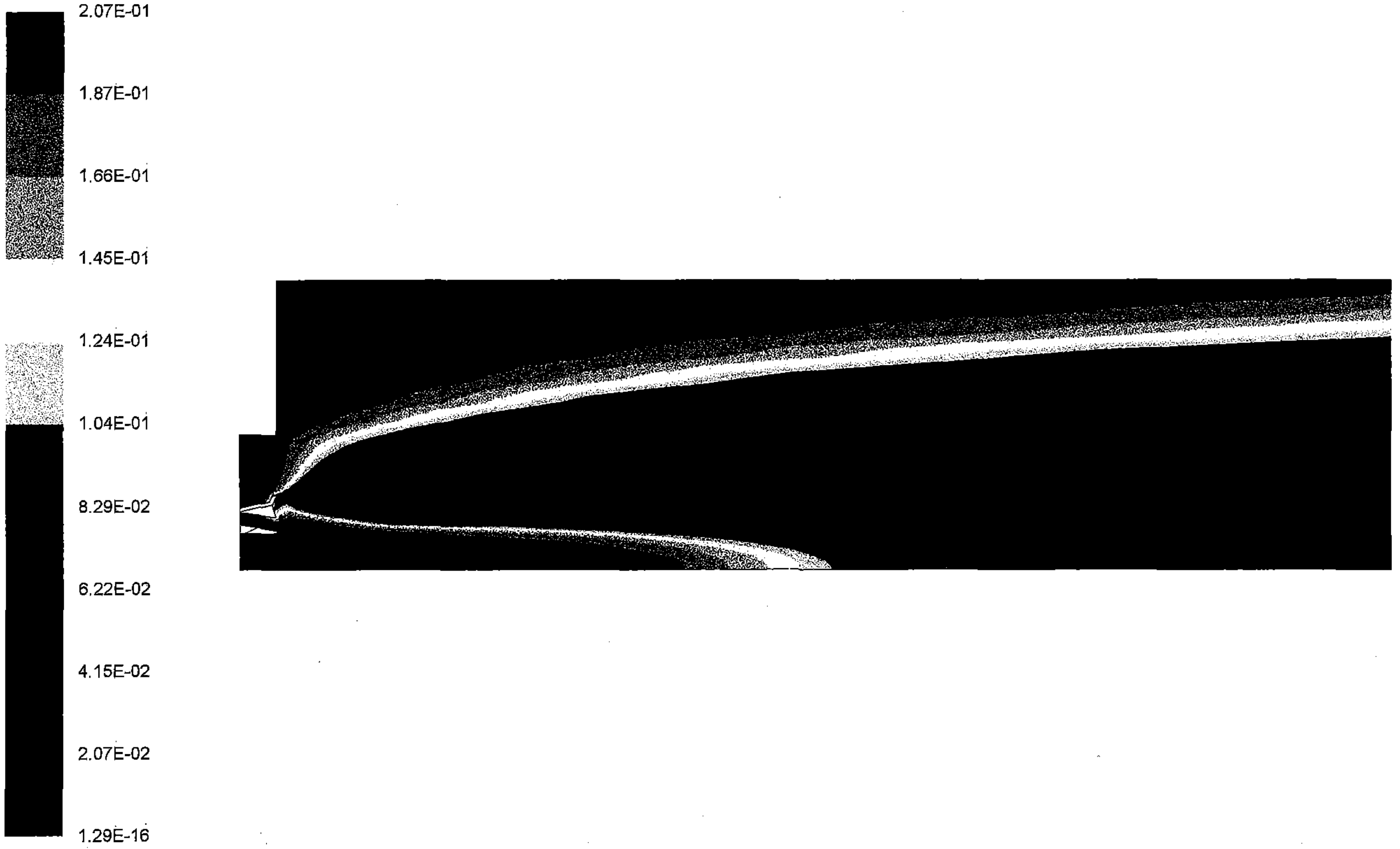

fig. A16, case 49

O2 Mole Fraction

Lmax = 2.073E-01 Lmin = 1.286E-16

Nov 26 1998

Fluent 4.47

Fluent Inc.

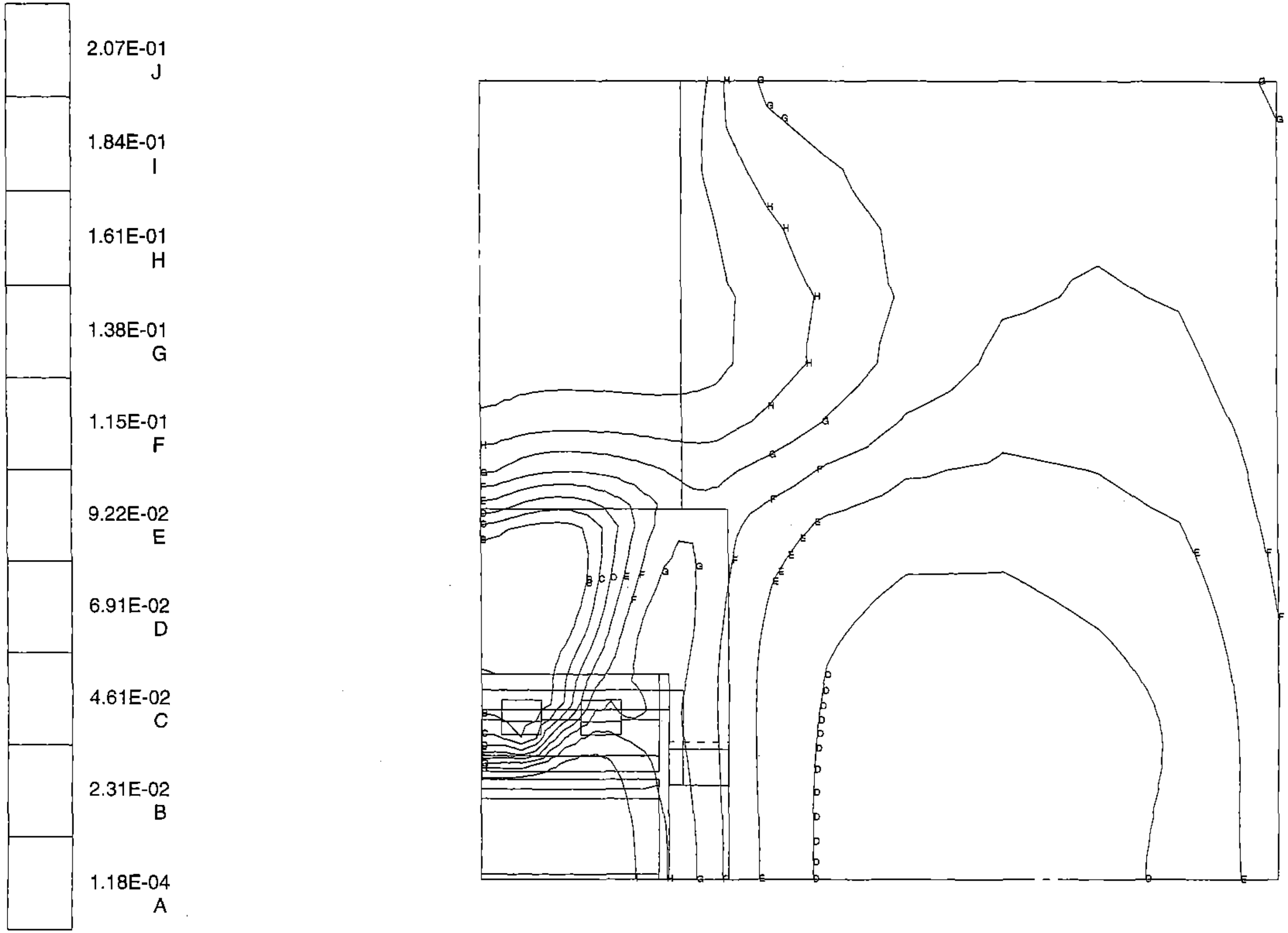

fig. A17, case 49

O2 Mole Fraction

Lmax = 2.072E-01 Lmin = 1.178E-04

Nov 19 1998

Fluent 4.47

Fluent Inc.

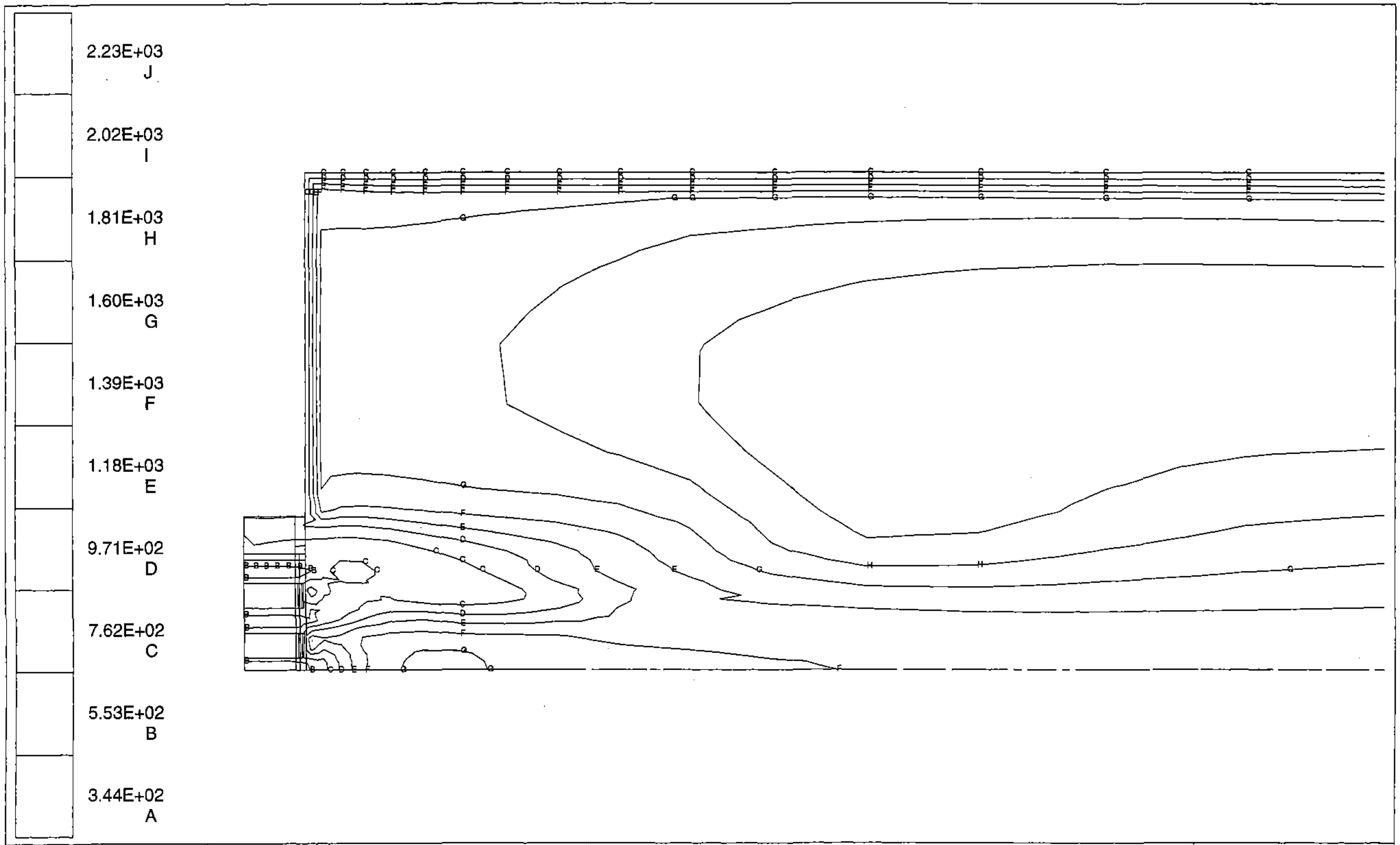

x
z

fig. A18, case 49

Temperature (K)

Lmax = 2.226E+03   Lmin = 3.440E+02

Nov 19 1998

Fluent 4.47

Fluent Inc.

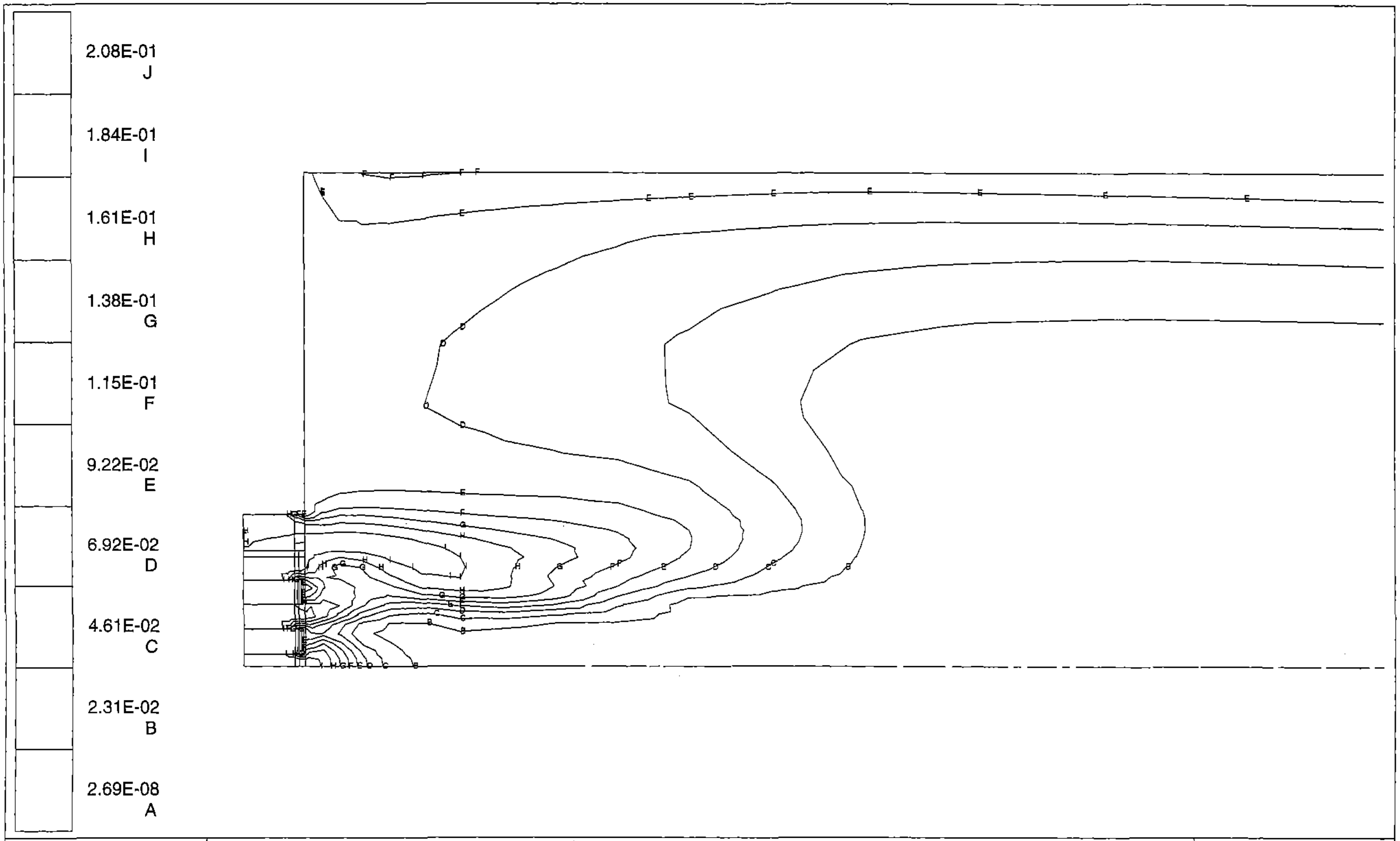

fig. A19, case 49

O2 Mole Fraction

Lmax = 2.075E-01   Lmin = 2.686E-08

Nov 19 1998

Fluent 4.47

Fluent Inc.

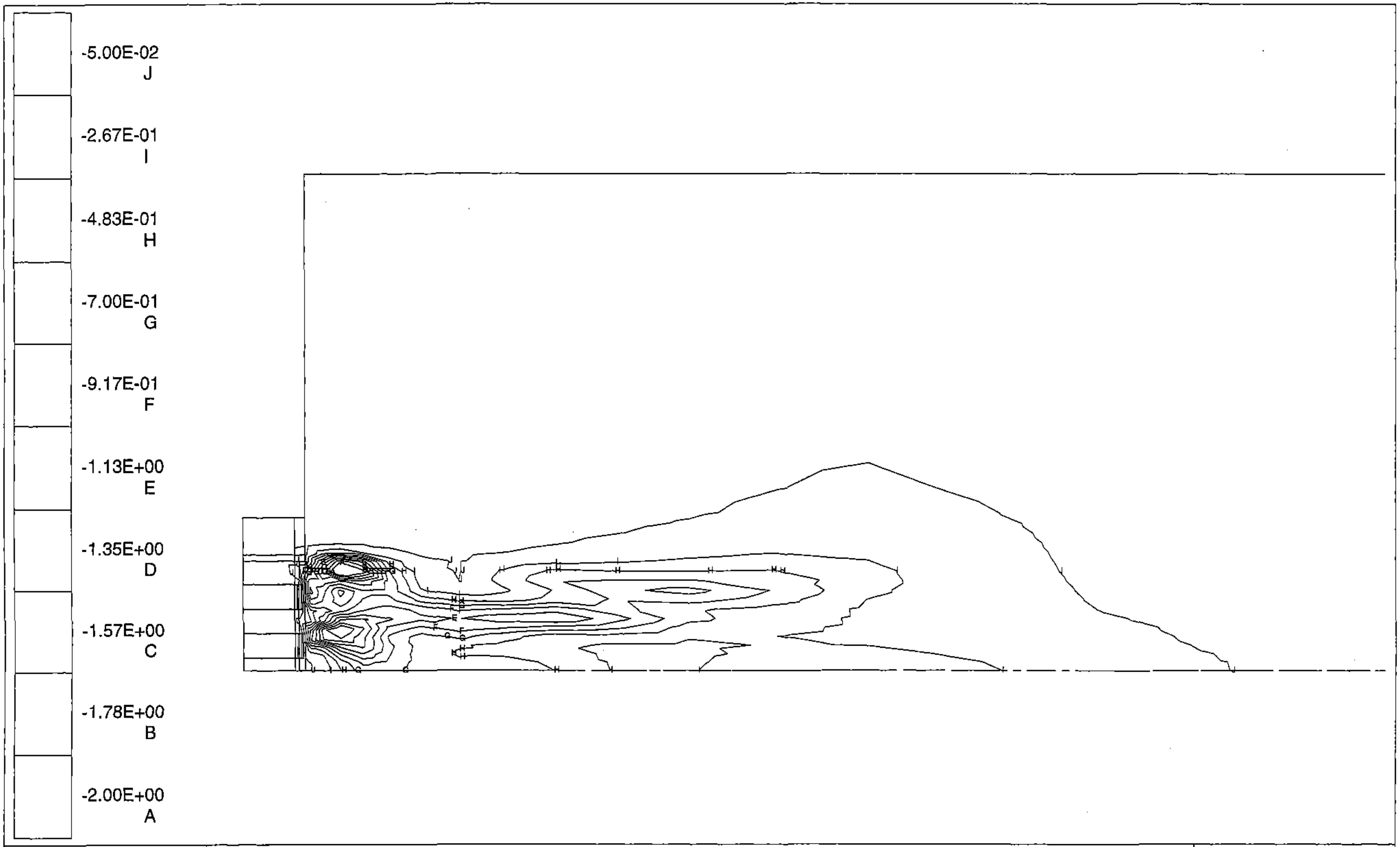

fig. A20, case 49

Volatile reaction rate (kg/M3/s)

Lmax = -5.000E-02 Lmin = -2.000E+00

Nov 19 1998
Fluent 4.47
Fluent Inc.

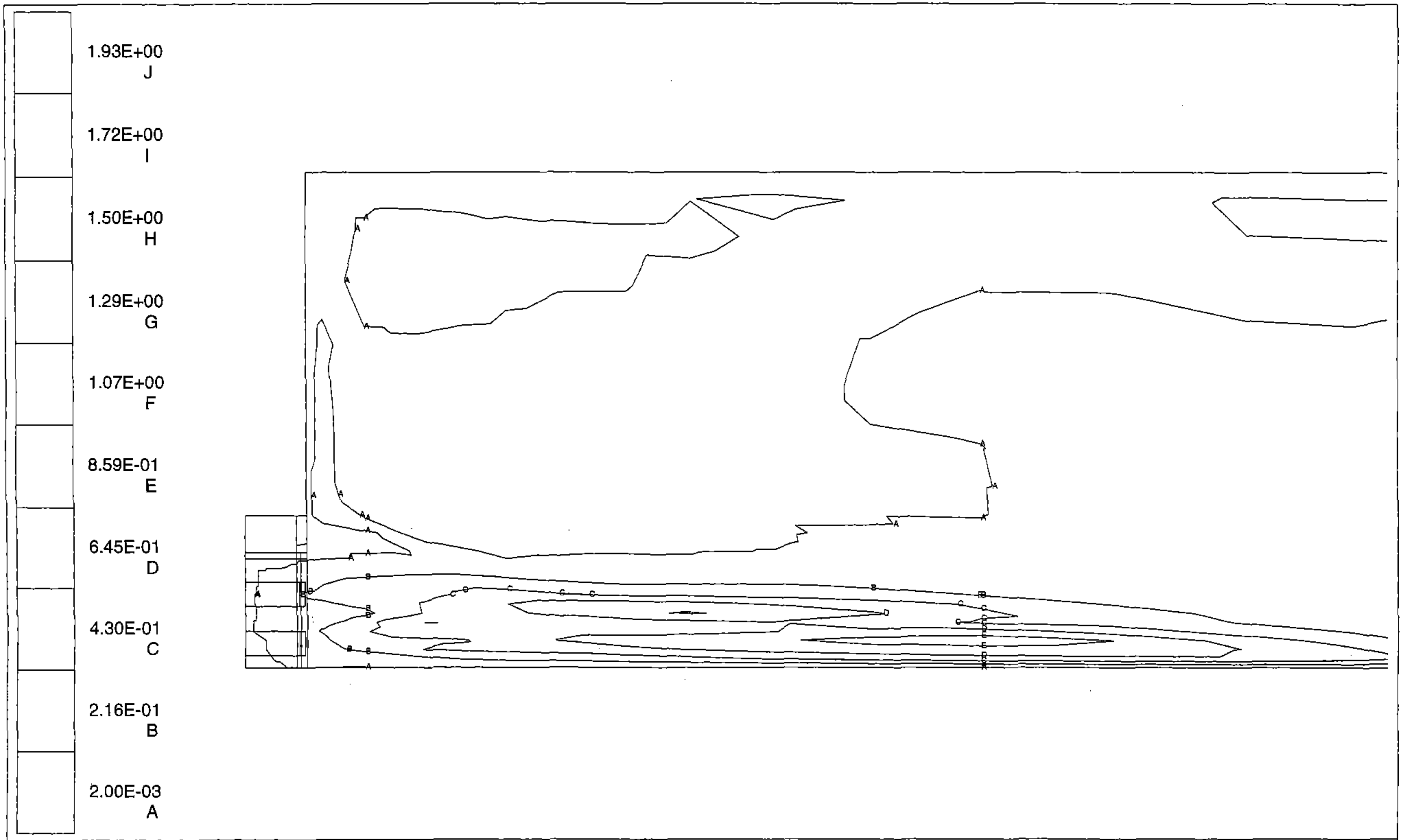

fig. A21, case 49
Particle Concentration (kg/M3)
Lmax = 1.930E+00 Lmin = 2.000E-03

Nov 19 1998
Fluent 4.47
Fluent Inc.

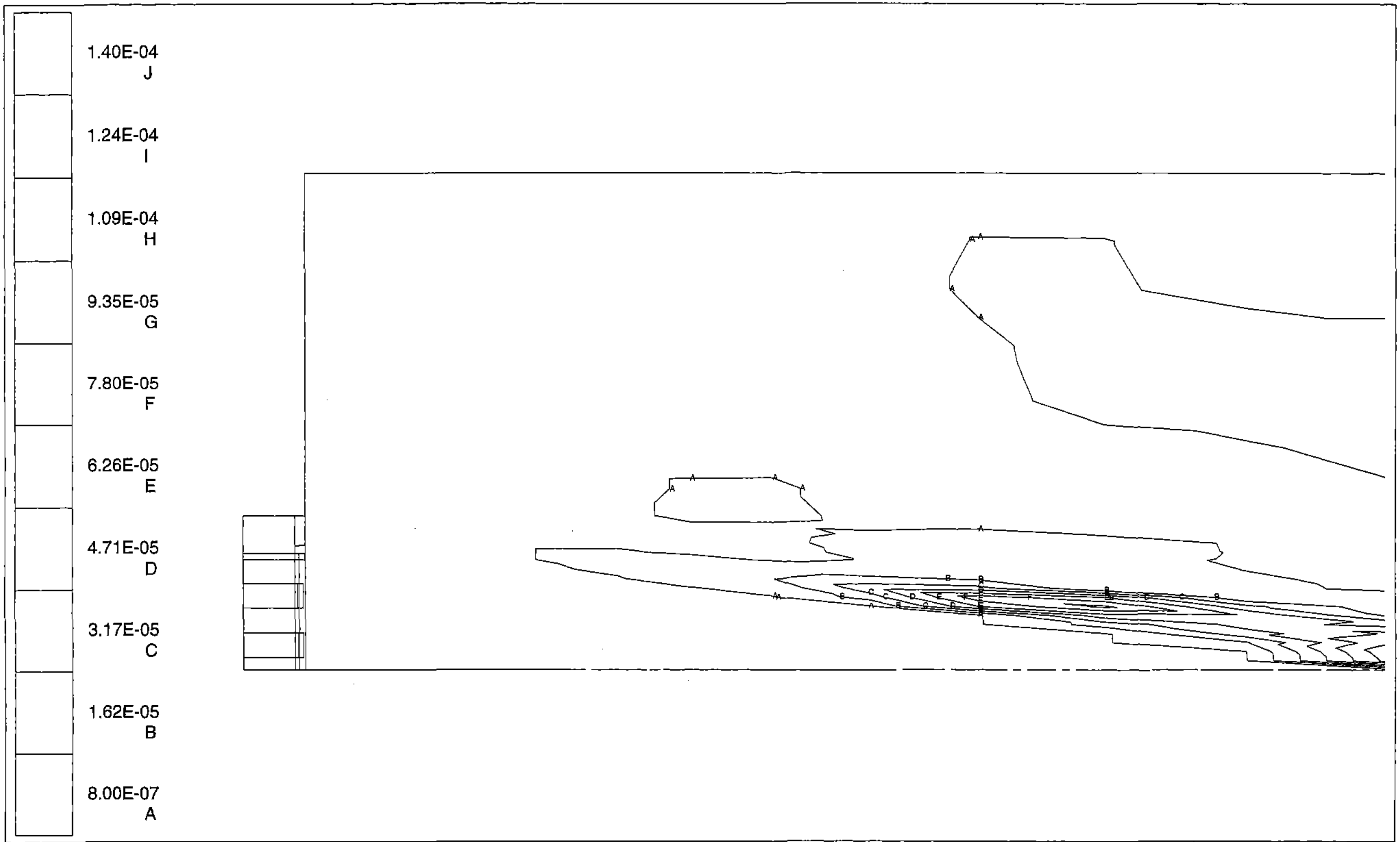

fig. A22, case 49
Char Burnout Rate (Kg/S)
Lmax = 1.398E-04   Lmin = 8.000E-07

Nov 19 1998
Fluent 4.47
Fluent Inc.

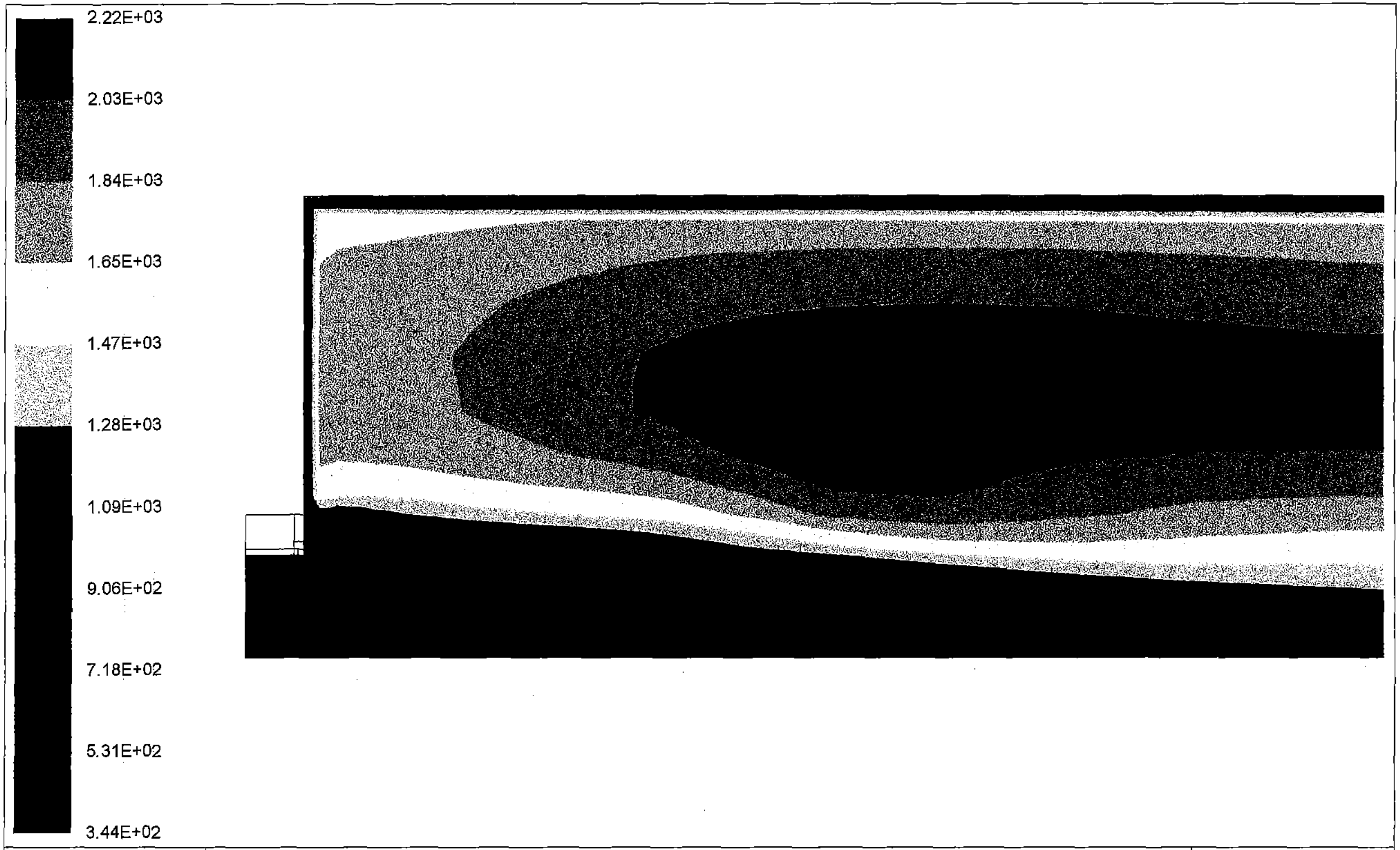

fig. A23, case 49
Temperature (K)
Lmax = 2.216E+03   Lmin = 3.442E+02

Nov 26 1998
Fluent 4.47
Fluent Inc.

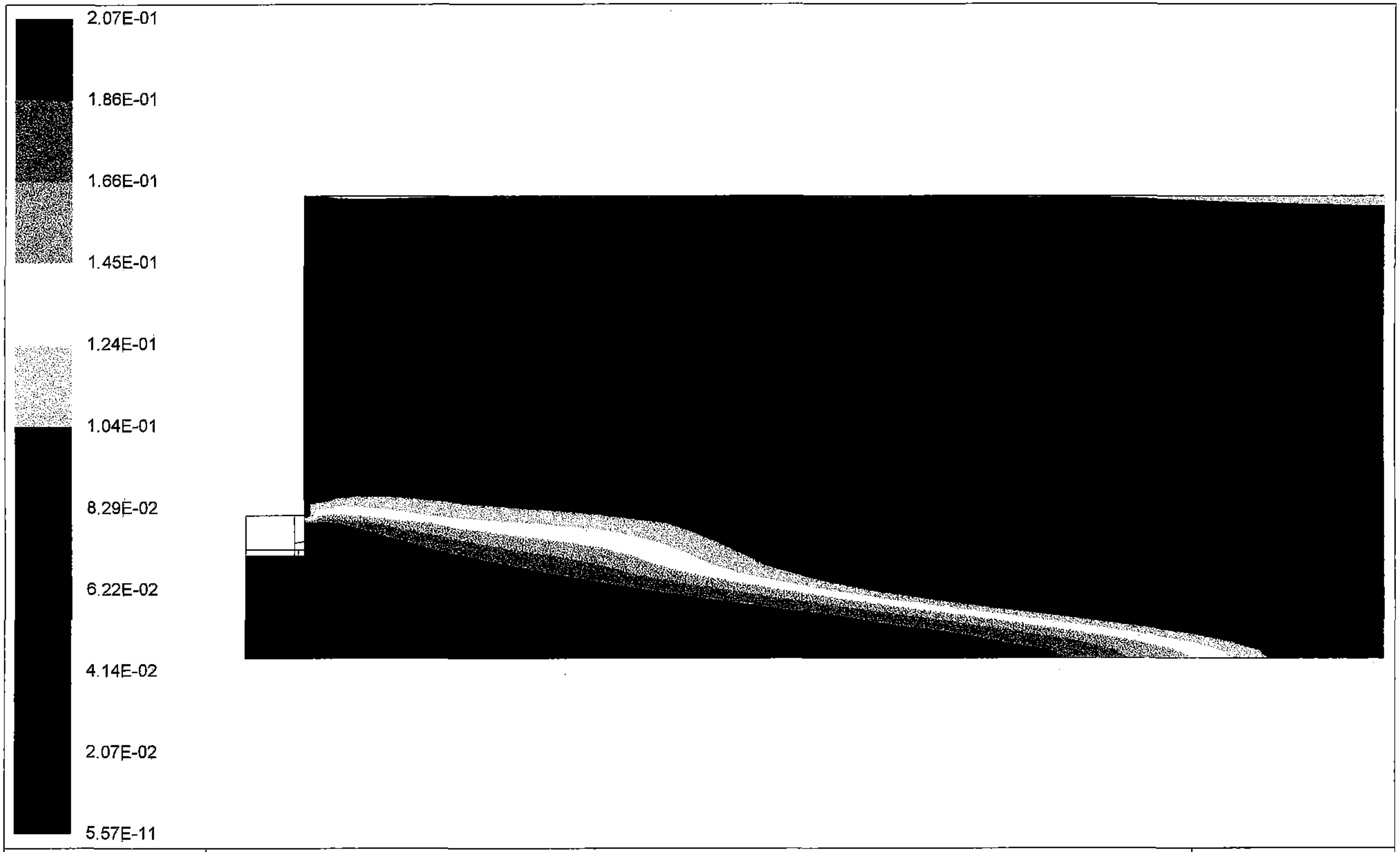

fig. A24, case 49
O2 Mole Fraction
Lmax = 2.072E-01   Lmin = 5.574E-11

Nov 26 1998
Fluent 4.47
Fluent Inc.

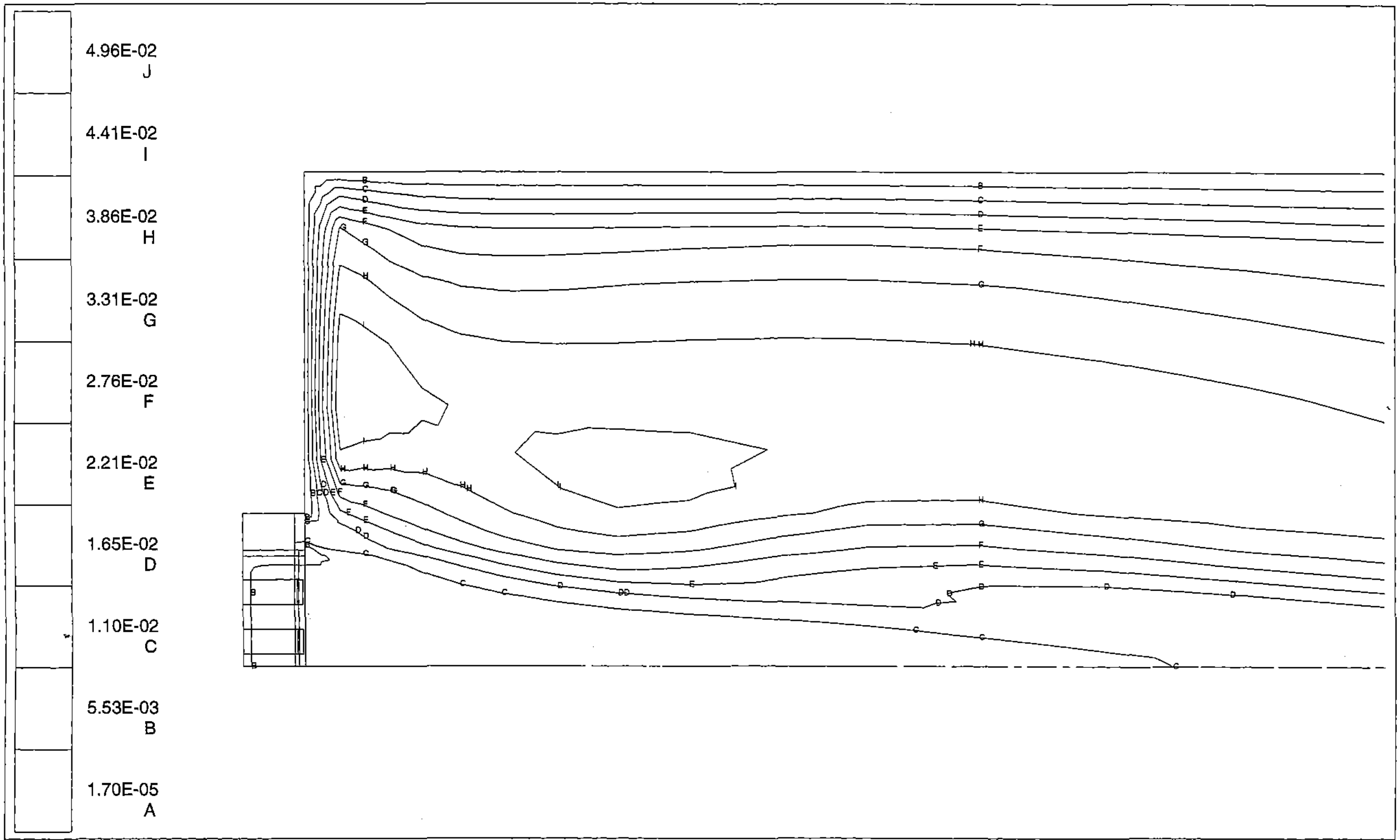

fig. A25, case 49

Effective Viscosity (Kg/M-S)

Lmax = 4.961E-02 Lmin = 1.700E-05

Nov 19 1998
Fluent 4.47
Fluent Inc.

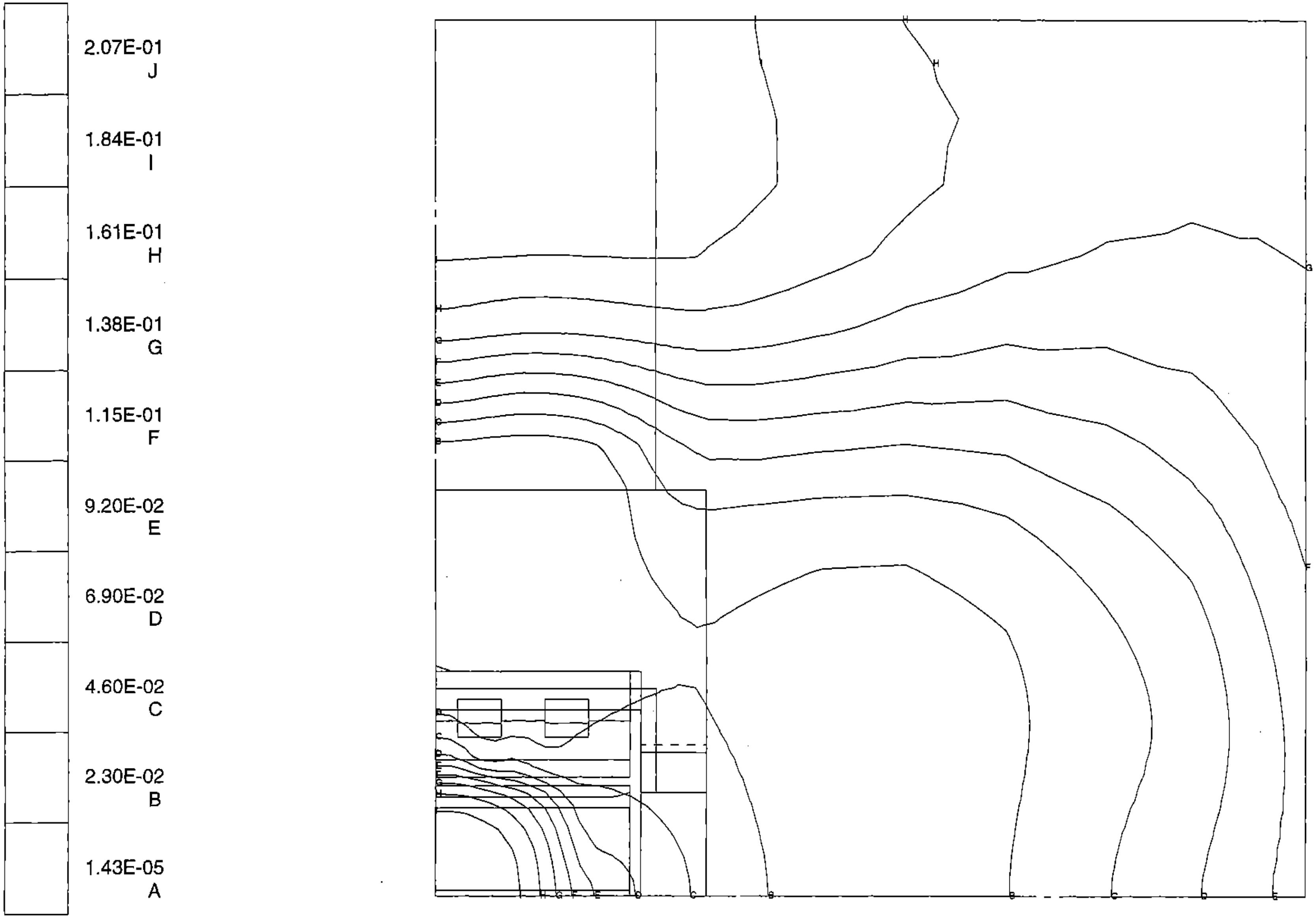

fig. A26, case 49
O2 Mole Fraction
Lmax = 2.070E-01   Lmin = 1.429E-05

Nov 19 1998
Fluent 4.47
Fluent Inc.

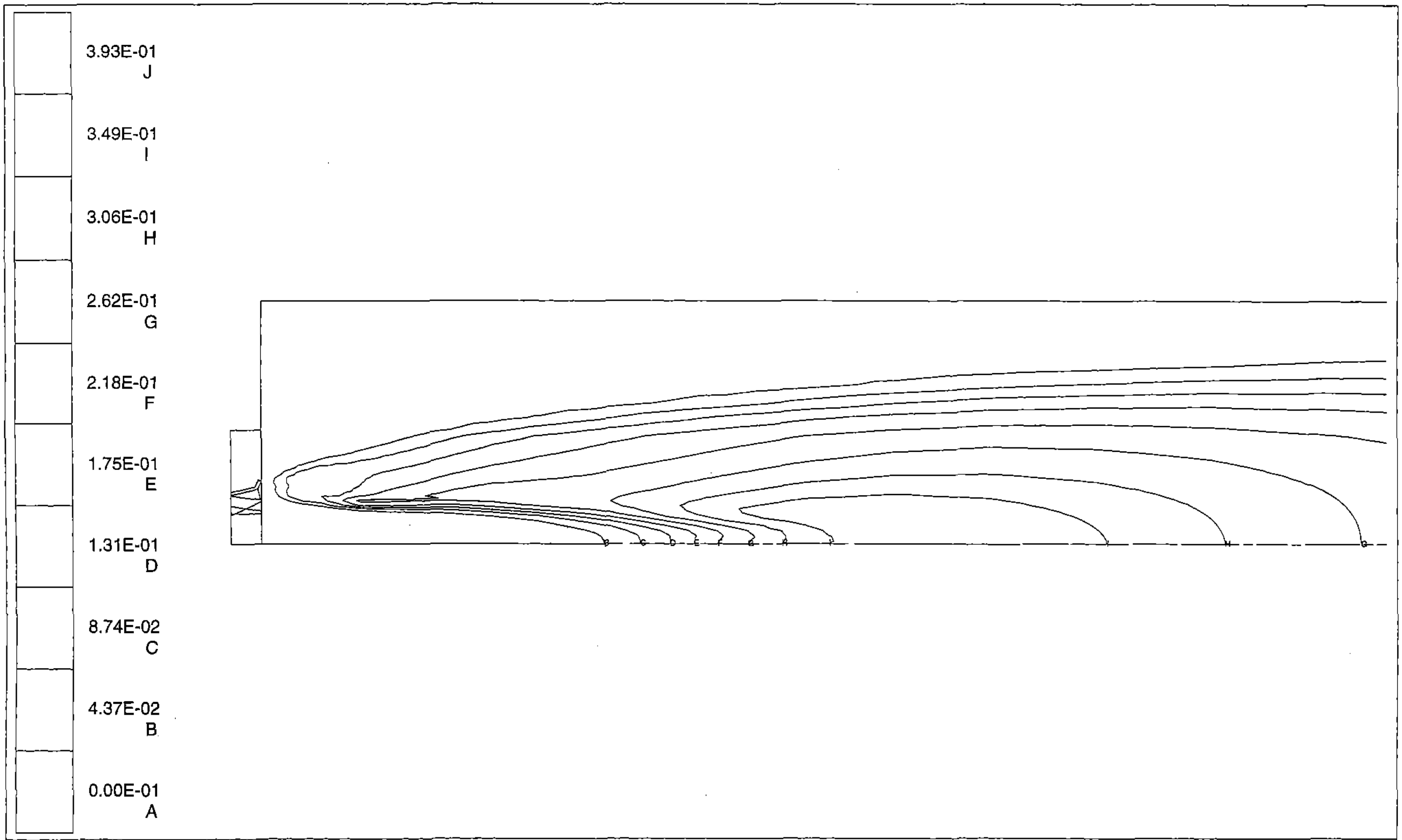

fig. A27, case 49
Volatile Mole Fraction
Lmax = 3.931E-01   Lmin = 0.000E-01

Nov 19 1998
Fluent 4.47
Fluent Inc.

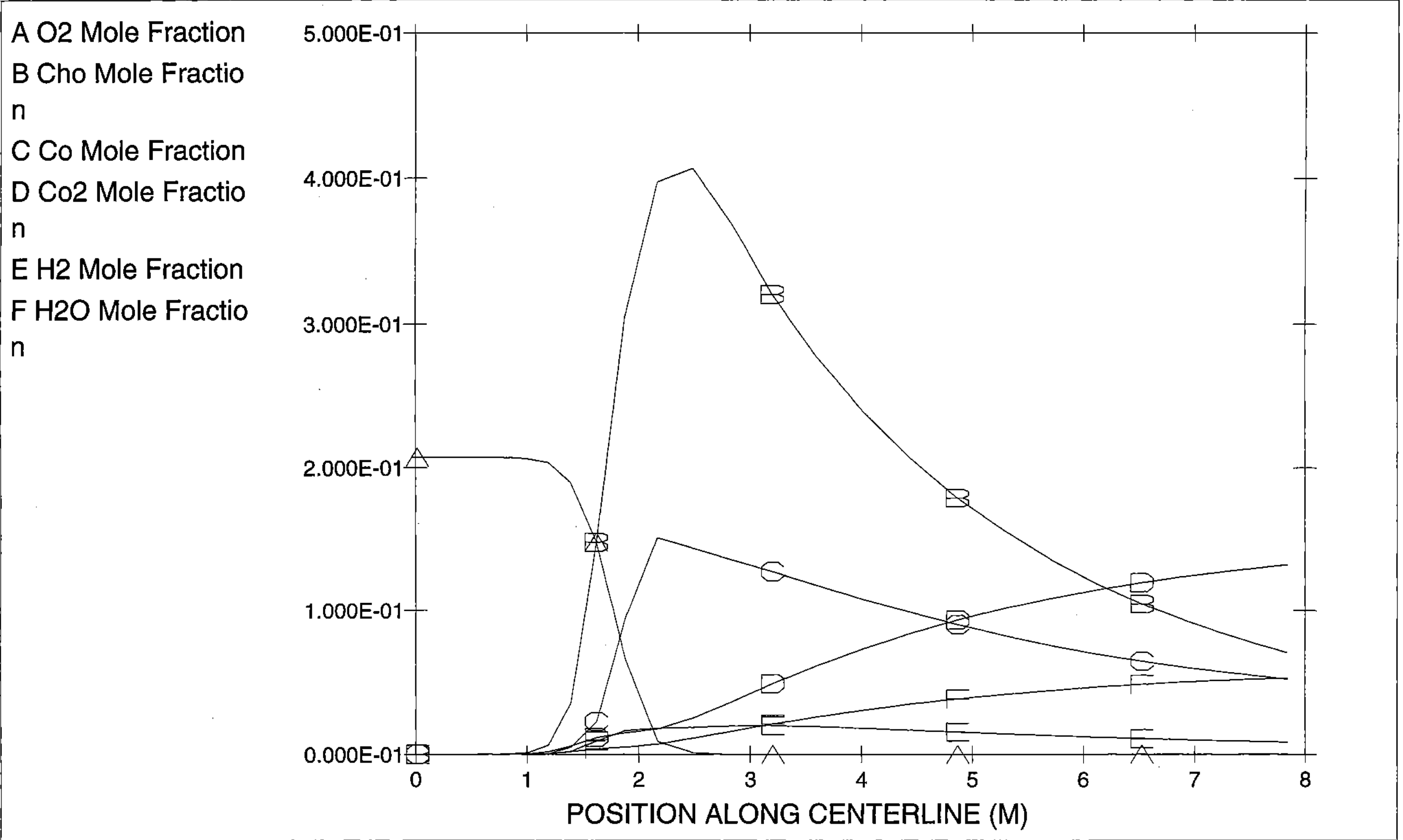

fig A28, case 49
Species molefractions along furnace centerline
xy-plot

Sep 01 1996
Fluent 4.32
Fluent Inc.

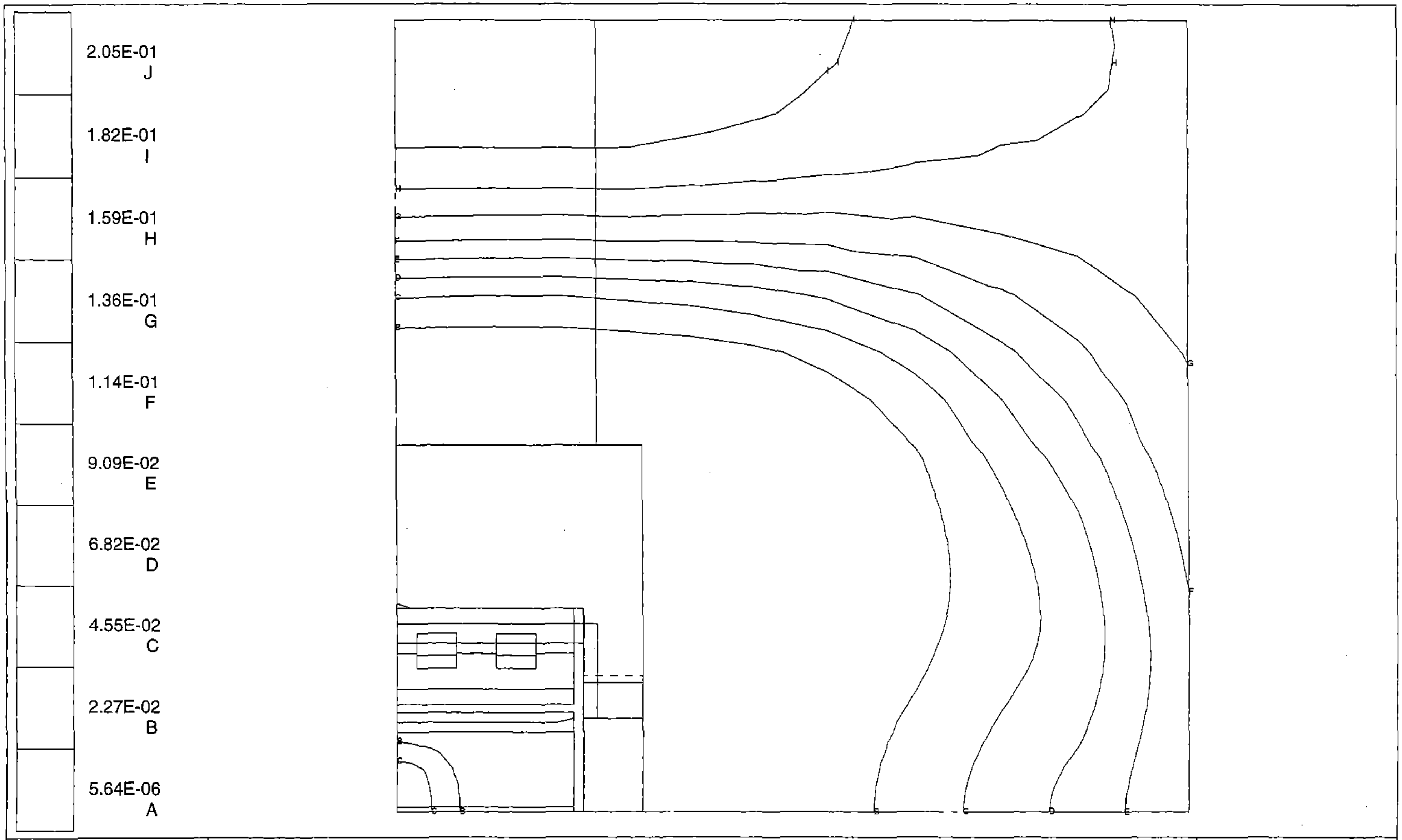

fig. A29, case 49
O2 Mole Fraction
Lmax = 2.046E-01 Lmin = 5.636E-06

Nov 19 1998
Fluent 4.47
Fluent Inc.

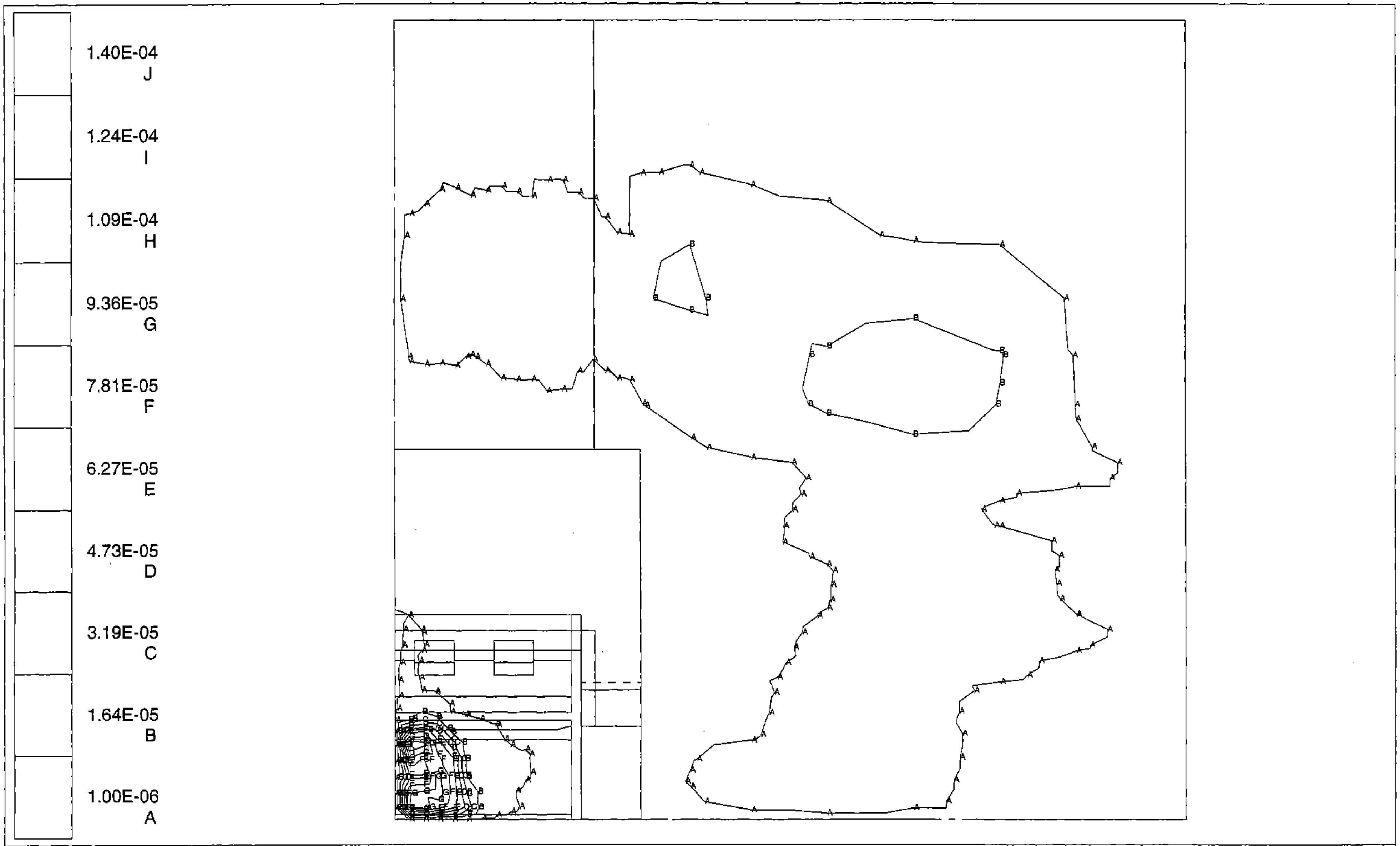

fig. A30, case 49

Char Burnout Rate (Kg/S)

Lmax = 1.398E-04   Lmin = 1.000E-06

Nov 19 1998

Fluent 4.47

Fluent Inc.

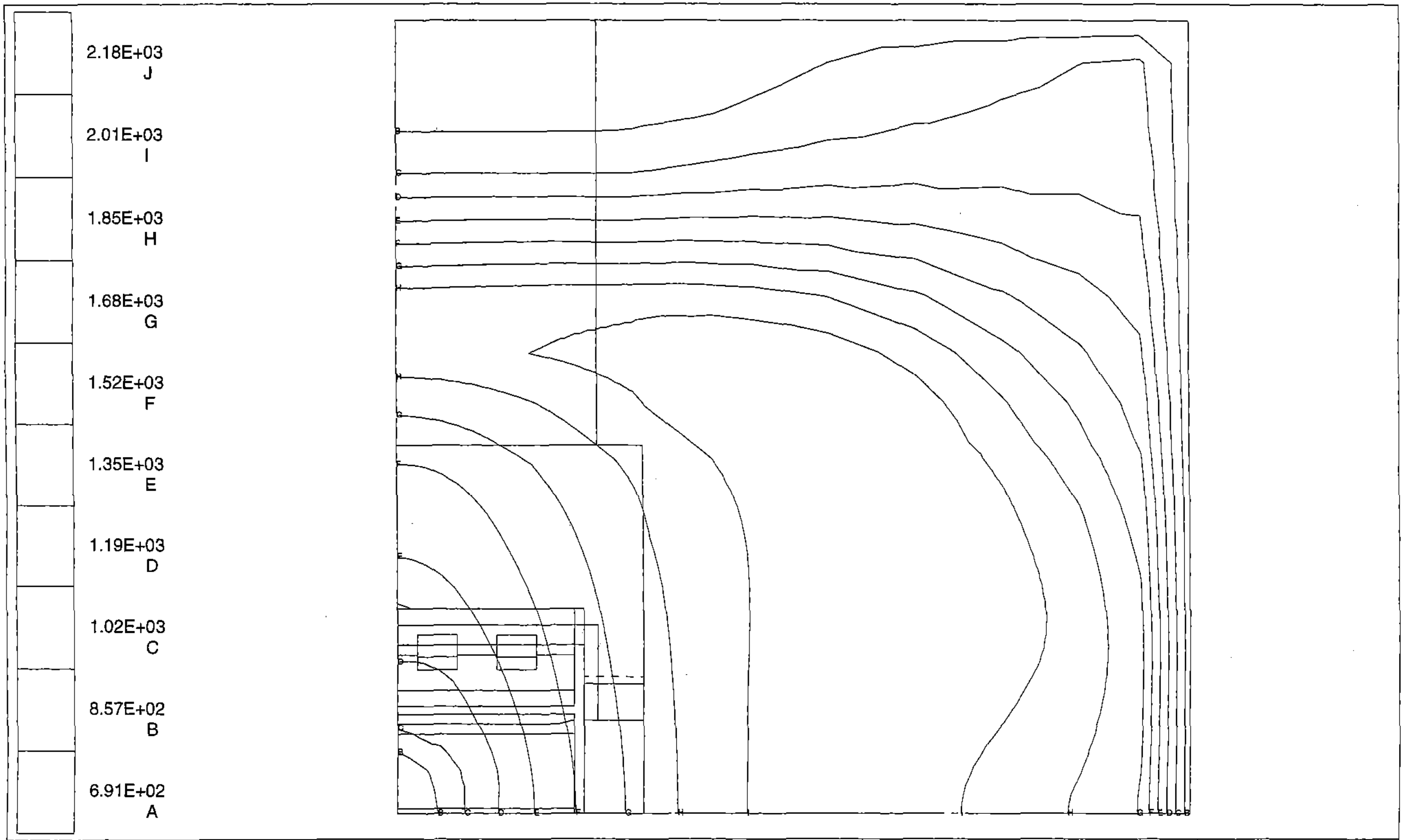

fig. A31, case 49
Temperature (K)
Lmax = 2.179E+03   Lmin = 6.913E+02

Nov 19 1998
Fluent 4.47
Fluent Inc.

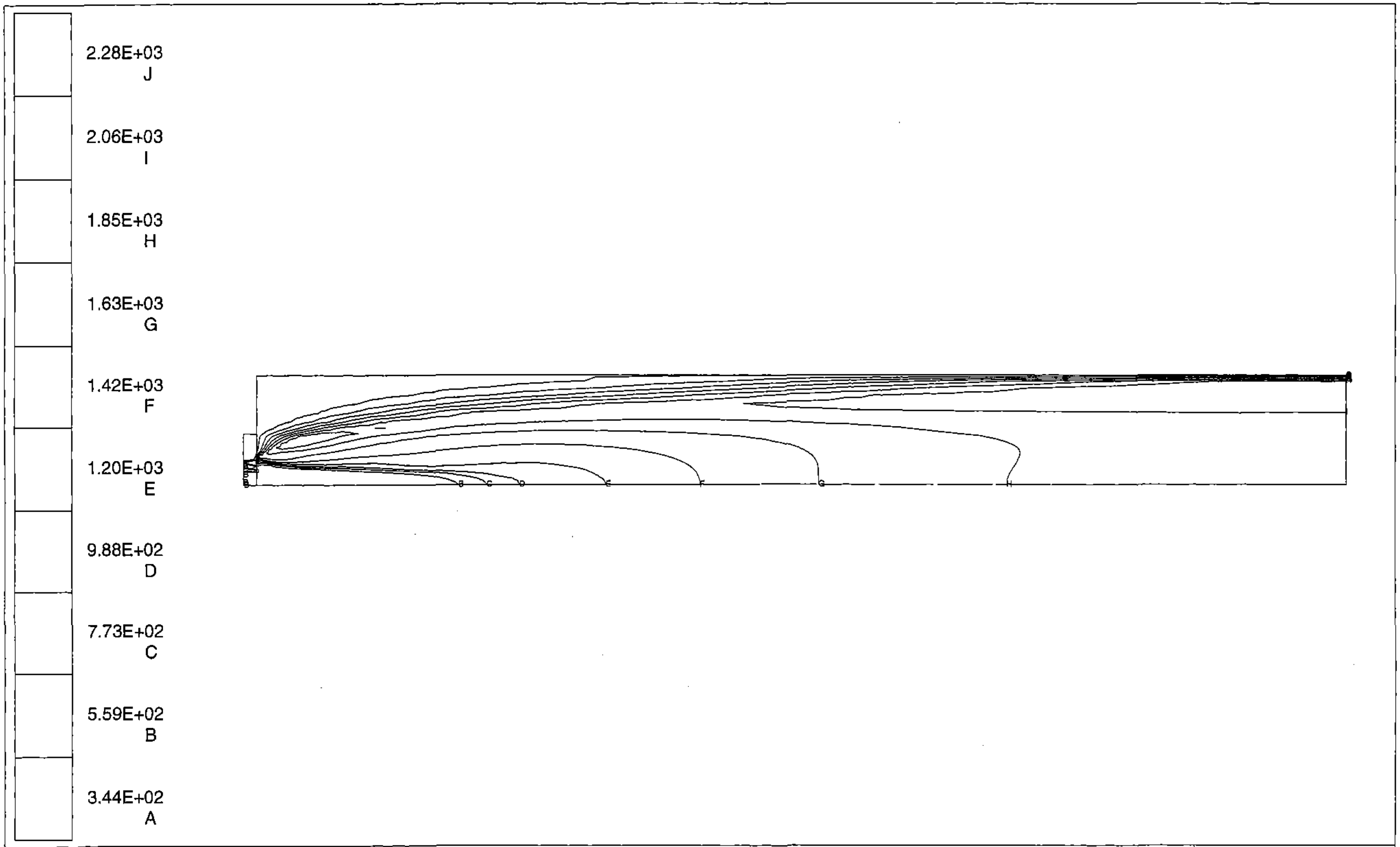

fig. A32, case 49

Temperature (K)

Lmax = 2.276E+03 Lmin = 3.440E+02

Nov 19 1998

Fluent 4.47

Fluent Inc.

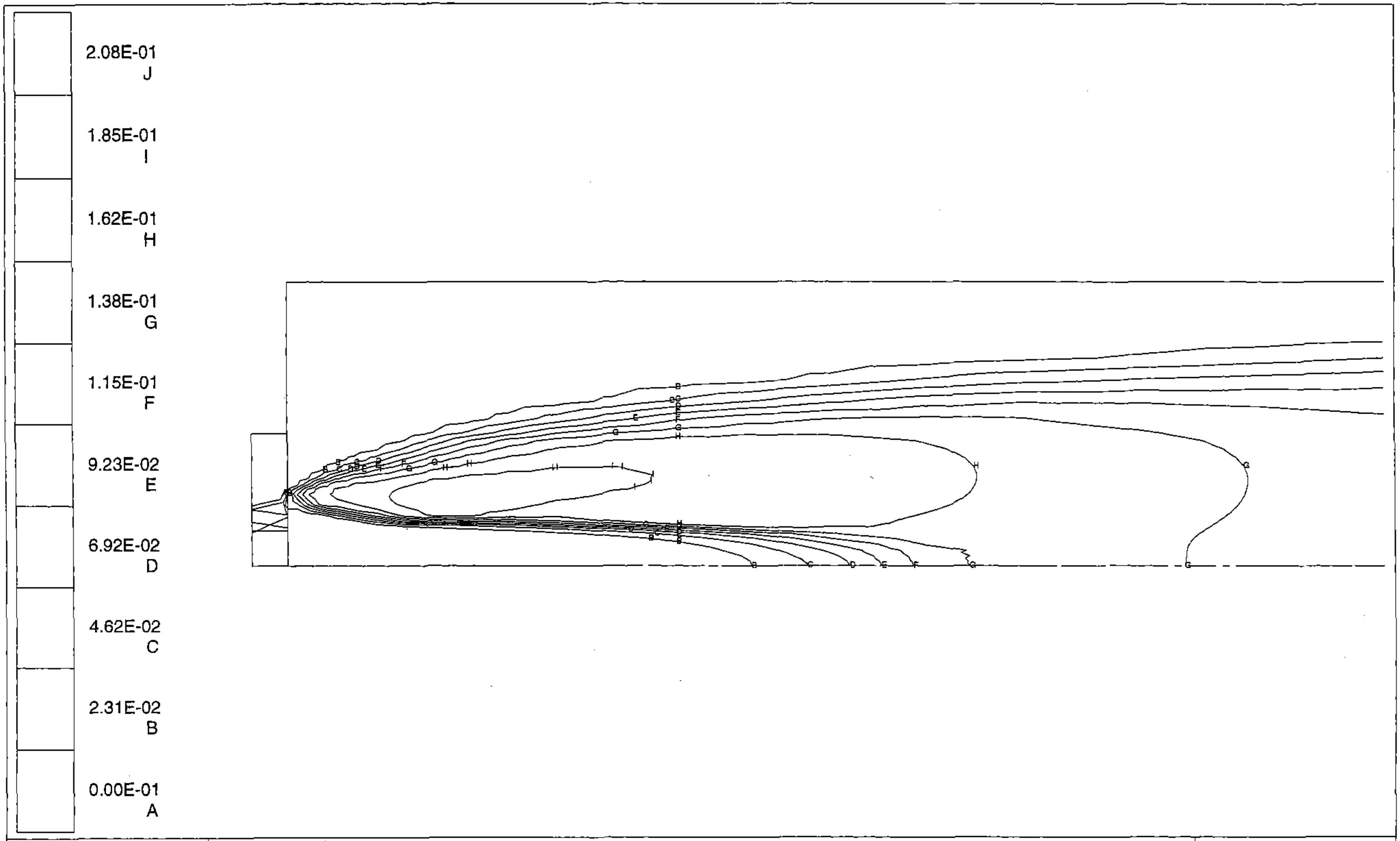

Y
Z

fig. A32b, case 49

Co Mole Fraction

Lmax = 2.077E-01   Lmin = 0.000E-01

Nov 19 1998

Fluent 4.47

Fluent Inc.

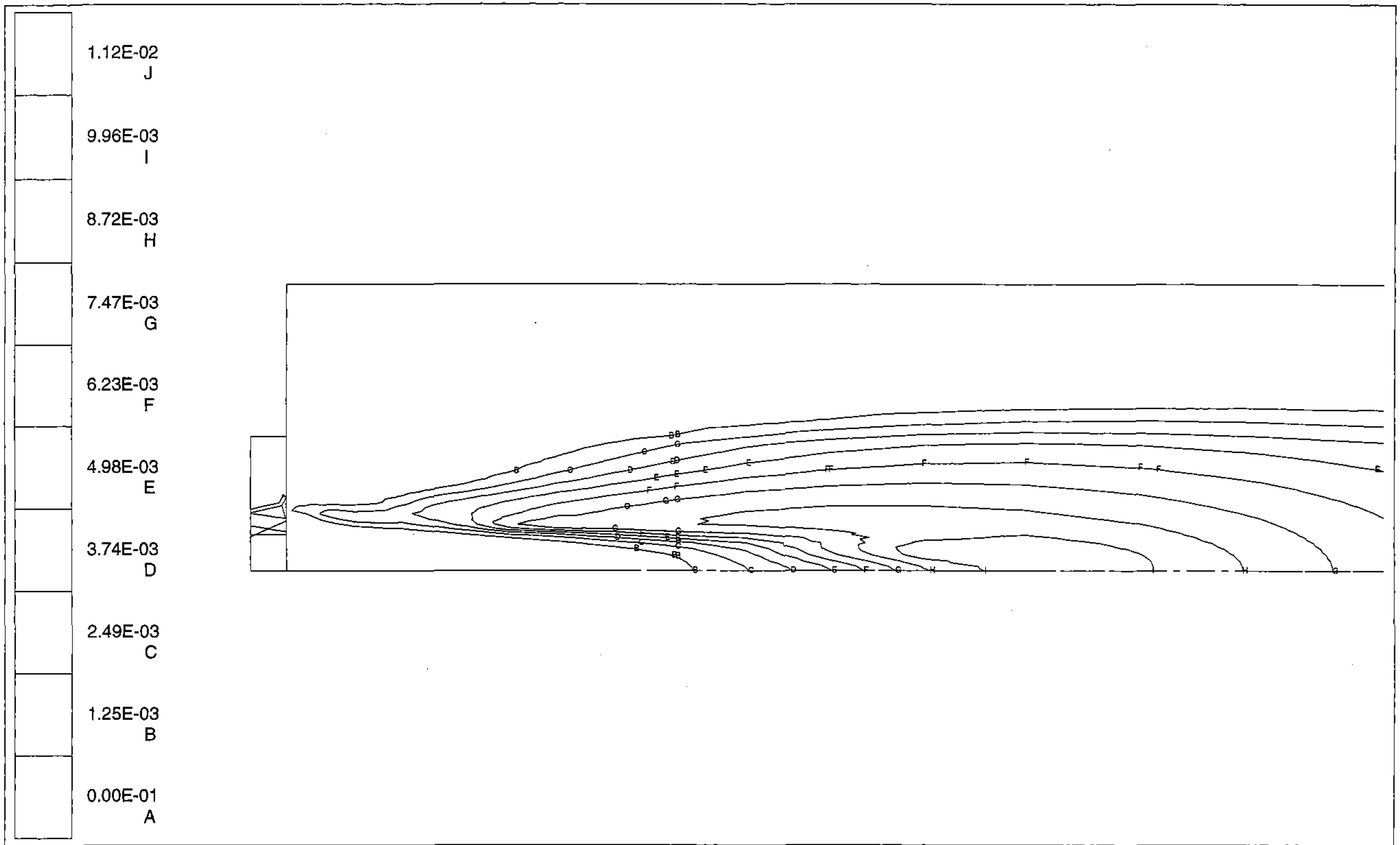

fig. A33, case 49
Hcn Mole Fraction
Lmax = 1.121E-02   Lmin = 0.000E-01

Nov 19 1998
Fluent 4.47
Fluent Inc.

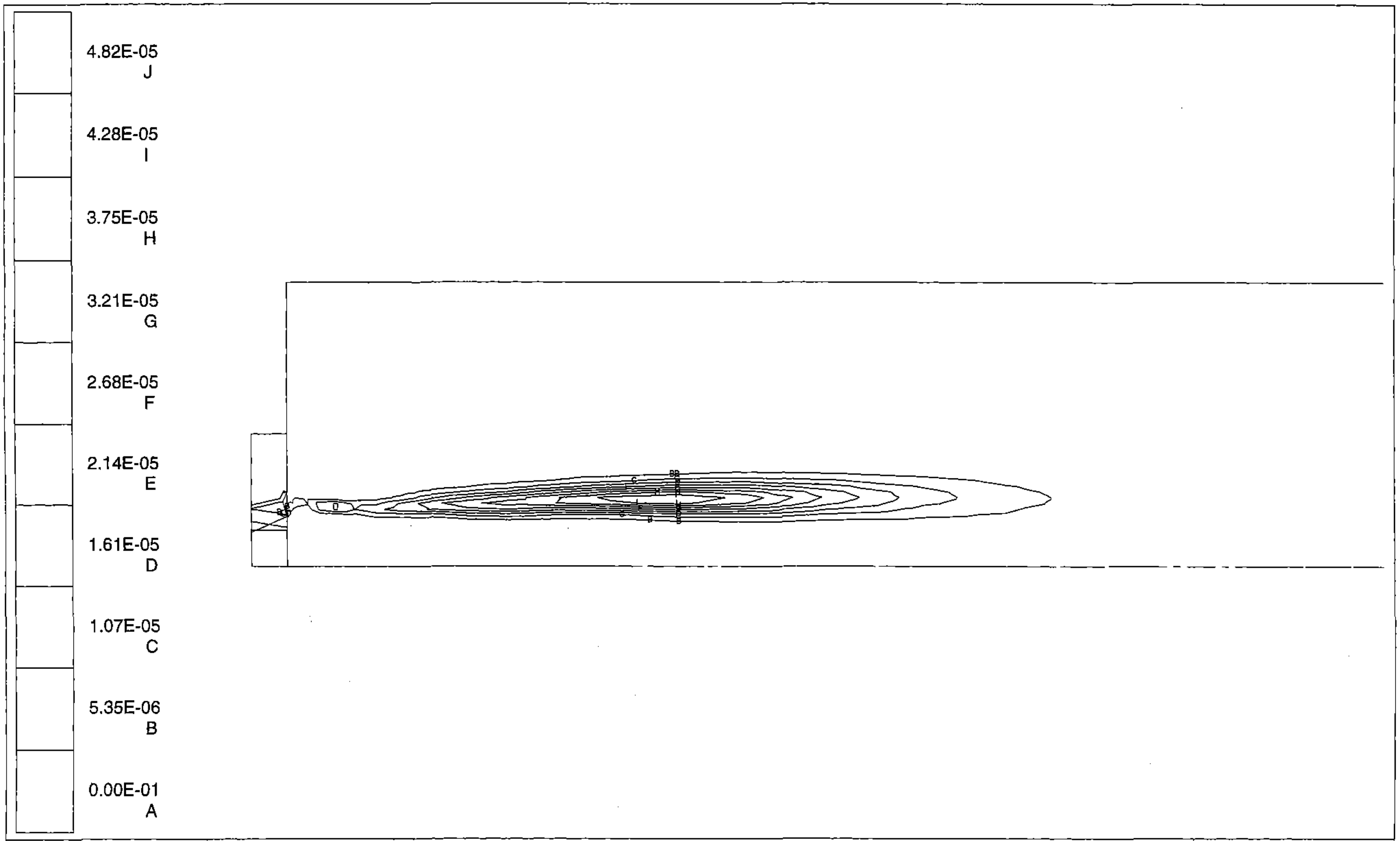

fig. A34, case 49
Nh3 Mole Fraction
Lmax = 4.818E-05   Lmin = 0.000E-01

Nov 19 1998
Fluent 4.47
Fluent Inc.

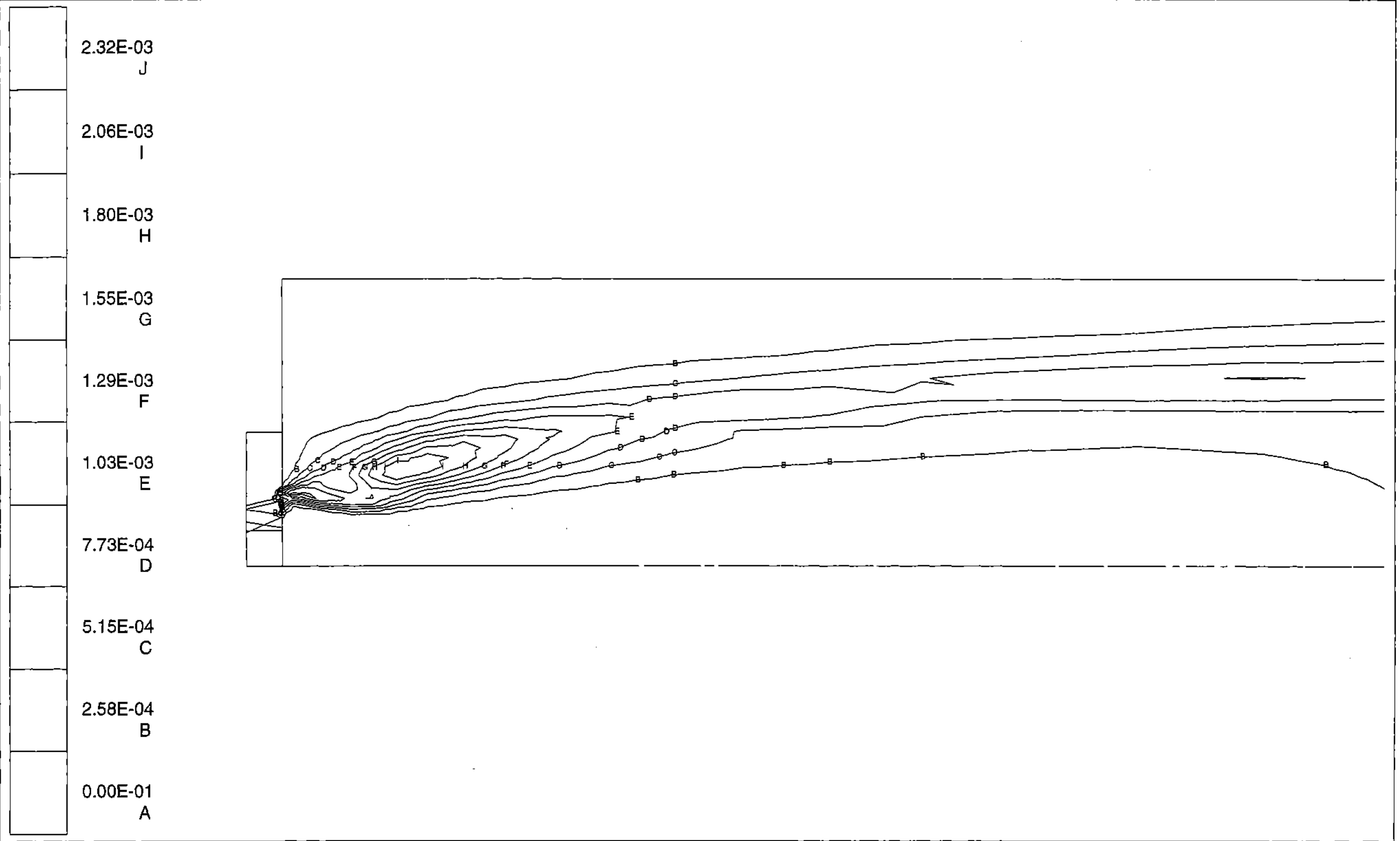

fig. A35, case 49

No Mole Fraction

Lmax = 2.319E-03   Lmin = 0.000E-01

Nov 19 1998

Fluent 4.47

Fluent Inc.

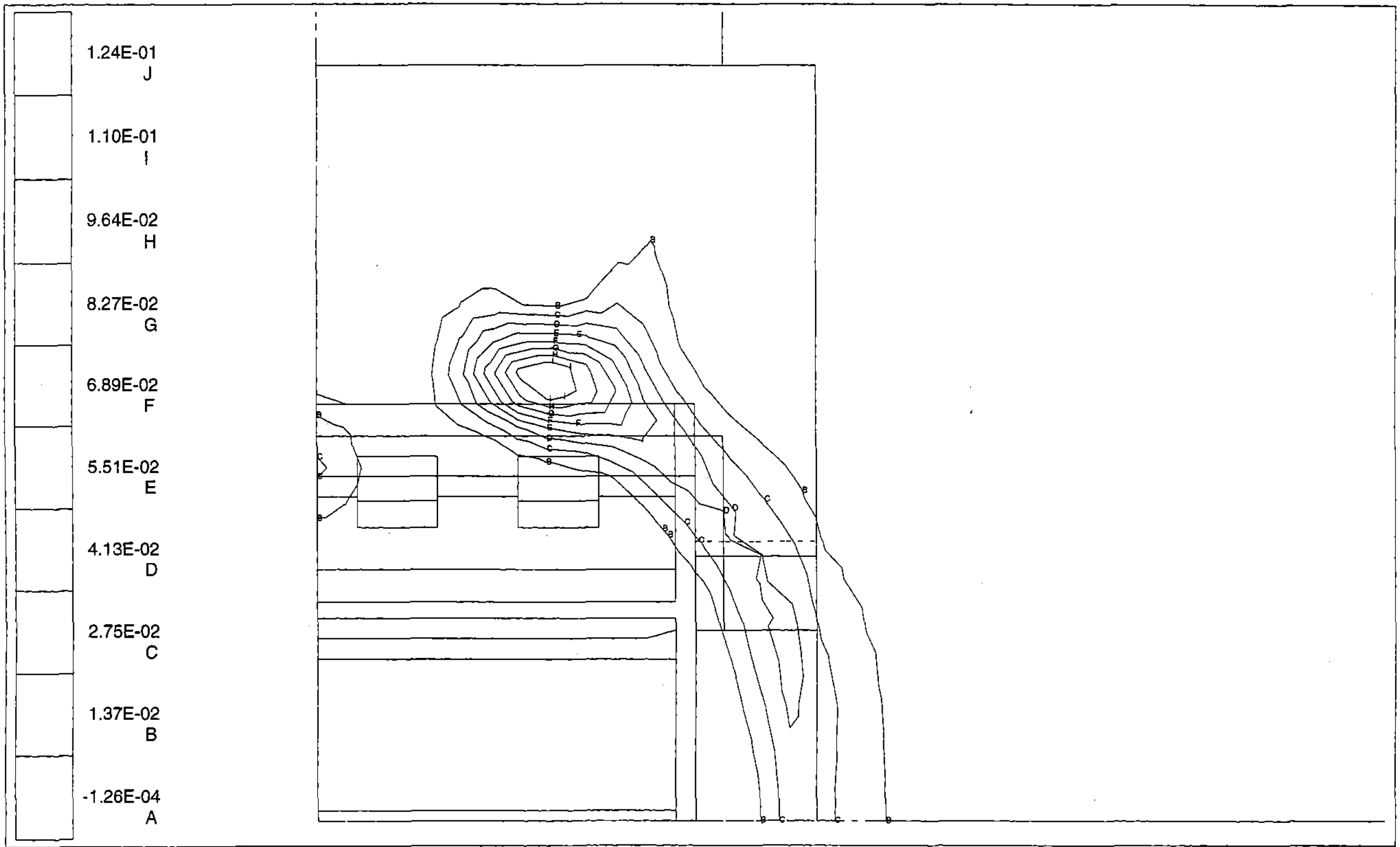

fig. A36, case 49

No Reaction Rate (Kg/M3/S)

Lmax = 1.240E-01 Lmin = -1.258E-04

Nov 19 1998

Fluent 4.47

Fluent Inc.

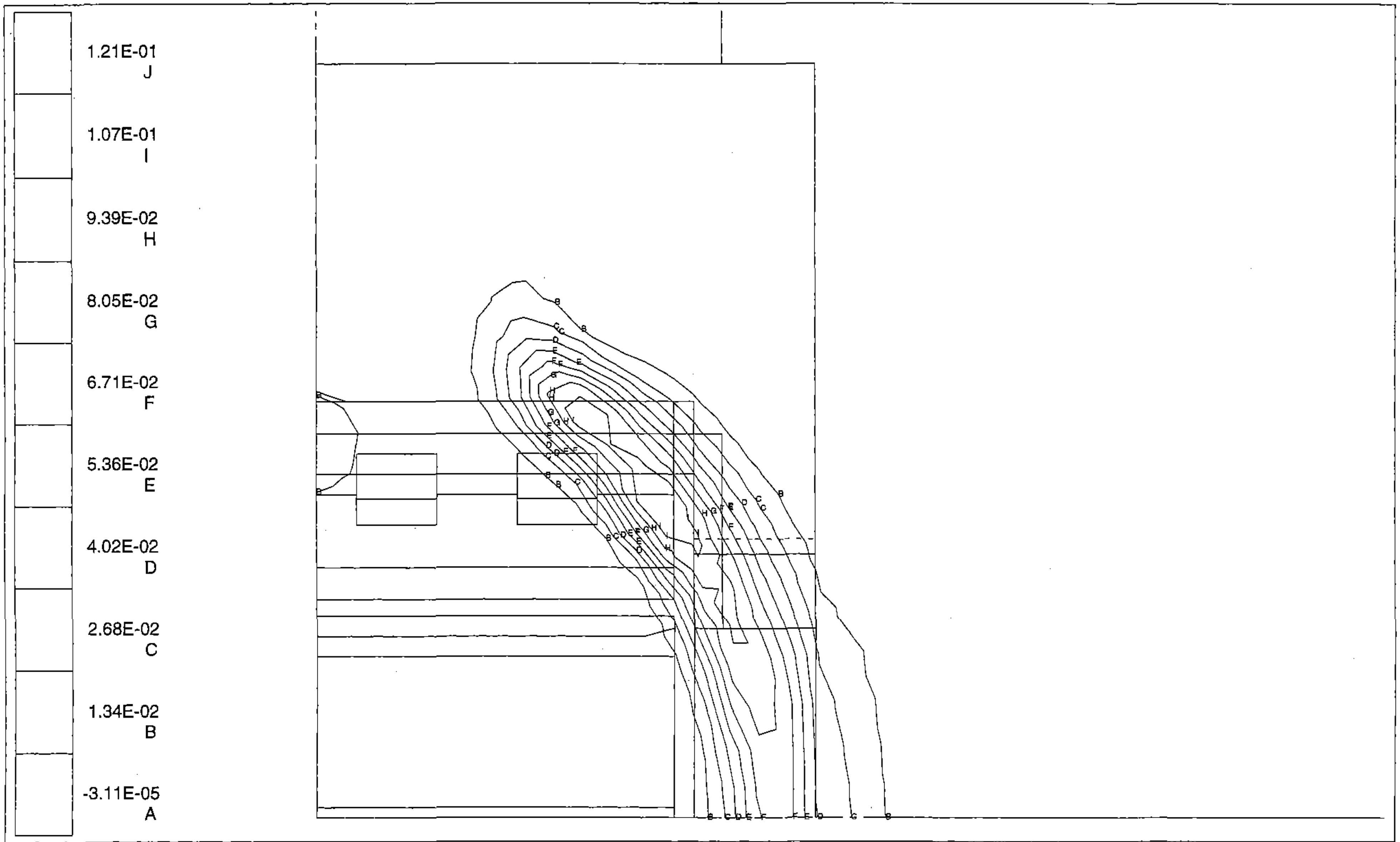

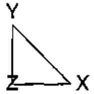

fig. A37, case 49

No Reaction Rate (Kg/M3/S)

Lmax = 1.207E-01 Lmin = -3.112E-05

Nov 19 1998

Fluent 4.47

Fluent Inc.

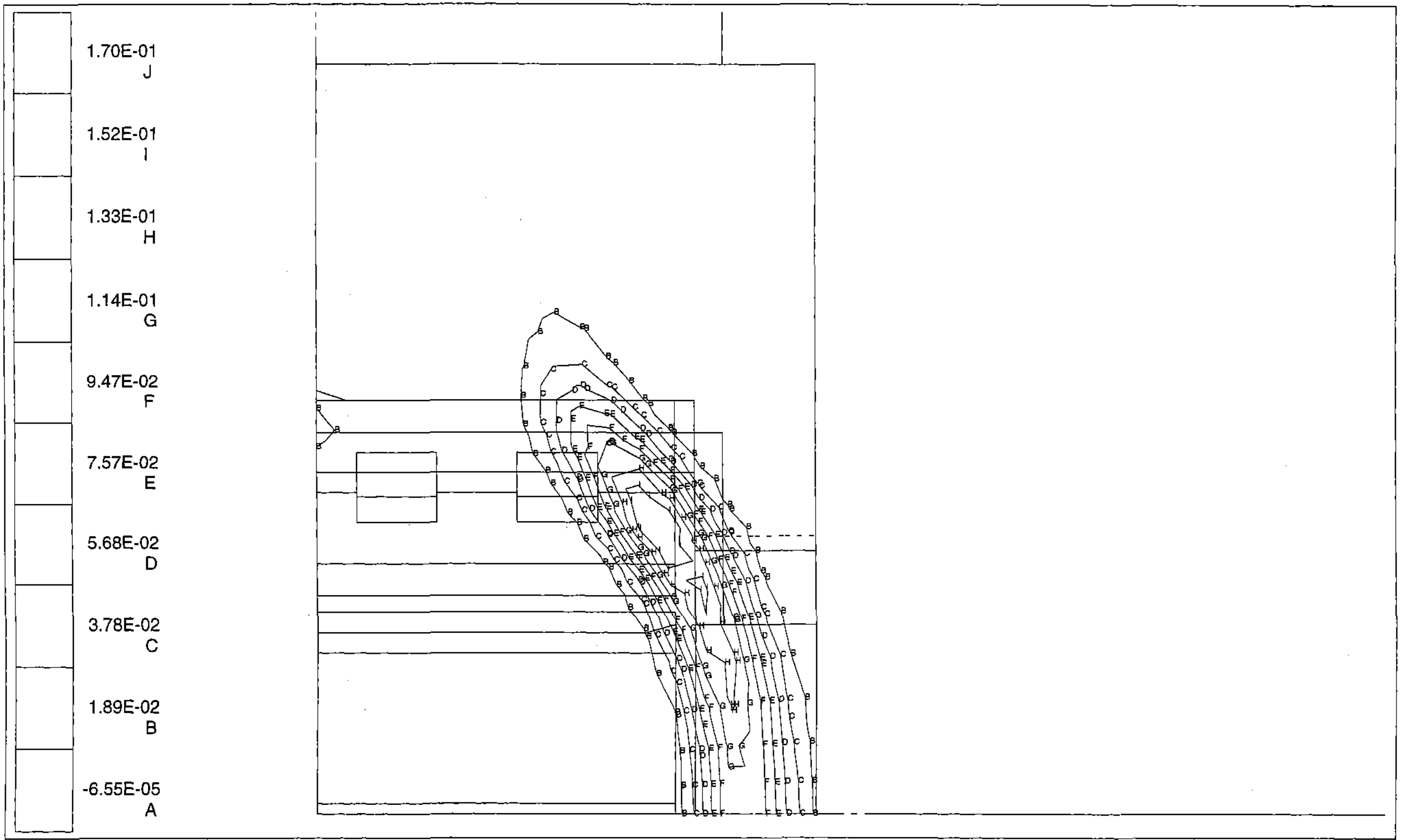

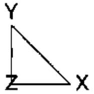

fig. A38, case 49

No Reaction Rate (Kg/M3/S)

Lmax = 1.705E-01   Lmin = -6.552E-05

Nov 19 1998

Fluent 4.47

Fluent Inc.

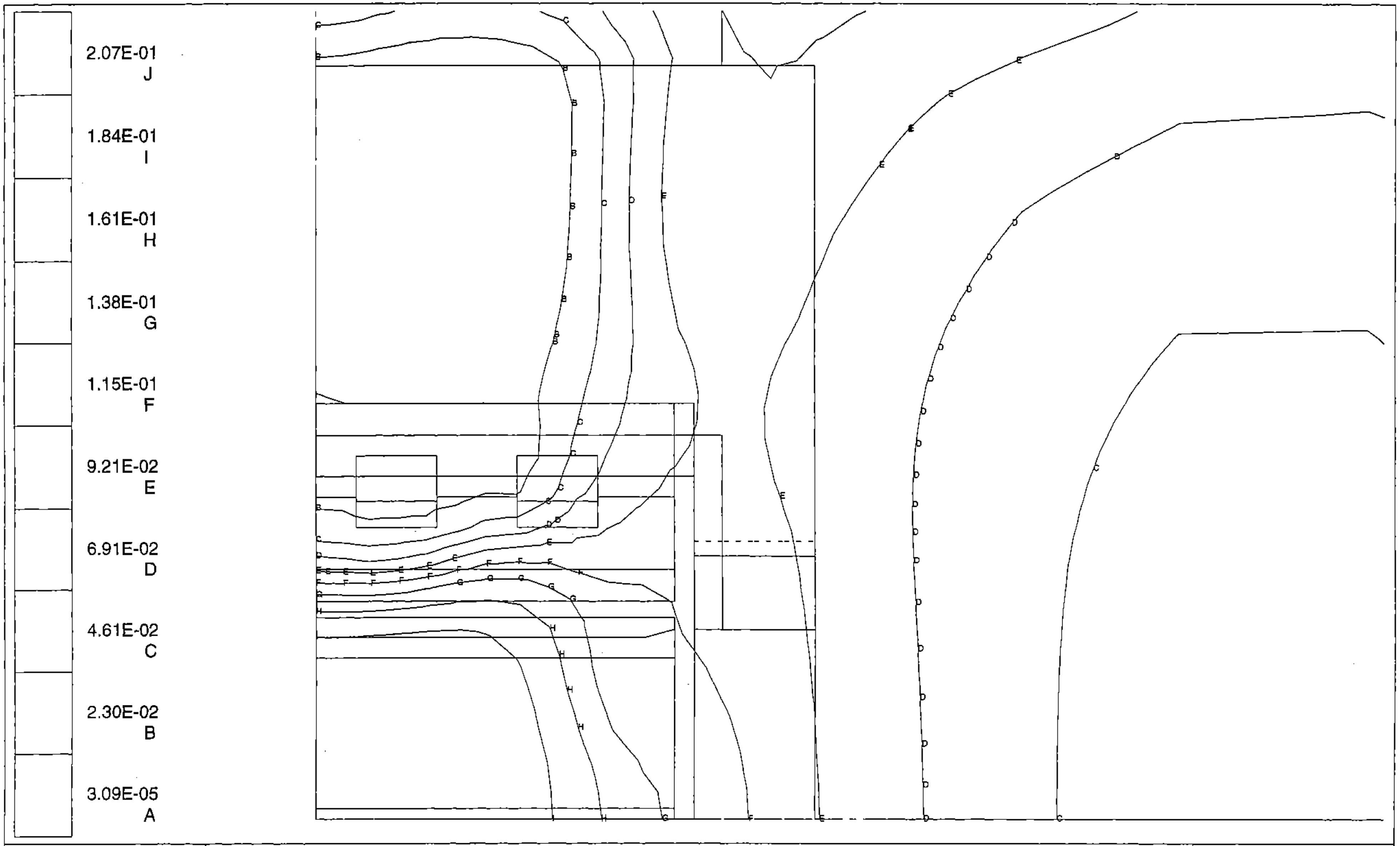

fig. A39, case 49

O2 Mole Fraction

Lmax = 2.072E-01   Lmin = 3.094E-05

Nov 19 1998

Fluent 4.47

Fluent Inc.

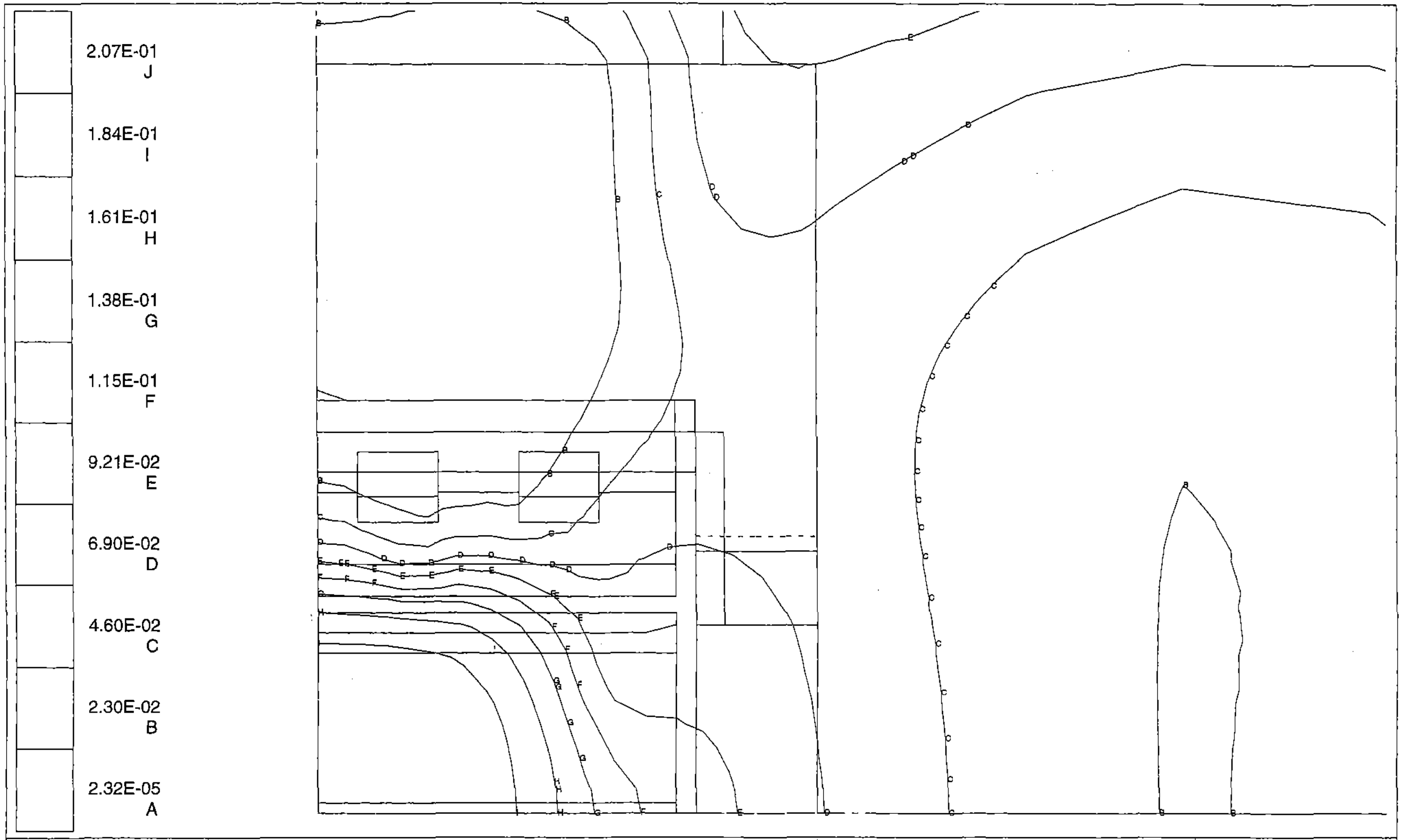

fig. A40, case 49
O2 Mole Fraction
Lmax = 2.071E-01   Lmin = 2.317E-05

Nov 19 1998
Fluent 4.47
Fluent Inc.

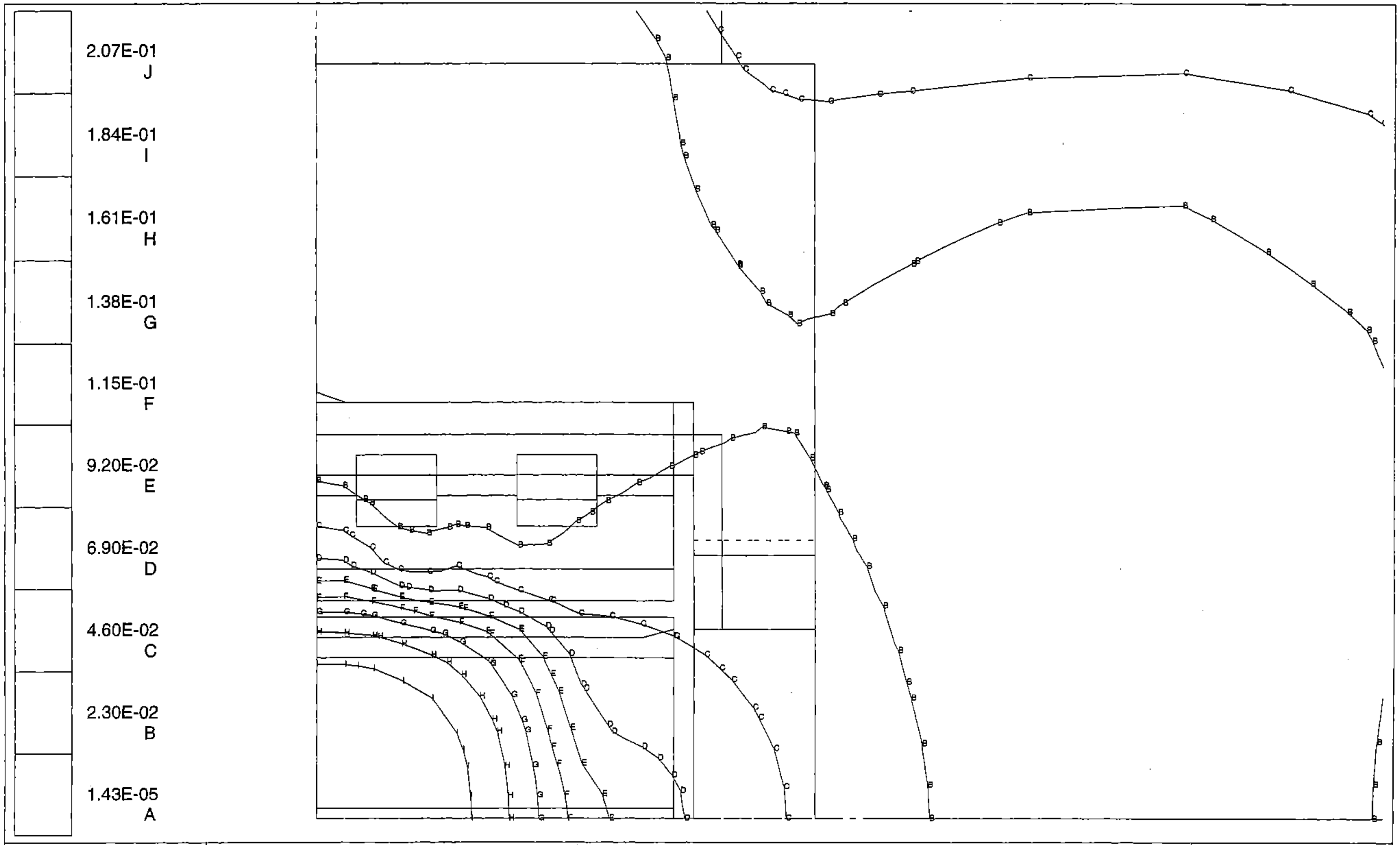

fig. A41, case 49

O2 Mole Fraction

Lmax = 2.070E-01 Lmin = 1.429E-05

Nov 19 1998

Fluent 4.47

Fluent Inc.

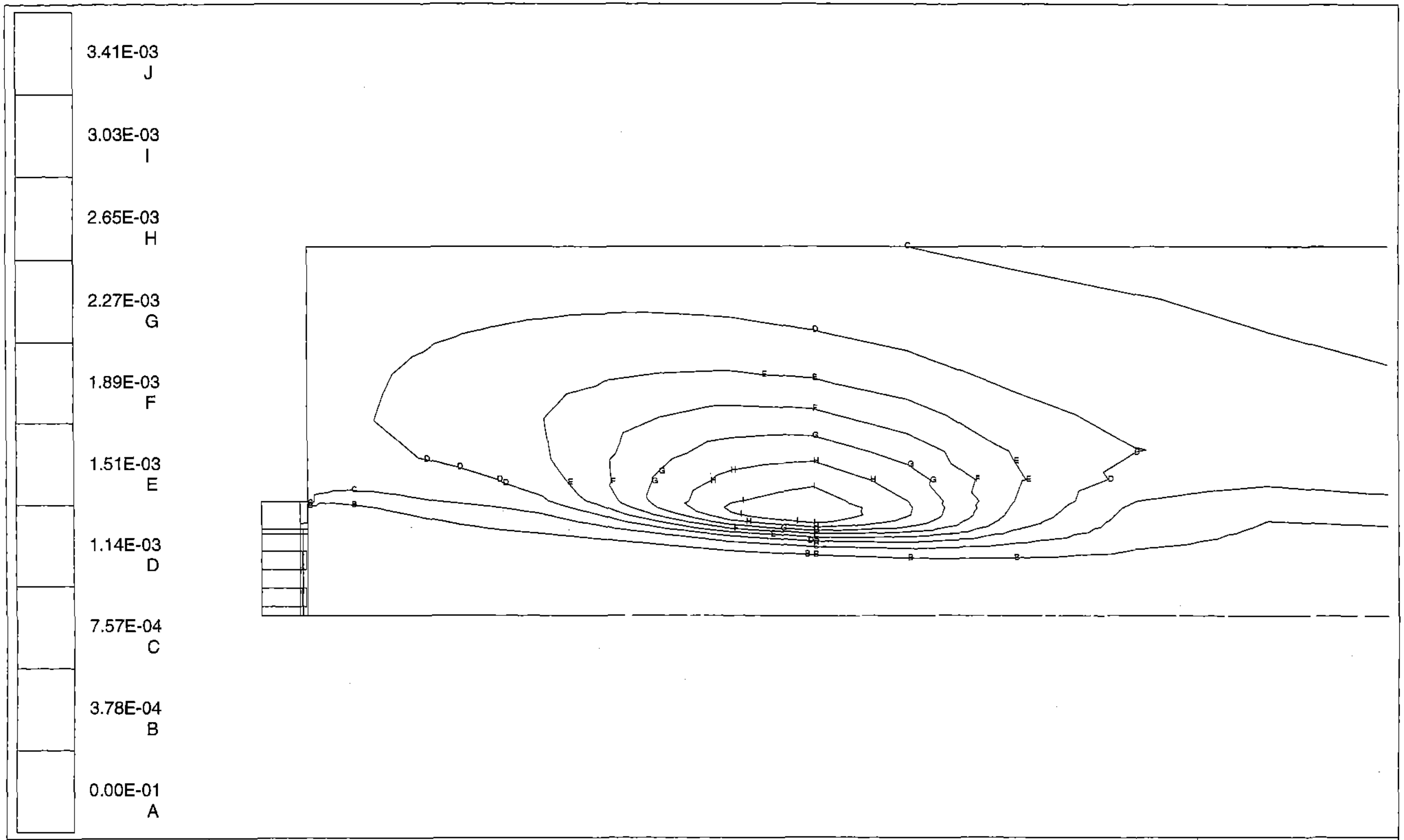

fig. A42, case 49

No Mole Fraction

Lmax = 3.406E-03 Lmin = 0.000E-01

Nov 19 1998

Fluent 4.47

Fluent Inc.

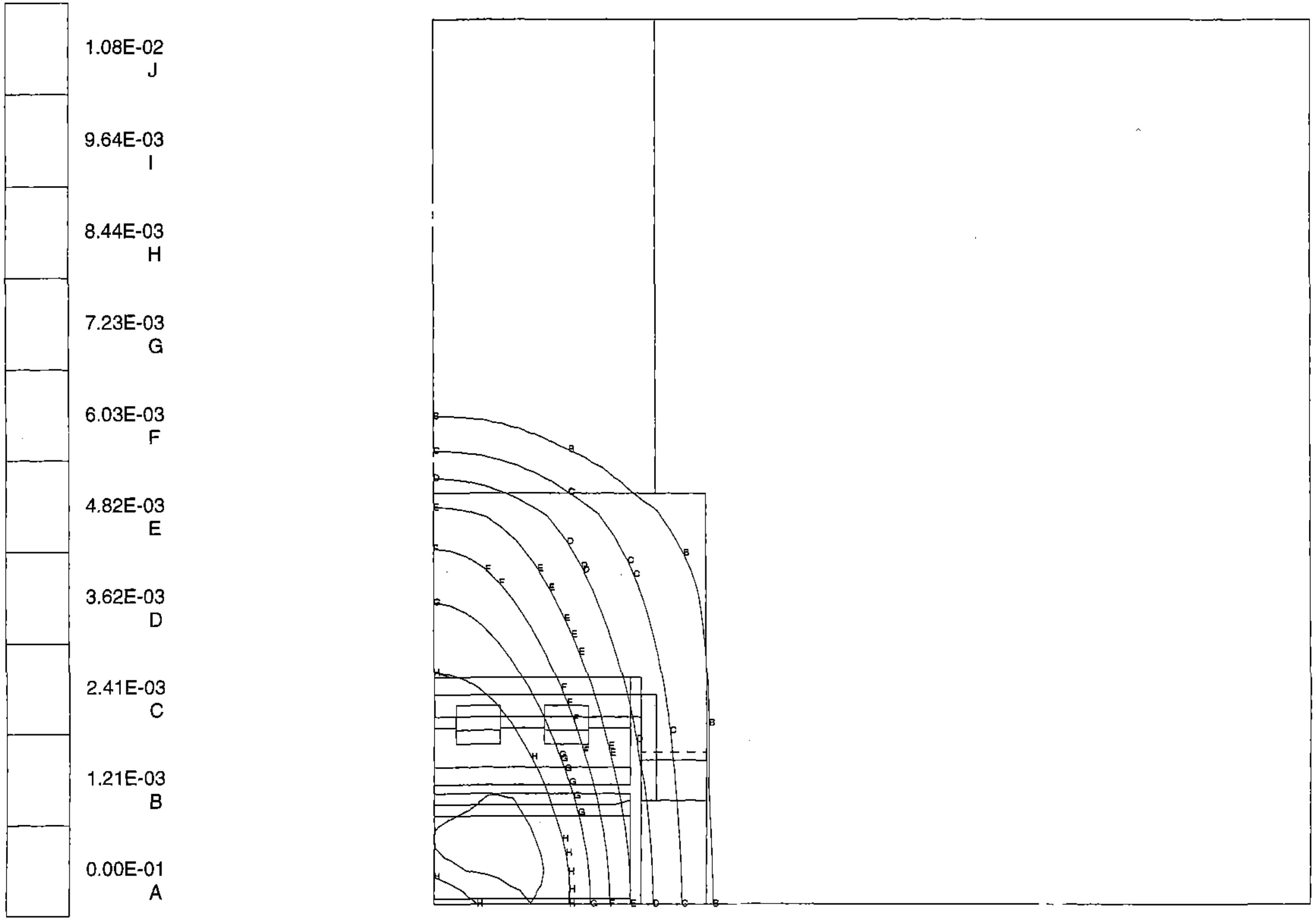

fig. A43, case 49

Hcn Mole Fraction

Lmax = 1.085E-02   Lmin = 0.000E-01

Nov 19 1998

Fluent 4.47

Fluent Inc.

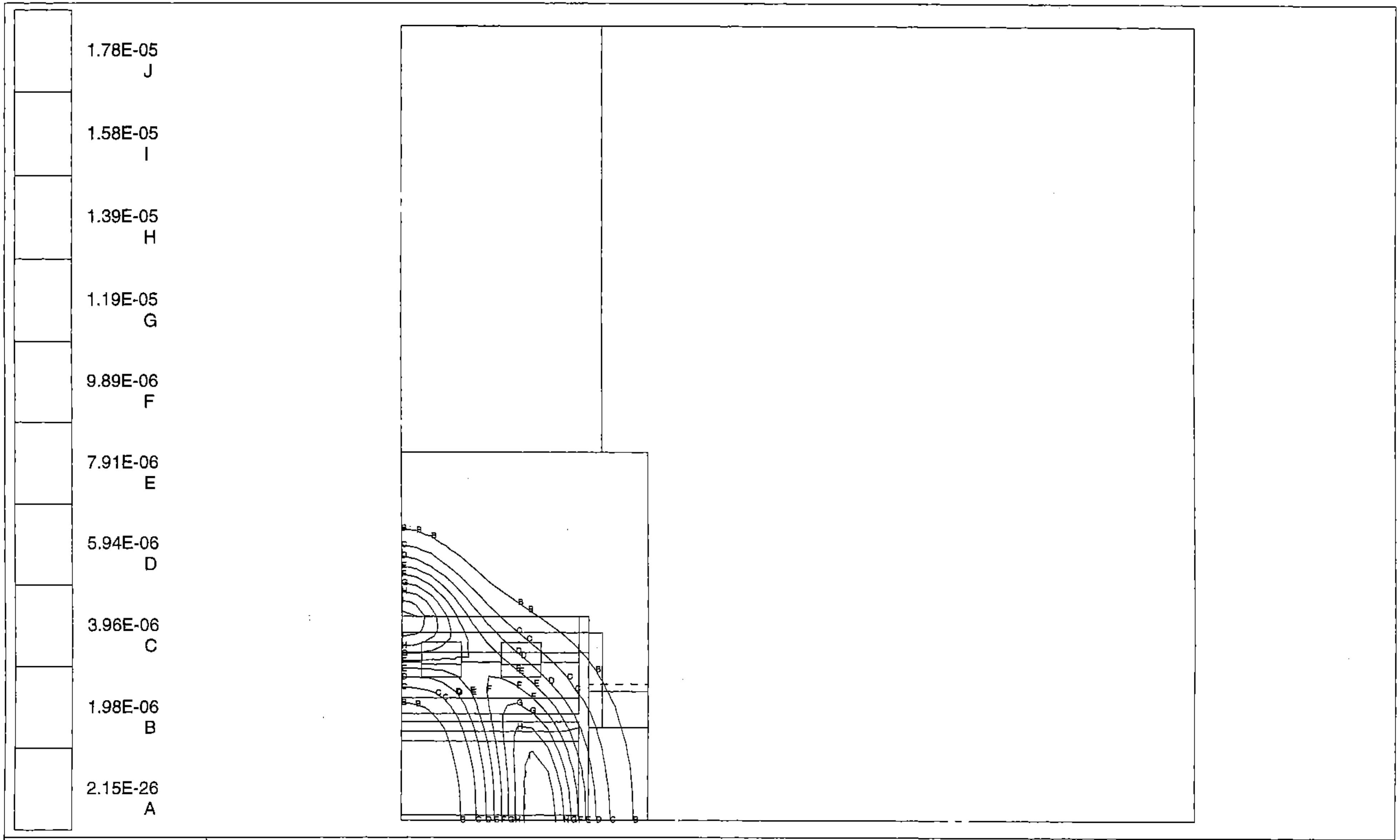

fig. A44, case 49
Nh3 Mole Fraction
Lmax = 1.781E-05   Lmin = 2.150E-26

Nov 19 1998
Fluent 4.47
Fluent Inc.

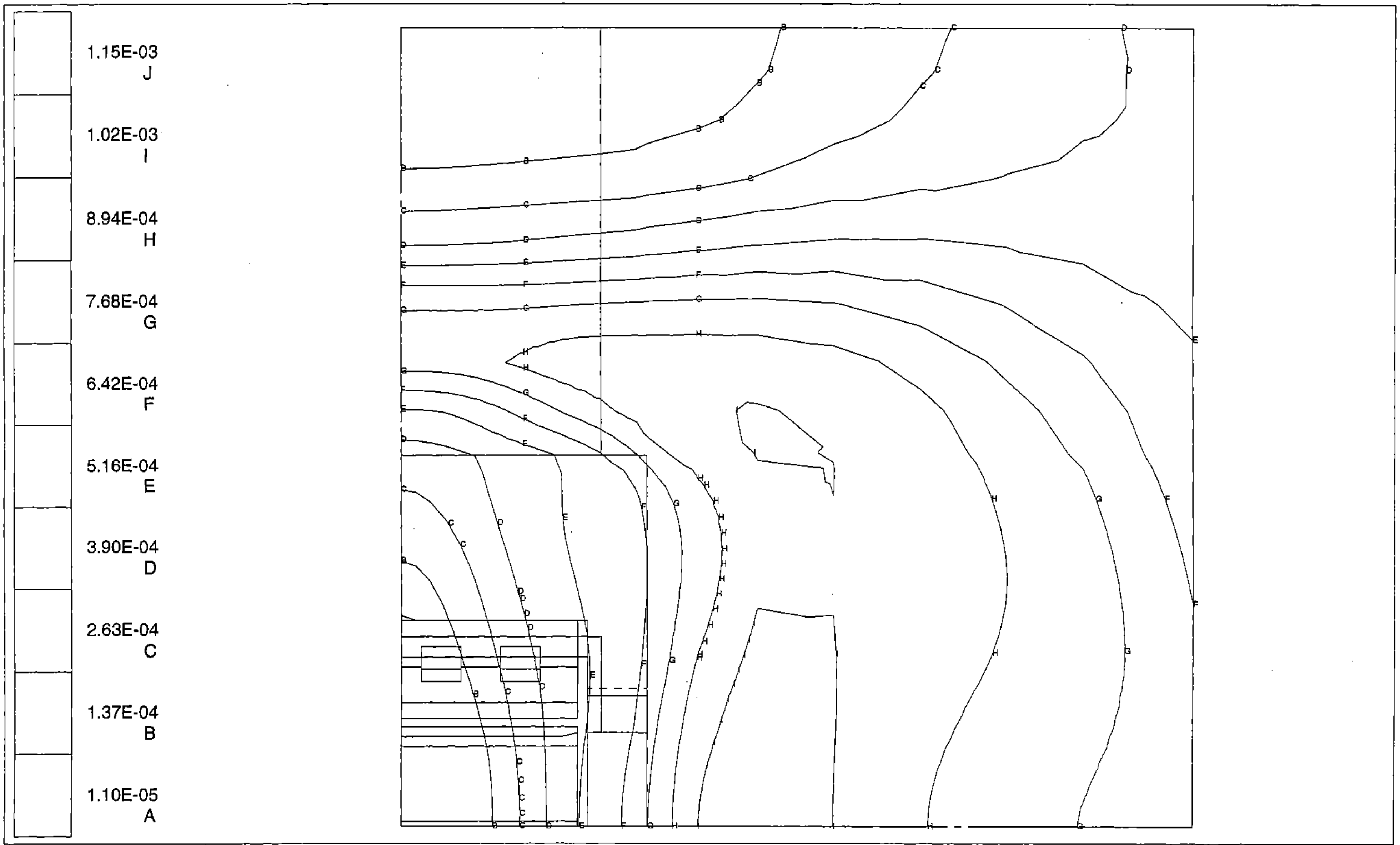

fig. A45, case 49

No Mole Fraction

Lmax = 1.147E-03   Lmin = 1.096E-05

Nov 19 1998

Fluent 4.47

Fluent Inc.

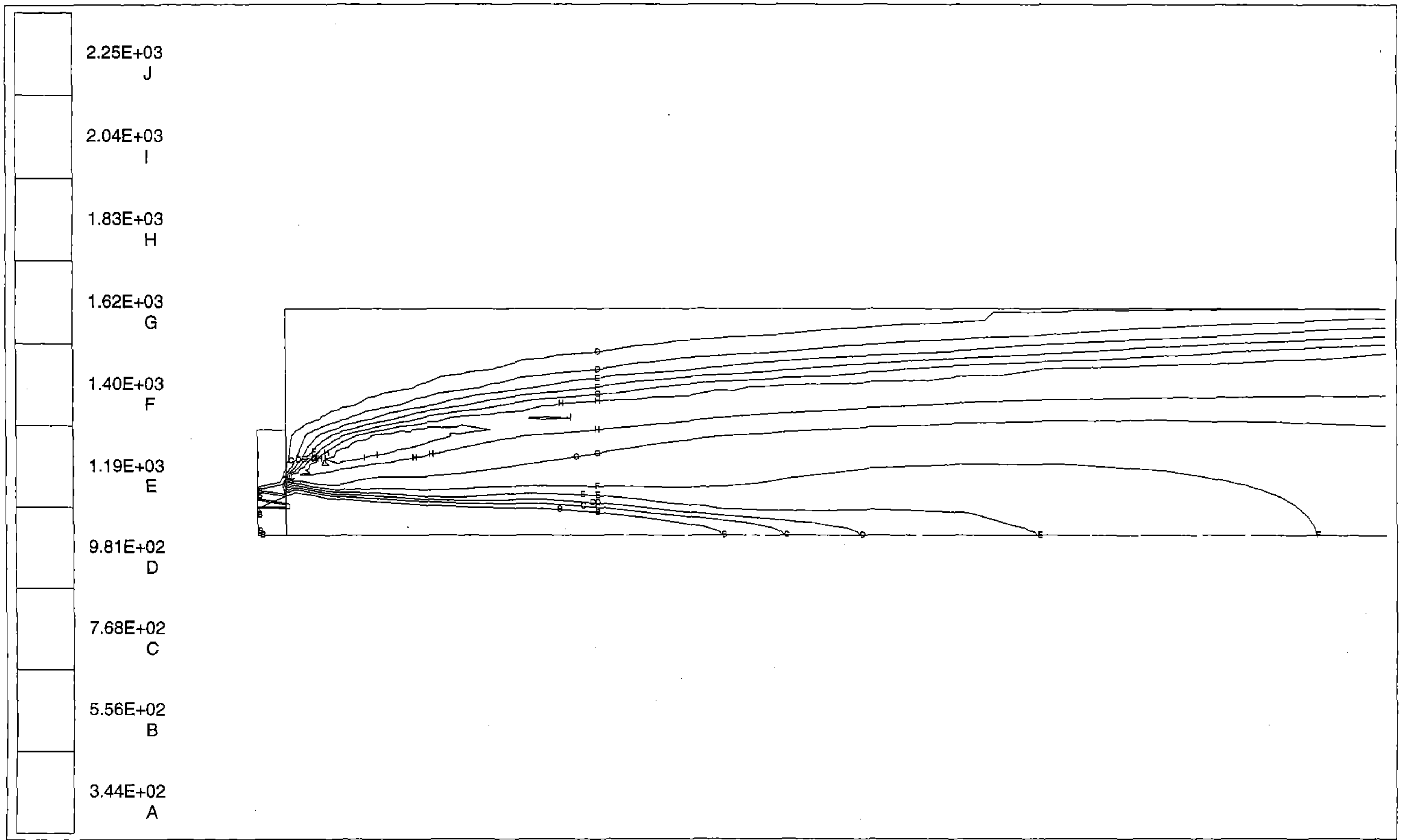

fig. A46, case 44

Temperature (K)

Lmax = 2.254E+03 Lmin = 3.440E+02

Nov 19 1998

Fluent 4.47

Fluent Inc.

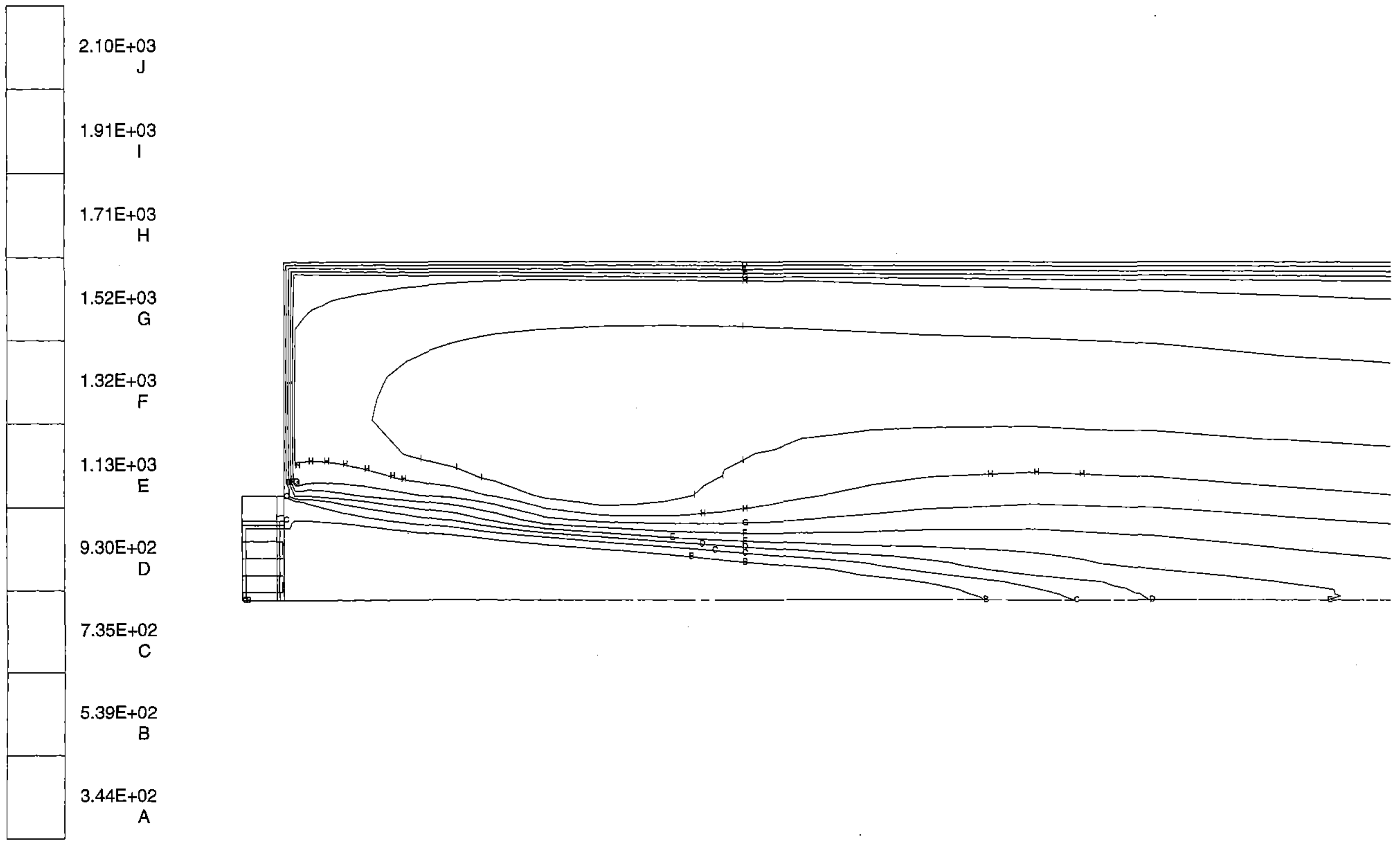

fig. A47, case 44
Temperature (K)
Lmax = 2.102E+03 Lmin = 3.442E+02

Nov 19 1998
Fluent 4.47
Fluent Inc.

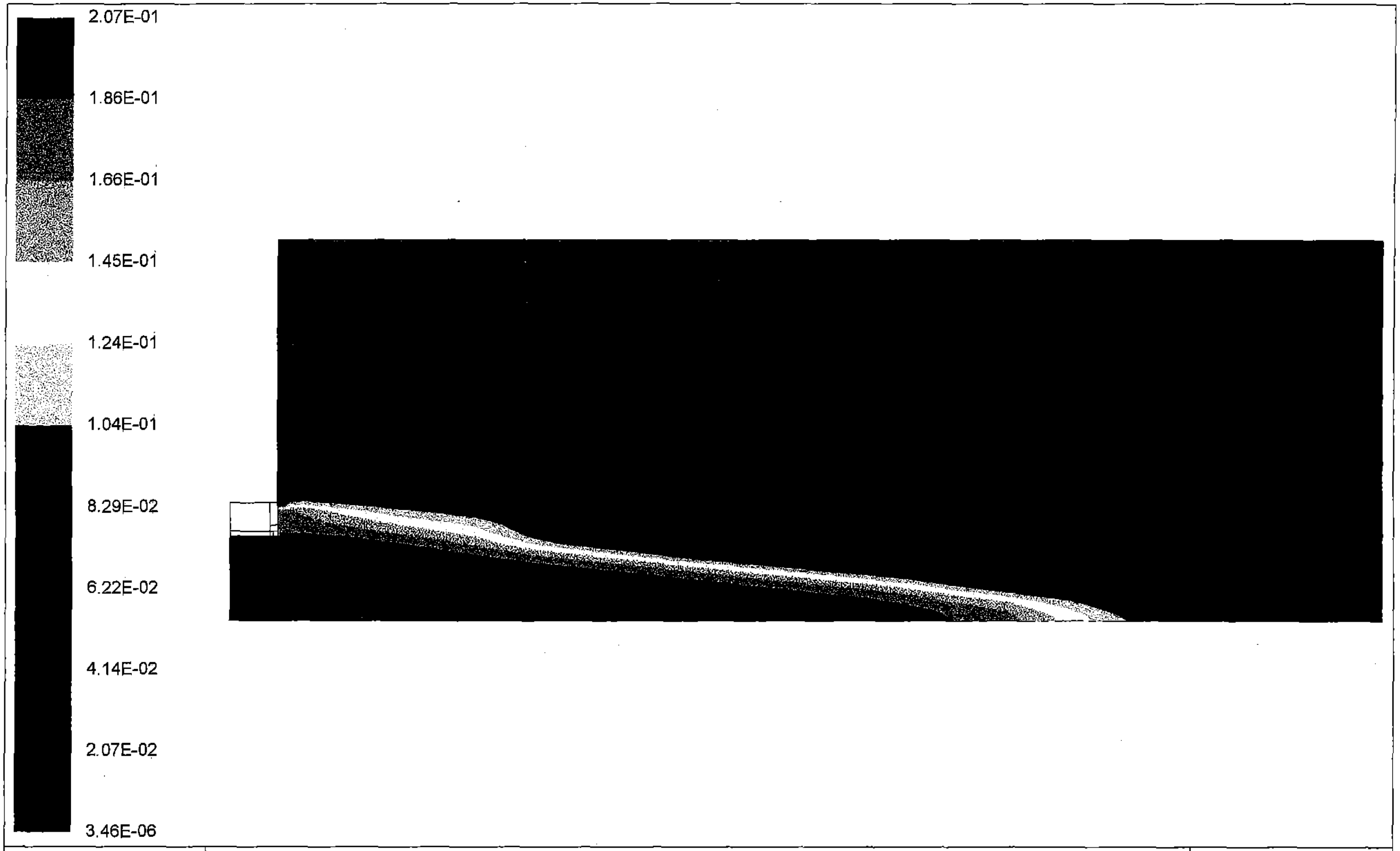

fig. A48, case 44
O2 Mole Fraction
Lmax = 2.072E-01   Lmin = 3.464E-06

Nov 26 1998
Fluent 4.47
Fluent Inc.

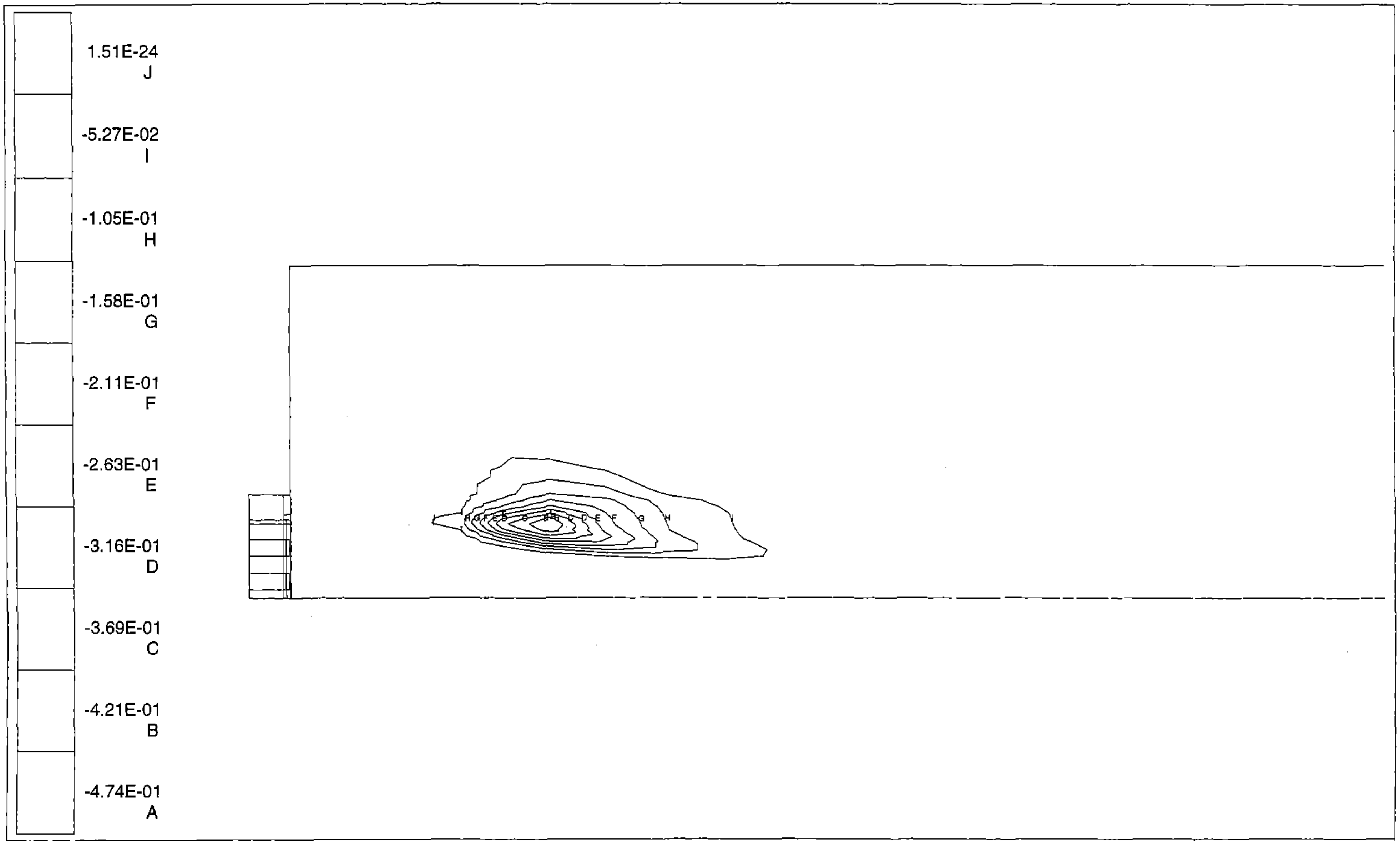

fig. A49, case 44

Ch4 Reaction Rate (Kg/M3/S)

Lmax = 1.510E-24 Lmin = -4.741E-01

Nov 19 1998
Fluent 4.47
Fluent Inc.

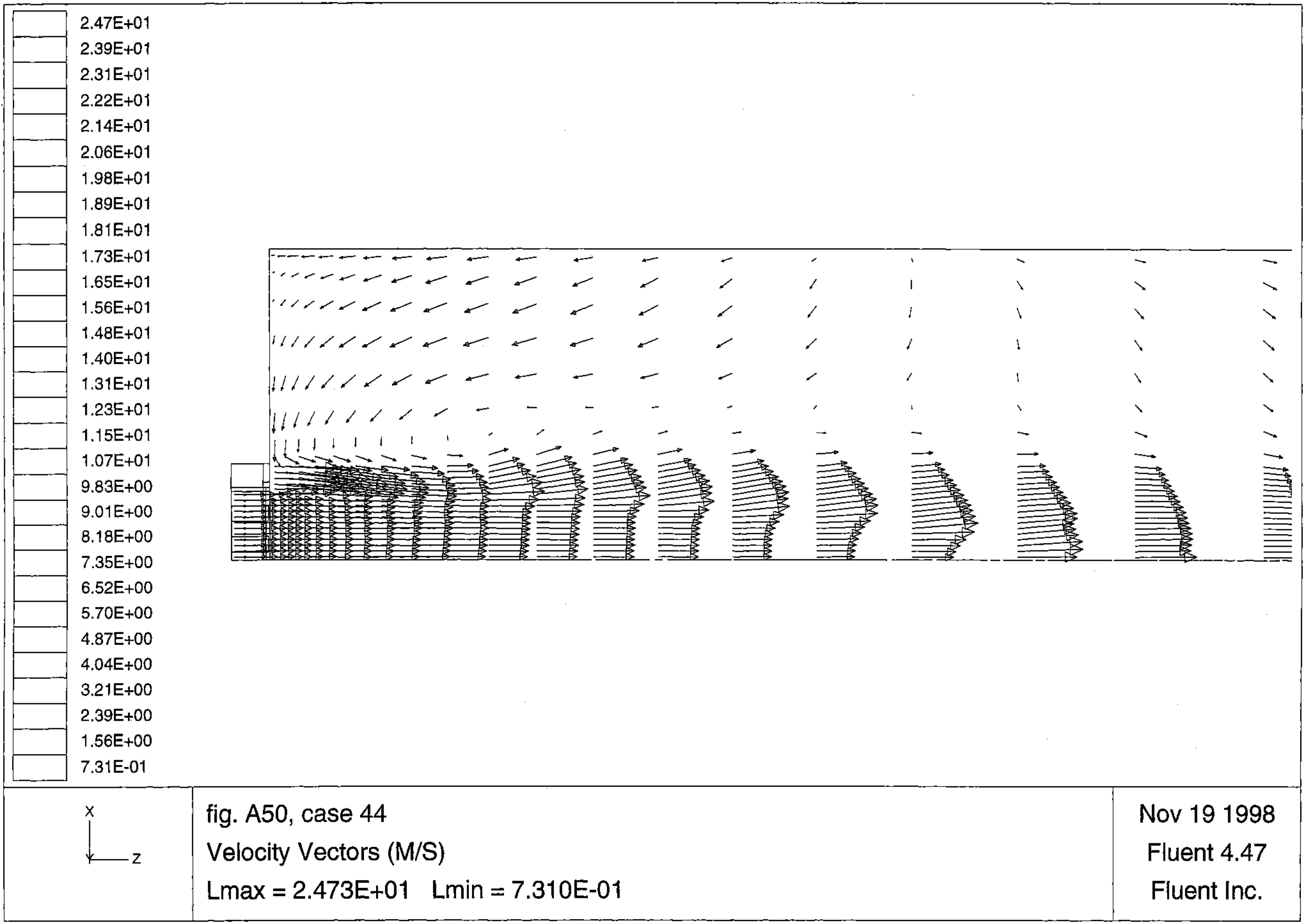

fig. A50, case 44

Velocity Vectors (M/S)

Lmax = 2.473E+01 Lmin = 7.310E-01

Nov 19 1998

Fluent 4.47

Fluent Inc.

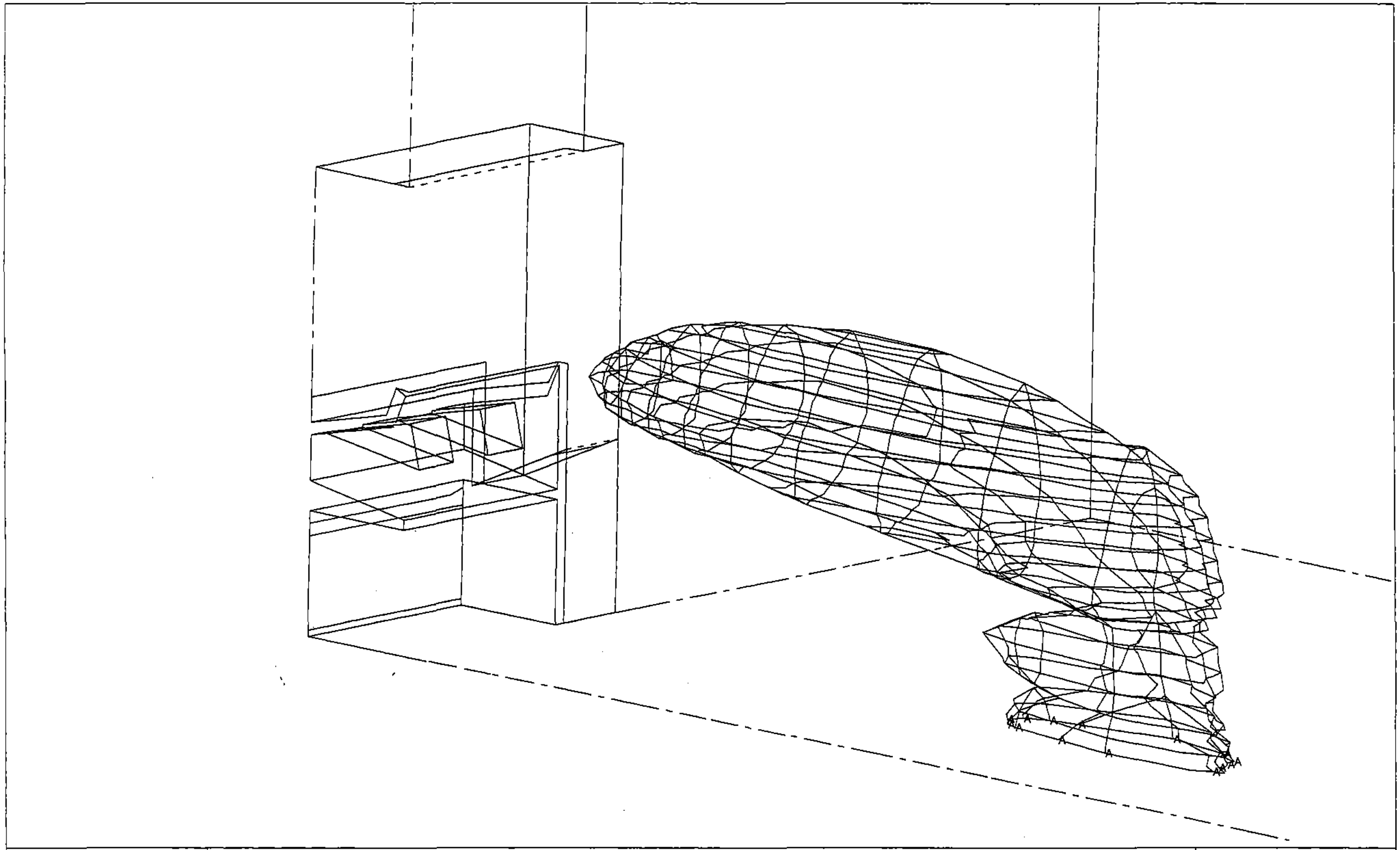

fig. A51, case 44

Surface Of Constant Ch4 Reaction Rate (Kg/M3/S)

Value = -3.000E-01

Sep 01 1996

Fluent 4.32

Fluent Inc.

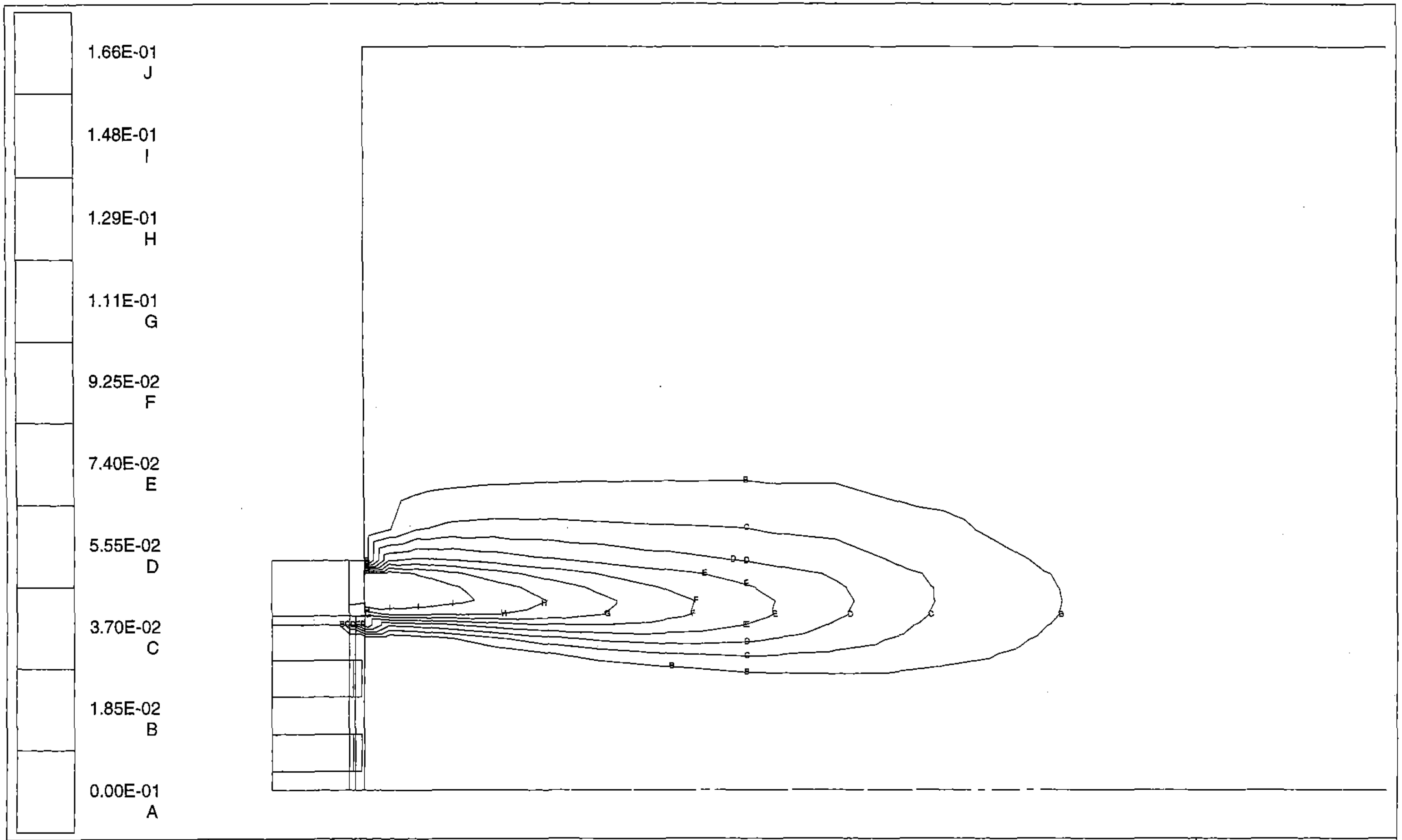

fig. A52, case 44

Ch4 Mole Fraction

Lmax = 1.665E-01 Lmin = 0.000E-01

Nov 19 1998

Fluent 4.47

Fluent Inc.

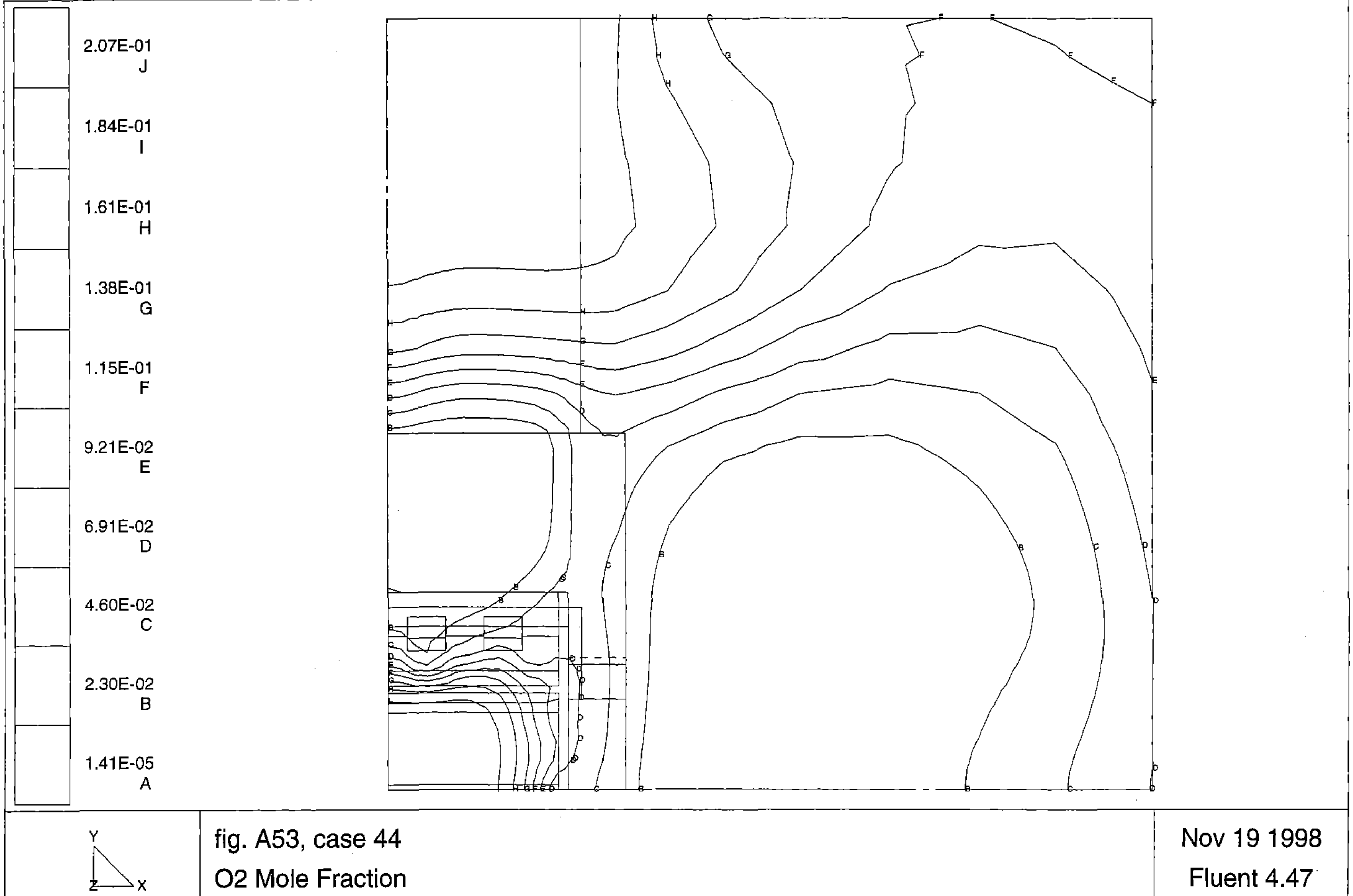

fig. A53, case 44

O2 Mole Fraction

Lmax = 2.072E-01 Lmin = 1.411E-05

Nov 19 1998

Fluent 4.47

Fluent Inc.

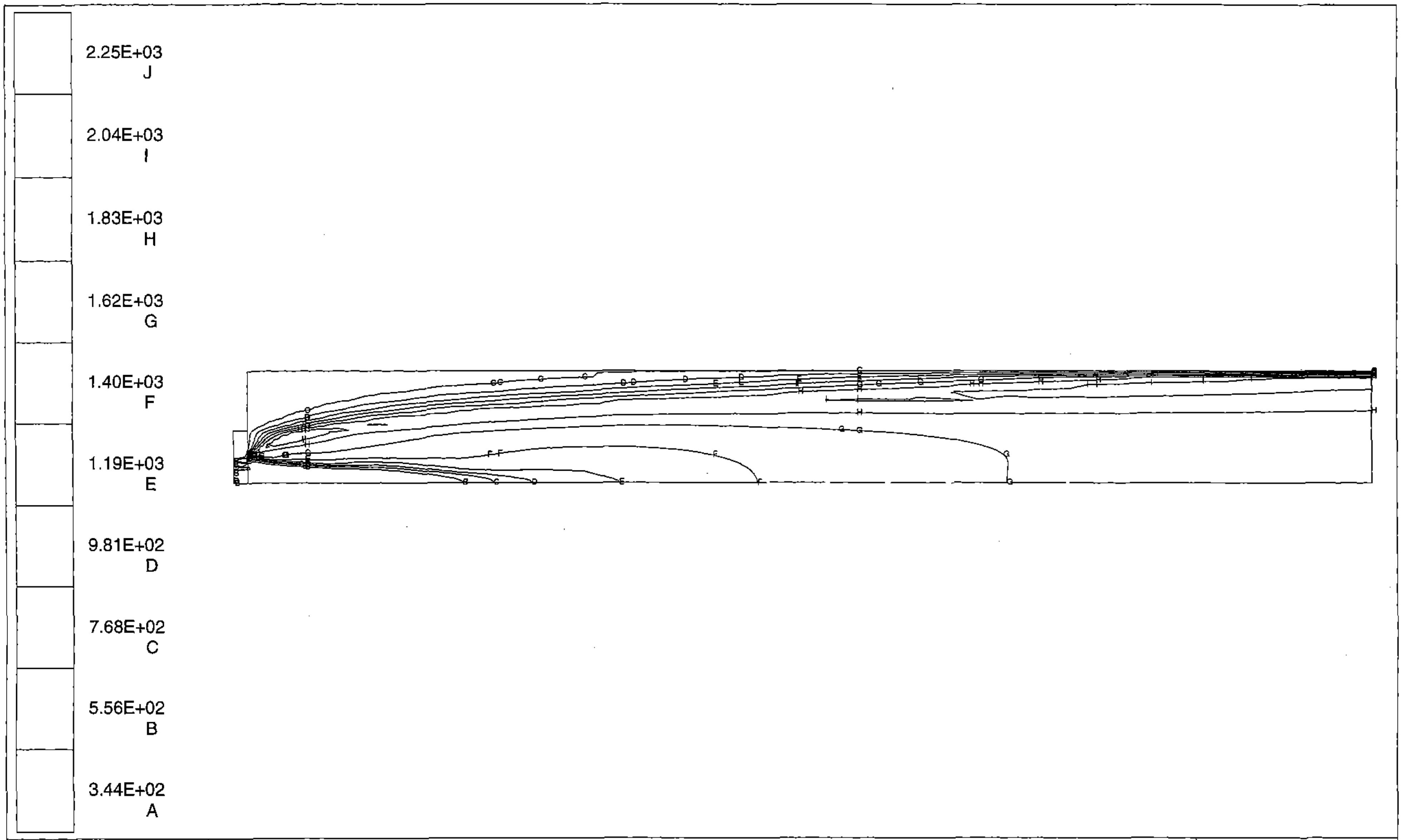

fig. A53b, case 44

Temperature (K)

Lmax = 2.254E+03   Lmin = 3.440E+02

Nov 19 1998

Fluent 4.47

Fluent Inc.

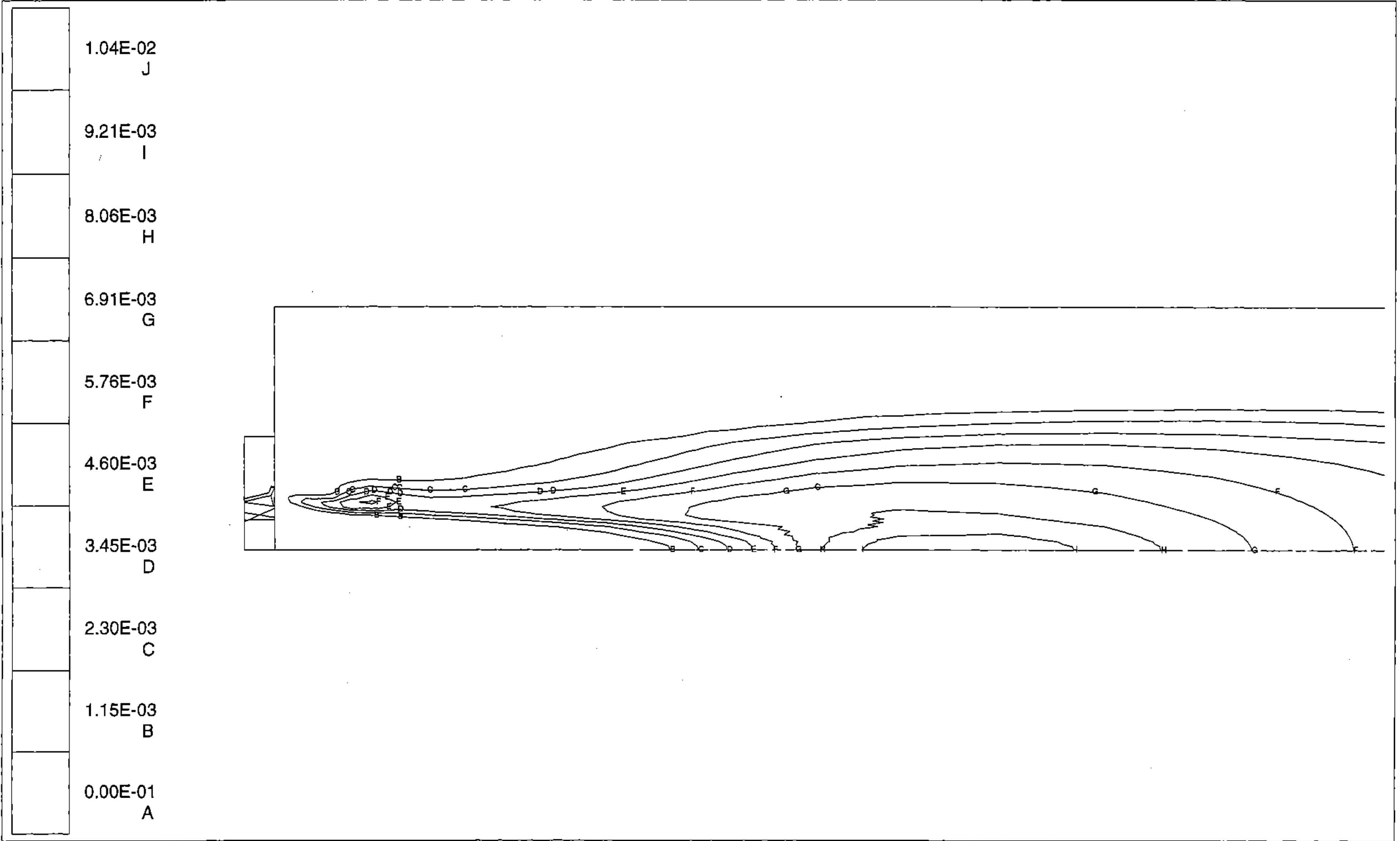

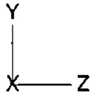

fig. A54, case 44

Hcn Mole Fraction

Lmax = 1.036E-02   Lmin = 0.000E-01

Nov 19 1998

Fluent 4.47

Fluent Inc.

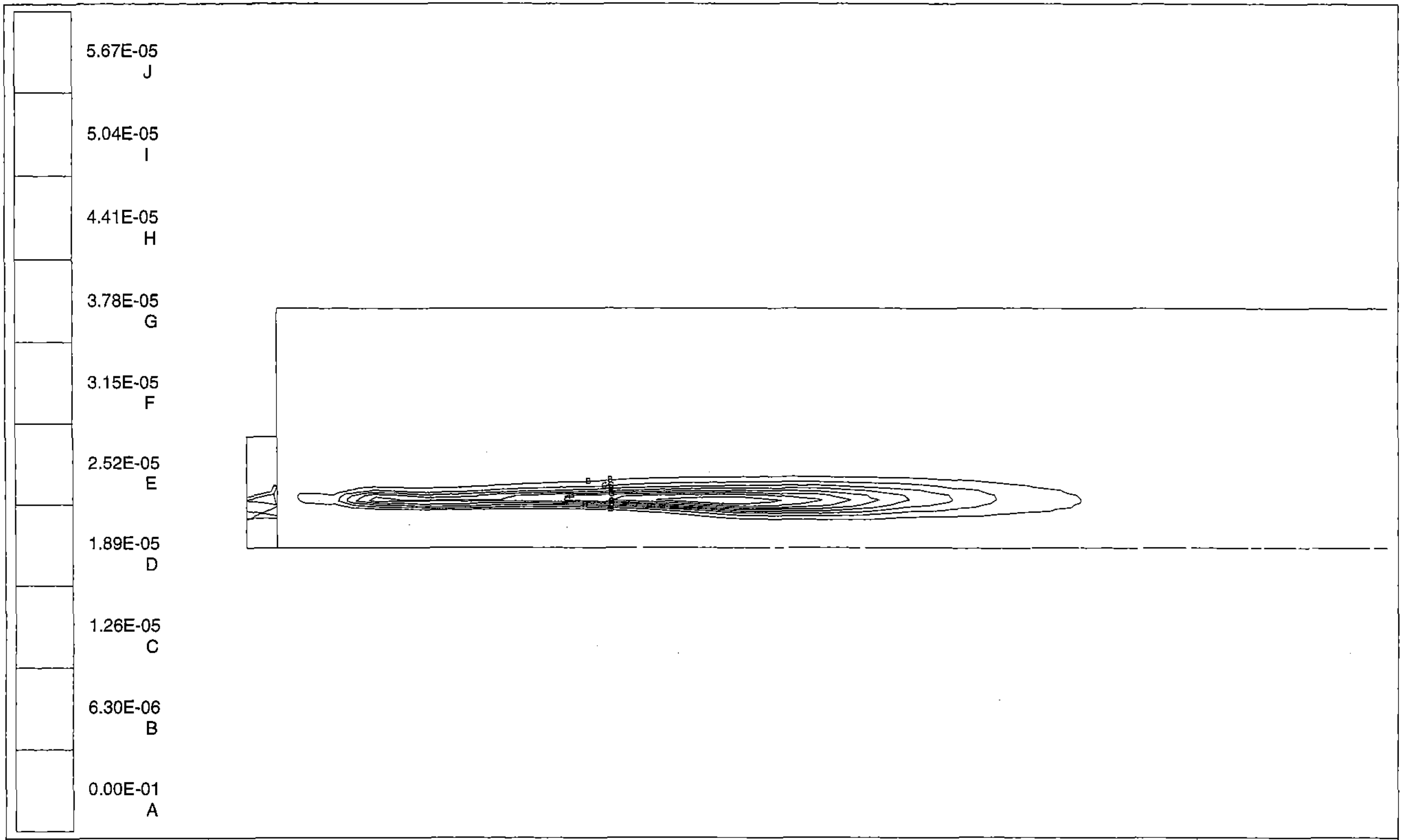

fig. A55, case 44
Nh3 Mole Fraction
Lmax = 5.672E-05   Lmin = 0.000E-01

Nov 19 1998
Fluent 4.47
Fluent Inc.

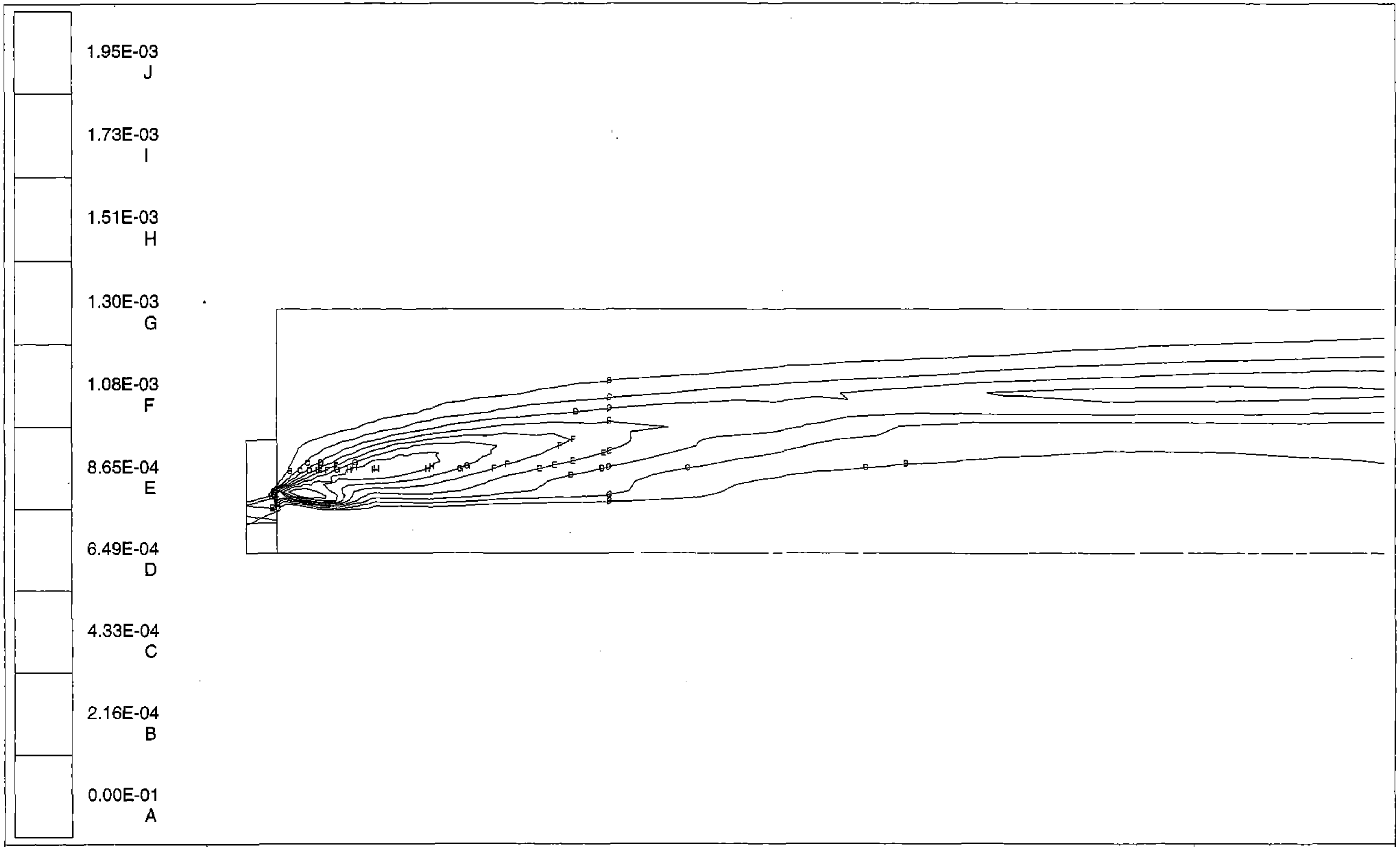

fig. A56, case 44

No Mole Fraction

Lmax = 1.946E-03 Lmin = 0.000E-01

Nov 19 1998

Fluent 4.47

Fluent Inc.

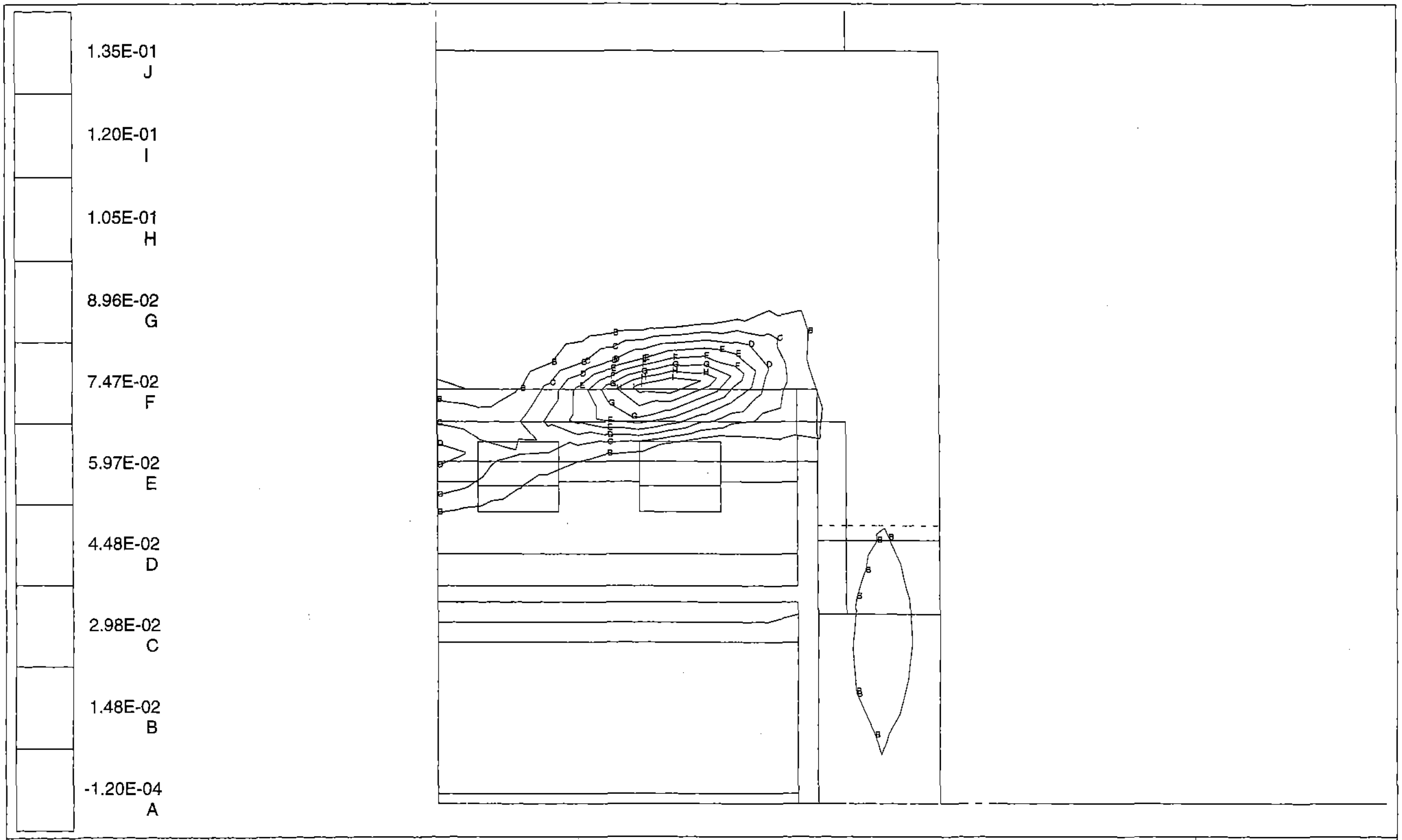

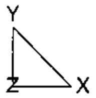

fig. A57, case 44

No Reaction Rate (Kg/M3/S)

Lmax = 1.345E-01 Lmin = -1.199E-04

Nov 19 1998

Fluent 4.47

Fluent Inc.

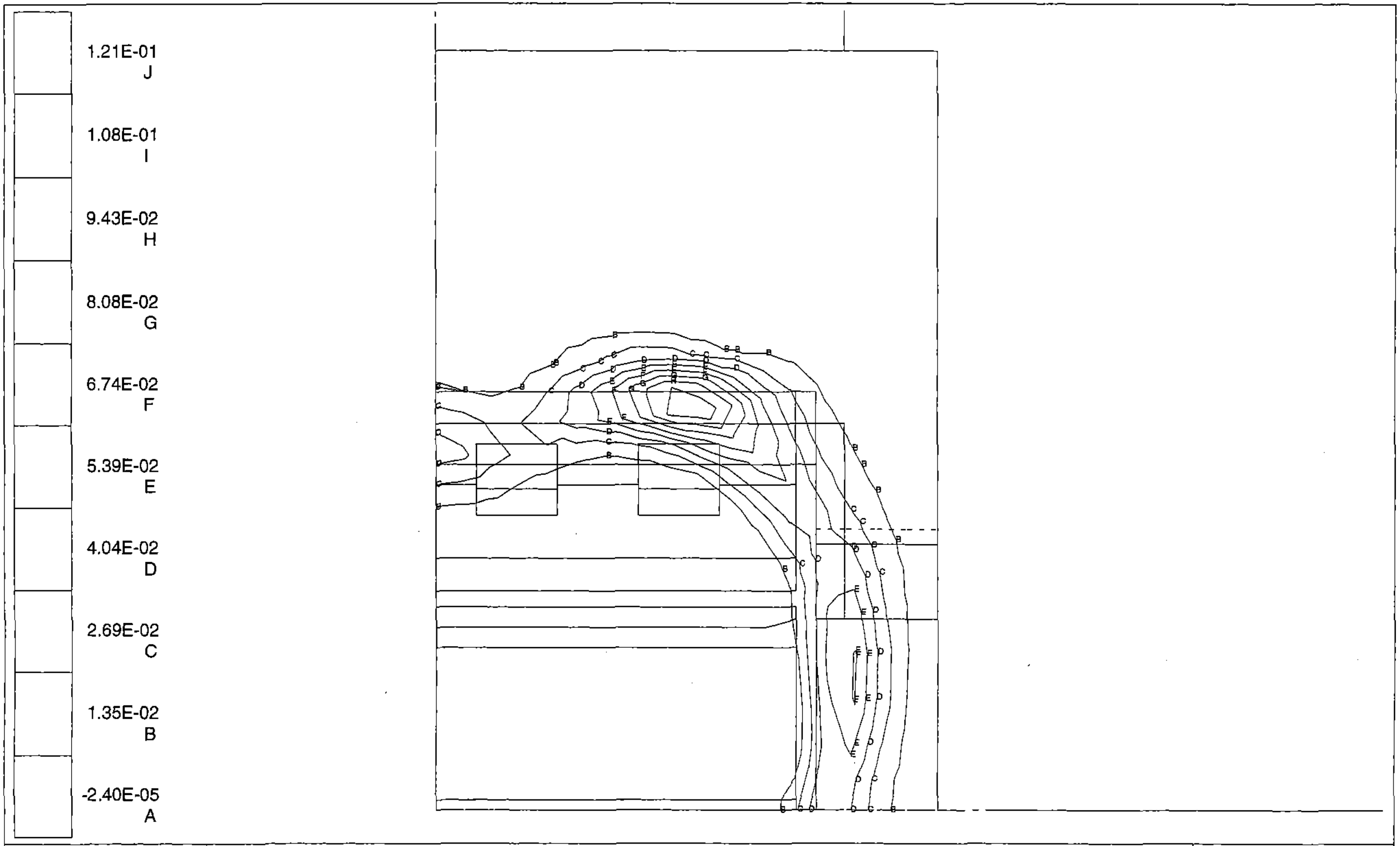

fig. A58, case 44
No Reaction Rate (Kg/M3/S)
Lmax = 1.213E-01 Lmin = -2.402E-05

Nov 19 1998
Fluent 4.47
Fluent Inc.

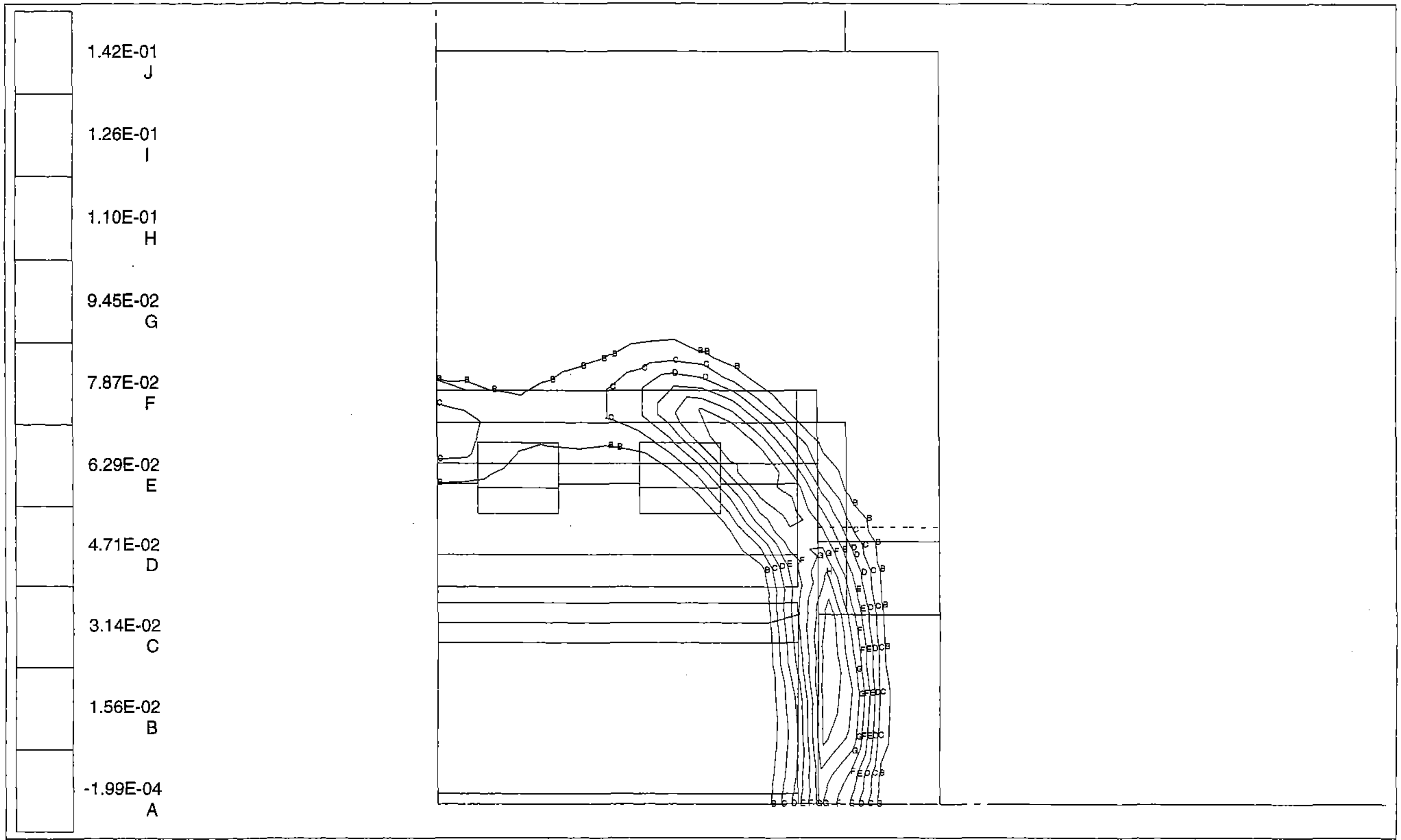

Y
Z X

fig. A59, case 44

No Reaction Rate (Kg/M3/S)

Lmax = 1.418E-01 Lmin = -1.992E-04

Nov 19 1998

Fluent 4.47

Fluent Inc.

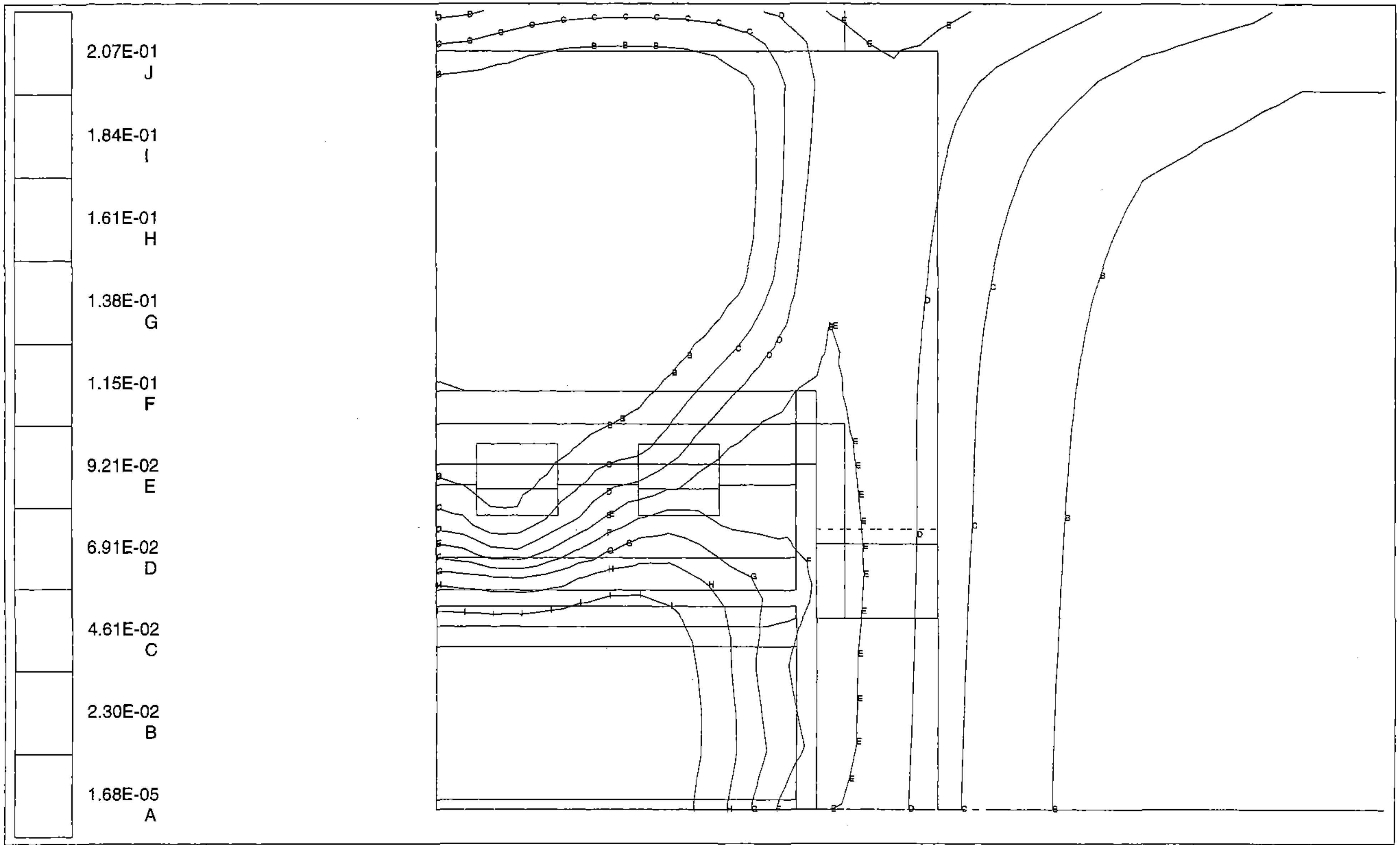

fig. A60, case 44
O2 Mole Fraction
Lmax = 2.072E-01   Lmin = 1.683E-05

Nov 19 1998
Fluent 4.47
Fluent Inc.

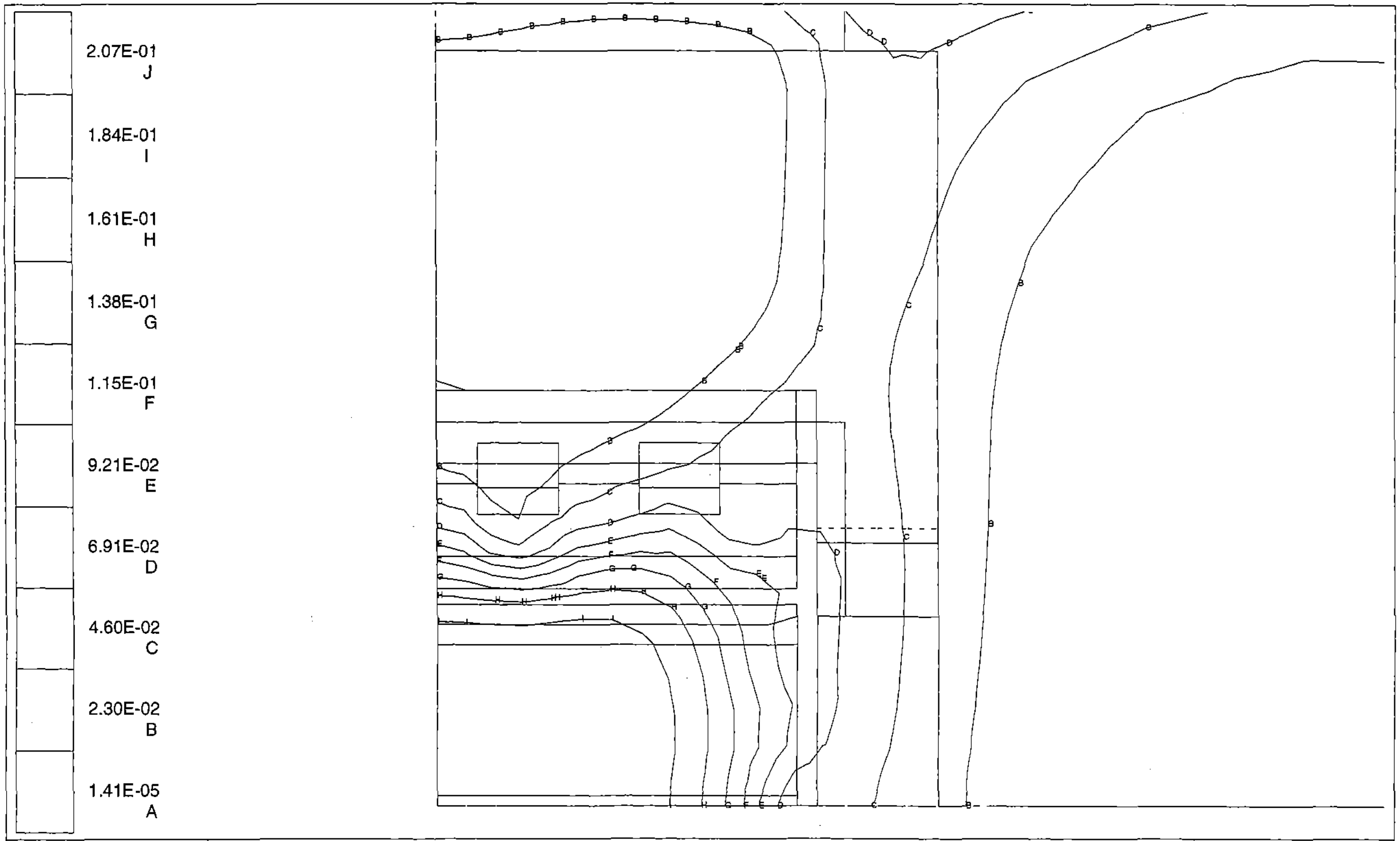

fig. A61, case 44

O2 Mole Fraction

Lmax = 2.072E-01 Lmin = 1.411E-05

Nov 19 1998

Fluent 4.47

Fluent Inc.

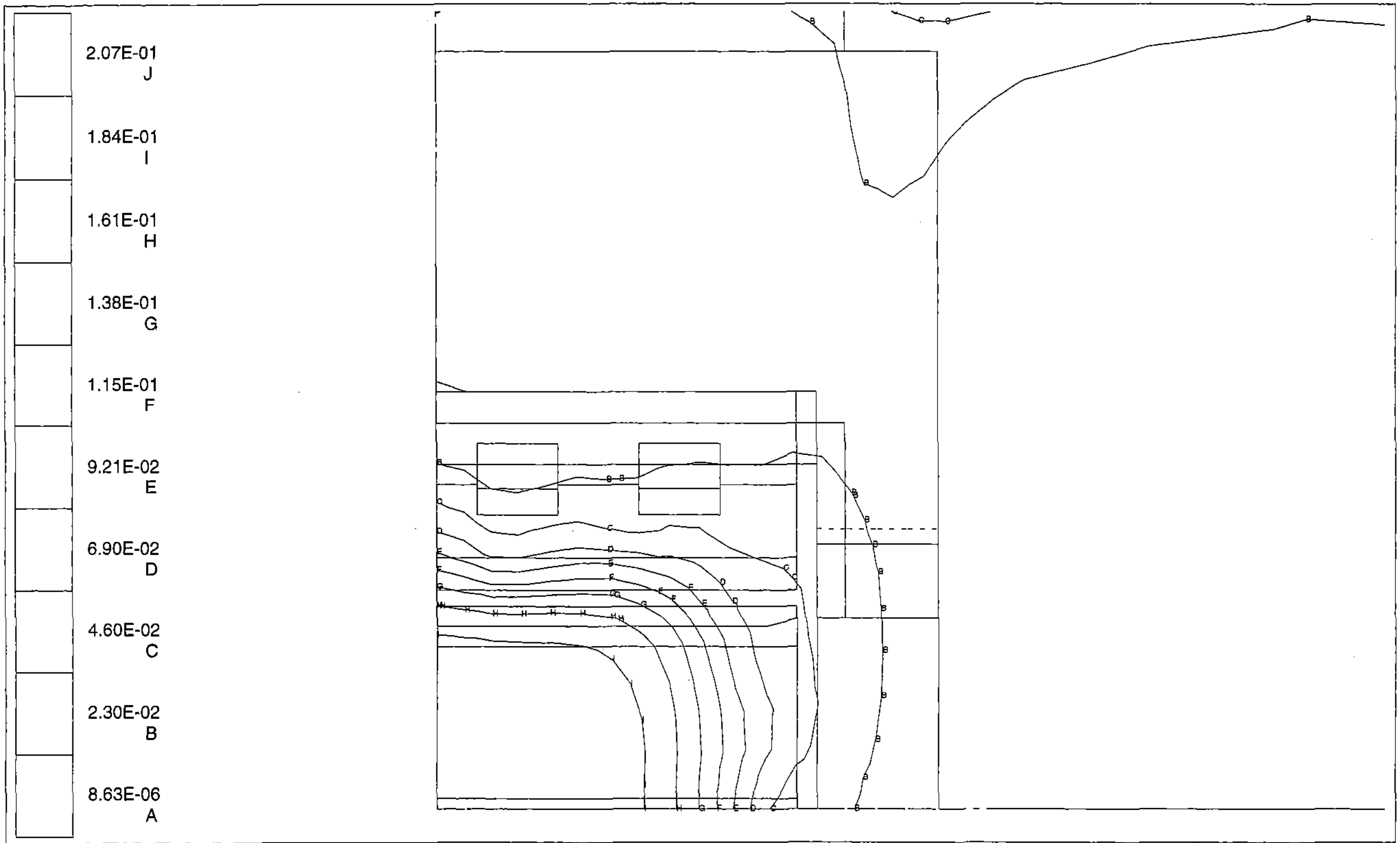

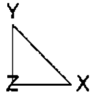

fig. A62, case 44

O2 Mole Fraction

Lmax = 2.071E-01 Lmin = 8.626E-06

Nov 19 1998

Fluent 4.47

Fluent Inc.

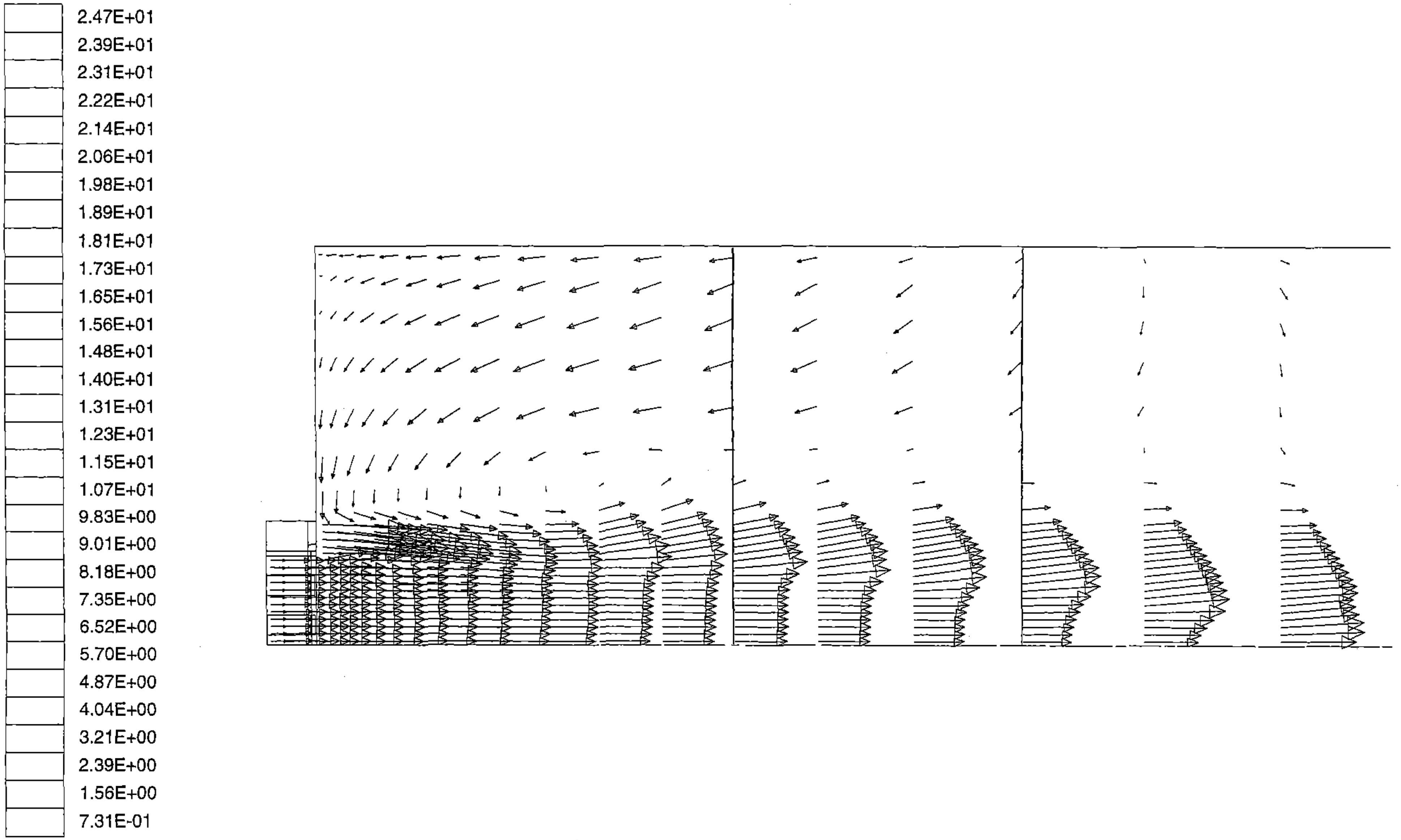

fig. A63, case 44

Velocity Vectors (M/S)

Lmax = 2.473E+01 Lmin = 7.310E-01

Nov 19 1998

Fluent 4.47

Fluent Inc.

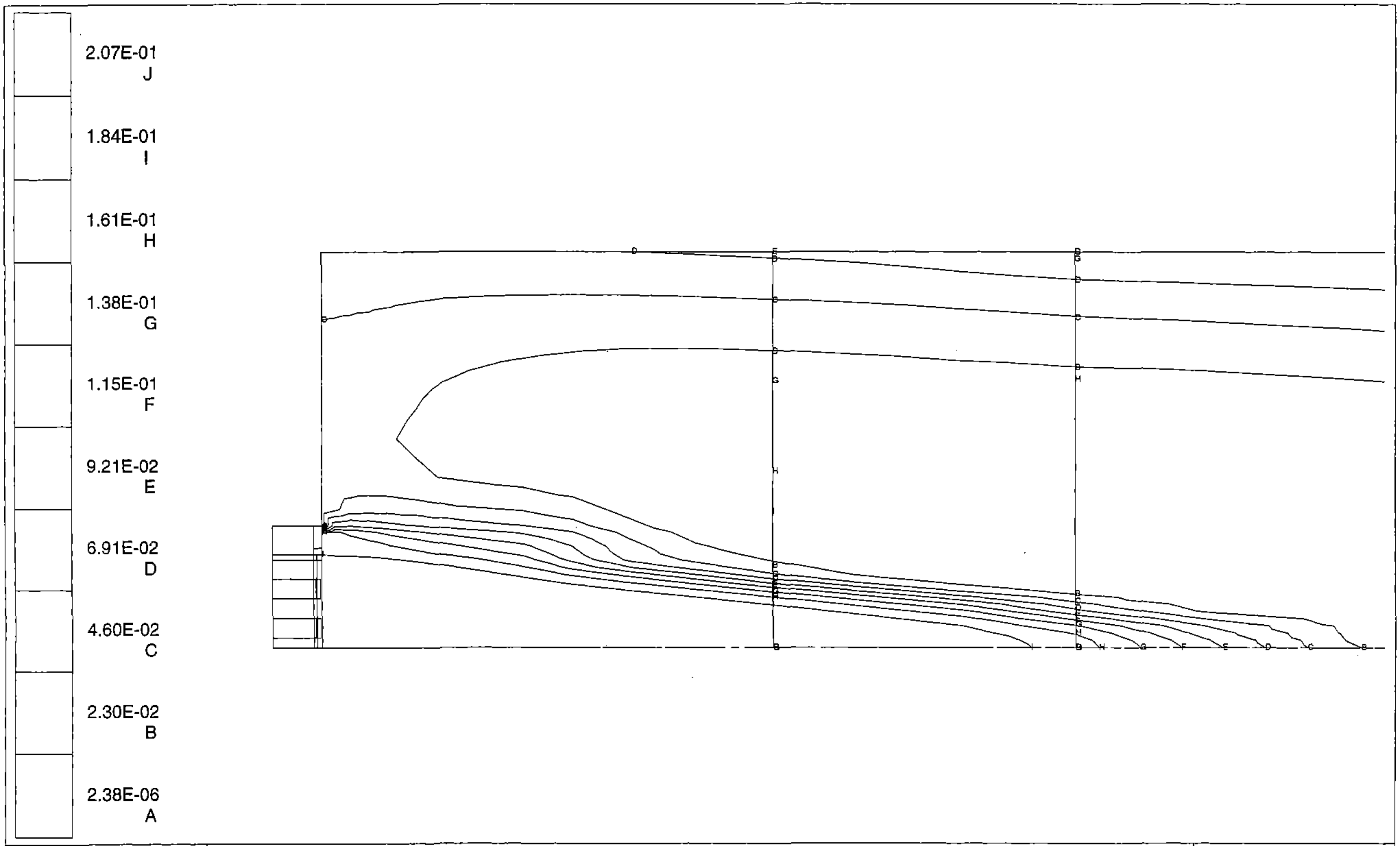

fig. A64, case 44

O2 Mole Fraction

Lmax = 2.072E-01 Lmin = 2.375E-06

Nov 19 1998

Fluent 4.47

Fluent Inc.

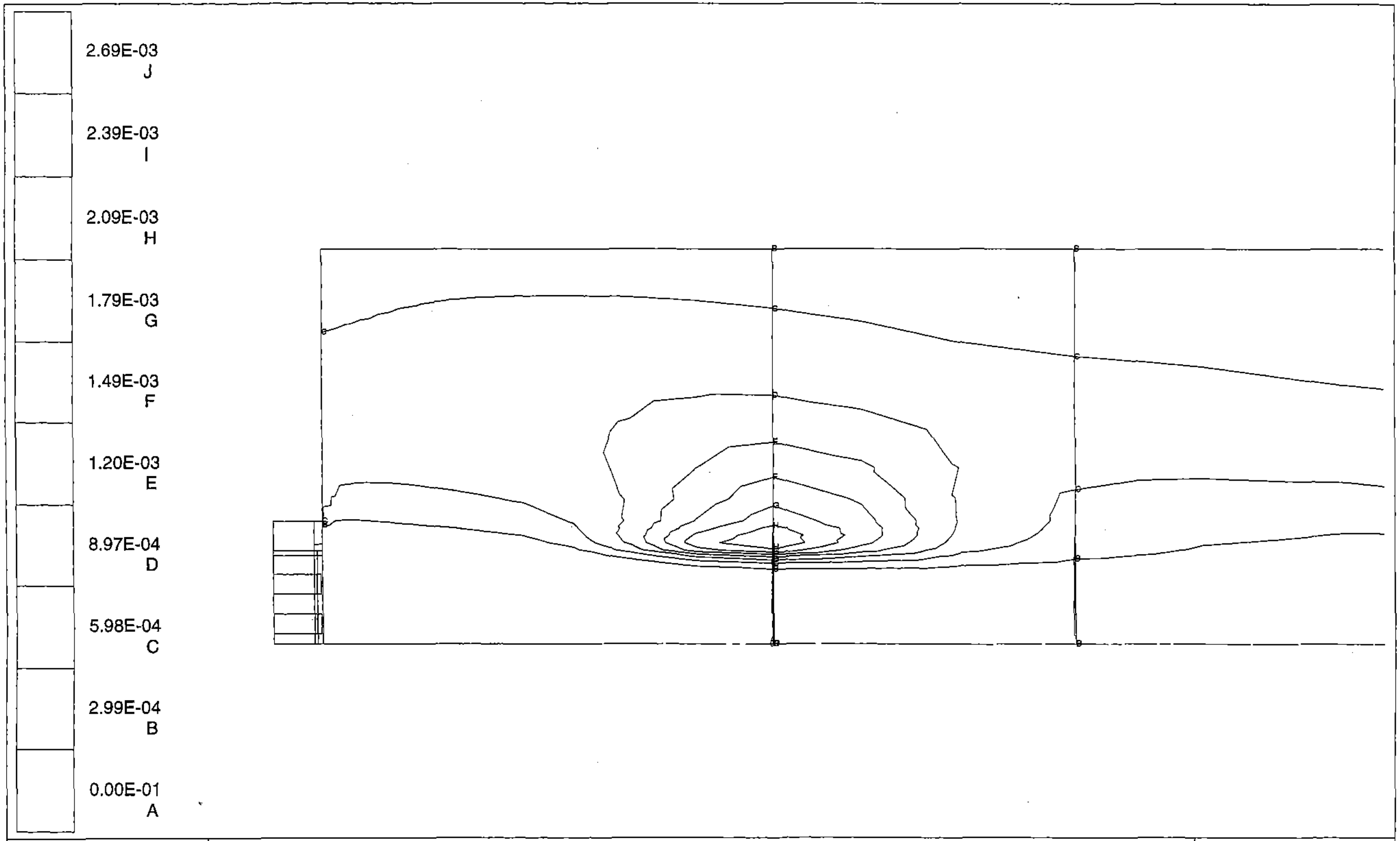

fig. A65, case 44

No Mole Fraction

Lmax = 2.691E-03   Lmin = 0.000E-01

Nov 19 1998
Fluent 4.47
Fluent Inc.

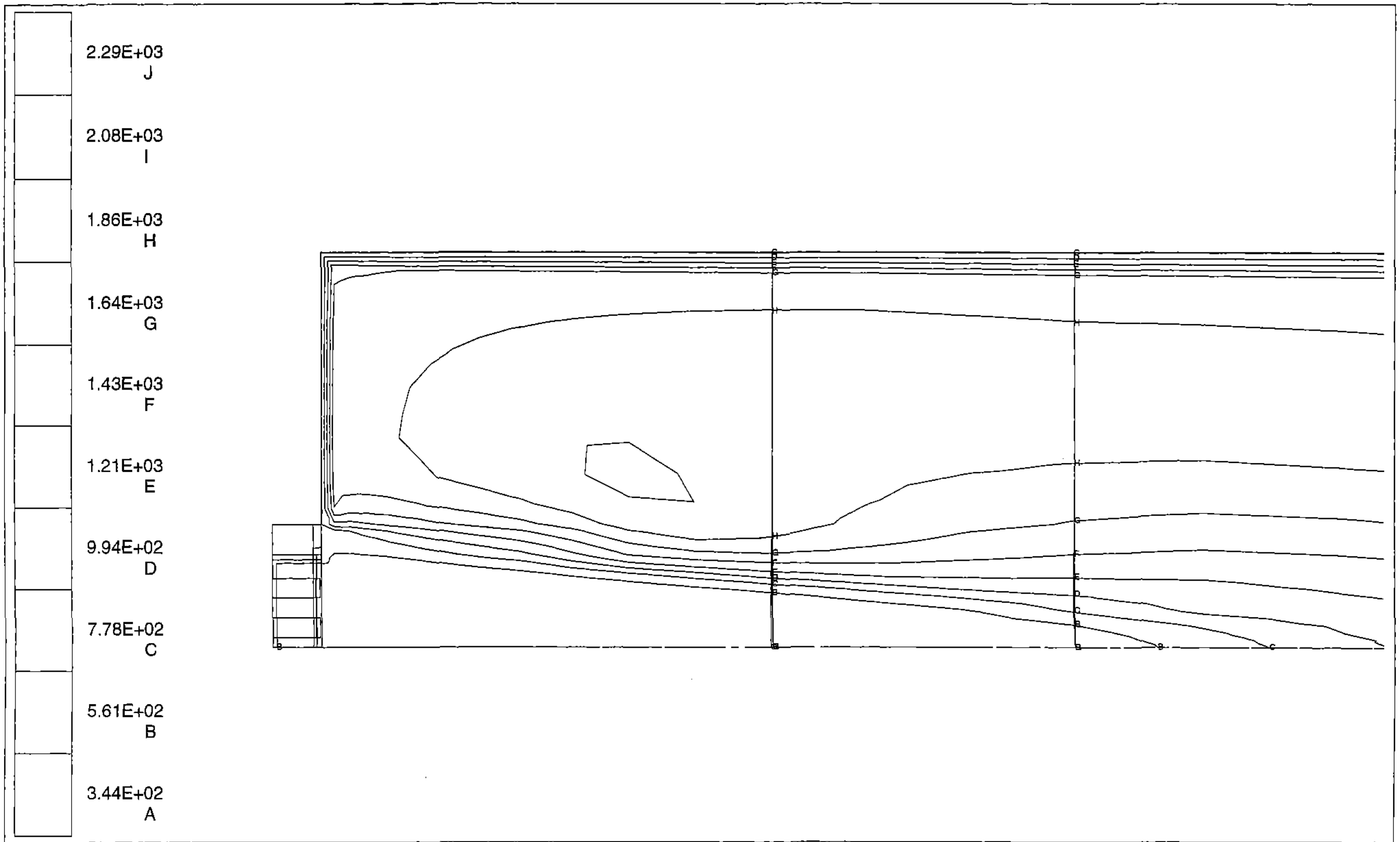

fig. A66, case 44

Temperature (K)

Lmax = 2.294E+03 Lmin = 3.442E+02

Nov 19 1998

Fluent 4.47

Fluent Inc.

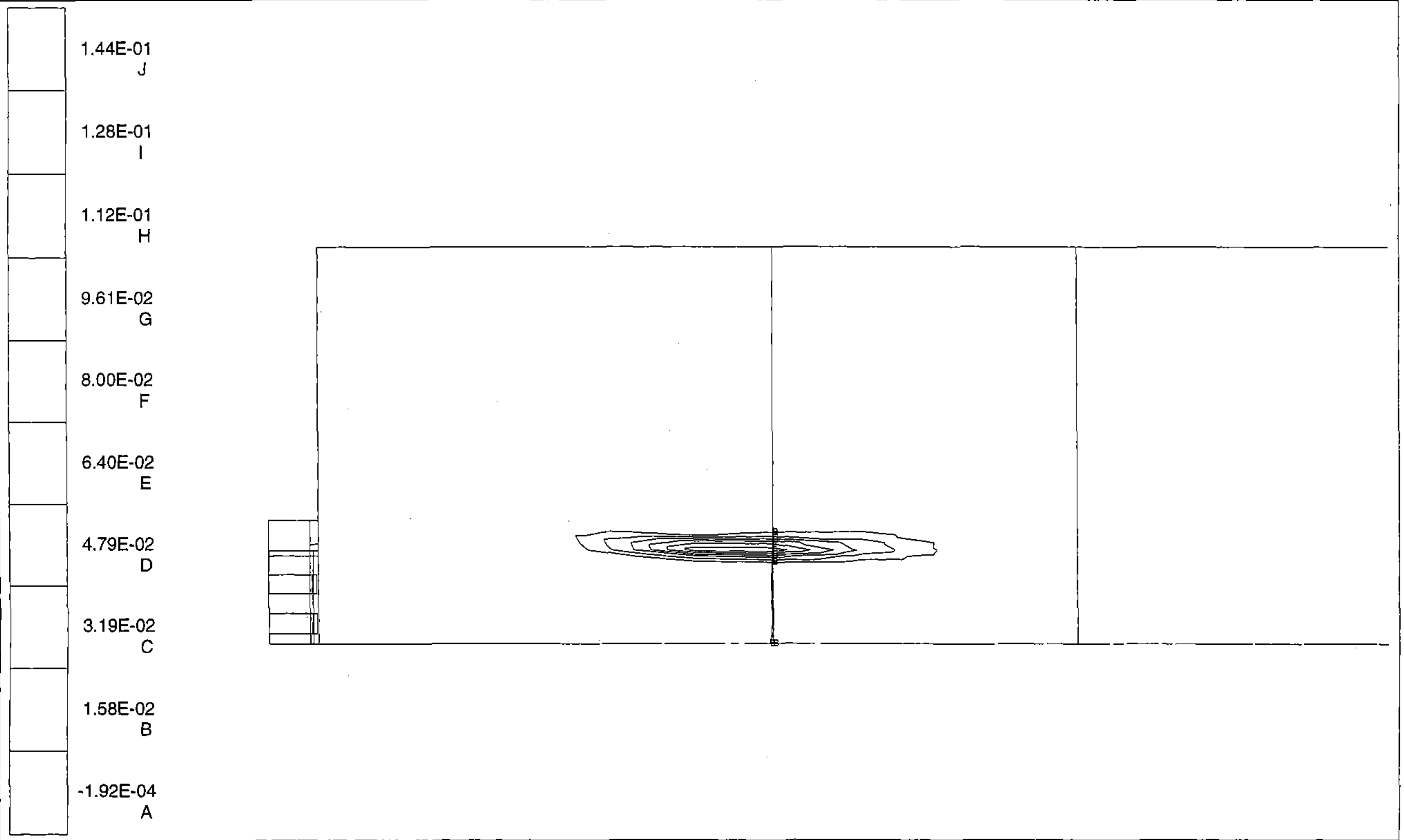

fig. A67, case 44

No Reaction Rate (Kg/M3/S)

Lmax = 1.442E-01 Lmin = -1.922E-04

Nov 19 1998

Fluent 4.47

Fluent Inc.

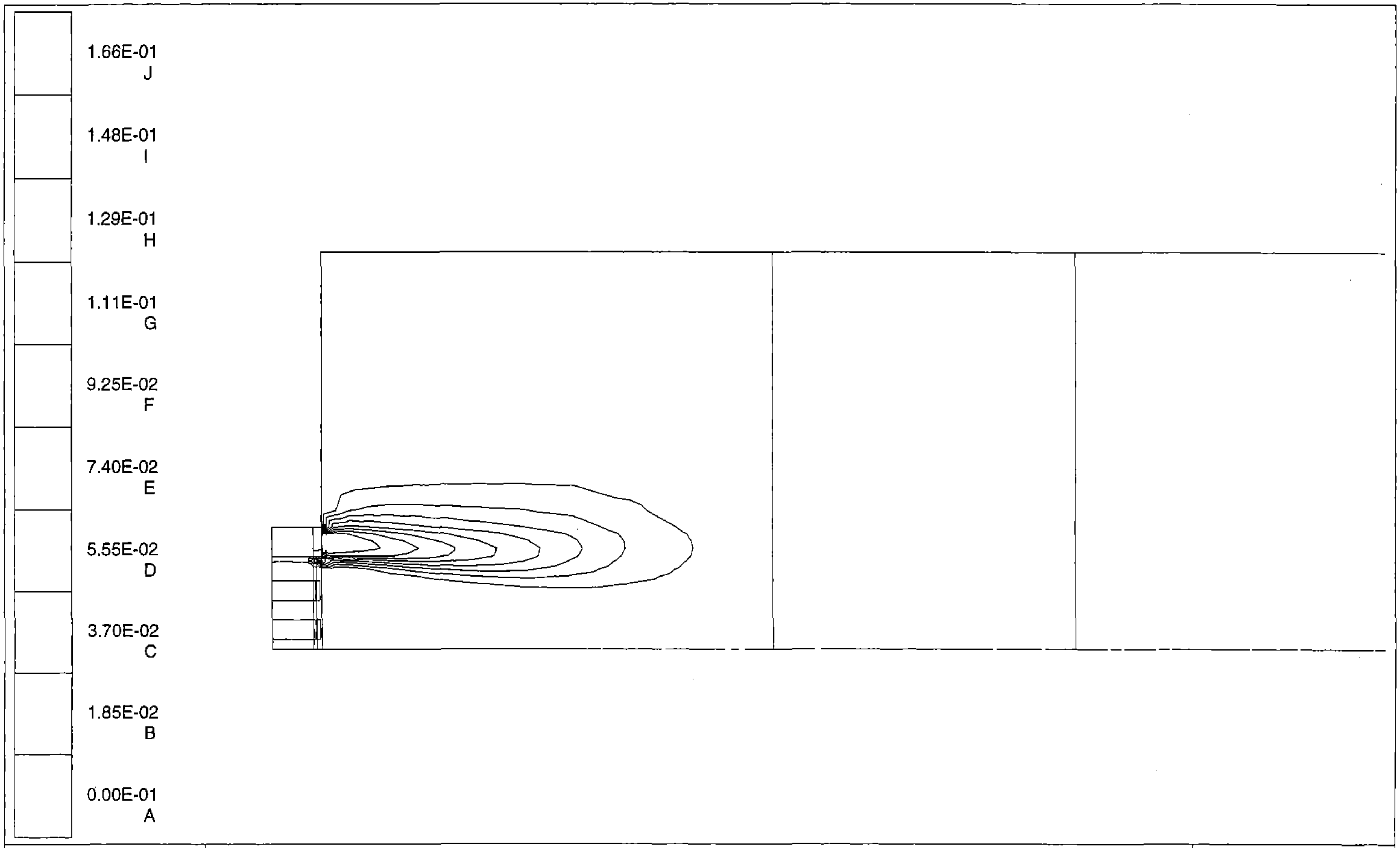

fig. A68, case 44

Ch4 Mole Fraction

Lmax = 1.665E-01   Lmin = 0.000E-01

Nov 19 1998

Fluent 4.47

Fluent Inc.

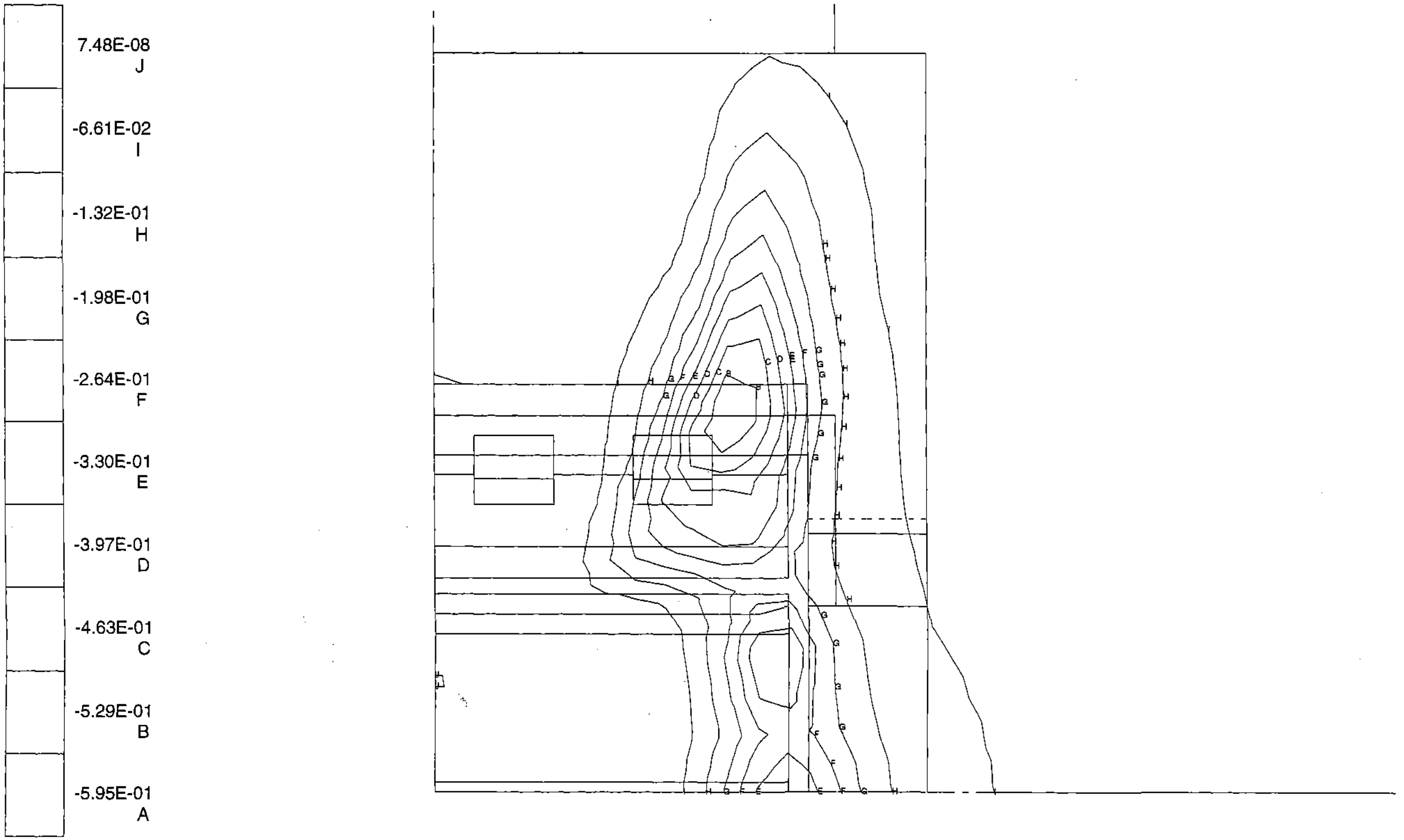

fig. A69, case 44

Ch4 Reaction Rate (Kg/M3/S)

Lmax = 7.485E-08 Lmin = -5.948E-01

Nov 19 1998

Fluent 4.47

Fluent Inc.

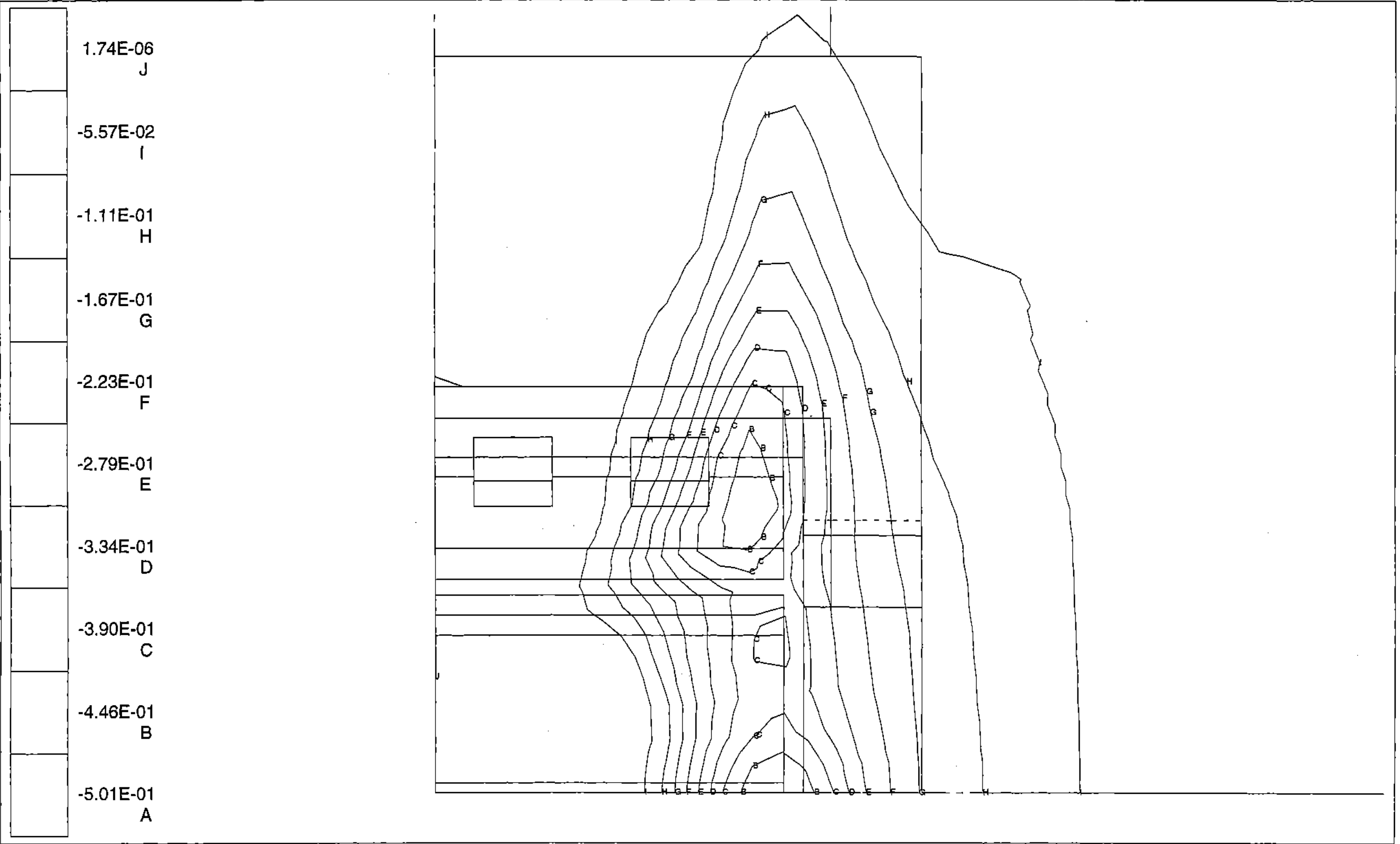

fig. A70, case 44
Ch4 Reaction Rate (Kg/M3/S)
Lmax = 1.736E-06 Lmin = -5.014E-01

Nov 19 1998
Fluent 4.47
Fluent Inc.

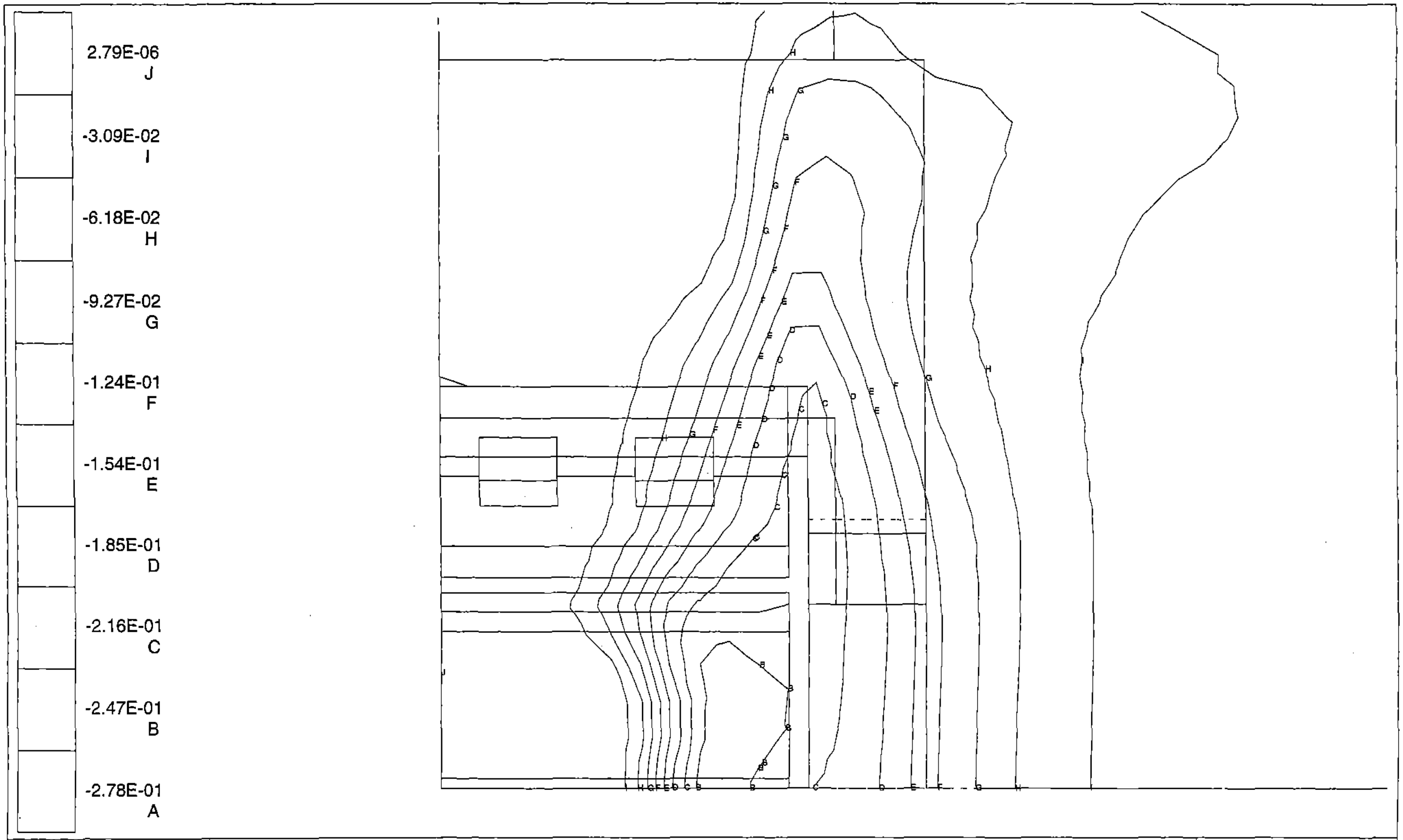

fig. A71, case 44

Ch4 Reaction Rate (Kg/M3/S)

Lmax = 2.794E-06   Lmin = -2.781E-01

Nov 19 1998

Fluent 4.47

Fluent Inc.

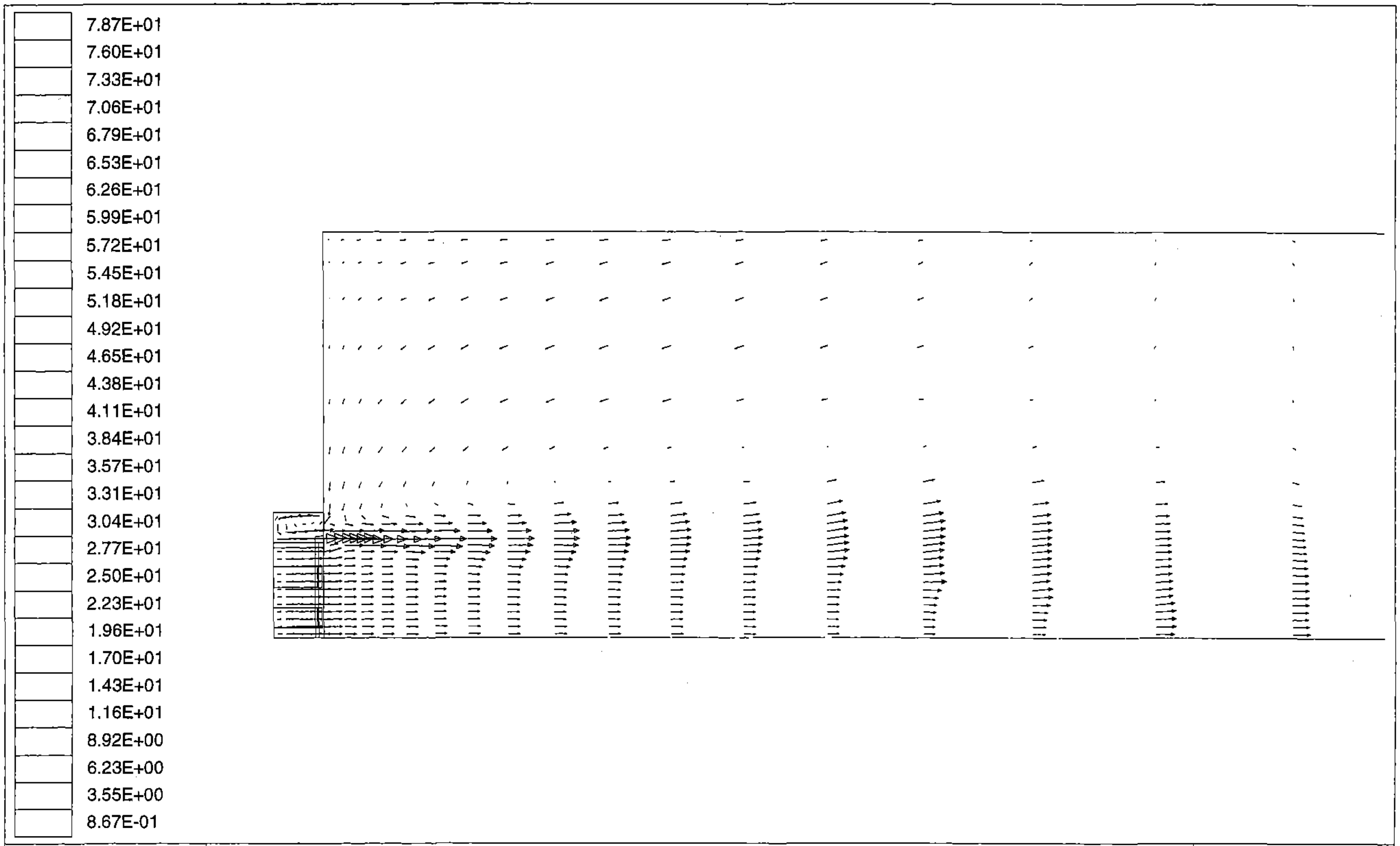

fig. A72, case 24
Velocity Vectors (M/S)
Lmax = 7.868E+01 Lmin = 8.673E-01

Nov 19 1998
Fluent 4.47
Fluent Inc.

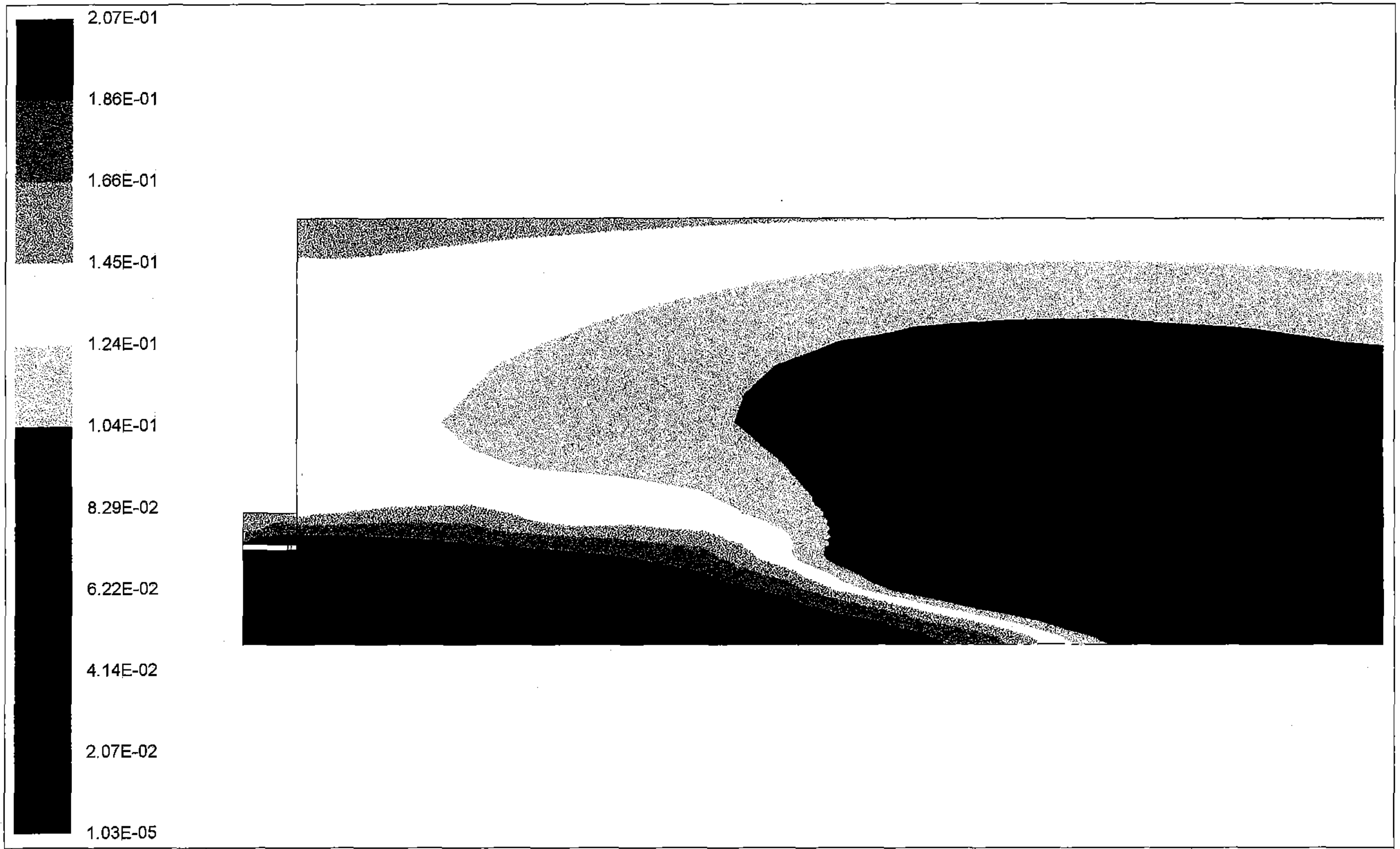

fig. A73, case 24
O2 Mole Fraction
Lmax = 2.072E-01   Lmin = 1.030E-05

Nov 26 1998
Fluent 4.47
Fluent Inc.

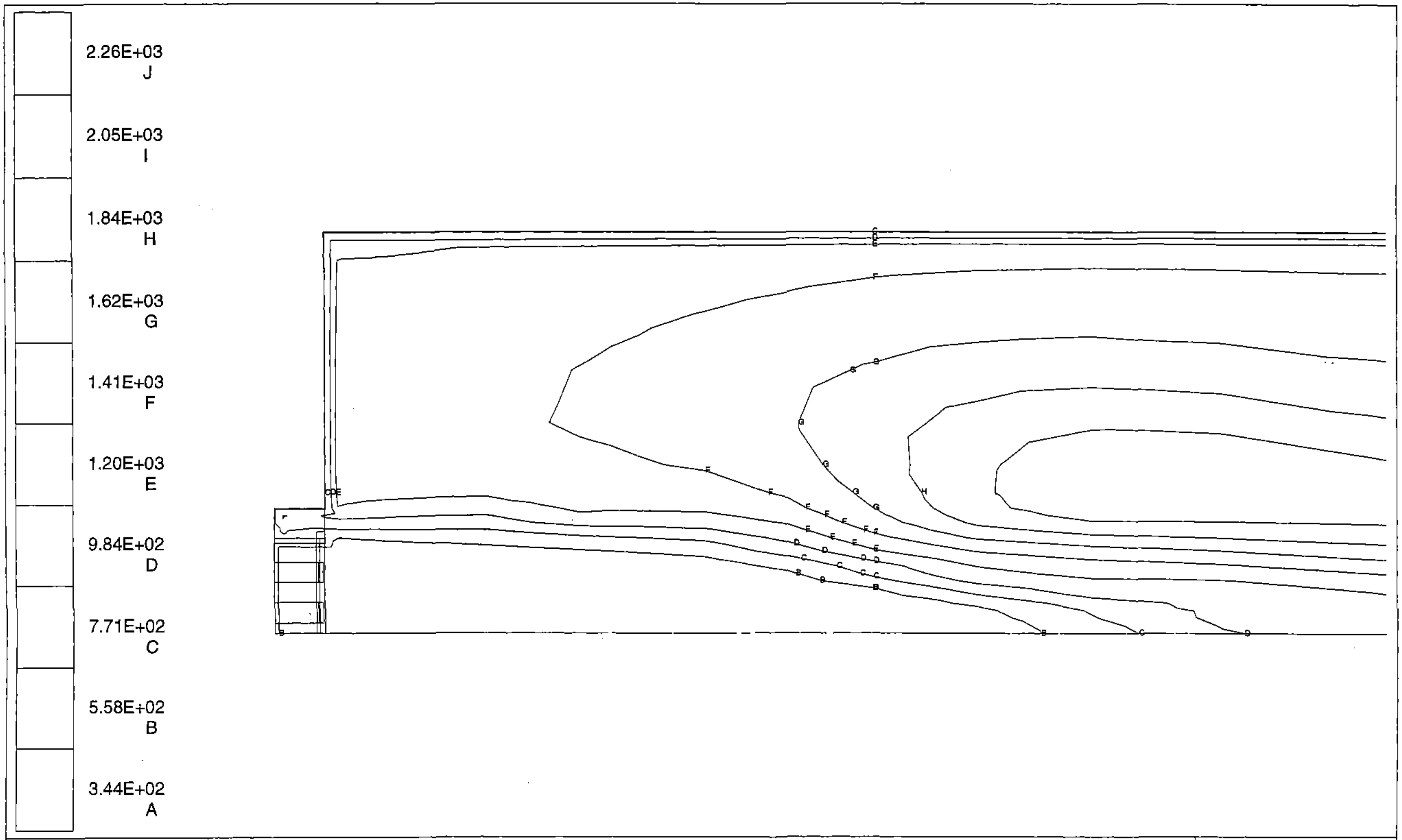

fig. A74, case 24
Temperature (K)
Lmax = 2.265E+03 Lmin = 3.442E+02

Nov 19 1998
Fluent 4.47
Fluent Inc.

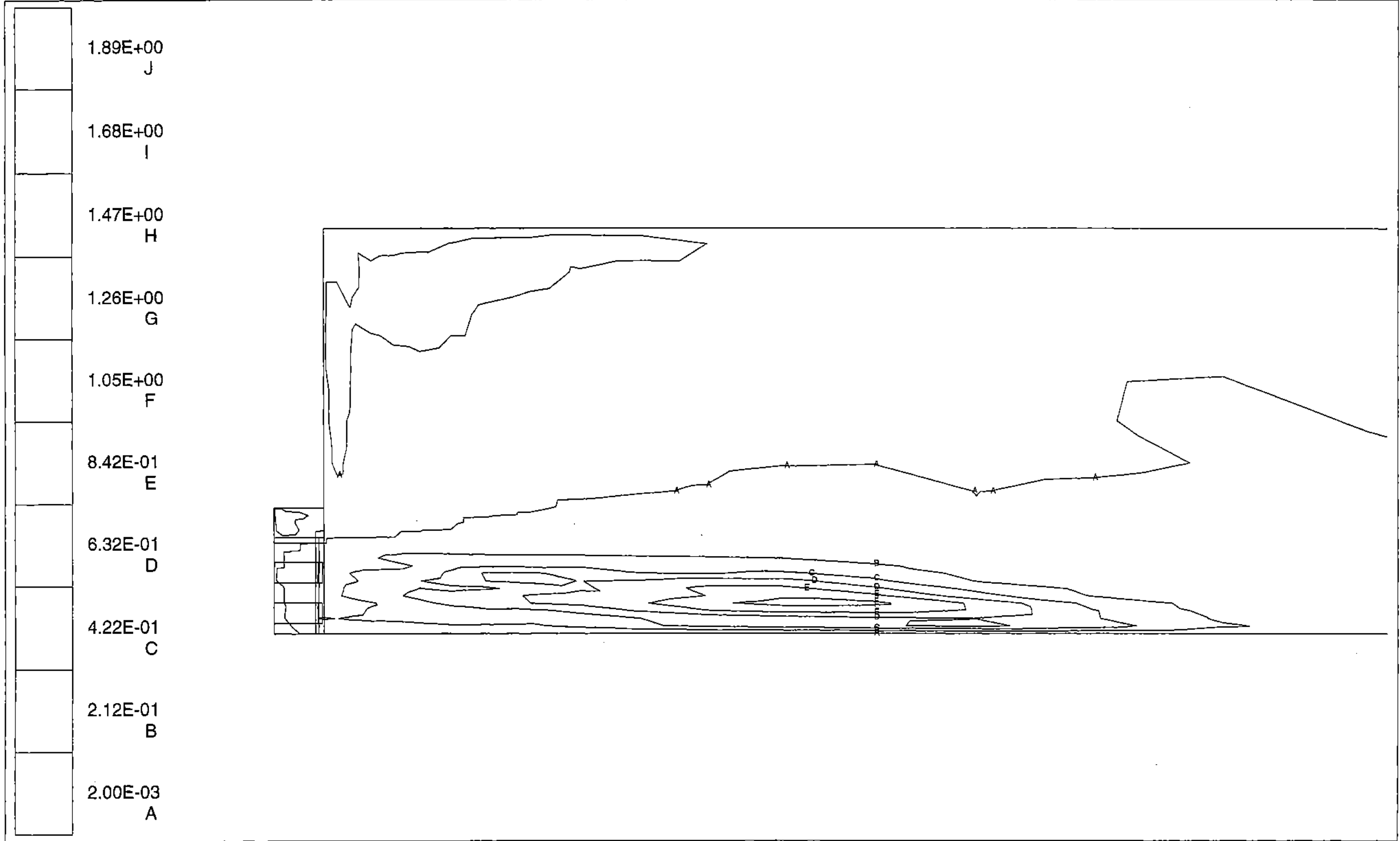

fig. A75, case 24

Phase 2 Conc. (Kg/M3)

Lmax = 1.893E+00   Lmin = 2.000E-03

Nov 19 1998

Fluent 4.47

Fluent Inc.

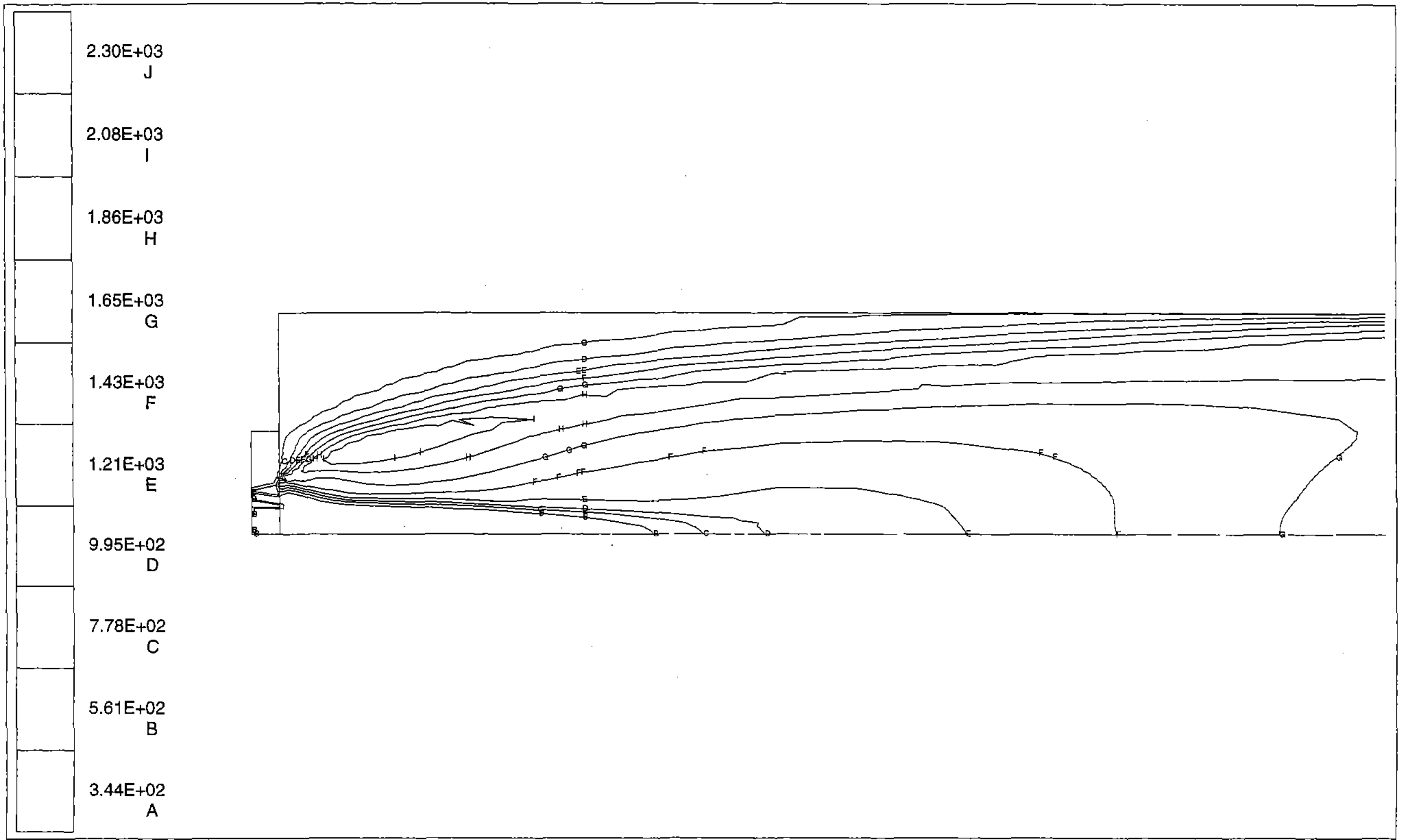

fig. A76, case 24

Temperature (K)

Lmax = 2.298E+03   Lmin = 3.440E+02

Nov 19 1998

Fluent 4.47

Fluent Inc.

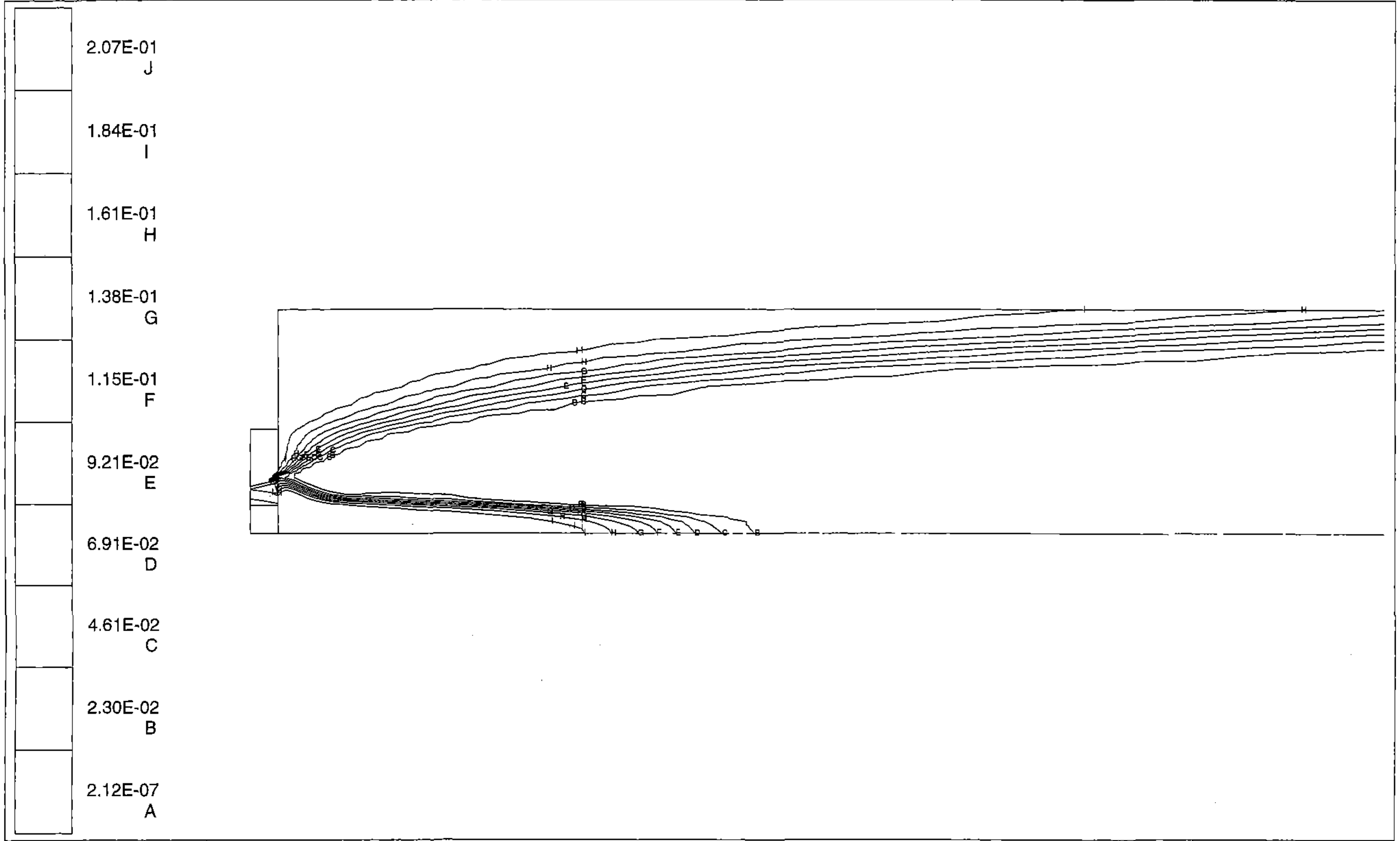

fig. A77, case 24

O2 Mole Fraction

Lmax = 2.072E-01 Lmin = 2.115E-07

Nov 19 1998

Fluent 4.47

Fluent Inc.

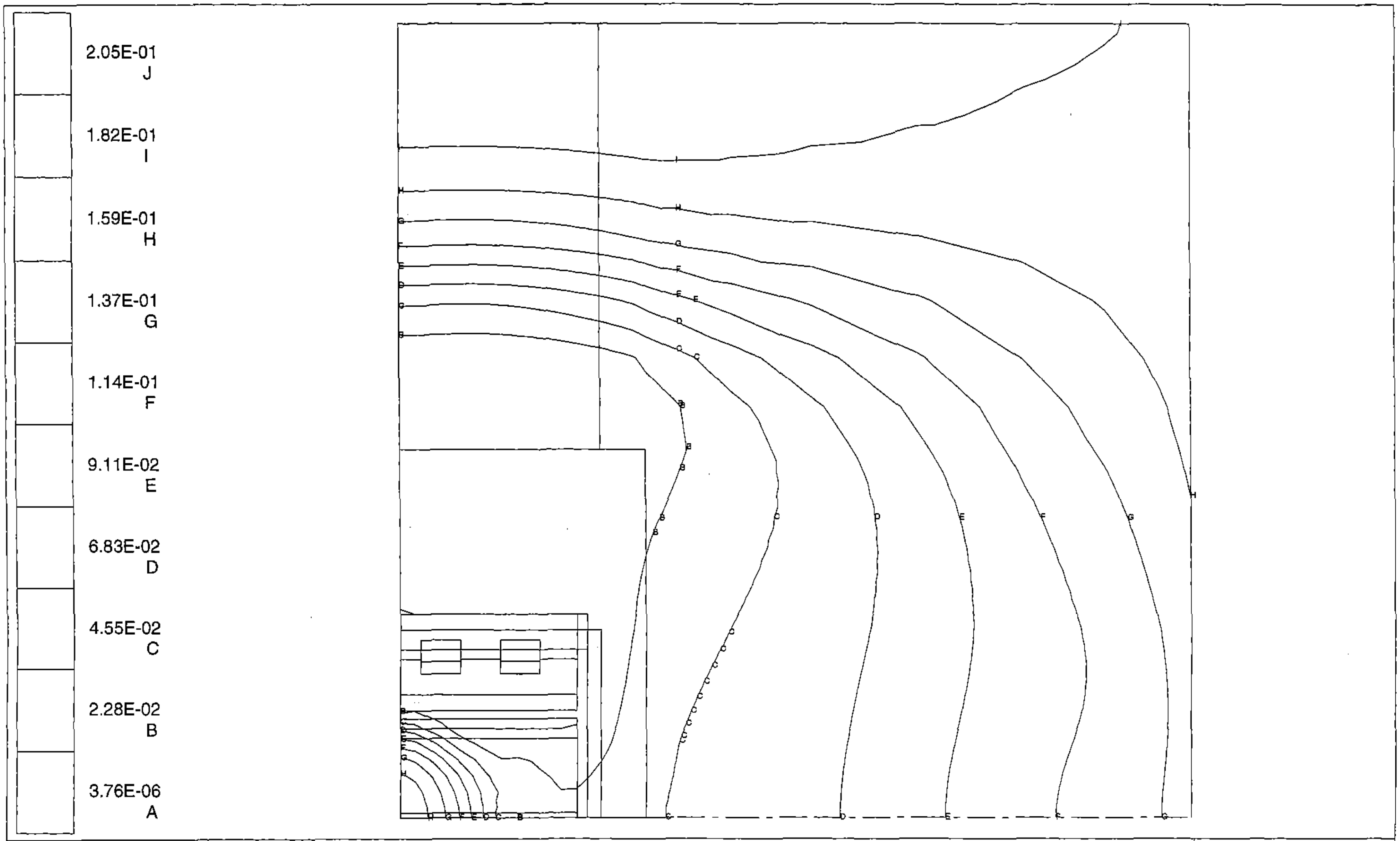

fig. A78, case 24

O2 Mole Fraction

Lmax = 2.049E-01   Lmin = 3.758E-06

Nov 19 1998

Fluent 4.47

Fluent Inc.

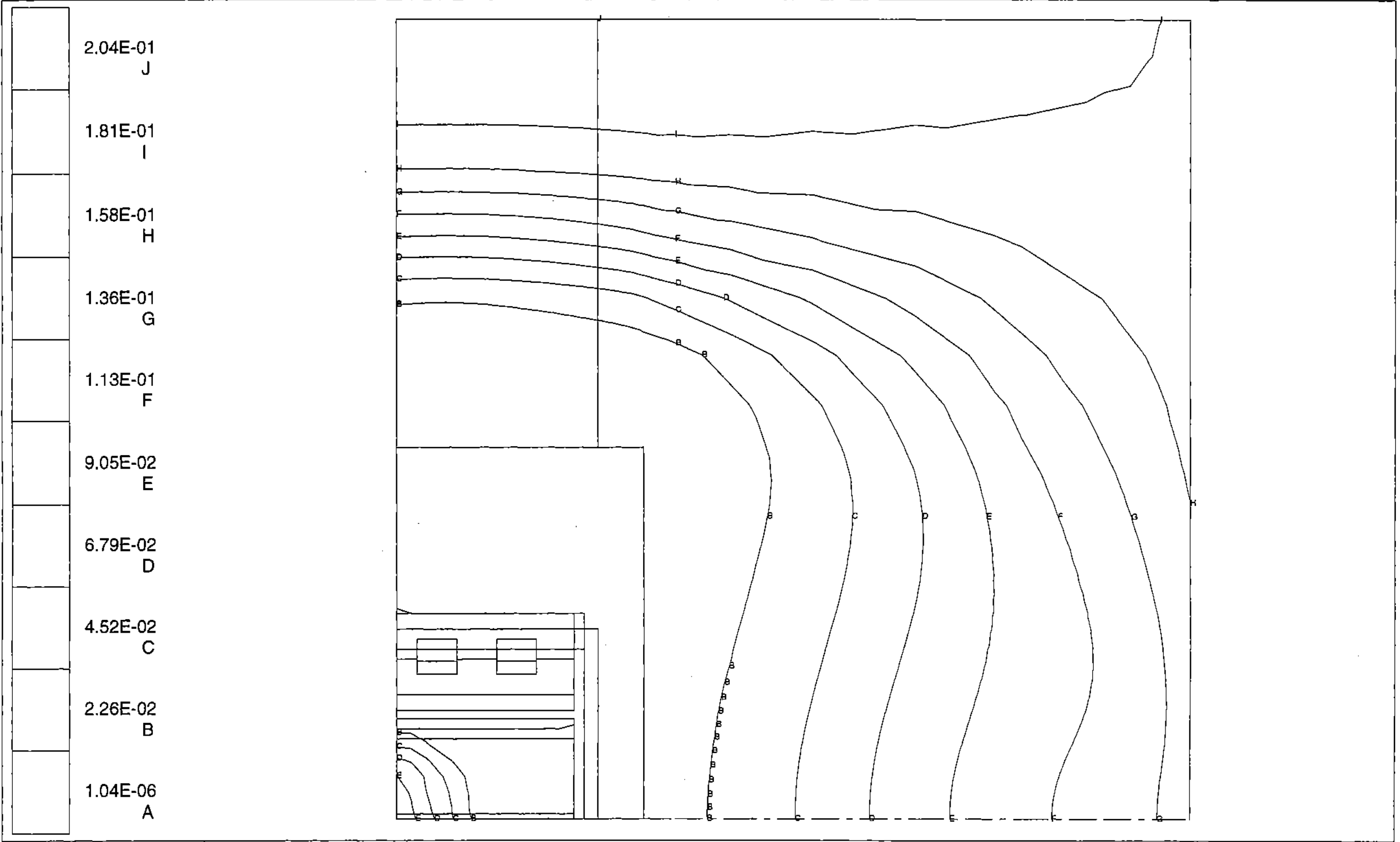

Y
Z X

fig. A79, case 24

O2 Mole Fraction

Lmax = 2.036E-01 Lmin = 1.035E-06

Nov 19 1998

Fluent 4.47

Fluent Inc.

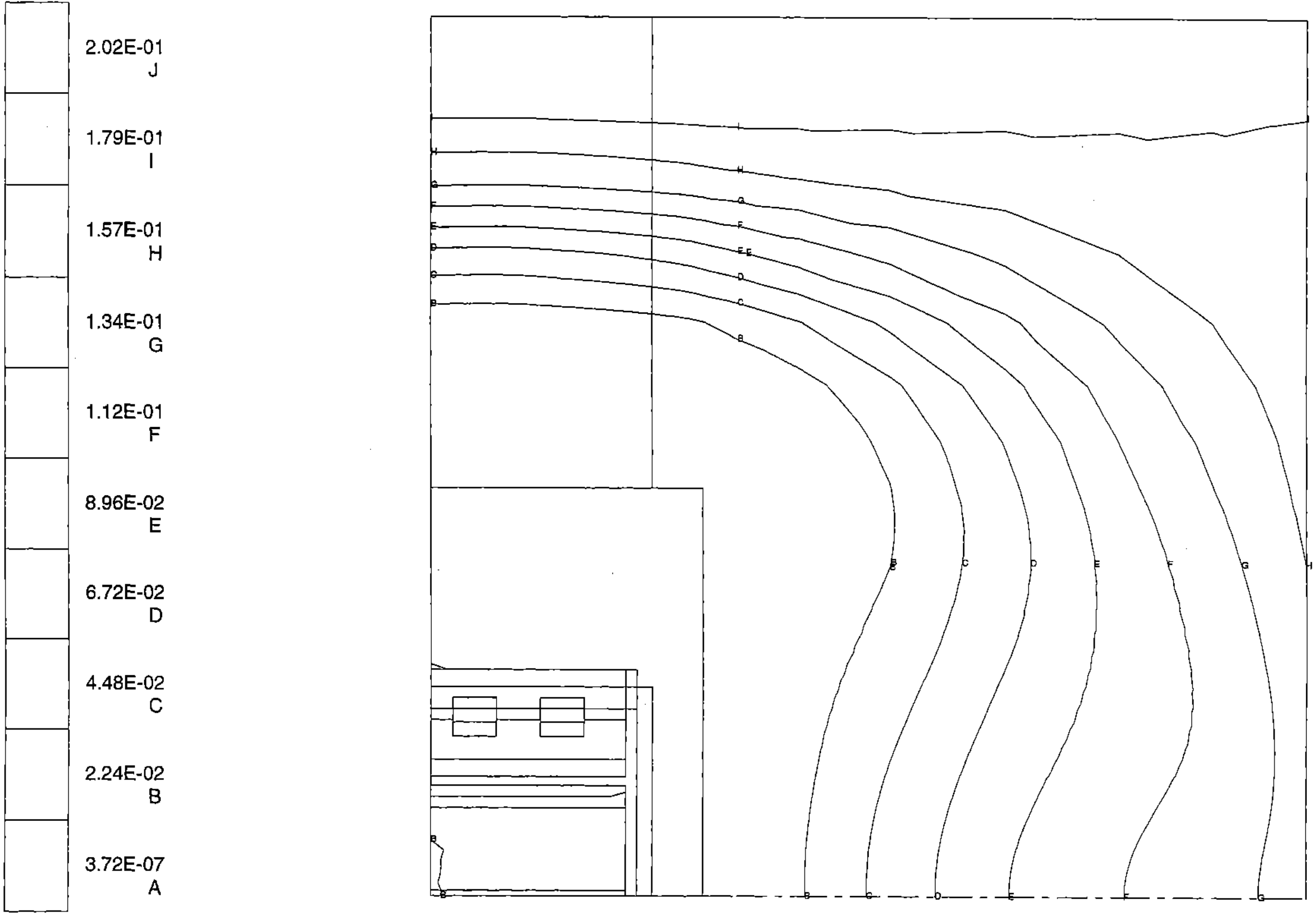

fig. A80, case 24

O2 Mole Fraction

Lmax = 2.016E-01 Lmin = 3.718E-07

Nov 19 1998

Fluent 4.47

Fluent Inc.

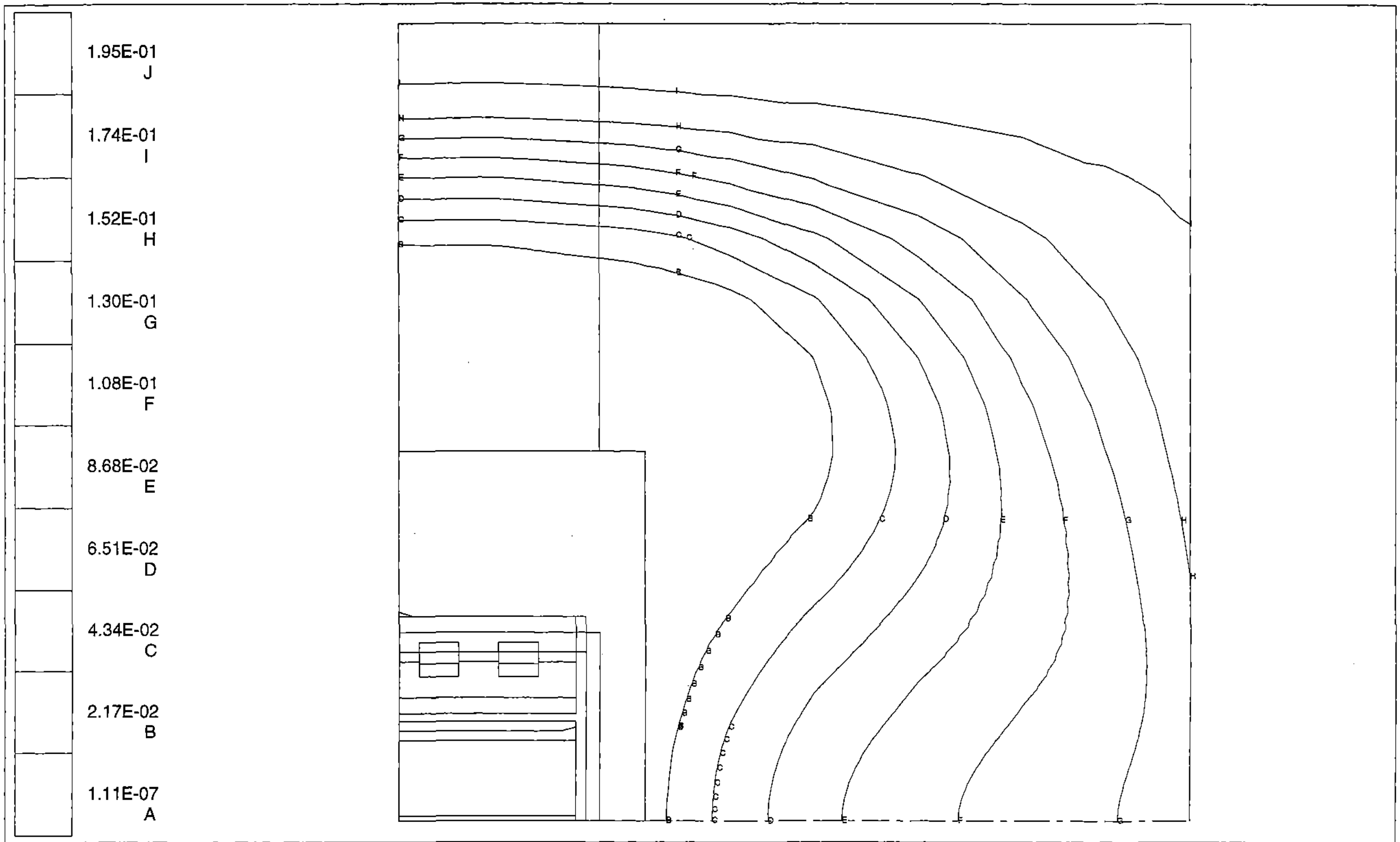

Y
Z X

fig. A81, case 24

O2 Mole Fraction

Lmax = 1.953E-01 Lmin = 1.112E-07

Nov 19 1998

Fluent 4.47

Fluent Inc.

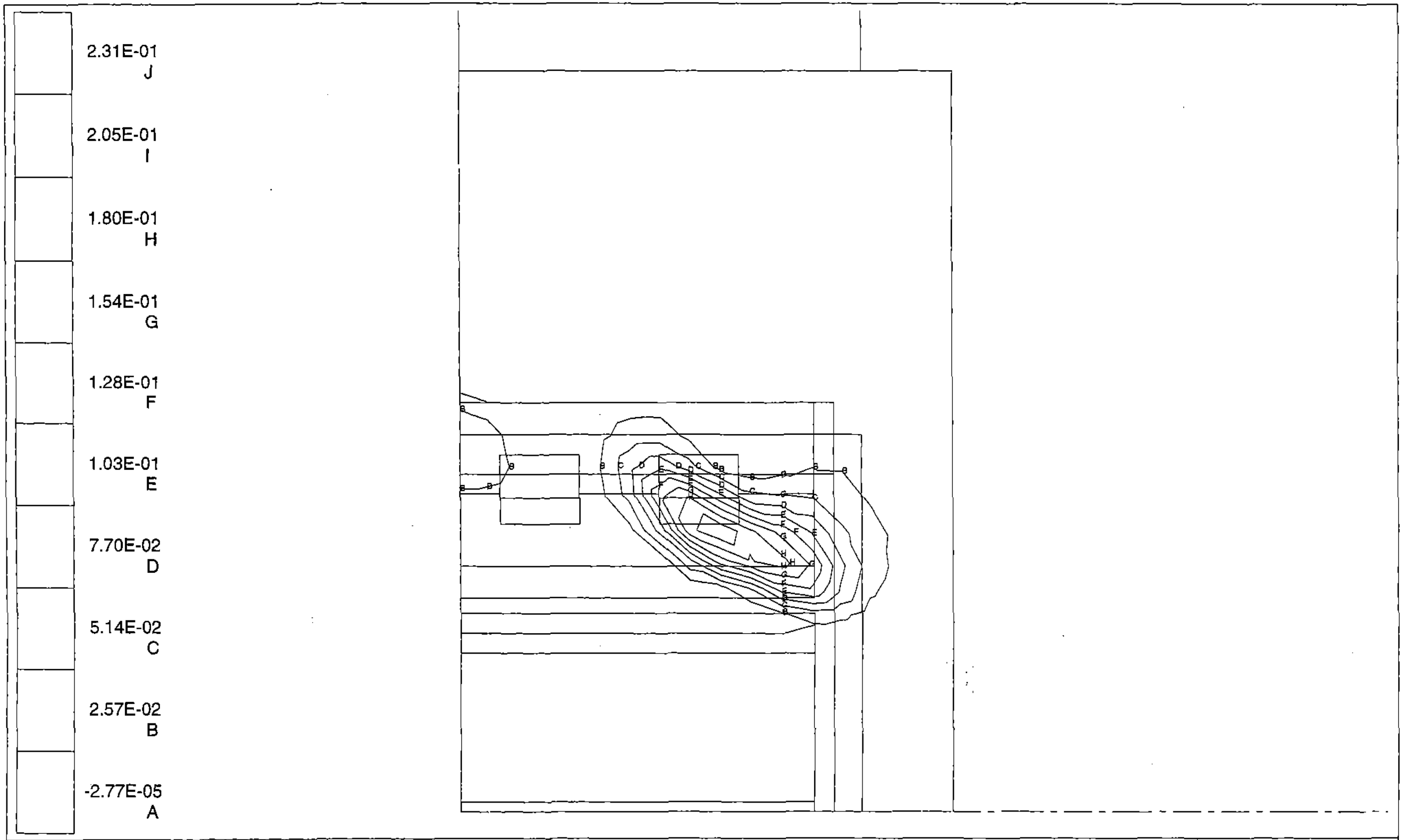

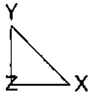

fig. A82, case 24

No Reaction Rate (Kg/M3/S)

Lmax = 2.312E-01 Lmin = -2.770E-05

Nov 19 1998

Fluent 4.47

Fluent Inc.

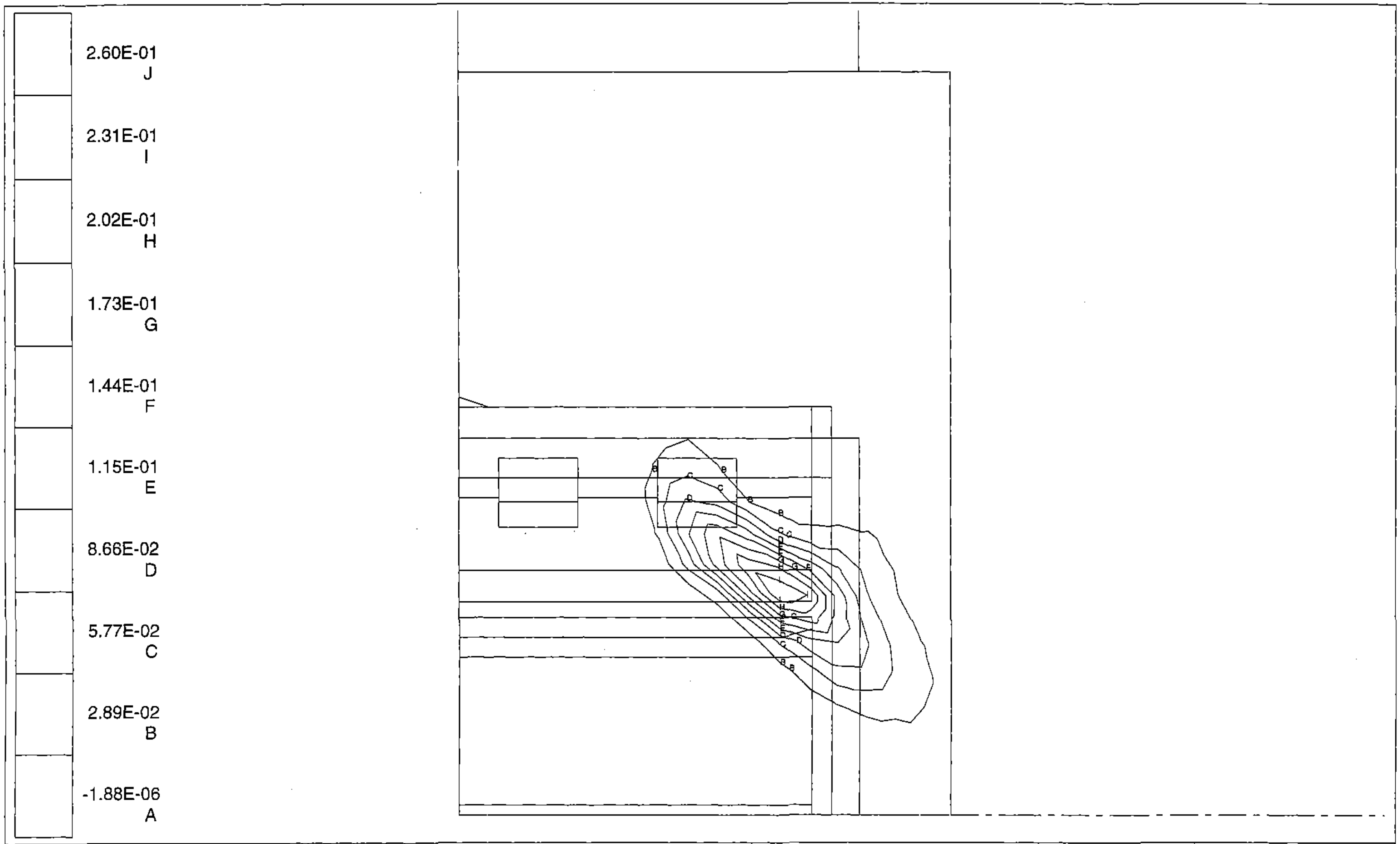

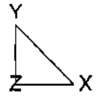

fig. A83, case 24

No Reaction Rate (Kg/M3/S)

Lmax = 2.597E-01 Lmin = -1.879E-06

Nov 19 1998

Fluent 4.47

Fluent Inc.

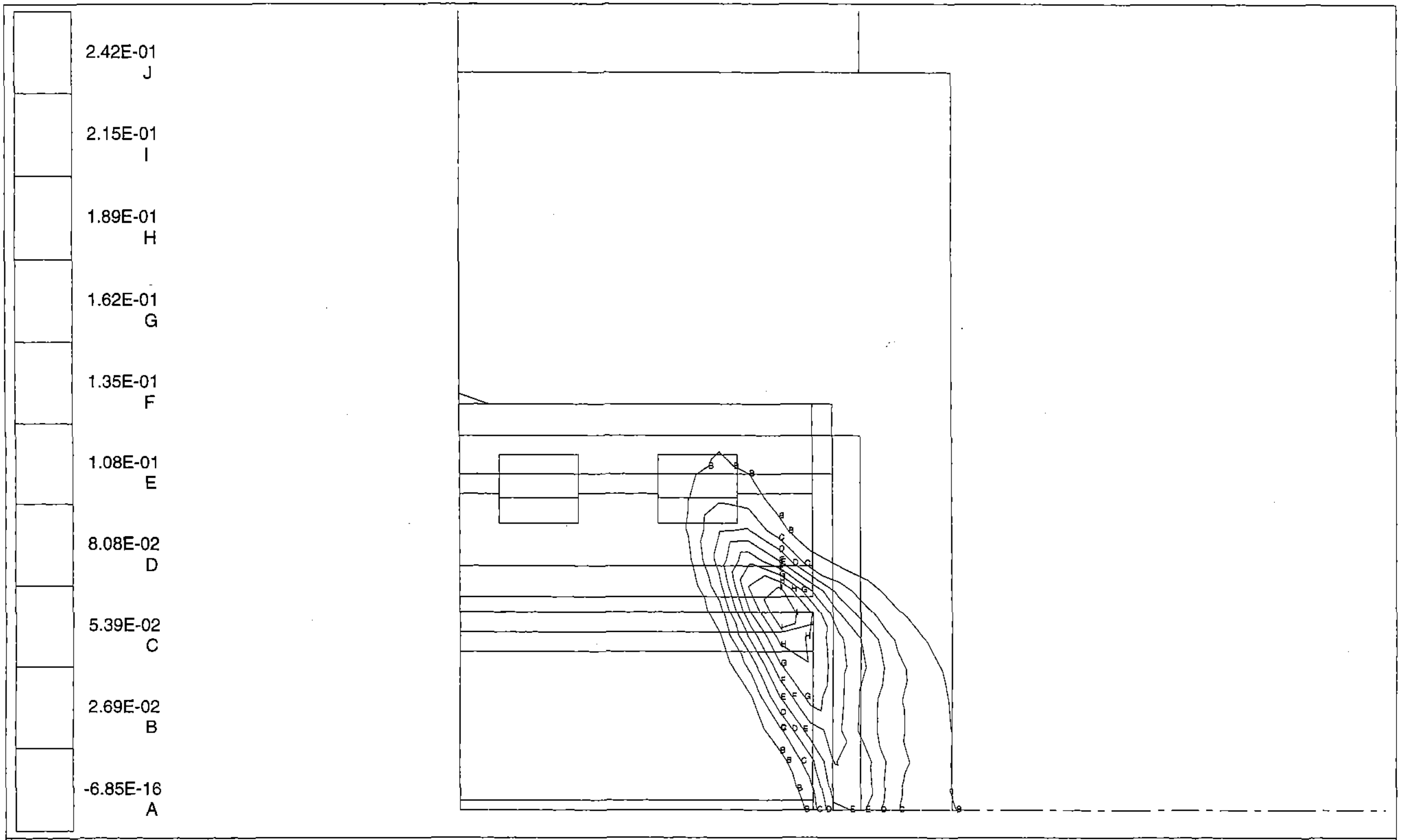

fig. A84, case 24

No Reaction Rate (Kg/M3/S)

Lmax = 2.424E-01 Lmin = -6.851E-16

Nov 19 1998

Fluent 4.47

Fluent Inc.

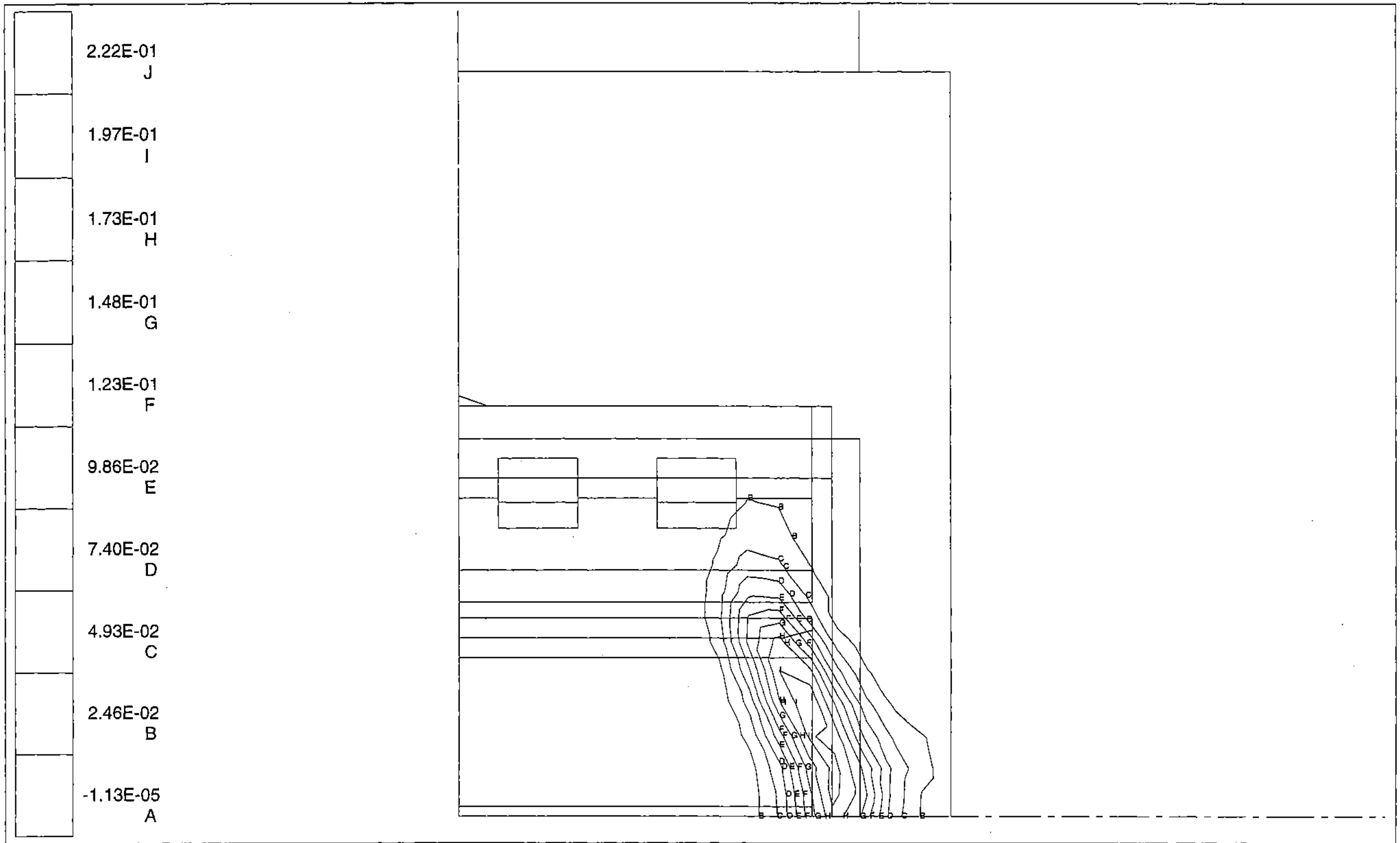

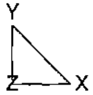

fig. A85, case 24
No Reaction Rate (Kg/M3/S)
Lmax = 2.219E-01   Lmin = -1.134E-05

Nov 19 1998
Fluent 4.47
Fluent Inc.

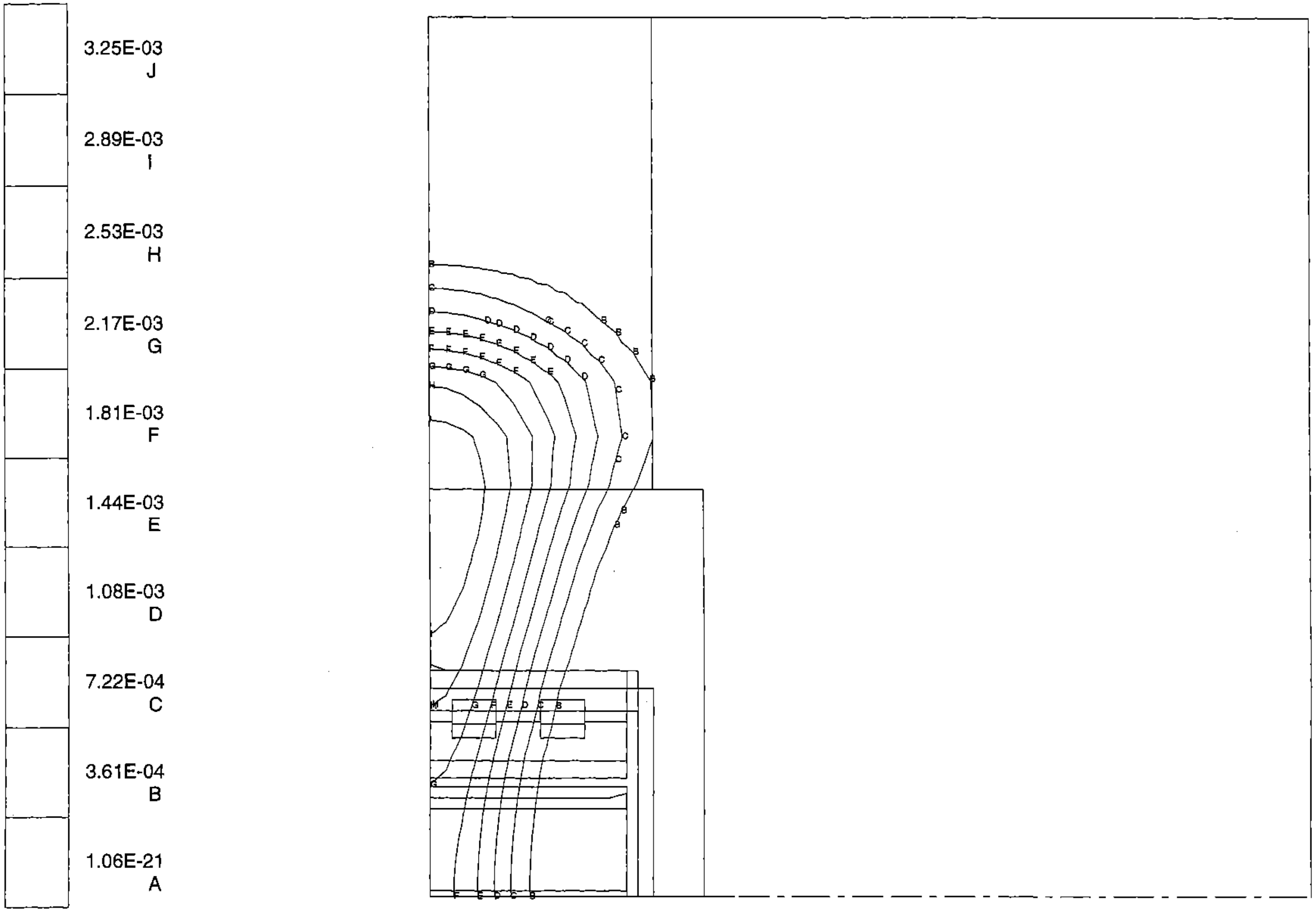

fig. A86, case 24

Hcn Mole Fraction

Lmax = 3.250E-03 Lmin = 1.056E-21

Nov 19 1998

Fluent 4.47

Fluent Inc.

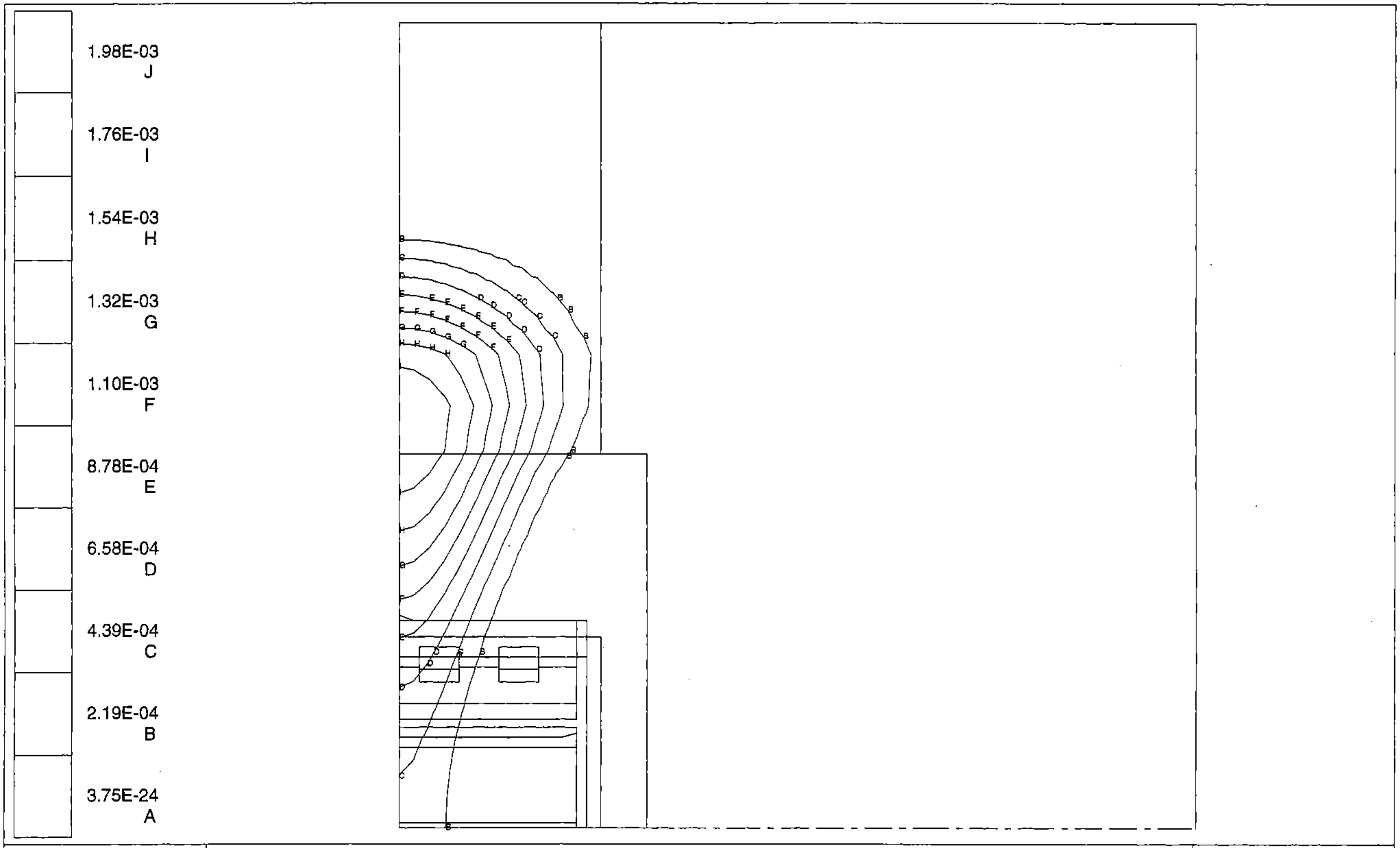

fig. A87, case 24

Hcn Mole Fraction

Lmax = 1.975E-03   Lmin = 3.746E-24

Nov 19 1998

Fluent 4.47

Fluent Inc.

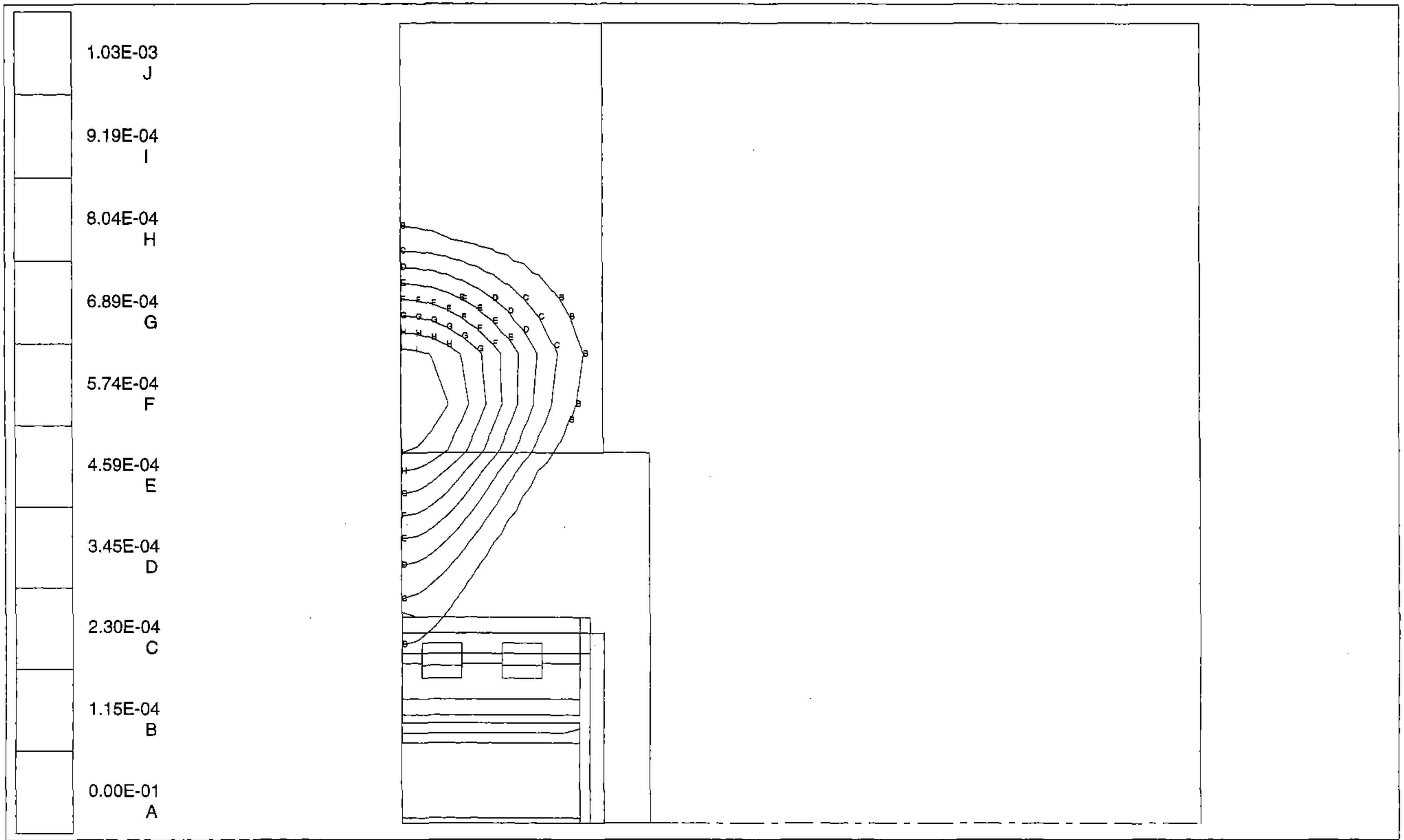

fig. A88, case 24

Hcn Mole Fraction

Lmax = 1.034E-03 Lmin = 0.000E-01

Nov 19 1998

Fluent 4.47

Fluent Inc.

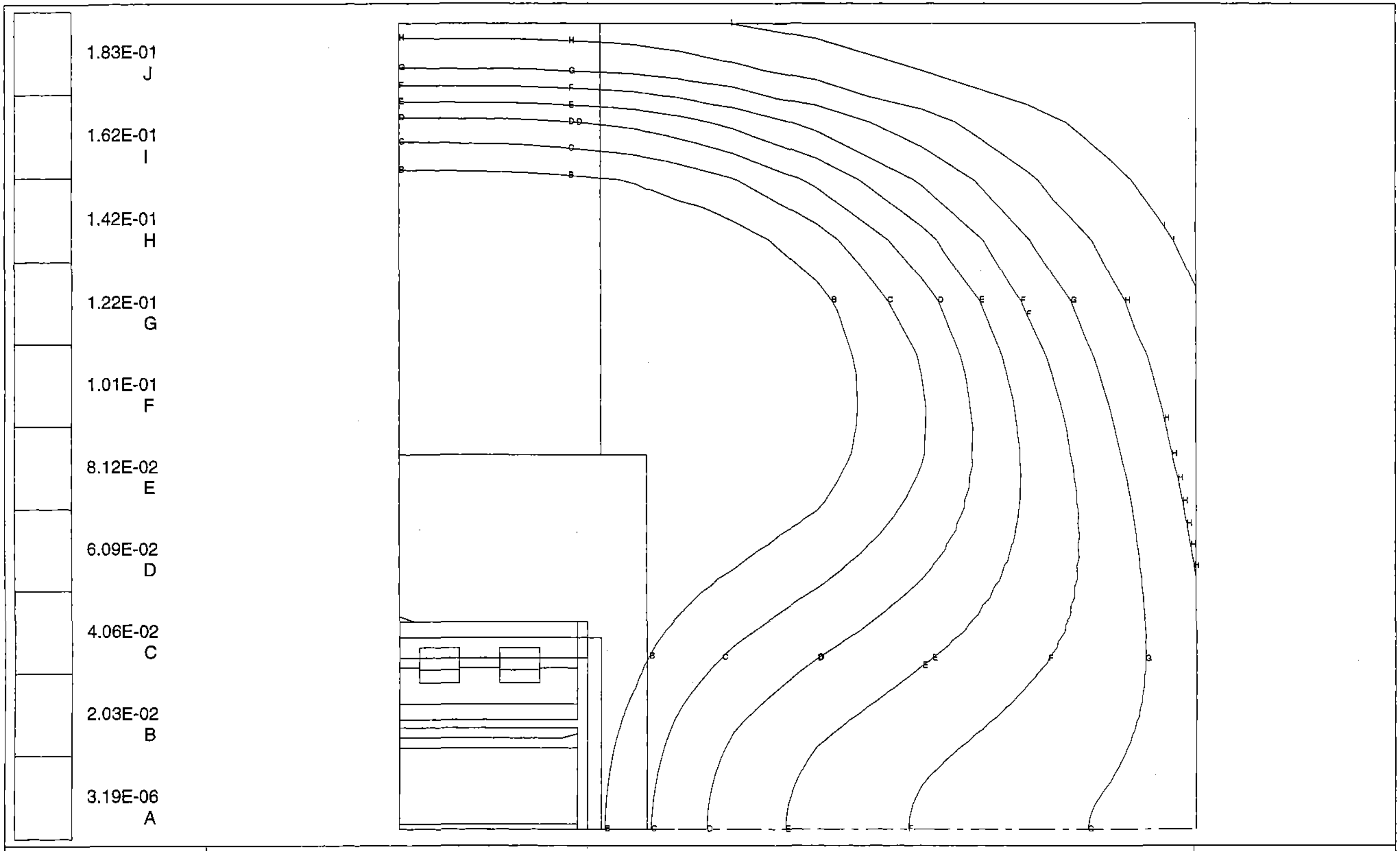

fig. A89, case 24

O2 Mole Fraction

Lmax = 1.827E-01 Lmin = 3.191E-06

Nov 19 1998

Fluent 4.47

Fluent Inc.

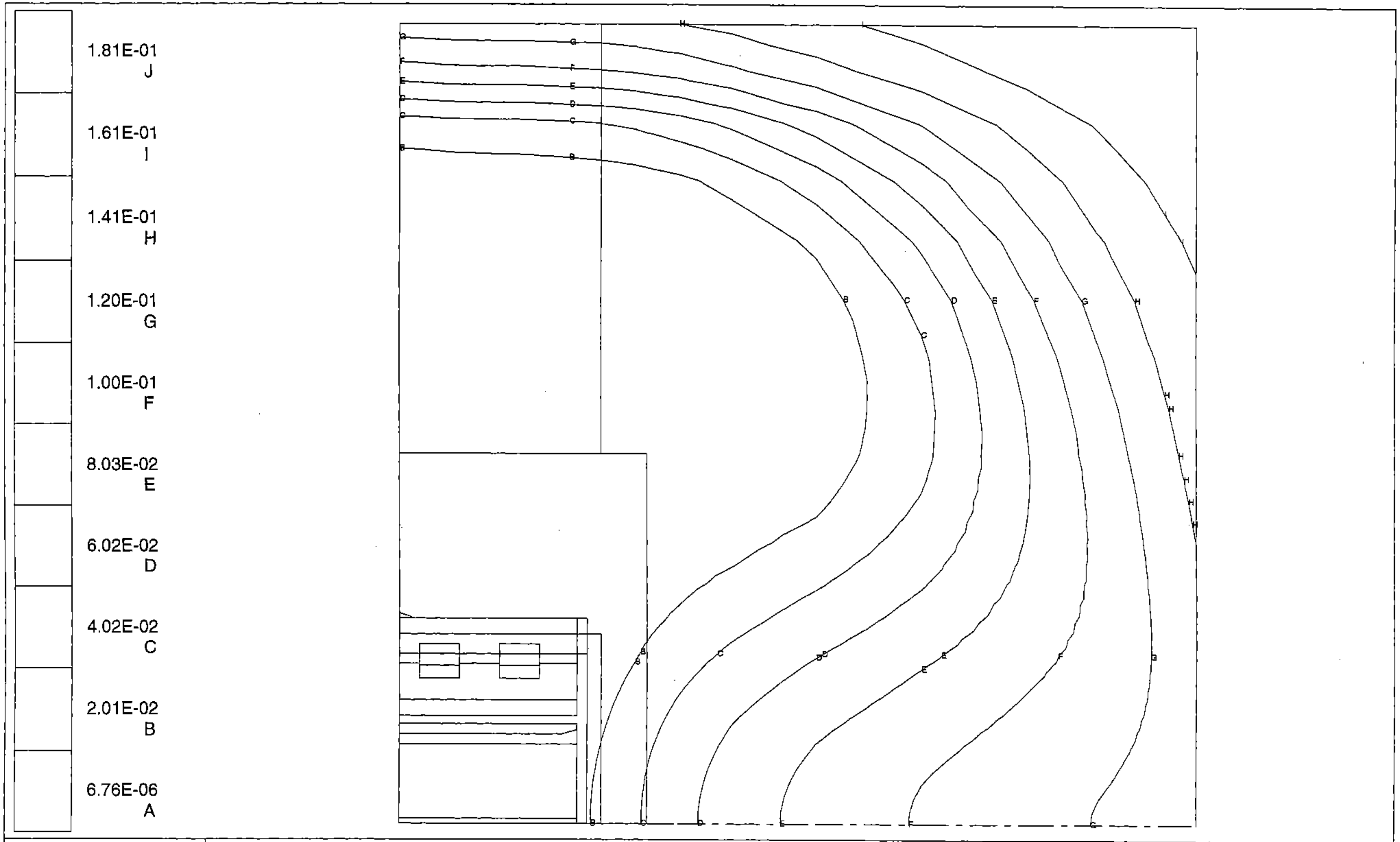

fig. A90, case 24

O2 Mole Fraction

Lmax = 1.807E-01 Lmin = 6.759E-06

Nov 19 1998
Fluent 4.47
Fluent Inc.

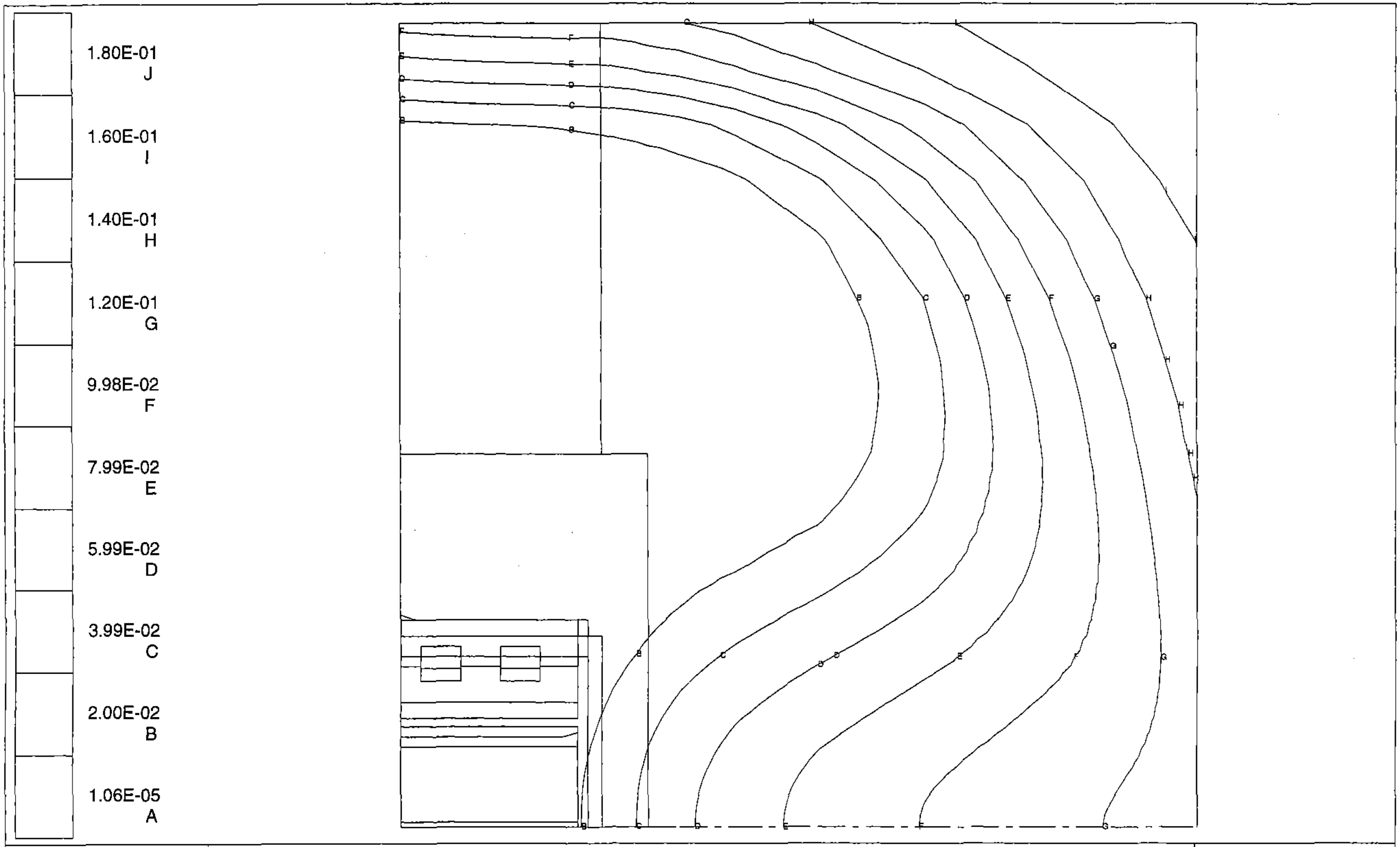

fig. A91, case 24

O2 Mole Fraction

Lmax = 1.797E-01 Lmin = 1.065E-05

Nov 19 1998

Fluent 4.47

Fluent Inc.

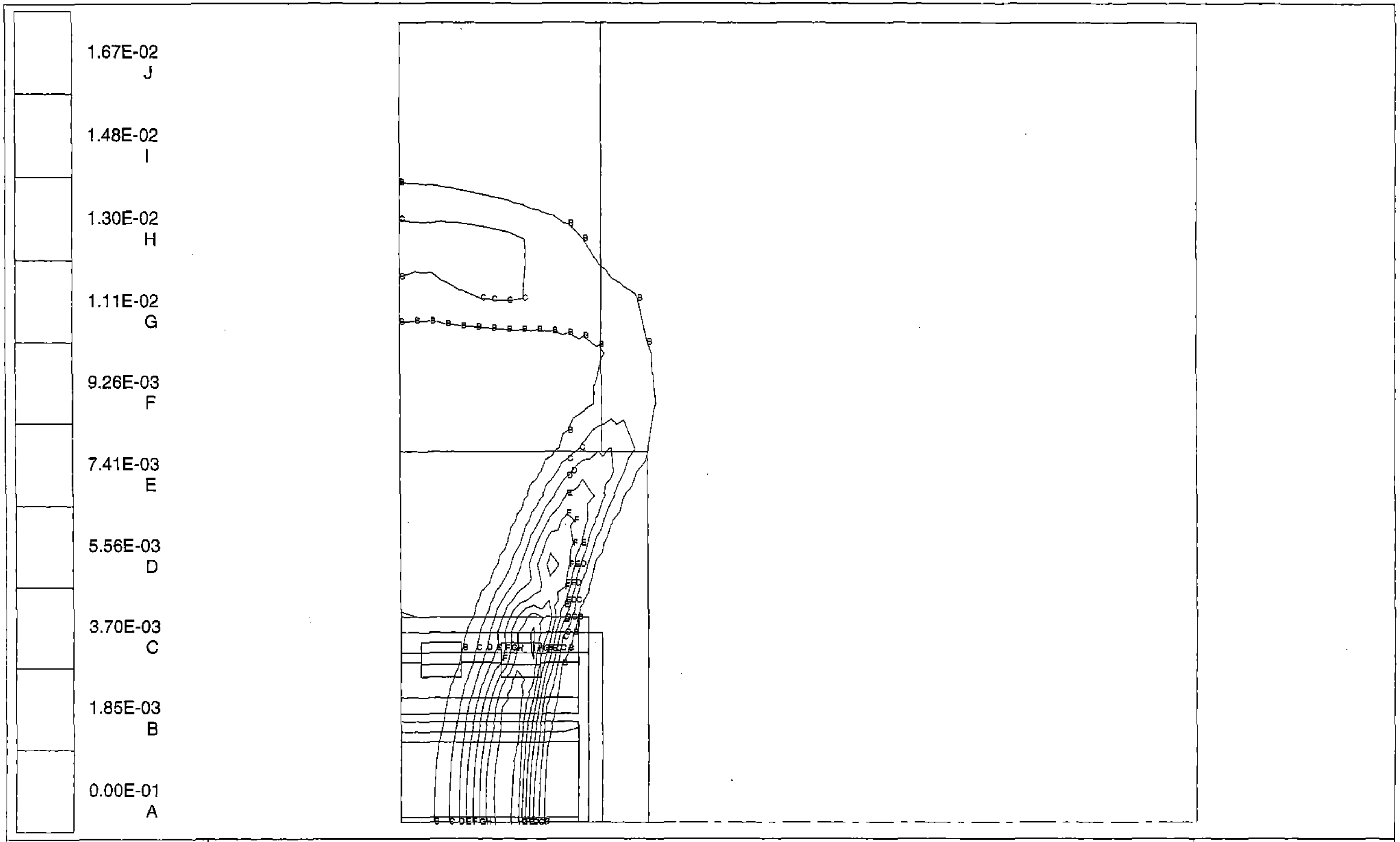

fig. A92, case 24

No Reaction Rate (Kg/M3/S)

Lmax = 1.667E-02   Lmin = 0.000E-01

Nov 19 1998

Fluent 4.47

Fluent Inc.

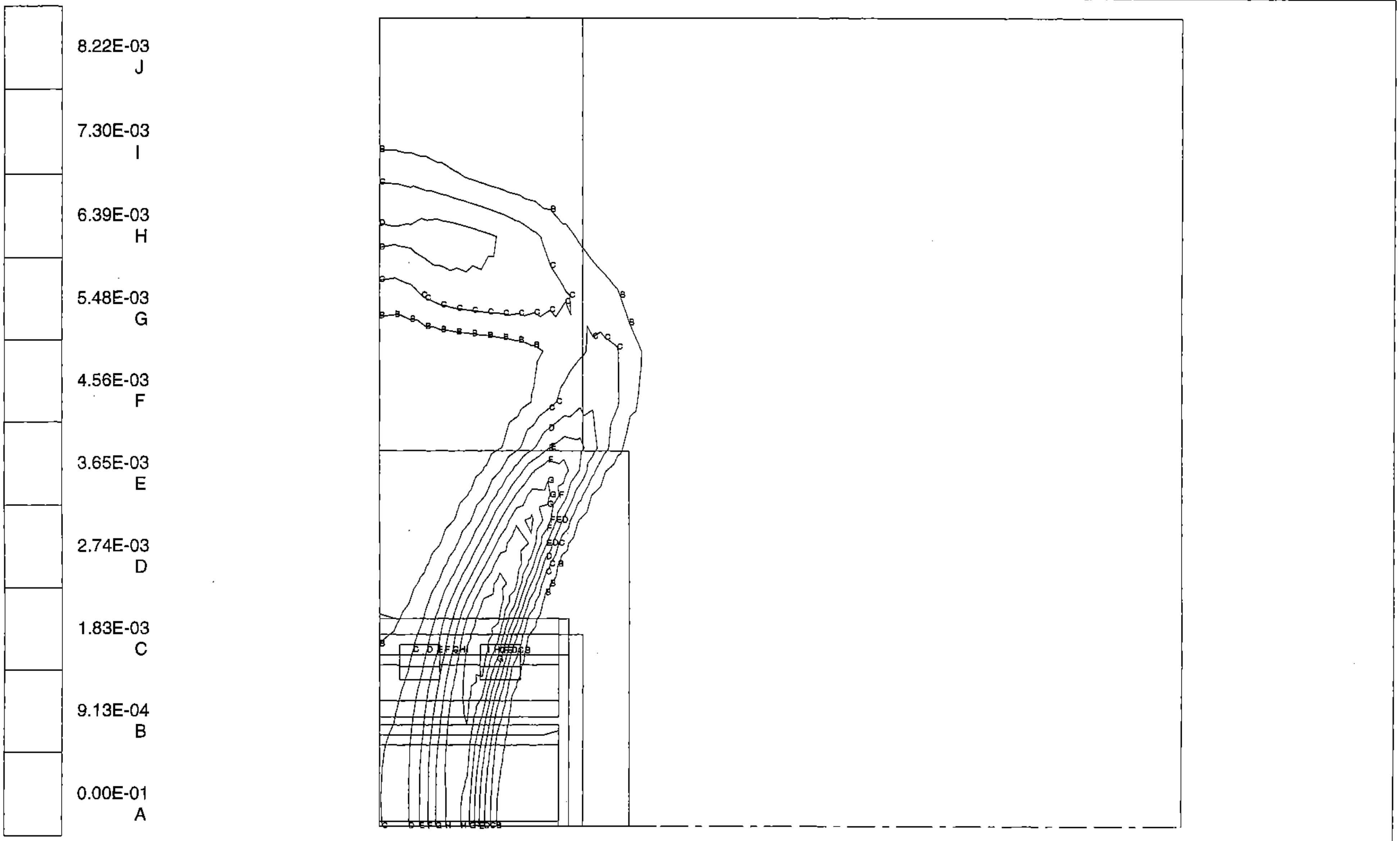

fig. A93, case 24
No Reaction Rate (Kg/M3/S)
Lmax = 8.216E-03   Lmin = 0.000E-01

Nov 19 1998
Fluent 4.47
Fluent Inc.

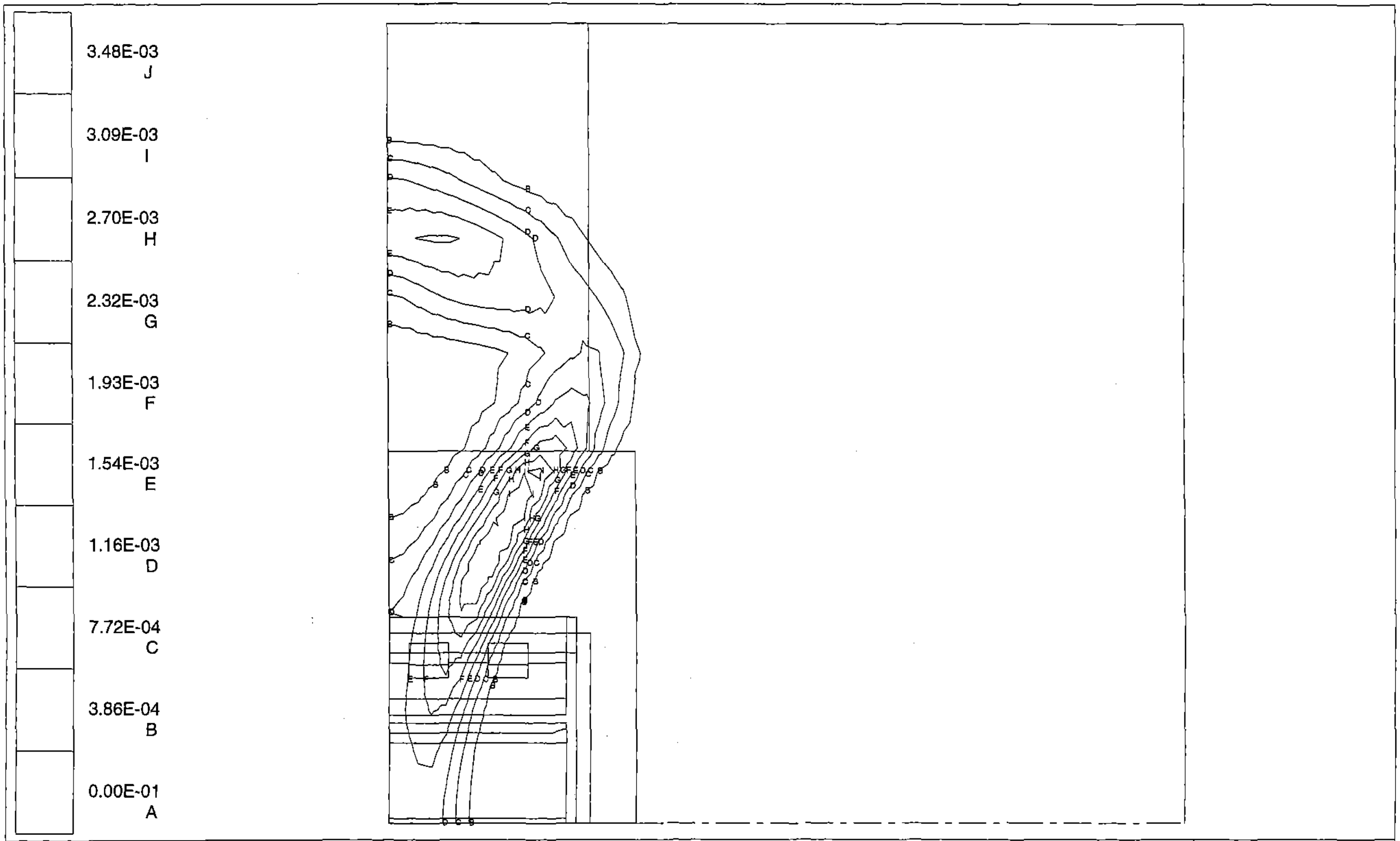

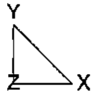

fig. A94, case 24

No Reaction Rate (Kg/M3/S)

Lmax = 3.475E-03 Lmin = 0.000E-01

Nov 19 1998

Fluent 4.47

Fluent Inc.

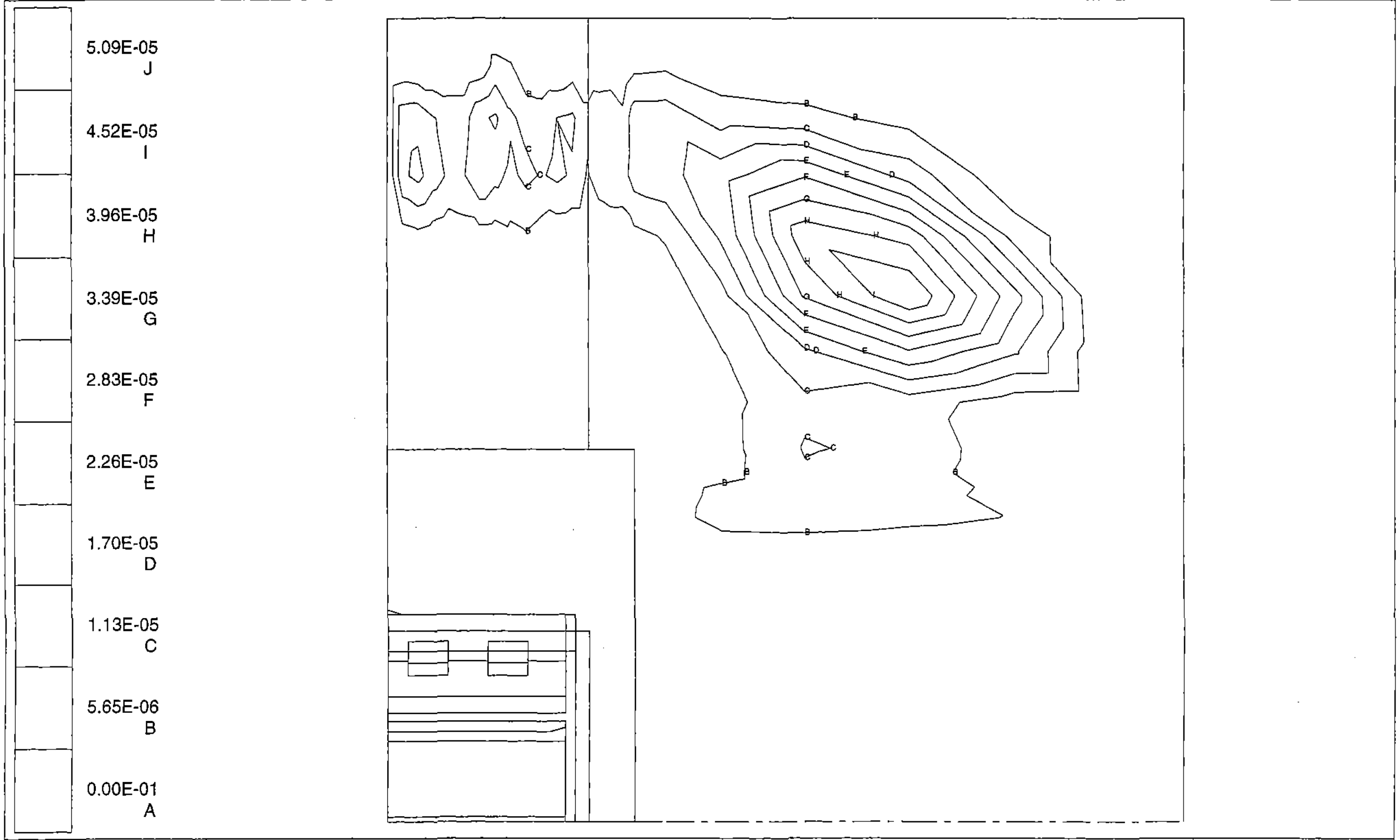

fig. A95, case 24

Char Burnout Rate (Kg/S)

Lmax = 5.088E-05   Lmin = 0.000E-01

Nov 19 1998
Fluent 4.47
Fluent Inc.

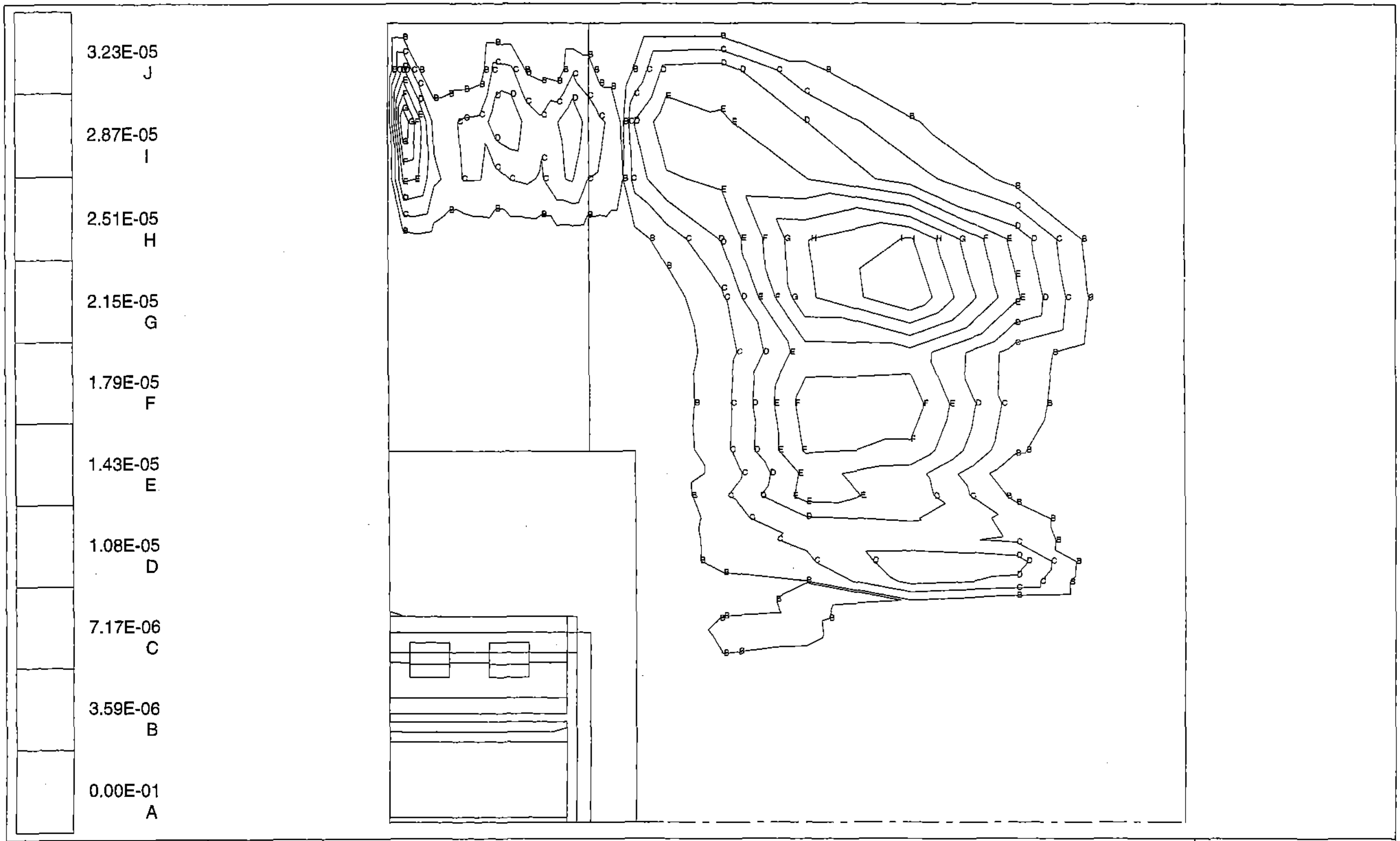

fig. A96, case 24

Char Burnout Rate (Kg/S)

Lmax = 3.227E-05 Lmin = 0.000E-01

Nov 19 1998

Fluent 4.47

Fluent Inc.

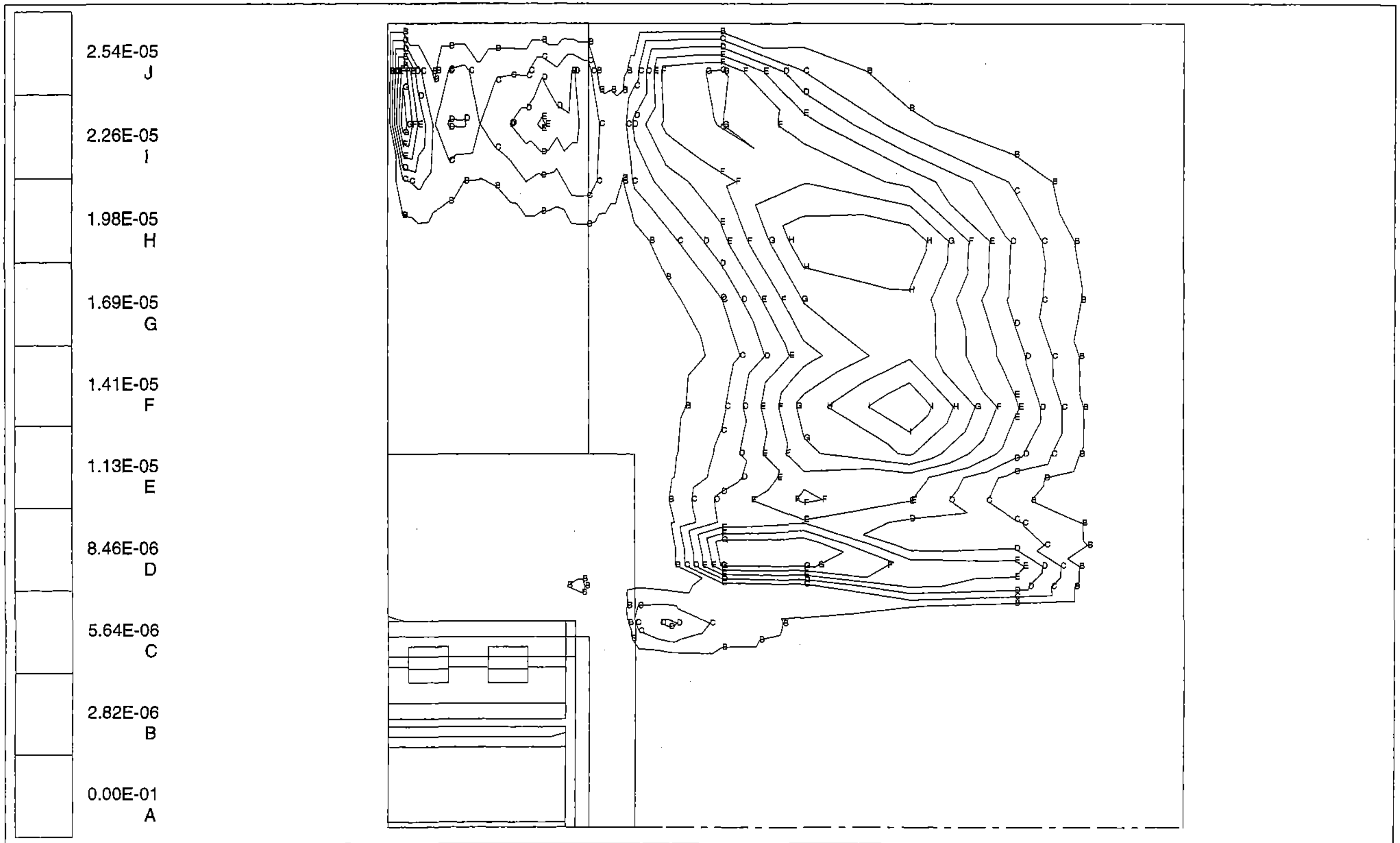

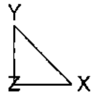

fig. A97, case 24

Char Burnout Rate (Kg/S)

Lmax = 2.539E-05   Lmin = 0.000E-01

Nov 19 1998

Fluent 4.47

Fluent Inc.

99-04-19

RAPPORTFÖRTECKNING

SGC Nr	Rapportnamn	Rapport datum	Författare	Pris kr
001	Systemoptimering vad avser ledningstryck	Apr 91	Stefan Grudén TUMAB	100
002	Mikrokraftvärmeverk för växthus. Utvärdering	Apr 91	Roy Ericsson Kjessler & Mannerstråle AB	100
004	Krav på material vid kringfyllnad av PE -gasledningar	Apr 91	Jan Molin VBB VIAK	50
005	Teknikstatus och marknadsläge för gasbaserad minikraftvärme	Apr 91	Per-Arne Persson SGC	150
006	Keramisk fiberbrännare - Utvärdering av en demo-anläggning	Jan 93	R Brodin, P Carlsson Sydkraft Konsult AB	100
007	Gas-IR teknik inom industrin. Användnings- områden, översiktlig marknadsanalys	Aug 91	Thomas Ehrstedt Sydkraft Konsult AB	100
009	Läcksökning av gasledningar. Metoder och instrument	Dec 91	Charlotte Rehn Sydkraft Konsult AB	100
010	Konvertering av aluminiumsmältugnar. Förstudie	Sep 91	Ola Hall, Charlotte Rehn Sydkraft Konsult AB	100
011	Integrerad naturgasanvändning i tvätterier. Konvertering av torktumlare	Sep 91	Ola Hall Sydkraft Konsult AB	100
012	Odöranter och gasolkondensats påverkan på gasrörsystem av polyeten	Okt 91	Stefan Grudén, F. Varmedal TUMAB	100
013	Spektralfördelning och verkningsgrad för gaseldade IR-strålare	Okt 91	Michael Johansson Drifttekniska Inst. vid LTH	150
014	Modern gasteknik i galvaniseringsindustri	Nov 91	John Danelius Vattenfall Energisystem AB	100
015	Naturgasdrivna truckar	Dec 91	Åsa Marbe Sydkraft Konsult AB	100
016	Mätning av energiförbrukning och emissioner före o efter övergång till naturgas	Mar 92	Kjell Wanselius KW Energiprodukter AB	50
017	Analys och förslag till handlingsprogram för området industriell vätskevärmning	Dec 91	Rolf Christensen ÅF-Energikonsult Syd AB	100
018	Skärning med acetylen och naturgas. En jämförelse.	Apr 92	Åsa Marbe Sydkraft Konsult AB	100

RAPPORTFÖRTECKNING

SGC Nr	Rapportnamn	Rapport datum	Författare	Pris kr
019	Läggning av gasledning med plöjteknik vid Glostorp, Malmö. Uppföljningsprojekt	Maj 92	Fallsvik J, Haglund H m fl SGI och Malmö Energi AB	100
020	Emissionsdestruktion. Analys och förslag till handlingsprogram	Jun 92	Thomas Ehrstedt Sydkraft Konsult AB	150
021	Ny läggningsteknik för PE-ledningar. Förstudie	Jun 92	Ove Ribberström Ove Ribberström Projekt. AB	150
022	Katalog över gastekniska FUD-projekt i Sverige. Utgåva 4	Aug 92	Svenskt Gastekniskt Center	150
023	Läggning av gasledning med plöjteknik vid Lillhagen, Göteborg. Uppföljningsproj.	Aug 92	Nils Granstrand m fl Göteborg Energi AB	150
024	Stumsvetsning och elektromuffsvetsning av PE-ledningar. Kostnadsaspekter.	Aug 92	Stefan Grudén TUMAB	150
025	Papperstorkning med gas-IR. Sammanfattning av ett antal FUD-projekt	Sep 92	Per-Arne Persson Svenskt Gastekniskt Center	100
026	Koldioxidgödsling i växthus med hjälp av naturgas. Handbok och tillämpn.exempel	Aug 92	Stig Arne Molén m fl	150
027	Decentraliserad användning av gas för vätskevärmning. Två praktikfall	Okt 92	Rolf Christensen ÅF-Energikonsult	150
028	Stora gasledningar av PE. Teknisk och ekonomisk studie.	Okt 92	Lars-Erik Andersson, Åke Carlsson, Sydkraft Konsult	150
029	Catalogue of Gas Techn Research and Development Projects in Sweden (På engelska)	Sep 92	Swedish Gas Technology Center	150
030	Pulsationspanna. Utvärdering av en demo -anläggning	Nov 92	Per Carlsson, Åsa Marbe Sydkraft Konsult AB	150
031	Detektion av dräneringsrör. Testmätning med magnetisk gradiometri	Nov 92	Carl-Axel Triumf Triumf Geophysics AB	100
032	Systemverkn.grad efter konvertering av vattenburen elvärme t gasvärme i småhus	Jan 93	Jonas Forsman Vattenfall Energisystem AB	150
033	Energiuppföljning av gaseldad panncentral i kvarteret Malörten, Trelleborg	Jan 93	Theodor Blom Sydkraft AB	150
034	Utvärdering av propanexponerade PEM-rör	Maj 93	Hans Leijström Studsvik AB	150

99-04-19

RAPPORTFÖRTECKNING

SGC Nr	Rapportnamn	Rapport datum	Författare	Pris kr
035	Hemmatankning av naturgasdriven personbil. Demonstrationsprojekt	Jun 93	Tove Ekeborg Vattenfall Energisystem	150
036	Gaseldade genomströmningsberedare för tappvarmvatten i småhus. Litteraturstudie	Jun 93	Jonas Forsman Vattenfall Energisystem	150
037	Verifiering av dimensioneringsmetoder för distributionsledningar. Litt studie.	Jun 93	Thomas Ehrstedt Sydkraft Konsult AB	150
038	NOx-reduktion genom reburning med naturgas. Fullskaleförsök vid SYSAV i Malmö	Aug 93	Jan Bergström Miljökonsulterna	150
039	Pulserande förbränning för torkändamål	Sep 93	Sten Hermodsson Lunds Tekniska Högskola	150
040	Organisationer med koppling till gasteknisk utvecklingsverksamhet	Feb 94	Jörgen Thunell SGC	150
041	Fältsortering av fyllnadsmassor vid läggning av PE-rör med läggningsbox.	Nov 93	Göran Lustig Elektro Sandberg Kraft AB	150
042	Deponigasens påverkan på polyetenrör.	Nov 93	Thomas Ehrstedt Sydkraft Konsult AB	150
043	Gasanvändning inom plastindustrin, handlingsplan	Nov 93	Thomas Ehrstedt Sydkraft Konsult AB	150
044	PA 11 som material ledningar för gasdistribution.	Dec 93	Thomas Ehrstedt Sydkraft Konsult AB	150
045	Metoder att höja verkningsgraden vid avgaskondensering	Dec 93	Kjell Wanselius KW Energiprodukter AB	150
046	Gasanvändning i målerier	Dec 93	Charlotte Rehn et al Sydkraft Konsult AB	150
047	Rekuperativ aluminiumsmältugn. Utvärdering av degelugn på Värnamo Pressgjuteri.	Okt 93	Ola Hall Sydkraft Konsult AB	150
048	Konvertering av dieseldrivna reservkraftverk till gasdrift och kraftvärmeprod	Jan 94	Gunnar Sandström Sydkraft Konsult AB	150
049	Utvecklad teknik för gasinstallationer i småhus	Feb 94	P Kastensson, S Ivarsson Sydgas AB	150
050	Korrosion i flexibla rostfria insatsrör (Finns även i engelsk upplaga)	Dec 93	Ulf Nilsson m fl LTH	150

99-04-19

RAPPORTFÖRTECKNING

SGC Nr	Rapportnamn	Rapport datum	Författare	Pris kr
051	Nordiska Degelugnsprojektet. Pilot- och fältförsök med gasanvändning.	Nov 93	Eva-Maria Svensson Glafo	150
052	Nordic Gas Technology R&D Workshop. April 20, 1994. Proceedings.(På engelska)	Jun 94	Jörgen Thunell, Editor Swedish Gas Center	150
053	Tryckhöjande utrustning för gas vid metallbearbetning -- En förstudie av GT -PAK	Apr 94	Mårten Wärnö MGT Teknik AB	150
054	NOx-reduktion genom injicering av naturgas i kombination med ureainsprutning	Sep 94	Bent Karll, DGC P Å Gustafsson, Miljökons.	100
055	Trevägskatalysatorer för stationära gasmotorer.	Okt 94	Torbjörn Karlelid m fl Sydkraft Konsult AB	150
056	Utvärdering av en industriell gaseldad IR -strålare	Nov 94	Johansson, M m fl Lunds Tekniska Högskola	150
057	Läckagedetekteringssystem i storskaliga gasinstallationer	Dec 94	Fredrik A Silversand Katator AB	150
058	Demonstration av låg-NOx-brännare i växthus	Feb 95	B Karll, B T Nielsen Dansk Gasteknisk Center	150
059	Marknadspotential naturgaseldade industriella IR-strålare	Apr 95	Rolf Christensen Enerkon RC	150
060	Rekommendationer vid val av flexibla insatsrör av rostfritt i villaskorstenar	Maj 95	L Hedeen, G Björklund Sydgas AB	50
061	Polyamidrör för distribution av gasol i gasfas. Kunskapssammanställning	Jul 95	Tomas Tränkner Studsvik Material AB	150
062	PE-rörs tålighet mot yttre påverkan. Sammanställning av utförda praktiska försök	Aug 95	Tomas Tränkner Studsvik Material AB	150
063	Naturgas på hjul. Förutsättningar för en storskalig satsning på NGV i Sverige	Aug 95	Naturgasbolagens NGV- grupp	150
064	Energieffektivisering av större gaseldade pannanläggningar. Handbok	Aug 95	Lars Frederiksen Dansk Gasteknisk Center	200
065	Förbättra miljön med gasdrivna fordon	Aug 95	Göteborg Energi AB	150
066	Konvertering av oljeeldade panncentraler till naturgas. Handbok.	Nov 95	Bo Cederholm Sydkraft Konsult AB	150

RAPPORTFÖRTECKNING

SGC Nr	Rapportnamn	Rapport datum	Författare	Pris kr
067	Naturgasmodellen. Manual för SMHI:s program för beräkn av skorstenshöjder	Dec 95	Tingnert B, SKKB Thunell J, SGC	150
068	Energigas och oxyfuelteknik	Dec 95	Ingemar Gunnarsson Energi-Analys AB	150
069	CO2-gödsling med avgaser från gasmotor med katalysator	Dec 95	Bent Karll Dansk Gasteknisk Center	150
070	Utvärdering av naturgasförbränning i porösa bäddar	Mar 96	Henric Larsson Lunds Tekniska Högskola	150
071	Utvärdering av naturgasdrivna IR-boostrar i ugn för pulverlackering	Nov 95	Ole H Madsen Asger N Myken	150
072	Sammanställning av emissionsdata från naturgas-, biogas- o motorgasdrivna fordon	Jun 96	Hans-Åke Maltesson Svenskt Gastekniskt Center AB	150
073	Livslängdsbestämning för PE-rör för gasdistribution (EVOPE-projektet)	Jul 96	Tomas Tränkner Studsvik Material AB	100
074	Gasblandningar för fordonsdrift. Idéstudie.	Aug 96	Ola Hall Sydkraft Konsult AB	150
075	Gasbranschens miljöhandbok	Sep 96	Jörgen Thunell Svenskt Gastekniskt Center	500
076	Låg-NOx-teknik för gasdrivna processer - dagsläge	Okt 96	Mikael Näslund, LTH Inst.Värme- och Kraftteknik, LTH	150
077	Karakterisering av emissioner från naturgasdrivna lastbilar inom LB 50 -projektet	Dec 96	K-E Egebäck Roger Westerholm	150
078	Uppvärmning med gas i svenska småhus - erfarenheter och framtida teknikval	Nov 96	Mikael Näslund, LTH	150
079	Handledn. för inst av gaseldade IR -värmare. Rådgivning, analys och genomförande	Apr 97	Pär Dalin DITAB	150
080	Mikrokraftvärmeverk med Stirlingmotor	Jan 97	Tomas Nilsson Lunds Tekniska Högskola	150
081	Naturgasbaserad småskalig kraftvärme inom uppvärmningssektorn	Feb 97	Mats Nilsson LTH/MALMÖ	150
082	Kylning och klimatisering av byggnader och lokaler med hjälp av naturgas	Apr 97	Anders Lindkvist Vattenfall Energisystem	150

RAPPORTFÖRTECKNING

SGC Nr	Rapportnamn	Rapport datum	Författare	Pris kr
083	Naturgassystemet i Sverige - en teknisk beskrivning	Jun 97	Ronny Nilsson, KM	150
084	Livscykelanalyser - Är det något för gasbranschen	Sep 97	Jörgen Thunell	150
085	Konvertering av direktelvärmda småhus till naturgasuppvärmning	Dec 97	Mikael Näslund Inst Värme- och Kraftteknik, LTH	150
086	Uppgradering av biogas . Fas 2, Praktiska försök med kondenseringsmetoder.	Jun 97	Ola Lloyd / BioMil AB Johan Nilsson / LTH	150
087	Utveckling av katatalytisk rening av avgaser från befintlig panna	Dec 97	F Silversand, T Hargitai m fl Katator AB	150
088	Technical Description of the Swedish Natural Gas Distr System (På Engelska)	Jun 97	Ronny Nilsson, KM	150
089	Rening av avgaser från en naturgasdriven lean burn motor i en förbr.växlare	Okt 97	Björn Heed Inst för Energiteknik, CTH	150
090	Utsläpp av oreglerade ämnen vid förbränning av olika bränslen	Jun 98	Jörgen Thunell	150
091	Nya metoder för att säkerställa mätnoggrannheten i naturgasnät	Nov 97	Ulf R C Nilsson Luleå TH, Inst Systemteknik	150
092	LB30-projektet - Introduktion av naturgasdrivna tyngre lastbilar	Jan 99	Owe Jönsson Svenskt Gastekniskt Center	150
093	Karaktärisering av emissioner från naturgasdrivna lastbilar inom LB50 -projektet	Sep 98	Karl Erik Egebäck	150
094	Gasdistribution och avgasinstallation i byggnader	Jan 99	Hans Christian Thiis Per Palm	150
095	Karaktärisering av emissioner från naturgasdrivna lastbilar inom LB50 -projektet	Okt 98	Karl Erik Egebäck	150
096	Lifetime of PE-pipes subjected to squeeze off	Nov 98	Tomas Tränkner	150
097	Svensk högskoleförlagd energigasforskning Nutid och framtid	Jan 99	Mikael Näslund, LTH Owe Jönsson, SGC	150
098	Metoder för snabb kvalitetskontroll av PE -rör för gasdistribution	Apr 99	Tomas Tränkner	150

RAPPORTFÖRTECKNING

SGC Nr	Rapportnamn	Rapport datum	Författare	Pris kr
099	Gas co-firing for NOx-reduction in coal fired boilers	Apr 99	Fredrik Brogaard	200
A01	Fordonstankstation Naturgas. Parallellkoppling av 4 st Fuel Makers	Feb 95	Per Carlsson Göteborg Energi AB	50
A02	Uppföljning av gaseldade luftvärmare vid Arlövs Sockerraffinaderi	Jul 95	Rolf Christensen Enercon RC	50
A03	Gasanvändning för färjedrift. Förstudie (Endast för internt bruk)	Jul 95	Gunnar Sandström Sydkraft Konsult	0
A04	Bussbuller. Förslag till mätprogram	Jun 95	Ingemar Carlsson Ecotrans Teknik AB	50
A05	Värmning av vätskor med naturgas - Bakgrund till faktablad	Okt 95	Rolf Christensen Enerkon RC	50
A06	Isbildning i naturgasbussar och CNG -system (Endast för internt bruk)	Nov 95	Volvo Aero Turbines Sydgas, SGC	0
A07	Större keramisk fiberbrännare. Förstudie	Jan 96	Per Carlsson Sydkraft Konsult AB	50
A08	Reduktion av dioxin, furan- och klorfenoler vid avfallsförbränning	Maj 96	H Palmén, M Lampinen et al Helsingfors Tekniska Högskola	50
A09	Naturgas/mikrovågsteknik för sintring av keramer	Maj 96	Anders Röstin KTH	50
A10	NOx-reduktion genom naturgasinjektion o reburning. Demoprojekt på Knudmoseverket	Apr 96	Jan Flensted Poulsen Völund R & D Center	50
A11	Direkttorkning av socker med naturgas (Endast för internt bruk)	Jul 96	Rolf Christensen Enerkon RC	0
A12	Uppföljning, installation av gaspanna med avgaskondensor, kv Hornblåsaren 6, Råå	Sep 96	Bo Cederholm Sydkraft Konsult AB	50
A13	Klassningsplaner för gasinstallationer	Jun 97	Carl-Axel Stenberg Greger Arnesson	50
A14	Uppf av drift med natugaseldad kondenserande gaspanna i Rinnebäcksskolan	Okt 97	Bo Cederholm Sydkraft Konsult AB	50
A15	Undersökn o förstärkn av korr.skyddet på gasrör förl i skyddsrör - Delrapport 1	Nov 97	Åsa Marbe, C Johansson Sydkraft Konsult AB	100

RAPPORTFÖRTECKNING

SGC Nr	Rapportnamn	Rapport datum	Författare	Pris kr
A16	Ind - CO2-härdning av betong med naturgas	Feb 98	Åsa Marbe Sydkraft Konsult AB	50
A17	Reservförsörjning med fordonstransporterad LNG	Dec 97	Stig Johansen	50
A18	Emissions- och immissionsmätning vid en naturgaseldad villapanna	Mar 97	David Cooper IVL	50
A19	Katalytisk rening av gaseldade lean -burnmotorer etapp 1 - teoretisk förstudie	Aug98	Fredrik Silversand Katator	100
A20	Europeisk livscykelinventering för naturgas (endast för internt bruk)	Sep 98	Jörgen Thunell	0
A21	Naturgasdrivna järnvägsfordon - Förstudie	Dec 98	Rolf Öberg	100
A22	Catalytic abatement of CO- and UHC -emissions from Gas Fuelled Engines	Feb99	Fredrik Silversand	100
A23	Förläggning av gasrör av polyeten i befintliga massor	Mar 99	Gunnar Bergström Stefan Nilsson	100

SGC
Svenskt Gastekniskt Center AB

S-205 09 MALMÖ
Telefon: 040-24 43 10
Telefax: 040-24 43 14

KFS AB, LUND